Design, Synthesis and Properties of Multivalent DNA Nanomaterials for Cancer Diagnostics and Therapeutics

A thesis submitted to the Board of Mathematical, Physical and Life Sciences Division, Department of Chemistry in partial fulfilment for the degree of

Doctor of Philosophy

Jinfeng Chen

St. Cross College, University of Oxford
Trinity Term 2019



Design, Synthesis and Properties of Multivalent DNA Nanomaterials for Cancer Diagnostics and Therapeutics

Jinfeng Chen

Doctor of Philosophy, St. Cross College, Trinity Term 2019

Abstract

Aptamer-functionalised DNA nanostructures have been developed as drug nanocarriers for targeted cancer therapy and other *in vivo* applications. Among them, hierarchical DNA nanoflowers (DNA-NFs) with densely packed DNA that can self-assemble using rolling circle amplification (RCA) hold promise for cancer therapy. To expand the functionality of DNA-NFs, the inorganic core of the nanoflowers was chemically modified through substitution of Mg^{2+} with either Mn^{2+} or Co^{2+} during the RCA process, resulting in formation of nanomaterials in a range of morphologies. These nanoconstructs retain the stability against enzymatic degradation of their magnesium counterparts and the Mn^{2+} and Co^{2+} DNA-NFs were endowed with magnetic properties. Cyclic nucleic acid templates are essential substrates in RCA reactions, and are most commonly obtained *via* enzymatic cyclisation. However, the cyclisation efficiency mainly depends upon the length of the linear precursor and is inefficient when the linear oligonucleotide has complex secondary structures. To circumvent the limitations of enzyme-catalysed DNA cyclisation, three different chemical cyclisation approaches were explored for the preparation of single-stranded cyclic DNA constructs. These chemical cyclisation methods are cheaper and easier to carry out in a large scale than their ligase-mediated counterpart. They can also be carried out under denaturing conditions and are therefore particular valuable for cyclic DNA templates containing complicated secondary structure.

The resulting cyclic DNA templates contain a single unnatural backbone linkage at the ligation site (triazole, phosphoramidate or amide). They were compared to unmodified cyclic DNA templates in RCA reactions using Φ-29 and Bst 2.0 DNA polymerases. The phosphoramidate-modified cyclic templates were particularly well tolerated by Φ-29 DNA polymerase, consistently performing as well as the unmodified natural backbone in RCA. In contrast, the cyclic templates containing a triazole backbone linkage generally showed lower and more variable yields of RCA products, a significant proportion of which were double-stranded DNA side-products. The performance of the amide-modified cyclic templates fell in between those of the triazole- and phosphoramidate-modified cyclic templates. Moreover, all cyclic templates containing modified backbone linkage could be used to produce DNA-NFs during the RCA process.

Declaration of Authorship

I, Jinfeng Chen, declare that this thesis and the work presented in it are my own and have been generated by me as the result of my own original research.

I confirm that:

- This work was done wholly while in candidature for a research degree at this University;
- Where I have consulted the published work of others, this is always clearly attributed;
- Where I have quoted from the work of others, the source is always given. With the exception of such quotations, this thesis is entirely my own work;
- I have acknowledged all main sources of help;
- Where the thesis is based on work done by myself jointly with others, I have made clear exactly what was done by others and what I have contributed myself;

Acknowledgements

First and foremost, I would like to express my deepest gratitude to my supervisor Prof. Tom Brown for offering me a DPhil position and giving me this wonderful opportunity to work on fascinating research work. I am also thankful for the valuable guidance, support and encouragement during this DPhil. Also thank you for imparting so much nucleic acid knowledge, endless great ideas and enthusiasm for research. Many of these are already and will be valuable assets in my research career. This thesis would not have been possible without him.

I am also grateful to Prof. Afaf El-Sagheer for all her brilliant suggestions during my research work. Thank you for providing selfless care and sharing your knowledge and experience throughout these years. Your attitude and enthusiasm on scientific research are excellent example that are contagious and motivational for me.

Particular thanks to Dr. Ysobel R. Baker and Dr. Asha Brown for their contributions in the modified backbone RCA work. Many thanks to both of you for answering my questions and sharing your expertise. Great thanks to Dr. Baker for giving me so much help, advices and encouragement during my DPhil study. Additionally, I am so gratitude to Prof. Tom Brown, Prof. Afaf El-Sagheer, Dr. Ysobel R. Baker, Sara Walsh, Jack Hardwick, Ashley Tsai, Cameron Thorpe and Jia Zhao for their patience in proofreading this thesis making it much more comprehensible.

To all the Brownies – Ashley, Arun, Cam, Chunsen, Ellia, Jack H, Piotr, Pui, Phoebe, Sara, Sven, Sarah W, Thanishta, Tom F, Yssy and Yutong, I have enjoyed working with you all, and thank you for all the comforting conversations and good memories we have

shared throughout these years. You are the ones who made this DPhil fantastic and unforgettable.

I would like to acknowledge Prof. Robert Carlisle (The Institute of Biomedical Engineering, University of Oxford) and Megan Grundy (The Institute of Biomedical Engineering, University of Oxford) for helping me with FACS experiments and cell work.

Last but not least, I am deeply indebted to my parents for their endless love, support and encouragement in all my pursuits. Huge thanks to my beloved wife, for her support and understanding. Also, great thanks to my sister and brother-in-law, for their endless care and encouragement. I love you all – my families.

Thank you God, for all the blessings and for letting me through all the difficulties.

Abbreviations

A	Adenine
Å	Ångstrom
Abs	Absorbance
Apt	Aptamer(s)
Am	Amide linkage
aq	Aqueous
AMP/ATP	Adenosine monophosphate/triphosphate
BSA	Bovine serum albumin
C	Molar concentration
C	Cytosine
°C	Degree celsius
con.	Concentration
CoDNA-NFs	Cobalt DNA nanoflowers
CD	Circular dichroism
CuAAC	Copper-catalysed azide-alkyne cycloaddition
Cy3	Trimethine cyanine dye
Da	Dalton
DMF	Dimethylformamide
DMSO	Dimethyl sulfoxide
DMT	4,4′-dimethoxytrityl (protecting group)
DNA	Deoxyribonucleic acid
DNA-NFs	DNA nanoflowers
dNTPs	Deoxynucleoside triphosphates

DPBS	Dulbecco's phosphate-buffered saline
EDTA	Ethylenediaminetetraacetic acid
EDC·HCl	1-ethyl-3-(3-dimethylaminopropyl)carbodiimide hydrochloride
ESI	Electrospray ionisation
eq	Equivalent(s)
FACS	Fluorescence-associated cell sorting
FDA	Food and Drug Administration
FITC	Fluorescein isothiocyanate
G	Guanine
h	Hour(s)
HER2	Human epidermal growth factor receptor 2
HEPES	4-(2-hydroxyethyl)-1-piperazineethanesulfonic acid
HPLC	High performance liquid chromatography
HRCA	Hyperbranched rolling circle amplification
Kb	Kilobase pair
K_d	Dissociation constant
l	Light path length in cm
M	Molar concentration
min	Minute(s)
MgDNA-NFs	Magnesium DNA nanoflowers
MnDNA-NFs	Manganese DNA nanoflowers
MRI	Magnetic resonance imaging
mRNA	Messenger RNA
MUC1	Mucin 1
nt	Nucleotide(s)

NTri-SAAP	Nanotriangle-scaffolded multivalent split activatable aptamer probe
μM	Micromolar concentration
NHS	N-hydroxysuccinimide
ODN	Oligonucleotide
PA	Phosphoramidate linkage
PAGE	Polyacrylamide gel electrophoresis
PBS	Phosphate buffered saline
PCR	Polymerase cycling reaction
PPi	Pyrophosphate
RCA	Rolling circle amplification
RCT	Rolling circle transcription
RNA	Ribonucleic acid
RNA-MSs	RNA microsponges
RP-HPLC	Reversed-phase high performance liquid chromatography
RT	Room temperature
SELEX	Systematic evolution of ligands by exponential enrichment
SEM	Scanning electron microscopy
siRNA	Small interfering RNA
sgRNA	Single guide RNA
SNPs	Single nucleotide polymorphisms
ssDNA	Single-stranded DNA
T	Thymine
TBE	Tris/Borate/EDTA
TBDMS	*Tert*-butyldimethylsilyl (protecting group)
TCA	Trichloroacetic acid

TEAB	Triethylammonium bicarbonate
THPTA	Tris(3-hydroxypropyltriazolylmethyl)amine
T_m	Melting temperature
Tz	Triazole linkage
U	Uracil
UV	Ultraviolet
W	Watt(s)
ε	Extinction coefficient

Contents

Abstract i

Declaration of Authorship iii

Acknowledgements iv

Abbreviations vi

Contents x

Chapter 1 – General introduction 2

1.1 Nucleic acids 2

1.1.1 Primary structure of nucleic acids 2

1.1.2 Secondary structure of nucleic acids 5

1.2 Aptamers 11

1.2.1 Aptamers versus antibodies 12

1.2.2 Applications of aptamers 13

1.3 Solid-phase synthesis of oligonucleotides 13

1.4 Cyclisation of single-stranded oligonucleotides 17

1.4.1 Enzymatic cyclisation 18

1.4.2 Chemical cyclisation 19

1.4.2.1 "Click" cyclisation using the copper(I)-catalysed azide-alkyne cycloaddition reaction (CuAAC) 20

1.4.2.2 Phosphoramidate cyclisation using the di-imide coupling reaction 22

1.4.2.3 Amide cyclisation using the di-imide coupling reaction 22

1.4.3 Applications of cyclic oligonucleotides 23

1.5 Rolling circle amplification 23

1.5.1 Classification of RCA 25

1.5.1.1 Exponential RCA 25

1.5.1.2 Linear RCA 25

1.5.2 Applications of RCA 26

1.6 Aptamer-incorporated DNA nanostructures 26
1.6.1 Hybridisation-dependent nucleic acid assembly 27
1.6.2 Non-hybridisation-dependent DNA assembly 27
1.6.3 Application of aptamer-incorporated DNA nanostructures in cancer therapy 28
1.7 Research aims and thesis structure 29
Chapter 2 – Synthesis and characterisation of reported HER2 aptamers 32
2.1 Introduction and aims 32
2.2 Preparation and synthesis of reported HER2 aptamers 33
2.3 Characterisation of reported HER2 aptamers 35
2.3.1 Initial assessment of aptamer binding ability using fluorescence-associated cell sorting 35
2.3.2 Investigating aptamer structures using circular dichroism 38
2.3.3 Investigating aptamer secondary structure using native polyacrylamide gel electrophoresis 41
2.3.4 Investigating aptamer stability using UV melting 43
2.3.5 Assessment and optimisation of aptamer binding using fluorescence-associated cell sorting 44
2.3.5.1 Comparison of enzymatic and non-enzymatic cell dissociation effects on fluorescence-associated cell sorting assays 46
2.3.5.2 Investigating the effect of aptamer concentration on HER2 binding using fluorescence-associated cell sorting 47
2.3.5.3 Investigating the effect of incubation temperature on HER2 binding using fluorescence-associated cell sorting 48
2.3.5.4 Comparing new and old batches of MDA-MB-468 cell line 52
2.3.5.5 Investigating aptamer binding properties for MCF-7 cell line (HER1-/HER2-) using fluorescence-associated cell sorting 54
2.3.6 Investigating aptamer cellular uptake using confocal microscopy 55
2.4 Conclusions 58
Chapter 3 – Preparation and characterisation of manganese and cobalt DNA nanoflowers 61
3.1 Preface 61
3.2 Introduction and aims 61

3.3 Manganese DNA nanoflowers 63
3.3.1 Variables for controlling morphology and DNA levels within the manganese DNA nanoflowers 64
3.4 Cobalt DNA nanoflowers 71
3.5 Serum stability of DNA nanoflowers 76
3.6 Hybridisation properties 81
3.7 Conclusions 83
Chapter 4 – Synthesis of cyclic single-stranded DNA constructs and their application 85
4.1 Preface 85
4.2 Introduction and aims 85
4.3 Choice of backbone linkages and template sequences 88
4.4 Synthesis of cyclic oligonucleotides..... 93
4.4.1 Enzymatic cyclisation with a canonical phosphodiester backbone linkage…..... 93
4.4.2 Chemical cyclisation by introducing chemically modified backbone linkages……...101
4.4.2.1 Modified backbone with triazole linkage 102
4.4.2.2 Modified backbone with phosphoramidate linkage..... 108
4.4.2.3 Modified backbone with amide linkage 111
4.5 Rolling circle amplification of the cyclic oligonucleotides..... 113
4.5.1 RCA using the Φ-29 DNA polymerase..... 114
4.5.1.1 Probing the single-stranded RCA products with complementary fluorescent oligonucleotides 122
4.5.1.2 Probing the nature and quantity of the RCA products *via* a fluorometric plate-reading assay 126
4.5.2 RCA using the Bst 2.0 DNA polymerase 128
4.5.2.1 Probing the nature and quantity of the RCA products *via* a fluorometric plate-reading assay 134
4.6 Nanoflower formation 136
4.7 Conclusions 142
Chapter 5 – Conclusions and future work 145
Chapter 6 – Experimental..... 149
6.1 General information..... 149

6.2 Oligonucleotides synthesis and purification 151
6.2.1 General methods for synthesis and purification of linear oligonucleotides 151
6.3 Biophysical studies of aptamers 161
6.3.1 Structural study of aptamers using circular dichroism 161
6.3.2 Structural study of aptamers using native polyacrylamide gel electrophoresis 162
6.3.3 Thermal stability study of aptamers using UV melting 164
6.4 Cell biology 165
6.4.1 Fluorescence-associated cell sorting analysis (FACS) 166
6.4.2 Confocal microscopy imaging of cancer cells bound with Cy3 labelled aptamer…..... 171
6.5 Preparation of manganese and cobalt DNA nanoflowers 171
6.5.1 Screening experiments 172
6.5.2 Comparison of DNA levels using SYBR Gold 174
6.5.3 Preparation of manganese and cobalt particles using cyclic T2 175
6.5.4 Preparation of manganese and cobalt particles for magnetic studies 180
6.5.5 Enzymatic stability studies 181
6.5.6 Hybridisation studies 182
6.6 Synthesis of cyclic oligonucleotides using enzymatic and chemical methods.. 182
6.6.1 Enzymatic cyclisation of the linear oligonucleotides 182
6.6.2 Chemical cyclisation of the linear oligonucleotides 183
6.7 Rolling circle amplification 185
6.8 DNA nanoflower experiments 189
References 192
Appendix 212

Chapter 1

General introduction

Chapter 1 – General introduction

1.1 Nucleic acids

1.1.1 Primary structure of nucleic acids

Nucleic acids are important biopolymers responsible for storing genetic information in all forms of life. There are two types of nucleic acids, deoxyribonucleic acid (DNA) and ribonucleic acid (RNA), which have great chemical similarities. They are made up of nucleotide monomers, which are composed of three components: a pentose (five-carbon) sugar (2′-deoxy-D-ribose in DNA and D-ribose in RNA), a nitrogenous heterocyclic base and a phosphate group. The nucleobases can be divided into two groups: bicyclic purines (adenine and guanine), and pyrimidines (cytosine, thymine and uracil). Adenine, cytosine and guanine are found in both DNA and RNA, whereas thymine is replaced by uracil in RNA (Figure 1.1).[1]

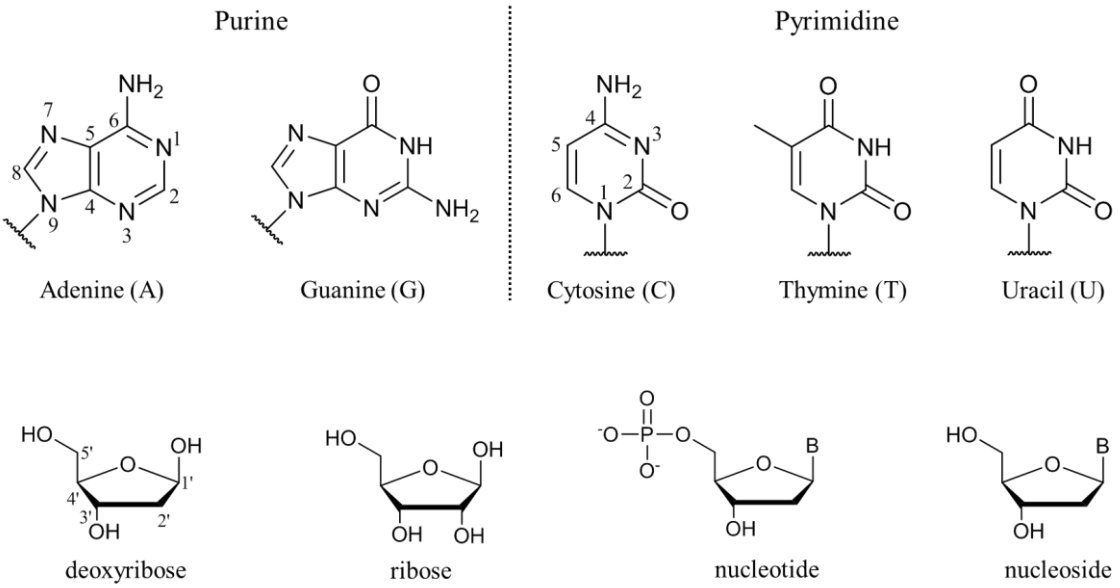


Figure 1.1. Chemical structure of heterocyclic bases of nucleic acids, nucleotide and nucleoside. Purine: adenine (A), guanine (G); pyrimidine: cytosine (C), thymine (T) and uracil (U). 'B' represents any of the heterocyclic bases.

The heterocyclic base is attached to the pentose sugar *via* an *N*-glycosidic bond involving the C-1′ of the pentose sugar ring and a nucleobase ring nitrogen (N-1 of pyrimidines or N-9 of purines) to give a nucleoside. The pentose sugar in DNA is 2′-deoxy-D-ribose, whereas in RNA it is D-ribose. There are four deoxynucleosides in DNA: deoxyadenosine, deoxyguanosine, deoxythymidine and deoxycytidine and four types of ribonucleosides in RNA: adenosine, guanosine, uridine and cytidine. The heterocyclic base joined to the sugar C-1′ can either lie on the same face of the sugar ring as the 5′-hydroxyl group (β-anomer) or on the opposite face (α-anomer). In DNA all nucleosides adopt the β-configuration (Figure 1.2).

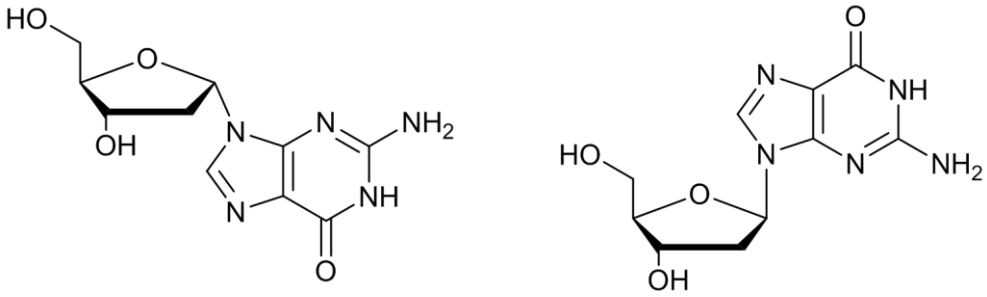


Figure 1.2. Chemical structures of nucleoside α- and β-anomers.

Nucleobases can rotate around the *N*-glycosidic bond giving rise to two extreme *syn*- and *anti*-conformations (Figure 1.3). Moreover, the *anti*-conformation predominates in naturally occurring nucleotides due to steric interference from the sugar moiety in the *syn*-conformation.[2]

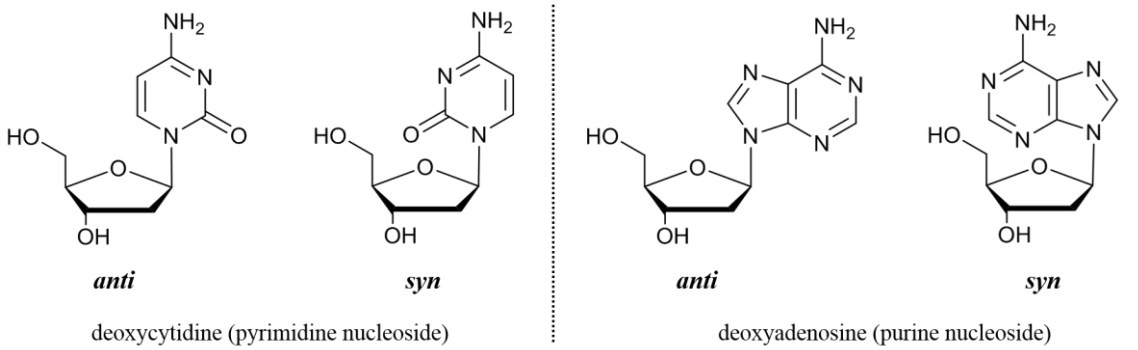


Figure 1.3. Chemical structures of *syn*- and *anti*-conformations of a pyrimidine nucleoside (deoxycytidine) and a purine nucleoside (deoxyadenosine).

The primary structure of nucleic acids (single-strand form) has directionality. The specific nucleobase sequence is conventionally written from the 5′- to 3′-direction (Figure 1.4).

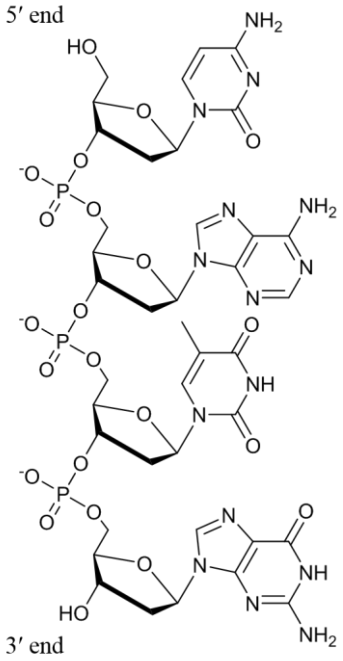
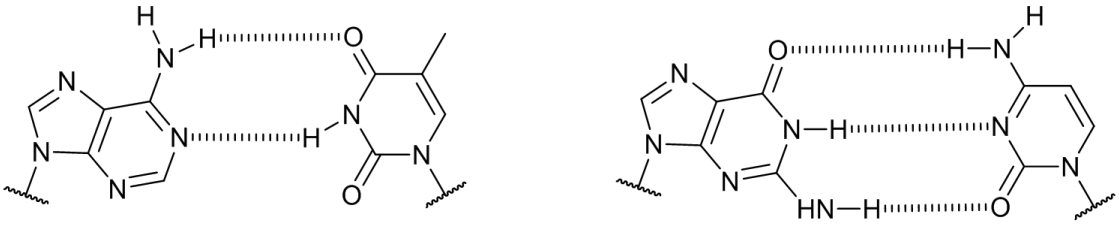


Figure 1.4. Primary structure of oligonucleotides. The example shown here is a single-stranded DNA with 5′-CATG-3′ sequence.

1.1.2 Secondary structure of nucleic acids

One of the crucial discoveries on DNA structure was proposed by Erwin Chargaff in 1949, suggesting the amount of adenine always equalled the amount of thymine, and similarly for guanine and cytosine.[3] This was followed by the findings from X-ray diffraction of DNA fibres by Maurice Wilkins and Rosalind Franklin, who proposed that the secondary structure of DNA is helical, and also the precise form can differ depending on the humidity.[4-6] In 1953 James Watson and Francis Crick consolidated this information and elucidated the biologically relevant structure of DNA, which is a double helix.[7] They found that the two strands are antiparallel, i.e. running in opposite directions - one strand 5′ - 3′ and the other 3′ - 5′. These two complementary nucleic acid strands are held together *via* hydrogen bonds between nucleobases, yielding Watson-Crick base pairs. Specifically, adenine pairs with thymidine (uridine in RNA) by two hydrogen bonds and cytosine interacts with guanine *via* three hydrogen bonds (Figure 1.5).



AT base pair **GC base pair**

Figure 1.5. Watson-Crick base pairing: AT and GC pairs. Hydrogen bonds are presented as dashed lines.

Three major conformations adopted by double-stranded DNA are A-, B-, and Z-forms (Figure 1.6). Both A-DNA and B-DNA are right-handed helices, whereas Z-form is left-handed. B-DNA is the most common form found in DNA at neutral pH and physiological conditions. In B-DNA, the base pairs are positioned directly on the helix axis so that the

major groove and minor groove are roughly equivalent in depth, but with a wider major groove compared to the minor groove. Both minor and major grooves provide binding opportunities for external molecules. Many large molecules interact in the major groove,[8,9] whereas a few proteins and small molecules are known to bind in the minor groove.[10,11] Within the helical structure the hydrophobic bases are stacked upon each other. The distance between two successive base pairs, known as inter-base distance, is around 3.4 Å. Each 36 Å helix pitch contains 10.5 base pairs, and the helix diameter is 20 Å. The sugars have the C2′-*endo* pucker and all the glycosides adopt the *anti*-conformation.[2] This is shown in Figure 1.6B.

The A-form helix is wider and more compact length-wise than that of B-form. It has 11 base pairs in each full turn of 28 Å, and the inter-base distance is 2.55 Å. In order to maintain the normal van der Waals separation, the stacked bases are displaced off-axis and tilted sideways. The furanose sugars have a C3′-*endo* pucker and the glycosylic bonds are in the *anti*-conformation. As a result of these features, the major groove of this form is narrow and deep, and the minor groove is extremely wide and shallow (Figure 1.6A).[2,12,13] The A-form is also a major conformation in RNA:DNA duplexes and RNA:RNA duplexes.

The Z-DNA is also an anti-parallel duplex but is quite different from its A- and B-form counterparts. It has a left-handed helical structure that repeats every other base pair and is the least compact. Unlike A- and B-DNA, the major and minor grooves of Z-form have little difference in width. Z-DNA is thinner and more elongated, with a flat major groove and deep, narrow minor groove (Figure 1.6A).[4] It has 11.6 base pairs in each helical turn periodicity and the helix diameter is approximately 18 Å. The base pairs are displaced off-axis and the phosphate backbone has a zig-zag appearance. The purines are in the *syn*-

conformation and the sugars have C3′-*endo* pucker, while the pyrimidines adopt the *anti*-conformation with the sugars in C2′-*endo* conformation. Z-form is generally unfavourable, although specific conditions can afford it such as synthesis of double-stranded nucleic acid consisting of an alternating purine-pyrimidine sequence, especially poly(dCpG)$_n$. It is difficult to study the Z-form DNA because it does not easily form a stable feature of the double helix. Although it is occasionally induced to be a transient structure under required biological conditions, this conformation will quickly disappear.[4,14]

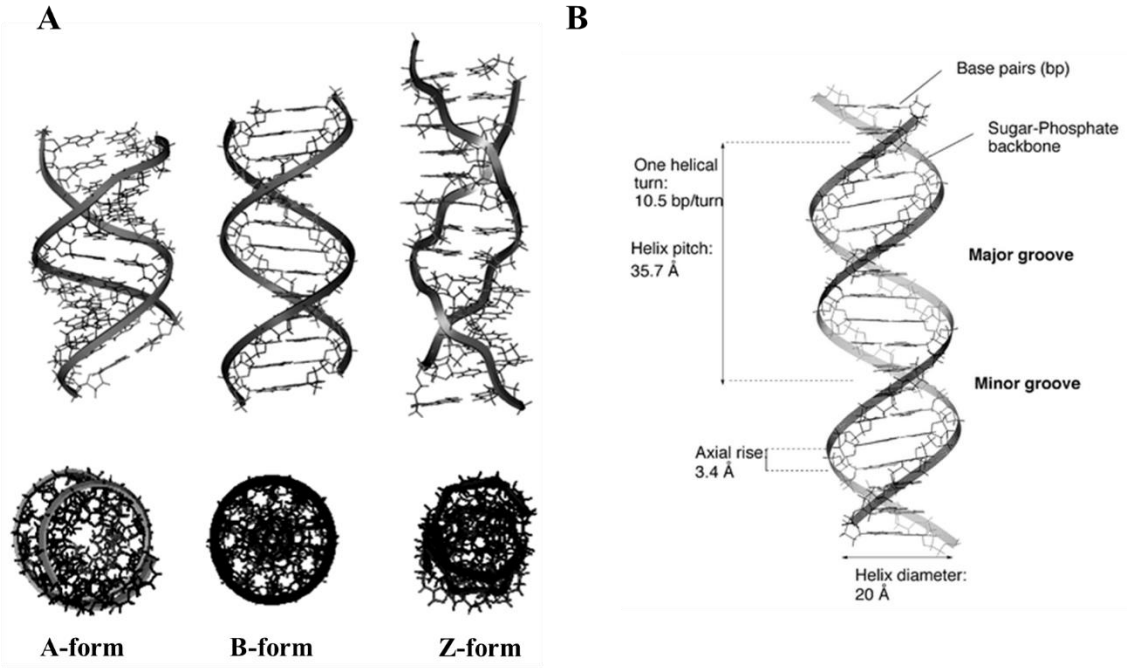


Figure 1.6. (A) Major duplex conformations in DNA (A-, B- and Z-forms) top and side views. The sugar-phosphate backbone is represented as a ribbon. (B) Structure of B-form of nucleic acids with parameters. The figures are adapted with permission from[4].

Apart from Watson-Crick base pairing, nucleobases can also form hydrogen bonds *via* Hoogsteen or reverse Hoogsteen hydrogen bonds.[15] This allows a third single-stranded region of DNA to pair with duplex DNA helix. The resultant three-stranded structures are referred to as triplex DNA. Two main structural motifs of triplex formation have been

characterised depending on the base composition and binding orientation of the third strand;[16] purine rich third strands bind to the duplex purine strand in an antiparallel fashion and include A·AT, T·AT and G·GC triplets, whereas pyrimidine rich oligonucleotides bind in parallel orientation and induced T·AT and C^+·GC (Figure 1.7). Although triplexes are formed by sequence specific binding rules, they are generally less stable than duplexes due to their slower formation rate and the electrostatic repulsion between the three polyanionic backbones.[17] In general, parallel triplexes formation require low pH (<6) conditions to protonate cytosines in the third strand, whereas antiparallel structures are formed without base protonation exhibiting pH independence.

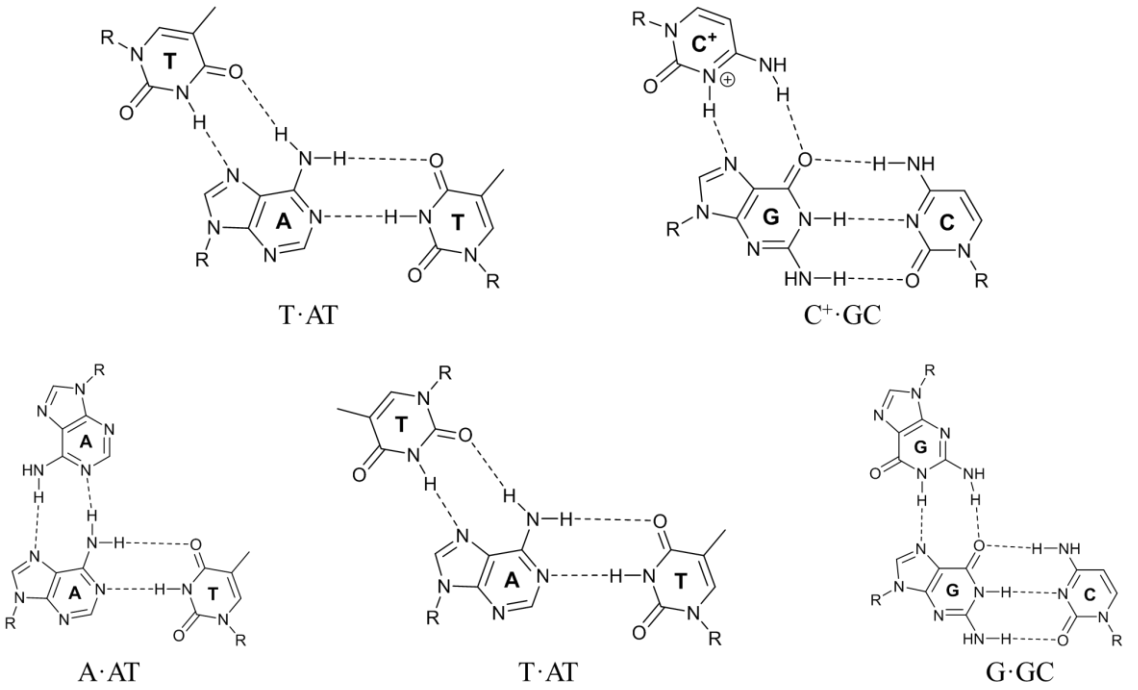


Figure 1.7. Chemical structures of parallel triplets: T·AT and C^+·GC (top) and antiparallel triplets: A·AT, T·AT and G·GC (bottom).

Hoogsteen-type base pairing can also occur between four guanines to form a square planar structure, termed as guanine tetrad (G-tetrad) (Figure 1.8A). Two or more tetrads can stack up on top of one another to form a G-quadruplex structure that differs from the

canonical Watson-Crick base paired double helix.[18-20] G-quadruplexes can be formed from one, two or four separate strands of oligonucleotides with specific repetitive guanine-rich sequences, and are stabilised by monovalent cations.[4] These stabilising cations can coordinate to the G-tetrad, where the closely spaced O-6 carbonyl oxygens of the G-tetrad interact with the cation *via* the free electron pairs.[21,22] G-quadruplex stabilisation follows the general trend of $Li^+ < NH_4^+ < Na^+ < K^+$, and most studies involve sodium or potassium cations due to their prevalence in human cells.[23] Sodium ions bind in the central cavity of a single tetrad, whereas ions with large radii like potassium lie between two G-tetrads. G-quadruplexes are highly polymorphic in nature and can be classified into various types according to the orientation of the DNA strands (Figure 1.8B).[24] These structures therefore can be parallel, antiparallel or a combination of both. Furthermore, intramolecular complexes can be generated within one strand, whereas intermolecular quadruplexes are formed by the association of multiple strands.[23] The topology and stability of the G-quadruplex depend upon several factors, including the length and base composition of the oligonucleotide, strand stoichiometry, orientation, the nature of the coordination cations and the size of the loops between the guanines.[15,24]

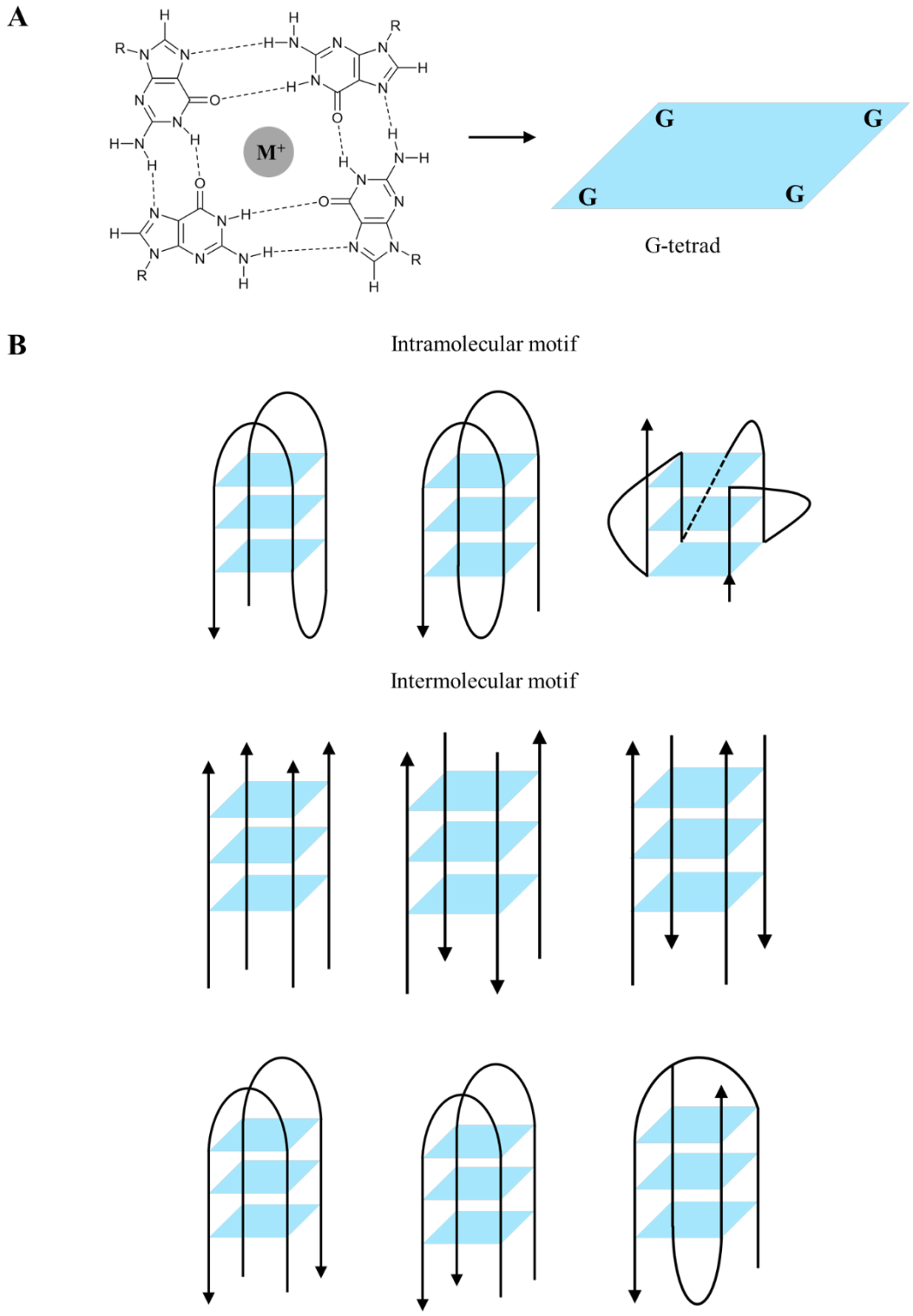
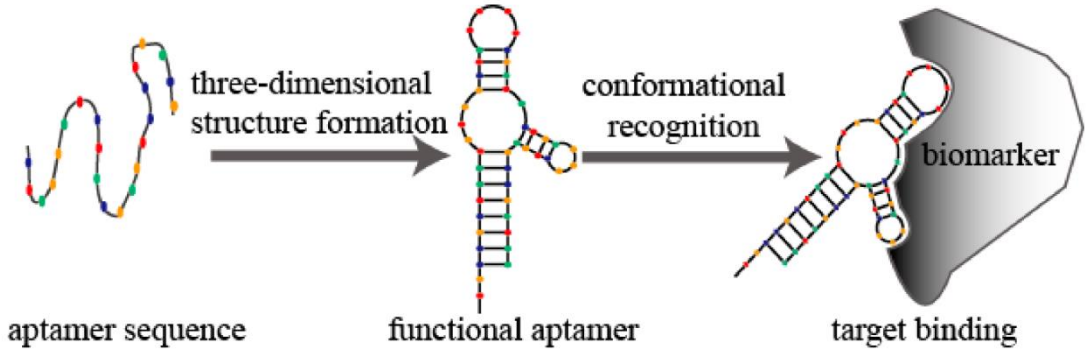


Figure 1.8. The structure of G-quadruplex. (A) Chemical structure of the G-tetrad. Hoogsteen hydrogen bonding shown as dotted lines give rise to G-tetrad. The formation of G-quadruplex is driven by monovalent cations (M^+). (B) Schematic illustration of intramolecular and intermolecular G-quadruplex structures. The intermolecular G-quadruplex structures are formed by the association of two (bottom) or four (up) strands.

1.2 Aptamers

Nucleic acid aptamers are short single-stranded DNA- or RNA-based oligonucleotides (ranging from 15 - 100 nucleotides (nt) in length),[25,26] which were first reported nearly 30 years ago by Gold and Ellington.[27,28] They are most often identified using an *in vitro* method called systematic evolution of ligands by exponential enrichment (SELEX).[27] Aptamers can fold into unique three-dimensional conformations, possessing a combination of stems, hairpins, loops, bulges, G-quadruplexes and/or pseudoknots,[29-33] and are able to interact specifically with various chemical species (Scheme 1.1).[34,35] Aptamers can be composed of DNA or RNA. The binding of an aptamer to its target is through aromatic interactions, hydrogen bonding, π-π stacking, van der Waals forces, electrostatic interactions and shape complementarity.[33,36] Aptamer-target interactions can have low dissociation constants (K_d) ranging from pico- to nanomolar,[37] and can sometimes be comparable to antibodies. Therefore, aptamers are also known as "chemical antibodies".



Scheme 1.1. Schematic diagram of aptamer specifically recognising its target. The figure was adapted with permission from[38].

1.2.1 Aptamers versus antibodies

Over three decades, antibodies have been used for biomolecular recognition in many applications, in a wide range of research fields and with great success. There are limits to their utility that are imposed by their large size and biological nature, which could slow down their development, especially in therapeutics.[39] Aptamers are excellent candidates to replace monoclonal antibodies in some applications due to several potential advantages:

(i) higher stability of aptamers: Antibodies are easily denatured, lose their tertiary structure under non-physiological conditions, and cannot easily be re-folded correctly, whereas the activity and functionality of aptamers can be easily recovered since they undergo reversible denaturation.[40-43] Therefore, aptamers can be used under a wide range of experimental conditions.

(ii) lower immunogenicity of aptamers: Aptamers have lower-immunogenic properties and are less toxic. One important aspect is that nucleic acids aptamers cannot be directly recognised by the human immune system.[44]

(iii) variety of binding targets: Nucleic acid aptamers exhibit high affinity and specificity for diverse targets such as inorganic ions, small molecules, peptides, proteins or even complicated cells or tissues.[34,45-49] These targets include those which cannot be recognised by antibodies, suggesting that using aptamers as recognition units may significantly broaden their applications as biosensors.[39]

(iv) easy synthesis/modification: The process of production of monoclonal antibodies is time-consuming and quite expensive, which hinders their very large-scale production.[50] However, aptamers can be automatically synthesised on a large scale with excellent accuracy and reproducibility by the use of chemical methods such as solid-phase synthesis. More importantly, they can be readily chemically

modified in specific positions of their sugars, bases and/or phosphate backbone in order to enhance their stability and nuclease resistance. For example, sugar substitutions include 2′-fluoro,[51-54] 2′-hydroxymethyl, 2′-amino, 2′-azido and 2′-methoxy.[55-58] DNA backbone modifications include phosphorothioate and phosphorodithioate.[26,59]

1.2.2 Applications of aptamers

Based on the advantages described above, aptamers can be used as alternatives to antibodies in therapeutics,[60-63] as biosensors,[64-71] in disease diagnosis,[72-74] in biomarker discoveries,[75-77] in cell imaging,[78,79] as potential drugs in clinical applications,[80-83] as capture agents for food safety inspection[84,85] and as nanomaterials for targeted drug delivery.[86-89] It is noteworthy that the first nucleic acid aptamer drug, Macugen (pegaptanib), was approved by the US Food and Drug Administration (FDA) for the treatment of wet-age-related macular degeneration in 2004, which was a landmark in aptamer applications.[90] In addition, there are several potential therapeutics aptamer applications in the field of oncology with pre-clinical and clinical trials under way.[91-93]

1.3 Solid-phase synthesis of oligonucleotides

Aptamers are examples of oligonucleotides, and oligonucleotides are short single-stranded DNA or RNA molecules with user-specified sequences. Due to limitations in chemical reaction efficiency, the length limit of DNA oligonucleotides is approximately 200 nt. Chemical oligonucleotide synthesis allows the possibility of large-scale production. During the development of oligonucleotide synthesis, several methods were assessed including the H-phosphonate and phosphotriester described by A. M. Michelson and Alexander R. Todd;[94,95] the solid-phase approach developed by Robert Letsinger[96]

and the phosphoramidite method pioneered by Marvin Caruther,[97] which was universally adopted and massively broadened the applications of oligonucleotides.

The success in oligonucleotide synthesis by the phosphoramidite method is partly due to its coupling speed and efficiency (> 99%).[98] In this method, the reactive groups on the phosphoramidite monomers must be protected during the process of oligonucleotide synthesis. The 5′-position of the sugar is protected using an acid labile 4,4′-dimethoxytrityl (DMT) group (Figure 1.9). For the nucleobases, the exocyclic primary amino groups of both adenine and cytosine are protected,[99] whereas protection for thymidine (DNA) and uridine (RNA) is not required.[100] In order to enhance solubility in acetonitrile, the heterocyclic base of guanine is also protected.[101] The most commonly used protecting groups for the nucleobases are shown in Figure 1.9.

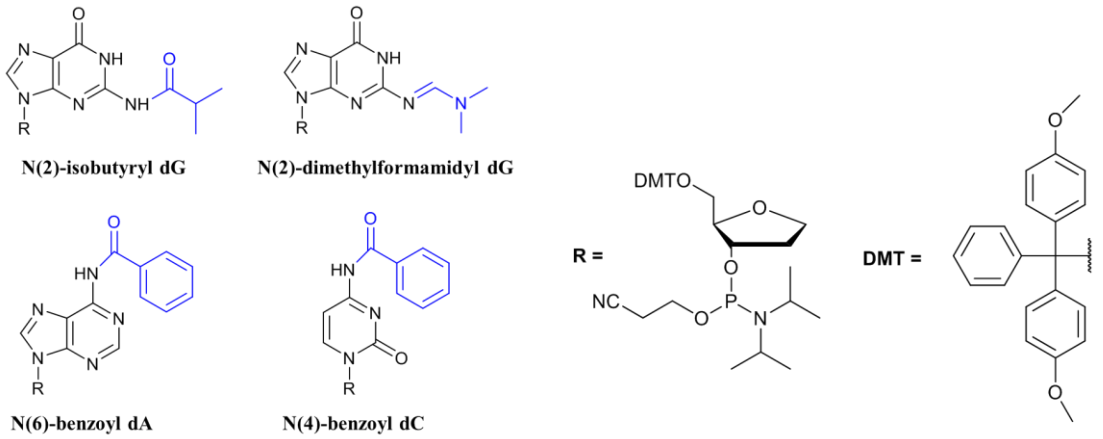


Figure 1.9. Protecting groups commonly used for adenine, cytosine and guanine bases in phosphoramidite oligodeoxynucleotide synthesis.

Unlike other methods such as enzymatic assembly of oligonucleotides, which is in the 5′ to 3′ direction, chemical oligonucleotide synthesis is performed in the 3′ to 5′ direction. Therefore, the 3′-end must be linked to the solid support and one nucleotide is added per synthesis cycle. The extended oligonucleotide product is assembled step by step and

assembly efficiency is monitored using the instrument's in-built automated facility.[102] Several steps are involved in each synthesis cycle; detritylation, coupling, capping and oxidation (Figure 1.10).[98] The first step is detritylation, the DMT group is removed by treatment with trichloroacetic acid (TCA) in which a reactive 5′-hydroxyl group is formed. In the coupling step, a phosphoramidite monomer is first activated by the use of tetrazole, which is a weak acid. Here, the diisopropylamino group of the incoming phosphoramidite monomer is protonated, converting it to a good leaving group. This phosphoramidite monomer then reacts with the 5′-hydroxyl group of the support-bound nucleoside, creating a phosphite triester linkage. Since 100% coupling efficiency is impossible, the third step, capping, is introduced to block the unreacted remaining 5′-hydroxyl group so that it cannot react in subsequent cycles. The two capping precursors, acetic anhydride and *N*-methylimidazole, are mixed on the synthesiser. As the phosphite triester linkage formed between the first and second nucleosides in the growing oligonucleotide chain is unstable, a fourth step - oxidation - is conducted to convert P(III) to a stable P(V) state. This is done by treatment with iodine, pyridine and water. Once the synthesis cycles are all completed, the oligonucleotide is ready to be cleaved from the solid support using concentrated aqueous ammonia. The oligonucleotide is then heated at 55 °C in ammonia to remove the protecting groups from the nucleobases and the cyanoethyl protecting groups from the phosphates.[103,104]

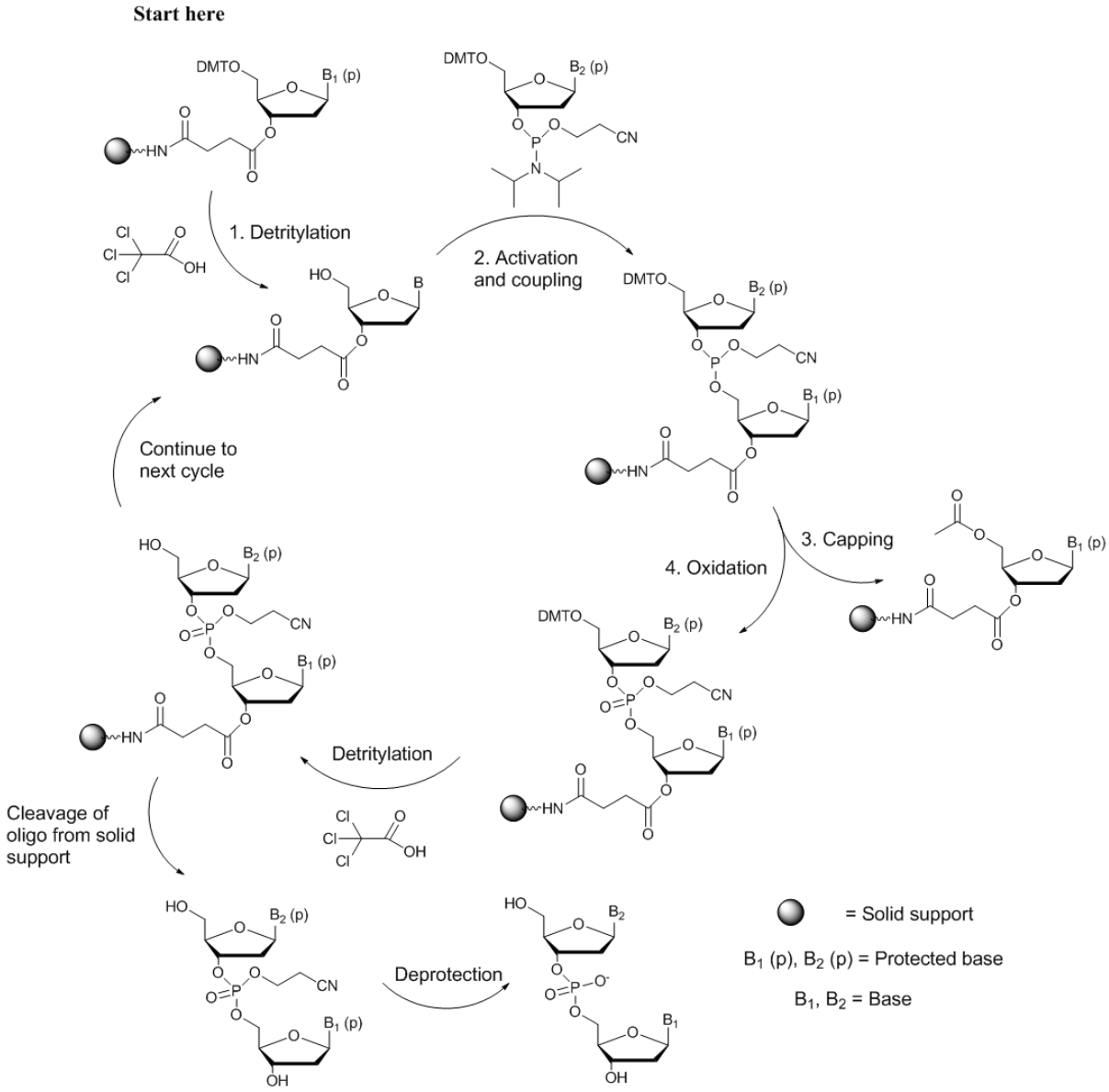


Figure 1.10. Automated solid-phase phosphoramidite oligonucleotide synthesis cycle.

RNA chemical synthesis is based on solid-phase DNA synthesis. The protecting groups used for the heterocyclic bases are similar to those used in DNA synthesis and are shown in Figure 1.11. The major difference between DNA and RNA synthesis is that the 2′-hydroxyl group of RNA must be protected throughout the solid-phase synthesis cycle and then cleanly removed at the end of the synthesis in order to prevent both 3′ to 2′ phosphate backbone migration and RNA chain cleavage. The bulky 2′-hydroxyl protecting group

decreases the coupling efficiency due to steric hindrance, and RNA oligonucleotides longer than 70 nt in length are difficult to prepare. In practice, the most commonly used protecting group for 2′-hydroxyl group protection is *tert*-butyldimethylsilyl (TBDMS), which is removed by using a source of fluoride ion such as triethylamine trihydrofluoride (Figure 1.11).[105]

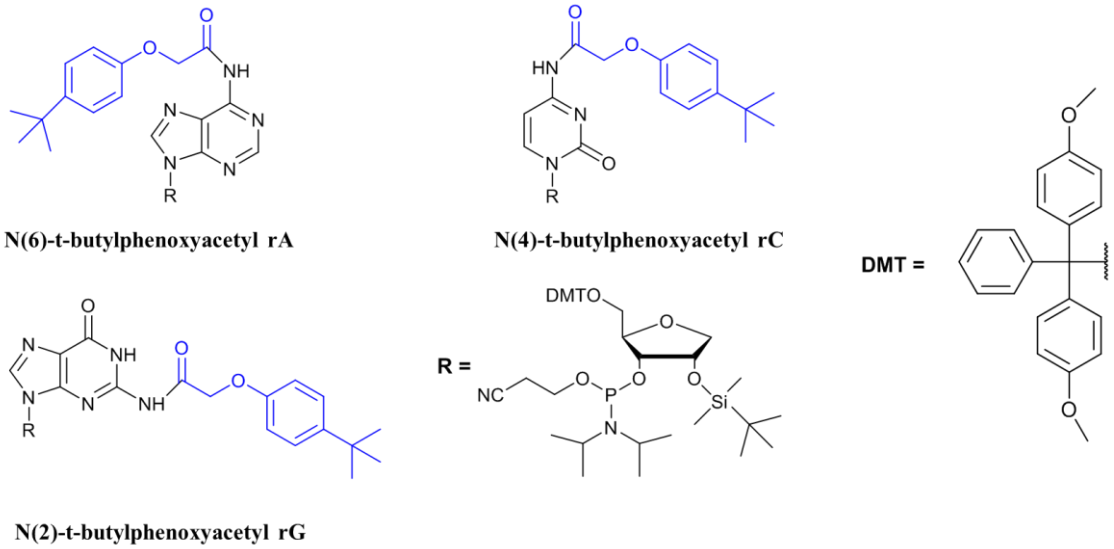


Figure 1.11. 2′-TBDMS-protected phosphoramidite monomers used in solid-phase RNA synthesis.

After synthesis and deprotection, oligonucleotides are purified and then characterised by mass spectrometry.

1.4 Cyclisation of single-stranded oligonucleotides

Two main strategies are utilised to cyclise linear oligonucleotides; enzymatic and chemical cyclisation.[106,107] Enzymatic cyclisation requires a linear oligonucleotide bearing a 5′-phosphate group, whereas chemical cyclisation requires the linear precursor to have mutually reactive groups at each end.

1.4.1 Enzymatic cyclisation

Linear oligonucleotides are usually cyclised by DNA ligase, an enzyme which is present in almost all forms of life.[108] In addition to bacteria, archaea and eukaryotes, some viruses also possess genes to encode ligases.[109-111] Ligase enzymes join linear DNA strands together by catalysing the formation of a phosphodiester bond. For the enzymatic synthesis of circular oligonucleotides, T4 DNA ligase is commonly used. It requires adenosine triphosphate (ATP) as cofactor and a complementary short oligonucleotide splint that brings the two reacting ends of the linear oligonucleotides into close proximity to facilitate reaction.

In enzymatic cyclisation, the covalent phosphodiester bond is formed as shown in Figure 1.12. First, the ATP cofactor is positioned close to the active pocket of the enzyme where the amino group of a lysine residue attacks the α-phosphate atom of ATP to form a covalent enzyme-adenosine monophosphate (AMP) intermediate. Pyrophosphate (PPi) is released from the cleaved ATP. In the second step, the activated adenylyl residue of the enzyme-AMP intermediate is transferred to the 5′-phosphate of the nick, forming the AMP-activated 5′-phosphate. Finally, the 3′-hydroxyl group on the other linear oligonucleotide acts as a nucleophile to attack the AMP-activated 5′-phosphate group to form a phosphodiester bond at the nick site, and eliminate AMP.[108,111]

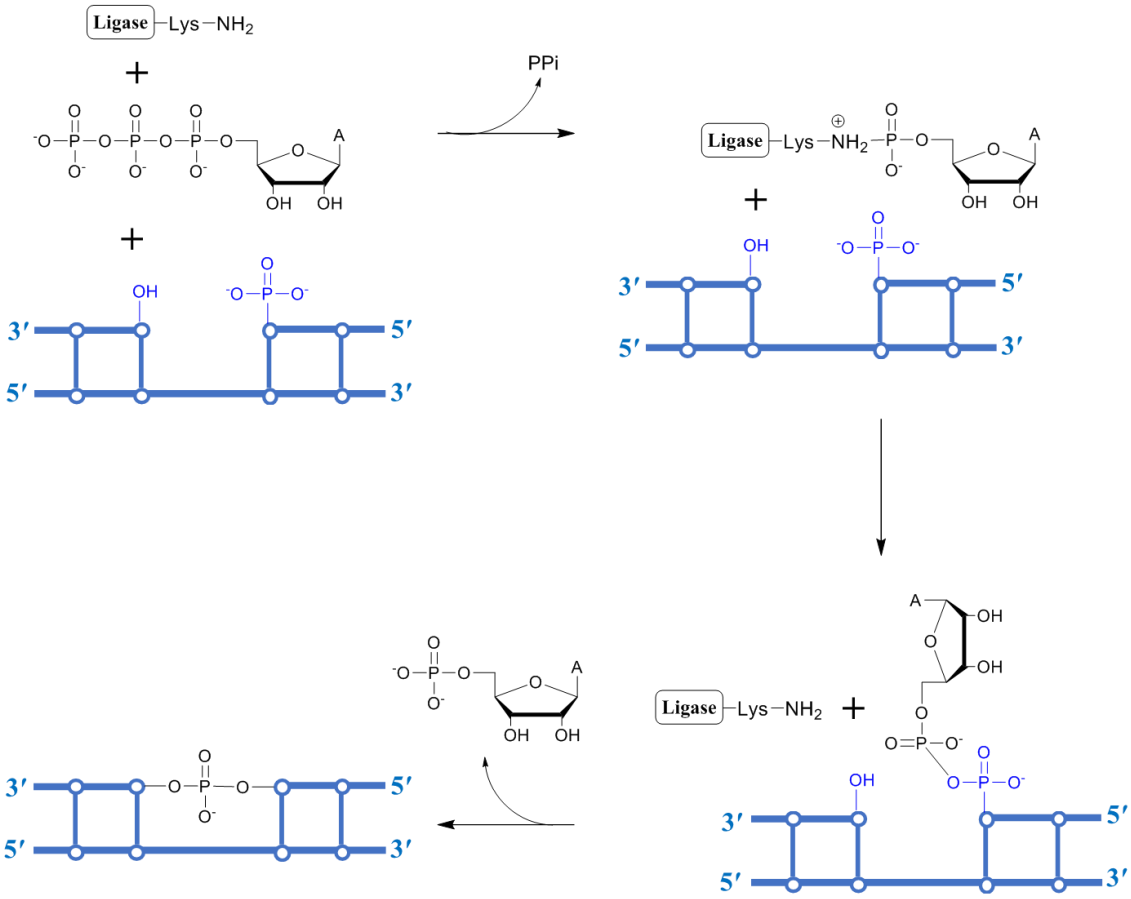


Figure 1.12. T4 DNA ligase catalysing oligonucleotide ligation in the presence of a splint oligonucleotide. A = adenine base.

1.4.2 Chemical cyclisation

Although the enzymatic approach is useful to provide circular oligonucleotides, it is expensive, and in practice is difficult to scale up. To address these issues, chemical cyclisation promises to be an alternative for the preparation of circular oligonucleotides by incorporating biocompatible artificial backbone linkages. Three chemical cyclisation methods have been used in this study.

1.4.2.1 "Click" cyclisation using the copper(I)-catalysed azide-alkyne cycloaddition reaction (CuAAC)

The concept of click chemistry was described by K. B. Sharpless *et al.* in 2001. The principle of click chemistry is that two carefully selected molecules can be selectively reacted with each other under mild conditions in high yield.[112] The copper(I)-catalysed azide-alkyne cycloaddition (CuAAC) reaction is an outstanding example of click chemistry. In this reaction, in the presence of Cu(I) catalysis, only one regioisomer - 1,4-disubstituted triazole product is generated.[113,114] The CuAAC reaction has several attractive features including regioselectivity, fast reaction rate, high yield with few or no by-products, ease of handling and mild reaction conditions (aqueous media at room temperature (RT)), all of which make the CuAAC reaction attractive for nucleic acid cyclisation.

Cyclisation of linear oligonucleotides *via* the CuAAC reaction requires them to have 5′-azide/3′-alkyne modifications at each end (Figure 1.13B). During the CuAAC reaction, the Cu(I) plays an essential role in facilitating the rate of reaction. It can be generated from a stable Cu(II) salt such as $CuSO_4 \cdot 5H_2O$. During the reaction, it is essential to keep copper in its +1 oxidation state, which is not normally thermodynamically stable, being readily oxidised to its inactive Cu(II) state (disproportionating to a mixture of Cu(0) and Cu(II) in aqueous conditions). For this reason, sodium ascorbate is added as a reducing agent to prevent the formation of oxidative homocoupling reaction products. In addition, the water-soluble ligand tris(3-hydroxypropyltriazolylmethyl)amine (THPTA) is used to stabilise copper in its Cu(I) oxidation state and accelerate the reaction. Furthermore, the CuAAC reaction must be performed in the absence of oxygen by degassing the solution with argon to maintain Cu(I).

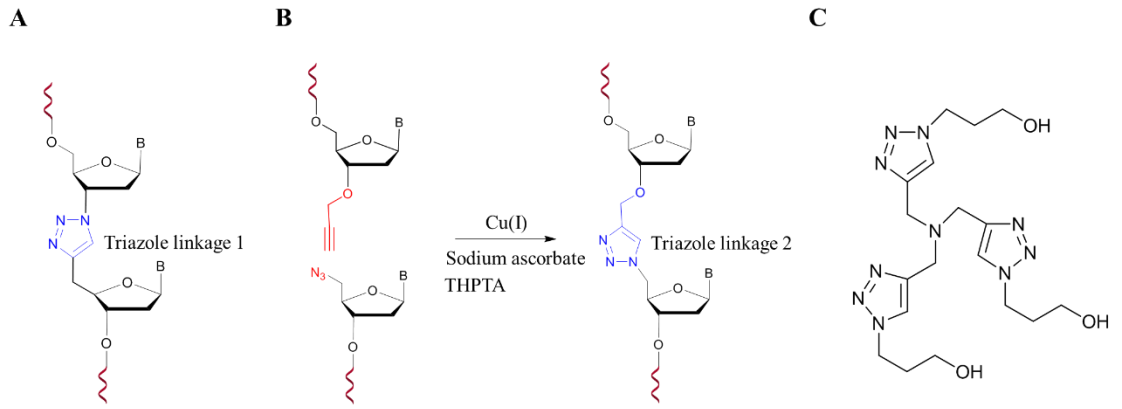


Figure 1.13. (A) Structure of a triazole linkage 1. (B) CuAAC cyclisation of linear oligonucleotides containing 5′-azide/3′-alkyne modifications to generate a triazole linkage 2. (C) Chemical structure of the THPTA ligand. B = DNA bases.

Triazole backbone linkages in DNA and RNA have been studied in detail. Fujino and Isobe *et al.* reported a triazole linkage 1 (Figure 1.13A) to construct DNA analogue in which every natural phosphate backbone is replaced by a triazole with increased rigidity.[115-117] In 2011, El-Sagheer *et al.* reported a triazole linkage 2 (Figure 1.13B) that mimics the biocompatibility of the phosphate groups.[118,119] Triazole linkage 2 was found to be accurately read through by DNA polymerase in the polymerase chain reaction (PCR) and is functional in *Escherichia coli*.[119] It can also be transcribed by T7-RNA polymerase to synthesise RNA in good yield.[120] In 2014, Birts *et al.* validated the biocompatibility of this unnatural DNA linkage in human cells by synthesising a click-linked gene encoding the fluorescent protein mCherry.[121] The biocompatibility of the triazole linkage 2 was further identified by the one-pot chemical synthesis of 335 base-pair iLOV fluorescent protein gene containing eight triazoles at the sites of chemical ligation, that was functional *in vitro* and in *Escherichia coli*.[122] More recently, Taemaitree *et al.* reported this artificial triazole linkage that is functional in critical regions of the single guide RNA (sgRNA), allowing for efficient target DNA cleavage *in vitro* and gene editing in cells.[123]

1.4.2.2 Phosphoramidate cyclisation using the di-imide coupling reaction

Another promising chemical cyclisation approach used in the nucleic acid field is phosphoramidate ligation. Richert *et al.* in 2016 used this method to construct DNA origami by ligation of scaffold strands.[124] Afterwards, El-Sagheer and Brown reported that one pot of synthesis a 762 nt gene for green fluorescent protein is achieved *via* phosphoramidate ligation.[125] Similar to the CuAAC reaction, this ligation approach uses mild aqueous conditions at RT with 1-ethyl-3-(3-dimethylaminopropyl)carbodiimide hydrochloride (EDC·HCl) and 1-(2-hydroxyethyl) imidazole as reactants. The cyclisation reaction requires an oligonucleotide modified with 5′-amine and 3′-phosphate to form the linkage. The artificial phosphoramidate backbone linkage has its advantages as it can be very efficiently read through by DNA polymerase in PCR amplification.

1.4.2.3 Amide cyclisation using the di-imide coupling reaction

Amide backbone linkages in oligonucleotides have been reported.[126,127] Following on from this, Shivalingam *et al.* in 2017 reported a new chemical ligation strategy to generate an amide DNA backbone linkage with high efficiency.[128] As with the biocompatible triazole backbone formed from CuAAC ligation, the amide linkage is compatible with DNA polymerases and offers fast read-through and good fidelity, showing that the natural phosphate group is not essential for DNA replication. Amide cyclisation shares several similarities with phosphoramidate cyclisation. It can be performed in aqueous buffer at RT and requires a linear oligonucleotide with 5′-amine/3′-carboxylate modifications. Ligation is achieved using EDC·HCl in combination with *N*-hydroxysuccinimide (NHS).

1.4.3 Applications of cyclic oligonucleotides

Over the past thirty years, oligonucleotide analogues have been evaluated extensively in order to expand their applications. Circular oligonucleotides have attracted increasing attention from researchers.[129-132] Since they are more resistant to attack/digestion by nuclease enzymes in comparison with their linear oligonucleotide counterparts,[133,134] cyclic oligonucleotides have potential as biomolecular tools. They have been investigated for their unique DNA recognition and binding properties,[131] are being used in diagnostic and therapeutic applications,[133,135-143] and have interesting properties that make them useful in the field of nanotechnology.[144-147]

1.5 Rolling circle amplification

Isothermal DNA/RNA amplification is a simple but important method. It can be used to rapidly and efficiently generate and copy long DNA constructs. Unlike PCR, which relies on heating and cooling cycles, isothermal nucleic acid amplification works at constant temperature. Moreover, it can be carried out under various conditions including *in vitro*, on the surface of cells or even inside living cells.[148] Since the 1990's, various isothermal nucleic acid amplification methods have been investigated.[149-154] Amongst these is rolling circle amplification (RCA); it mimics the replication of naturally occurring circular DNA such as viral genomes or plasmids.

RCA is used to make very long single-stranded DNA or RNA.[155] The resulting amplified products contain tens to hundreds of specific tandem sequence repeats which are encoded by the complementary circular template. A typical RCA reaction requires four components: (1) a circular DNA template; (2) a short DNA primer; (3) a DNA polymerase with a suitable amplification buffer; and (4) deoxynucleoside triphosphates (dNTPs),

used as building blocks of RCA products. In terms of polymerase, initially Bst DNA polymerase large fragment and Klenow fragment exo- were used in the RCA process, while Φ-29 DNA polymerase was not available until 1998.[138,151] Φ-29 is a highly processive DNA polymerase with stronger strand displacement activity compared with other polymerases. In addition, Φ-29 DNA polymerase can amplify a circular template with complicated structures such as four-arm branched junction and multi-crossovers during the RCA process.[155-157] In terms of the RCA primer, either DNA or RNA can be used, and the same oligonucleotide can theoretically also be utilised as a bridge splint in the cyclisation of the linear template. The cyclic DNA template can be intramolecularly cyclised either by enzymatic or chemical ligation (see Section 1.4). With intelligent design of sequences, composition, length and structure of template and primer, RCA is a hugely versatile technique.

Three steps are involved in the RCA reaction (Figure 1.14): (1) synthesis of circular template; (2) hybridisation of a DNA primer to the cyclic template; (3) primer-initiated single-stranded DNA elongation. In these steps, an extended long linear single-stranded RCA product can be obtained from the circular template. In order to detect and visualise RCA amplification products, agarose gel electrophoresis is most commonly used.

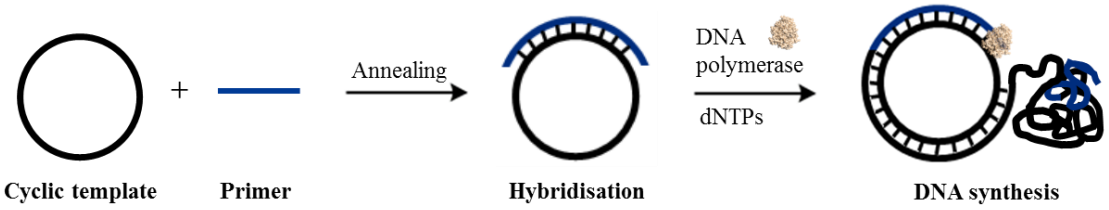


Figure 1.14. Rolling circle amplification catalysed by DNA polymerase.

1.5.1 Classification of RCA

In contrast to PCR, which depends on heating and cooling cycles, RCA can be carried out at one reaction temperature under simple conditions. It can be mainly classified into two groups; exponential RCA and linear RCA based on their reaction kinetics.[148]

1.5.1.1 Exponential RCA

One of the significant attributes of RCA is that cyclic templates can be read through by a polymerase so that a specific signal is amplified in an exponential manner.[155] Multiple amplification events can be initiated to generate multiple RCA products by the use of multiple primers that hybridise with the same circular template. The number of primers that can be used to hybridise with a cyclic template mainly relies on the length of the circular template and primers. Hyperbranched RCA (HRCA), another RCA-based exponential amplification method, is catalysed by Bst or Vent exo- DNA polymerase. In this type of reaction, RCA products serve as templates for further amplification by the use of sequential second and third sets of primers, generating large branching DNA fragments.[158,159]

1.5.1.2 Linear RCA

In the linear format, a very long single-stranded DNA product with a repeating sequence is generated during the RCA process. Unlike HRCA, linear RCA does not require a second set of primers in the amplification process, and DNA synthesis is catalysed by Φ-29 DNA polymerase rather than by other DNA polymerases as in HRCA.[148] The reaction temperature of linear RCA is normally set at about 30 °C, which is lower than that used in HRCA (around 60 °C). In linear RCA, approximately 10^3 - fold amplification can be

achieved within 1 hour (h), and the reaction efficiency can be further enhanced by employing single-stranded binding proteins.

1.5.2 Applications of RCA

RCA has become a very promising alternative technique to PCR due to its convenience and high amplification efficiency. To date, RCA has been extensively applied in many research areas; it has been used to achieve sensitive detection of a variety of small molecule targets, proteins, nucleic acids, single nucleotide polymorphisms (SNPs) in DNA, DNA methylation, to detect cell targets for diagnostics, in biosensing and genotyping.[155,160-167] In addition, RCA has also attracted significant attention as a tool in the synthesis of functional DNA nanomaterials including origami, nanotubes, nanosprings, hydrogels, templating nanoscaffolds and DNA nanoflowers (DNA-NFs).[168-174] Future applications of these nanomaterials could include their use as biosensors, drug delivery agents, and in targeted imaging and electronic circuit fabrication.

1.6 Aptamer-incorporated DNA nanostructures

Over the last three decades, DNA is emerging as an excellent building material for a wide variety of DNA nanostructures. Because it possesses many features including (1) predictable and programmable conformation; (2) mechanical rigidity and physicochemical stability; (3) Watson-Crick base pairing to control inter- and intra-molecular interactions and (4) compatibility with a wide range of enzymes including ligases, DNA polymerases and restriction endonucleases capable of manipulating DNA.[175,176] By using simple assembly methods and design rules, two-dimensional and three-dimensional nanostructures can be fabricated. Aptamers as promising therapeutic and diagnostic agents can be encoded into these DNA nanostructures *via* base paring

between nucleic acid aptamers and DNA nanostructures or as building blocks used in the assembly process.

1.6.1 Hybridisation-dependent nucleic acid assembly

Owing to the specificity of Watson-Crick base pairing, nucleic acid hybridisation dependent assembly has been used to engineer aptamer-integrated DNA nanostructures. For example, in 1997 Nilsen *et al* designed a new class of dendritic structure that could be fabricated from unique nucleic acid monomers,[177] and these dendrimer-like DNA structures were then generated using enzymatic ligation.[178] Afterwards, an aptamer-integrated DNA dendrimer nanocarrier for intracellular molecular probing was developed where the aptamer, as a component, directly participated in the assembly process.[179] In 2013, Tan *el al.* constructed aptamer-tethered, long linear DNA nanostructures termed DNA nanotrains, employing two independent short DNA strands upon initiation of an aptamer-tethered trigger probe *via* a hybridisation chain reaction.[87,180] Li *el al.* in 2017 constructed an aptamer-functionalised, tetrahedral DNA nanostructure that is capable of permeating cellular membranes for targeted drug delivery.[181] A novel DNA nanotriangle-scaffolded multivalent split activatable aptamer probe (NTri-SAAP) was recently assembled by conjugating multiple aptamer probes on a planar nanotriangle scaffold.[182] This nano-construction is capable of undergoing a conformation change with fluorescence activation and releasing the drug after internalising into cells.

1.6.2 Non-hybridisation-dependent DNA assembly

Conventional methods to construct DNA nanostructures mainly depend on Watson-Crick base pairing interactions. However, some other DNA nanostructures that rely on non-hybridisation-dependent assembly approach rather than Watson-Crick base pairing have

been reported and this has become a hot research field. For example, RCA has been used to fabricate DNA nanostructures.[175,183] In addition, nucleic acids can be readily modified with functional groups such as lipophilic groups and thiols, offering other strategies to develop novel nanostructures.[184,185]

Non-covalent interactions such as hydrophobic interactions between lipophilic groups in oligonucleotides have also been used to construct aptamer-encoded DNA spherical micelle nanostructures. Lipophilic moieties can be conjugated with oligonucleotides at either the 3'- or 5'-end, or even within the sequence, making lipophilic oligonucleotides convenient building blocks to fabricate micelle vesicles. Dentinger *et al.* engineered vesicular aggregates using alkylamine-modified nucleic acids for DNA-mediated delivery of drugs.[186] Tan *et al.* have also designed and constructed a self-assembled aptamer-micelle nanostructure, which consists of hydrophobic lipid tails and hydrophilic DNA heads, for detection and delivery applications.[187]

1.6.3 Application of aptamer-incorporated DNA nanostructures in cancer therapy

Although researchers have made huge advances in understanding various diseases, cancer is still one of the leading causes of death. Its high morbidity and high mortality are mainly a consequence of a lack of precise treatment methods. Improvements could be made by employing targeted drug delivery systems. Towards this end, nucleic acid aptamers have been developed to specifically recognise cancer cells. Owing to their predicable structures and opportunities for site-specific chemical modification, combinations of novel nanomaterials with aptamers have attracted widespread interest, resulting in a wide range

of applications for cancer therapy including photodynamic therapy,[188,189],immunotherapy,[190,191] gene therapy[192] and chemotherapy.[87,193]

1.7 Research aims and thesis structure

The unique and predictable structural and base pairing properties of DNA make it an excellent material for the assembly of nanostructures in comparison with other biomolecules. DNA nanostructures have enhanced stability to enzymatic degradation, and high tissue penetration efficiency, which facilitates their *in vitro* and *in vivo* applications.[175] Aptamers as chemical equivalents of antibodies can be generated to recognise a variety of targets with high affinity. Combining the specific properties of aptamers and DNA nanostructures, the broad objective of this research is to construct DNA superstructures functionalised with aptamer units for selective cancer cell recognition, intracellular imaging, anticancer drug delivery and for sensing specific messenger RNAs (mRNAs) in cancer cells.

This thesis consists of 6 chapters. Chapter 1 describes the project aims and introduces the fundamental knowledge related to it.

Chapter 2 focuses on synthesis and characterisation of previously reported human epidermal growth factor receptor 2 (HER2) DNA and RNA aptamers. From this characterisation, suitable aptamers were selected for utilisation in the construction of DNA-based nanostructures.

Chapter 3 demonstrates the assembly of novel DNA-metal-ion superstructures by replacing the commonly used Mg^{2+} cation with Mn^{2+} or Co^{2+} in RCA reactions, facilitating the formation of DNA nanomaterials in a range of morphologies. These

superstructures retain the enzymatic stability of their magnesium counterparts and the Mn^{2+} and Co^{2+} DNA nanoflowers (MnDNA-NFs and CoDNA-NFs) were additionally endowed with magnetic properties.

Chapter 4 reports research on the cyclisation of linear single-stranded oligonucleotides using chemical cyclisation methods, which provide a versatile expanded toolkit for scalable generation of cyclic DNA constructs. Three different chemical cyclisation approaches were explored and optimised, generating a single triazole, phosphoramidate or amide unnatural backbone linkage at the ligation point. The resulting cyclic oligonucleotides incorporating a modified backbone linkage were evaluated in RCA reactions; their polymerisation rates, product distribution and product yields being investigated. In addition, DNA-NFs were generated from all modified cyclic templates during the RCA process.

Chapter 5 draws overall conclusions obtained from current research and suggests some future works.

Chapter 6 describes experimental procedures and technical details used in the research.

Chapter 2

Synthesis and characterisation of reported HER2 aptamers

Chapter 2 – Synthesis and characterisation of reported HER2 aptamers

2.1 Introduction and aims

Breast cancer is a common malignancy among women worldwide. The human epidermal growth factor receptor 2 (HER2), a transmembrane receptor tyrosine kinase, is overexpressed in approximately 20 - 30% of malignant breast cancers. It is an established therapeutic target[194] and a potential "cellular entry point" for targeted drug delivery.[195] Traditional cancer therapies containing chemotherapy, photothermal therapy and radiotherapy can cause side effects due to their toxicity in healthy cells. Although antibody-based drugs have fewer side effects,[196] they are limited by immunogenicity and high production cost.[34,195,196] Aptamer-based tumour targeted drug delivery is being explored as an alternative therapeutic approach to complement these approaches, and potentially address some of these obstacles.[197]

Nucleic acid aptamers are single-stranded DNA or RNA, which fold into unique three-dimensional conformations[33] and specifically bind to various targets[34,35,198] with a low dissociation constant (K_d) ranging from pico- to nano-molar.[37,199] Aptamers serve as chemical antibodies and are usually selected from a random library of 10^{13} - 10^{16} single-stranded DNA or RNA *via* SELEX.[28] Compared to antibodies, aptamers have many advantages such as reduced molecular weight, reduced immunogenicity, lower toxicity and fast tissue penetration. They can also be easily chemically modified and synthesised on a large scale.[196] As with antibodies aptamers can be conjugated to drug molecules to form aptamer-drug complexes, either through a non-covalent intercalation or *via* a covalent bonding with a chemical linker.[49,200] The unique advantages of aptamers as

targeting ligands have resulted in increased interest in specific targeted drug delivery in the cancer cell field.[87,174,201] Therefore, aptamer-mediated drug delivery systems facilitate the development of active targeting therapies providing promising anticancer outcomes.

The aim of the work in this chapter was to synthesise and characterise several currently reported HER2 aptamers. After evaluating their receptor-binding properties, suitable aptamers will be used to construct oligonucleotide nanoflowers (Chapter 4).

2.2 Preparation and synthesis of reported HER2 aptamers

The previously reported HER2 DNA aptamers (including Apt1[202], Apt2[49] and Apt3[203]) and a HER2 RNA aptamer (Apt5[54]) were identified as promising candidates. Apt4[204] (a mutated version of Apt1) and Apt6[54] (the reported control for Apt5) were used as negative controls in our binding assays. The sequences of Apt1 and Apt5 are guanine-rich (sequences are listed in Table 2.1 and Table 2.2).

For the purpose of studies, Apt1 and Apt4 were labelled with Cyanine 3 dye (Cy3) at both 5' (5' Cy3-Apt) and 3' (3' Cy3-Apt) end of the aptamers while the remaining aptamers were labelled only at the 5'-end (shown in Table 2.3 and Table 2.4). Cy3 allows direct tracking of the aptamer binding to cancer cells through fluorescence imaging and fluorescence-associated cell sorting (FACS) in contrast to previous studies which used a secondary antibody linked to a detection system.[54,202]

For the RNA aptamers (Apt5 and Apt6), the 2′-hydroxyl group of the ribose sugar of cytosine and uracil was replaced by the use of fluorine as previously reported in order to enhance the stability against serum nuclease-mediated degradation (shown in Table 2.4).[54]

Table 2.1. Sequences of DNA aptamers reported in the literature.

Aptamer name	Sequence of oligonucleotide (5′→3′)	REF
Apt1	GCAGCGGTGTGGGGGCAGCGGTGTGGGGGCAGCGGTGTGGGG	202
Apt2	AACCGCCCAAATCCCTAAGAGTCTGCACTTGTCATTTTGTATATGTATTTGGTTTTTGGCTCTCACAGACACACTACACACGCACA	49
Apt3	GGGCCGTCGAACACGAGCATGGTGCGTGGACCTAGGATGACCTGAGTACTGTCC	203
Apt4	GCAGCAGTGTGAGGGCAGCAGTGTGAGGGCAGCAGTGTGAGG	204

Table 2.2. Sequences of RNA aptamers reported in the literature.

Aptamer name	Sequence of oligonucleotide (5′→3′)	REF
Apt5	AGCCGCGAGGGGAGGGAUAGGGUAGGGCGCGGCU	54
Apt6	GGGGGCAUACUUGUGAGACUUUUAUGUCACCCCC	54

Table 2.3. DNA aptamers synthesised for use in this chapter.

Oligonucleotide name	Sequence of oligonucleotide (5′→3′)	Length
Apt1	GCAGCGGTGTGGGGGCAGCGGTGTGGGGGCAGCGGTGTGGGG	42
5′ Cy3-Apt1	Cy3-GCAGCGGTGTGGGGGCAGCGGTGTGGGGGCAGCGGTGTGGGG	42
3′ Cy3-Apt1	GCAGCGGTGTGGGGGCAGCGGTGTGGGGGCAGCGGTGTGGGG-Cy3	42
5′ Cy3-Apt2	Cy3-AACCGCCCAAATCCCTAAGAGTCTGCACTTGTCATTTTGTATATGTATTTGGTTTTTGGCTCTCACAGACACACTACACACGCACA	86
5′ Cy3-Apt3	Cy3-GGGCCGTCGAACACGAGCATGGTGCGTGGACCTAGGATGACCTGAGTACTGTCC	54
5′ Cy3-Apt4	Cy3-GCAGCAGTGTGAGGGCAGCAGTGTGAGGGCAGCAGTGTGAGG	42
3′ Cy3-Apt4	GCAGCAGTGTGAGGGCAGCAGTGTGAGGGCAGCAGTGTGAGG-Cy3	42

Table 2.4. RNA aptamers synthesised for use in this chapter.

Oligonucleotide name	Sequence of oligonucleotide (5′→3′)	Length
5′ Cy3-Apt5	Cy3-AGCCGCGAGGGGAGGGAUAGGGUAGGGCGC GGCU	34
5′ Cy3-Apt6	Cy3-GGGGGCAUACUUGUGAGACUUUUAUGUCAC CCCC	34

The red bases of C and U in the sequences have the 2′-hydroxyl group of ribose sugar replaced by fluorine.

2.3 Characterisation of reported HER2 aptamers

2.3.1 Initial assessment of aptamer binding ability using fluorescence-associated cell sorting

The binding abilities of all Cy3 labelled aptamers (DNA and RNA) for HER2+ cancer cells were first evaluated using FACS. The human breast cancer cell line SKBR-3 (HER2+) which has approximately two million HER2 proteins at the tumour cell surface - around 100 times more than a normal cell,[205] and the negative control cell line MDA-MB-468 (HER2-) were used in this study. Cells were split and grown in fresh, complete-growth medium for 24 h prior to binding assays, and then detached by incubating with trypsin-EDTA at 37 °C for 2 minutes (min). A 2 min incubation time was used as longer dissociation treatments have been reported to damage the HER2 protein on the surface of the cells, which would be detrimental to the study.[206] The cells were then incubated in growth medium containing 1 μM of the Cy3 labelled aptamer and 1% bovine serum albumin (BSA) at 4 °C for 40 min in the dark. BSA was used to help prevent non-specific binding. After incubation, the cells were washed twice with Dulbecco's phosphate-buffered saline (DPBS) to remove any unbound aptamer before measurement. Prior to the binding assay, the Cy3 labelled aptamers were prepared in the DPBS containing 1%

BSA without any annealing step as previously reported.[207] As a control, the reference Anti-HER2 affibody (FITC) was also used for each experiment in place of the aptamers.

Preliminary results indicated that both 5' Cy3-Apt1 and 5' Cy3-Apt5 bound to SKBR-3 (HER2+) cancer cells, while 5' Cy3-Apt2, 5' Cy3-Apt3 and 3' Cy3-Apt1 did not (Figure 2.1). Negative control 5' Cy3-Apt6 showed slight unspecific binding to SKBR-3 (HER2+) cancer cells. In agreement with the literature, weak fluorescence intensities were detected for the negative control Apt4 which is presumably because it has not completely lost its binding ability to HER2 (Figure 2.1).[204] In addition, no shift in fluorescence intensity was detected when the aptamers were incubated with MDA-MB-468 (HER2-) control cells (Figure 2.2).

These results also indicated that the site of attachment of Cy3 had a significant effect on the aptamer's ability to bind HER2. We hypothesised that this was a result of the dye changing the conformation of Apt1, resulting in reduced affinity to HER2. This is discussed in further detail below.

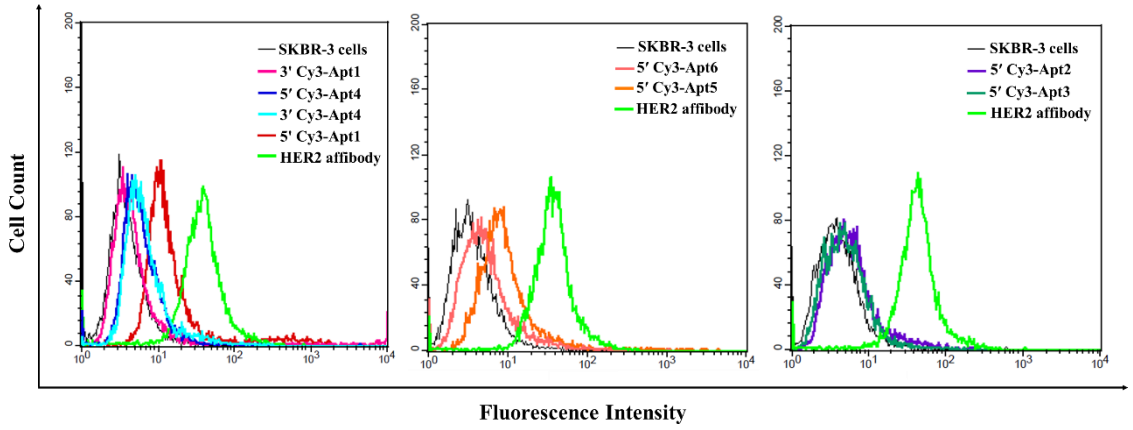


Figure 2.1. Assessment of aptamer binding properties by flow cytometry. SKBR-3 cells were incubated with different aptamers or FITC-labelled affibody for 40 min at 4 °C in the dark. The concentration of the aptamers was 1 μM.

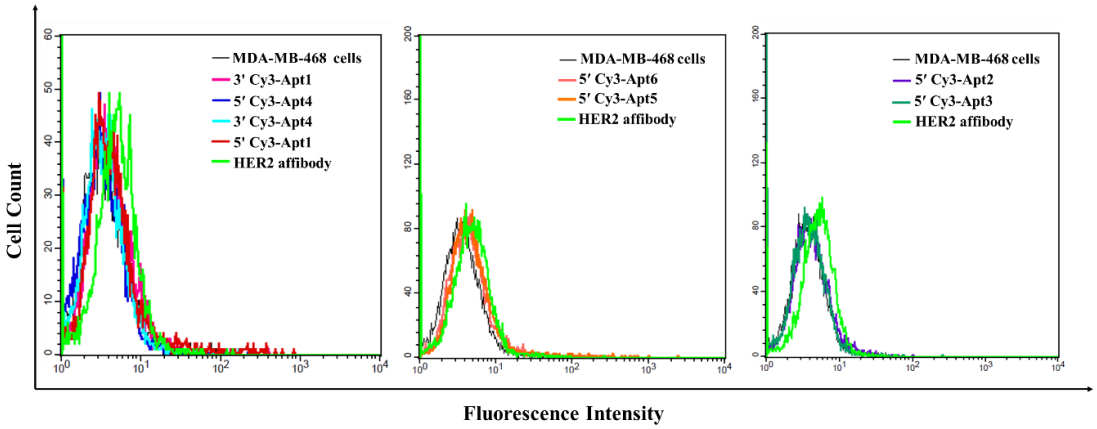


Figure 2.2. Assessment of aptamer binding properties by flow cytometry. MDA-MB-468 cells were incubated with different aptamers or FITC-labelled affibody for 40 min at 4 °C in the dark. The concentration of the aptamers was 1 μM.

Unexpectedly, we observed that the binding ability varied between synthetic batches of 5' Cy3-Apt1 (Figure 2.3). As Apt1 is guanine-rich, it might form a G-quadruplex structure. We hypothesised that the secondary structure of the aptamer varied depending on post-synthesis handling, resulting in a significant difference of binding capability in some batches.

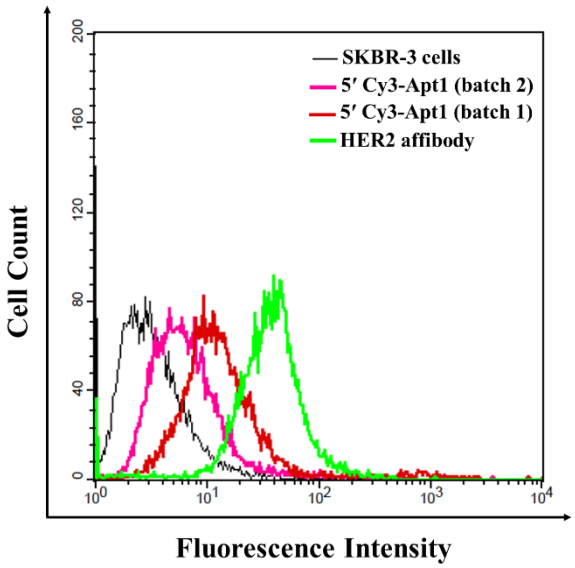


Figure 2.3. Assessment of aptamer binding properties by flow cytometry. SKBR-3 cells were incubated with aptamers from different batches or FITC-labelled affibody for 40 min at 4 °C in the dark. The concentration of the aptamers was 1 μM.

Based upon initial results, Apt1 and Apt5 were further investigated using circular dichroism (CD), UV melting and native polyacrylamide gel electrophoresis (PAGE) to test whether their structures are affected by different conditions such as dye modification, annealing process and buffer system.

2.3.2 Investigating aptamer structures using circular dichroism

Due to the guanine-rich nature, both Apt1 and Apt5 potentially could adopt G-quadruplex conformations. CD was used to determine the conformations of these aptamers by comparing their spectra with those of known DNA structures.[208,209] The CD spectra of Apt1 and Apt5 were first recorded in a phosphate-buffered saline (PBS) buffer containing 153 mM NaCl at pH 7.3. Prior to measurement, the aptamers were annealed under two different conditions including fast annealing (heating at 95 °C for 5 min followed by annealing rapidly - kept on ice for 10 min) and slow annealing (heating at 95 °C for 5 min and then annealing at a cooling rate of 0.5 °C/min) to support formation of potential secondary structures.

The CD spectrum of both the modified and unmodified versions of Apt1 contained positive bands near 260 nm and near 290 nm; however, these were lower in intensity than would be expected for a G-quadruplex (Figure 2.4).[208] This was possibly caused by a mixture of parallel and antiparallel G-quadruplex formation.[210] Typically parallel quadruplex structure shows a positive band near 260 nm, whilst a negative band near 260 nm is observed for the anti-parallel conformation. No significant differences were observed between 5' Cy3-Apt1 and 3' Cy3-Apt1, and different rates of annealing did not cause significant changes of the aptamer conformation.

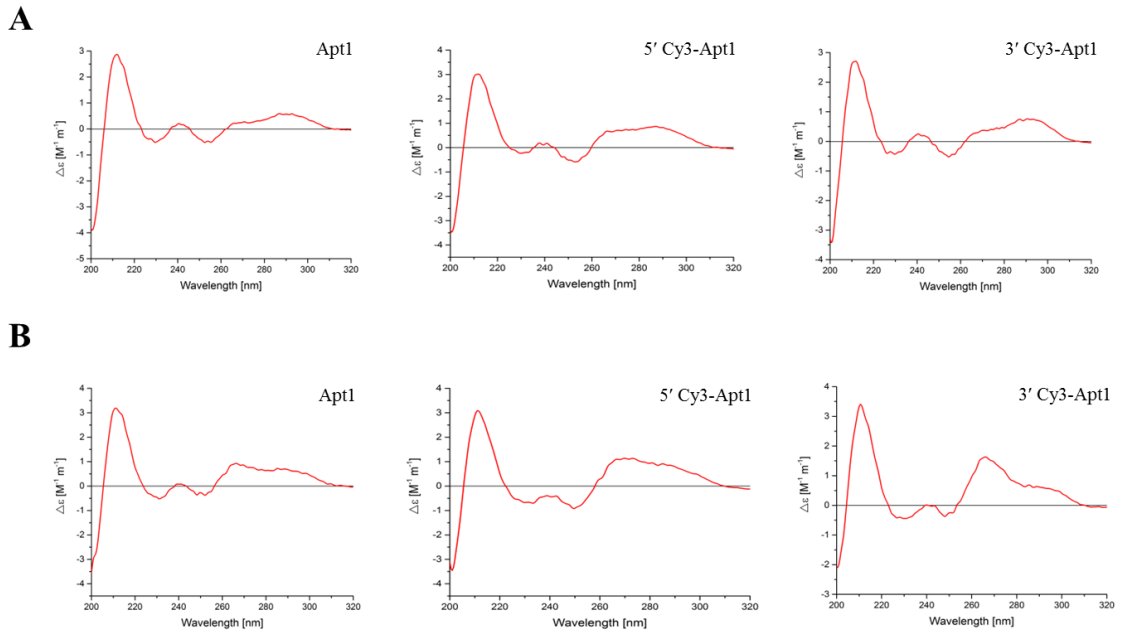


Figure 2.4. CD spectra of Apt1, 5' Cy3-Apt1 and 3' Cy3-Apt1. The aptamer was dissolved in PBS buffer at 10 μM and folded by fast annealing (A) and slow annealing (B) prior to measurement. Fast annealing refers to heating at 95 °C for 5 min followed by annealing rapidly kept on ice for 10 min. Slow annealing corresponds to heating at 95 °C for 5 min and then annealing at a cooling rate of 0.5 °C/min to RT. Spectra are shown as an average of four repeats.

G-quadruplex structures are non-canonical four stranded secondary structures that exhibit diverse topologies relying on the presence of monovalent cations (Na^+ or K^+).[211] With this in mind, CD was used to further investigate the effect of K^+ on the aptamer structure using a recommended concentration (100 mM K^+) for stabilisation of quadruplex sequences.[208] Prior to measurement, both 5' Cy3-Apt1 and 5' Cy3-Apt5 were heated at 95 °C for 5 min and then annealed in the K^+ buffer over 2 h in order to support G-quadruplex structure formation (more details see experimental Section 6.3.1).[208]

As expected, the addition of K^+ could induce and stabilise a G-quadruplex structure in 5' Cy3-Apt1. CD suggested that an external loop - parallel G-quadruplex structure formed with characteristic positive bands near 260 nm and 290 nm (Figure 2.5). The 260 nm band was assigned to the parallel strand quartets, and the band at 290 nm for the external loop

residues. Moreover, G-quadruplex also displayed another positive band at around 210 nm. These characteristic bands are in agreement with previous reports.[208,209,212,213]

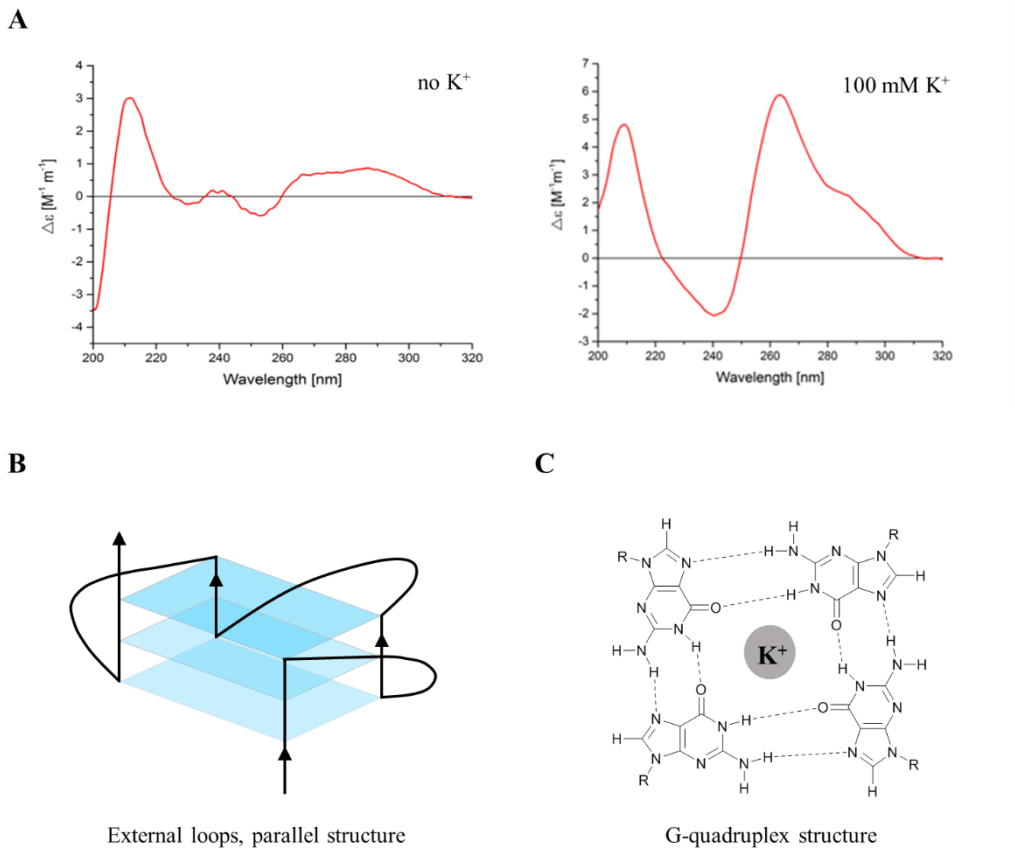


Figure 2.5. The aptamer of 5' Cy3-Apt1 was prepared at 10 µM and folded by slow annealing over 2 h prior to measurement. Slow annealing corresponds to heating at 95 °C for 5 min and then annealing at a cooling rate of 0.5 °C/min to RT. (A) CD spectra of 5' Cy3-Apt1 in the presence or absence of 100 mM K^+. Spectra were measured at 20 °C and shown as an average of four repeats. (B) External loops, parallel G-quadruplex structure. (C) Structure of a G-quartet.

The CD spectrum for 5' Cy3-Apt5 is characteristic of an A-form structure with a high positive band at 260 nm and a negative one at 210 nm,[209,213] and no differences were observed when the aptamer annealed at different conditions (Figure 2.6).

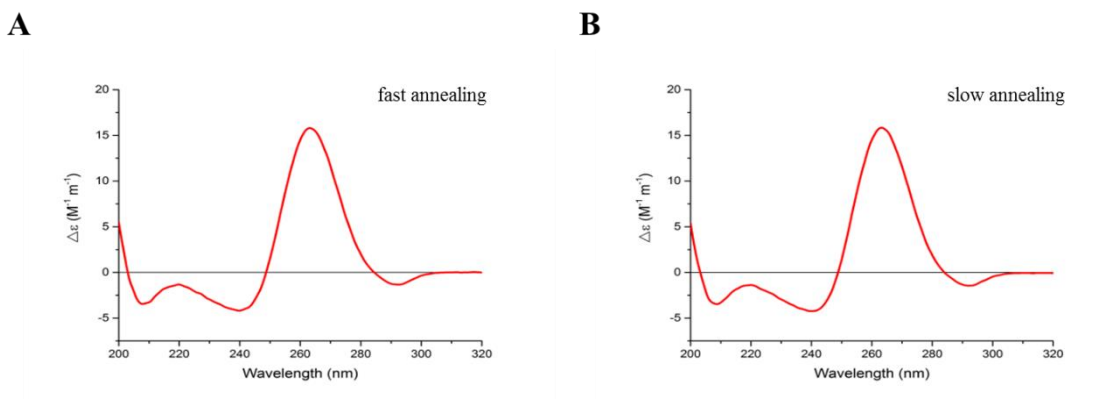


Figure 2.6. CD spectra of 5' Cy3-Apt5. The aptamer was dissolved in PBS buffer at 10 μM and folded by fast annealing (A) and slow annealing (B) prior to measurement. Fast annealing refers to heating at 95 °C for 5 min followed by annealing rapidly kept on ice for 10 min. Slow annealing corresponds to heating at 95 °C for 5 min and then annealing at a cooling rate of 0.5 °C/min to RT. Spectra are shown as an average of four repeats.

Despite being guanine-rich, no G-quadruplex structure was observed for 5' Cy3-Apt5 in the presence of 100 mM K^+ or in the Na^+ conditions. The CD spectrum again showed a positive band at 260 nm and a negative one at 210 nm, which is a characteristic of an A-form duplex structure.

2.3.3 Investigating aptamer secondary structure using native polyacrylamide gel electrophoresis

In order to further corroborate the results from CD studies, native PAGE was employed to determine whether the formed G-quadruplex for 5' Cy3-Apt1 is intermolecular or intramolecular in nature. This was done by preparing the 5' Cy3-Apt1 under varying conditions including concentrations ranging from 10 - 40 μM, different annealing processes as mentioned in the CD studies and buffer systems including sodium phosphate and potassium phosphate buffers.

In the presence of Na^+, no significant difference in band migration was observed for 5' Cy3-Apt1 in all conditions investigated, indicating a lack of secondary structure (Figure

2.7). Some slow migrating species were detected at a lower concentration of 10 μM, indicating that a dimer might be formed through Watson-Crick base pairing.

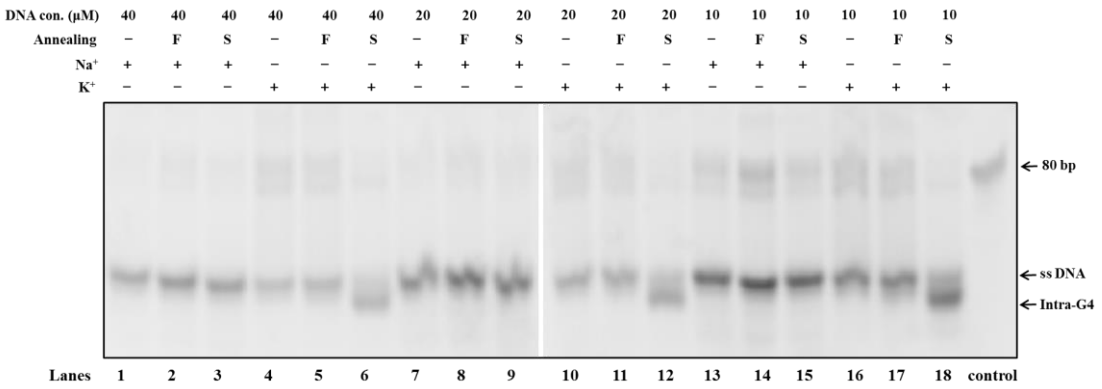


Figure 2.7. 16% native PAGE analysis of 5' Cy3-Apt1 at varying conditions. In annealing step, 'F' corresponds to fast annealing; 'S' represents slow annealing. Fast annealing refers to heating at 95 °C for 5 min followed by annealing rapidly kept on ice for 10 min. Slow annealing corresponds to heating at 95 °C for 5 min and then annealing at a cooling rate of 0.5 °C/min to RT. The gel was run at 4 °C in 1× TBE buffer supplemented with 20 mM KCl and visualised post staining with SYBR Gold.

In contrast, following the addition of K^+, differences were observed in some cases (Figure 2.7, lane 6, 12 and 18). More specifically, the 5' Cy3-Apt1 migrated faster under slow annealing condition, indicating intramolecular G-quadruplex structure formation which would adopt a more compact structure and migrate faster than unstructured DNA.[214-216] This result also suggests that no quadruplex structures form when annealing in the presence of Na^+. Interestingly, the result also demonstrated that the intramolecular G-quadruplex preferentially formed at the lower concentration of 10 μM under slow annealing condition (Figure 2.7, lane 18). One possible explanation for this observation is that the higher concentrations would lead to competition of intra- and intermolecular G-quadruplexes. Due to the above results, the conditions for intramolecular G-quadruplex formation were investigated further in subsequent experiments.

5' Cy3-Apt5 was also investigated under the same conditions as described above. No

intra- or intermolecular G-quadruplexes or other compact structures were observed in the presence of Na^+ or K^+ (Figure 2.8). This is in agreement with the CD spectra (Figure 2.6).

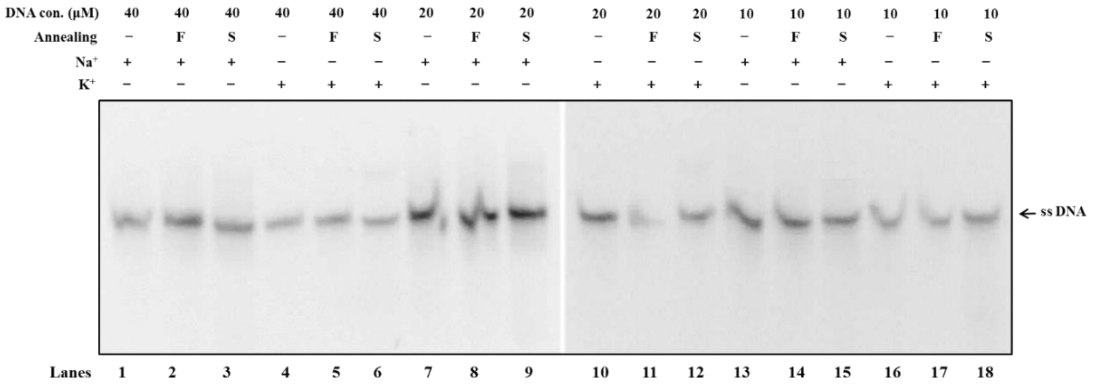


Figure 2.8. 16% native PAGE analysis of 5' Cy3-Apt5 at varying conditions. In annealing step, 'F' corresponds to fast annealing; 'S' represents slow annealing. Fast annealing refers to heating at 95 °C for 5 min followed by annealing rapidly kept on ice for 10 min. Slow annealing corresponds to heating at 95 °C for 5 min and then annealing at a cooling rate of 0.5 °C/min to RT. The gel was run at 4 °C in 1× TBE buffer supplemented with 20 mM KCl and visualised post staining with SYBR Gold.

2.3.4 Investigating aptamer stability using UV melting

Knowing that 5' Cy3-Apt1 forms a G-quadruplex structure in the presence of K^+, we further studied its thermal stability by performing UV melting assays in the presence of K^+. DNA G-quadruplexes display only small changes in absorbance at 260 nm during UV melting studies, while a significant signal can be obtained at 295 nm with a large decrease in absorbance upon melting.[217] Based on this, melting profiles were recorded at both wavelengths of 260 nm and 295 nm as a function of temperature.

As anticipated, sigmoidal curves were obtained at 295 nm for 5' Cy3-Apt1 at both concentration of 10 μM and 20 μM indicating the formation of G-quadruplex structure (Figure 2.9A). The melting temperature (T_m) from both cases was approximately 70 °C according to the absorbance recording at 295 nm, and the melting showed a single transition (single first derivative peak) (Figure 2.9B). This result also indicated that the

T_m did not depend on the concentration of oligonucleotide, suggesting intramolecular G-quadruplex formation.[218] In addition, non-identical heating and cooling curves were observed. This hysteresis phenomenon is likely due to the slow rate of G-quadruplex structure formation after denaturation.

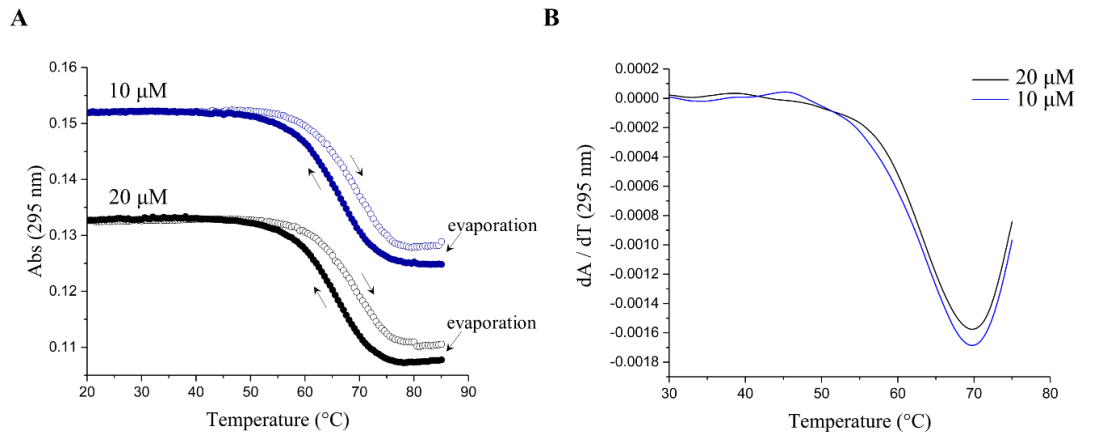


Figure 2.9. (A) Melting profiles obtained in the presence of 100 mM K^+ for 5' Cy3-Apt1 at wavelength of 295 nm. Data of both concentrations of 10 µM (blue curve) and 20 µM (black curve) were recorded with a temperature gradient of 0.2 °C/min. Open circles refer to heating profile, and filled circles indicate cooling profile. (B) T_m values were determined from the first derivative curves.

Combining the UV melting data with CD studies and native PAGE gel-shift assays, we can conclude that intramolecular G-quadruplex formation is occurring in the case of 5' Cy3-Apt1. The conditions for forming G-quadruplex structure of 5' Cy3-Apt1 were further utilised in the subsequent binding assays.

2.3.5 Assessment and optimisation of aptamer binding using fluorescence-associated cell sorting

5' Cy3-Apt1 was annealed using the conditions identified by CD, native PAGE and UV melting and its binding ability was re-assessed using FACS. Prior to each measurement, the 5' Cy3-Apt1 was pre-annealed in the presence of K^+ in order to form the G-quadruplex structure, which was considered the conformation likely to specifically recognise the

HER2 biomarker. The same binding conditions as Section 2.3.1 were used.

As expected, the cells incubated with annealed 5' Cy3-Apt1 showed higher fluorescent intensity than untreated cells, confirming that the G-quadruplex structure was necessary for binding to SKBR-3 (HER2+) cells (Figure 2.10A). This result supports the hypothesis that the structure of the 5' Cy3-Apt1 is a key factor in its ability to bind HER2, and suggests that the aptamer needs to be pre-annealed prior to incubation with cells. Moreover, no significant shift in fluorescence intensity was detected for MDA-MB-468 (HER2-) control cells (Figure 2.10 B).

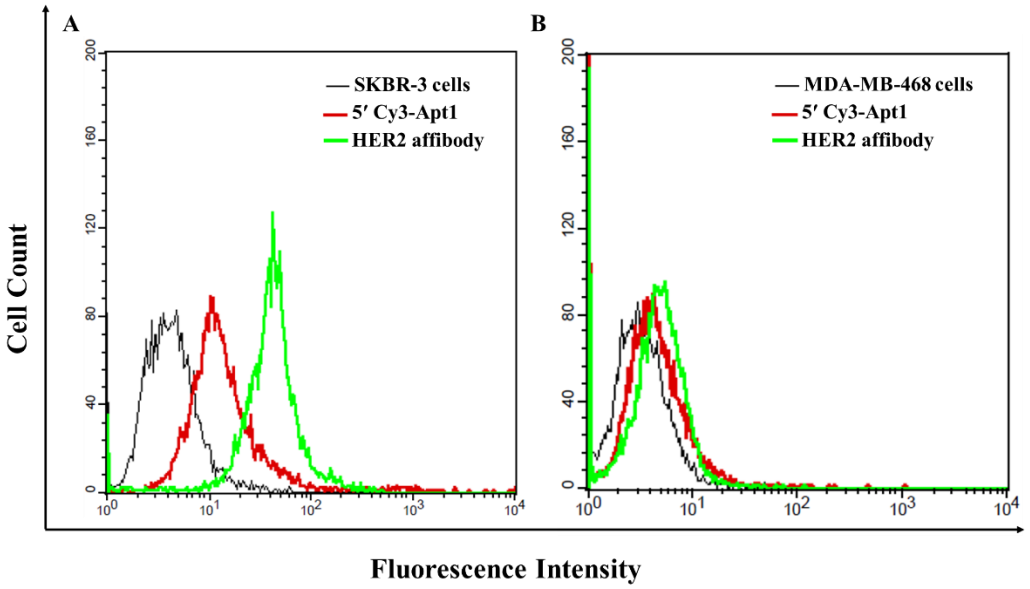


Figure 2.10. Assessment of aptamer binding properties by flow cytometry. SKBR-3 cells (A) and MDA-MB-468 cells (B) were incubated with 5' Cy3-Apt1 or FITC-labelled affibody for 40 min at 4 °C in the dark. The concentration of the aptamer was 1 μM.

Encouraged by above results, the aptamer binding conditions were further optimised and evaluated in the following sections.

2.3.5.1 Comparison of enzymatic and non-enzymatic cell dissociation effects on fluorescence-associated cell sorting assays

In order to ensure the structural integrity of the HER2 membrane protein, we first compared the binding properties of 5' Cy3-Apt1 using a non-enzymatic method of detaching the cells from the culture flasks as trypsin is known to digest the proteins on the outer surface of the cell.[206] This was achieved by using non-enzymatic cell dissociation solution. The same binding conditions described in Section 2.3.1 were used.

The results demonstrated that no differences were observed in the binding assays when using non-enzymatic dissociation method in comparison with 2 min trypsin-EDTA treatment (Figure 2.11).

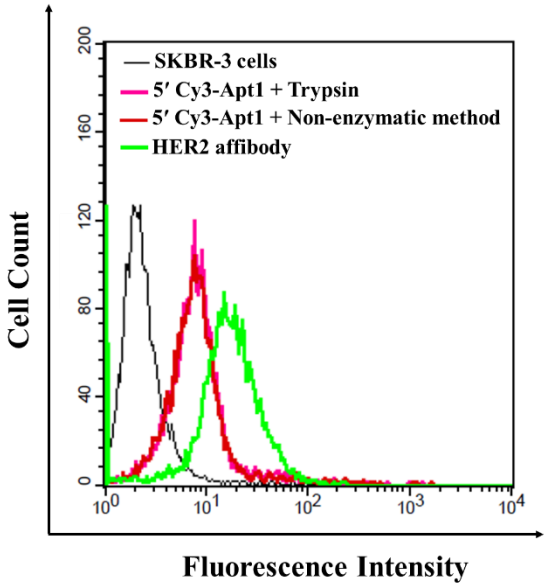


Figure 2.11. Assessment of aptamer binding properties by flow cytometry. SKBR-3 cells were incubated with 5' Cy3-Apt1 or FITC-labelled affibody for 40 min at 4 °C in the dark. The cells were detached using trypsin-EDTA treatment or non-enzymatic dissociation method. The concentration of the aptamer was 1 μM.

As no differences were detected between two cell dissociation methods, the non-enzymatic dissociation strategy was utilised in the following experiments in order to

maintain the reproducibility of experiments.

2.3.5.2 Investigating the effect of aptamer concentration on HER2 binding using fluorescence-associated cell sorting

To verify whether aptamer concentration is correlated with binding ability, three different concentrations including 1 μM, 5 μM, and 8 μM were investigated. In this experiment, 5' Cy3-Apt1 and its negative control 5′ Cy3-Apt4 (a mutated version) were evaluated.

5' Cy3-Apt1 exhibited increased binding affinity to SKBR-3 (HER2+) cells with increasing concentrations (Figure 2.12A), while the concentration did not significantly affect aptamer binding for MDA-MB-468 (HER2-) control cells (Figure 2.12B).

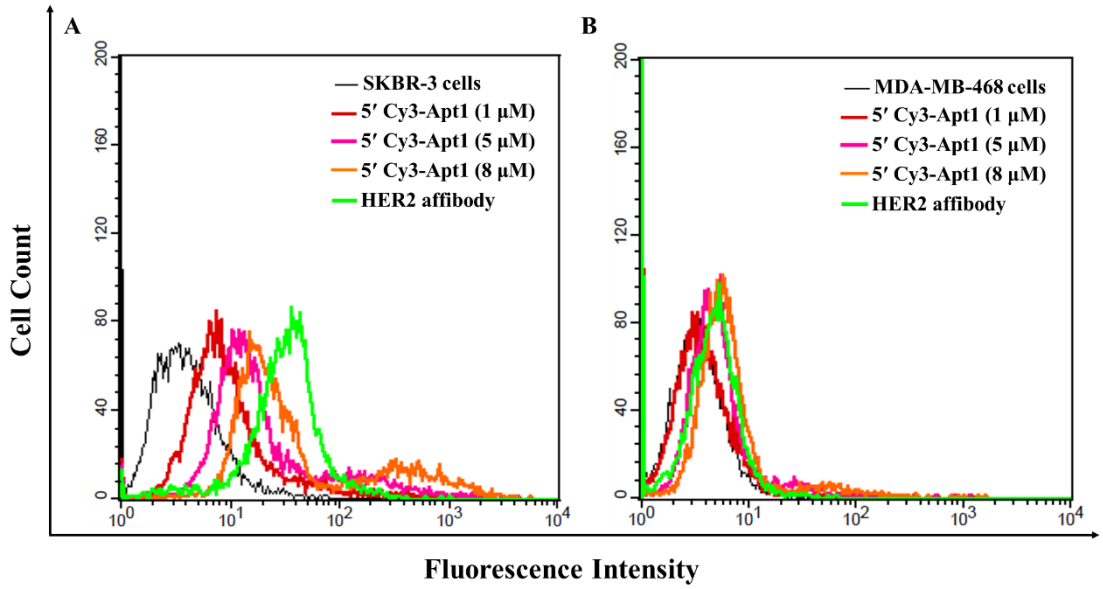


Figure 2.12. Assessment of aptamer binding properties by flow cytometry. SKBR-3 cells (A) and MDA-MB-468 cells (B) were incubated with various concentrations of 5' Cy3-Apt1 or FITC-labelled affibody for 40 min at 4 °C in the dark.

The same experiment was repeated for the negative control 5′ Cy3-Apt4 and a similar trend was observed showing fluorescence intensities increased with increasing aptamer concentrations; however, this occurred at a lower extent when compared with 5' Cy3-

Apt1 (Figure 2.13A). This is possibly because the reported mutated version is still able to bind HER2, albeit to a much lower extent,[204] and a better alternative would be to use a scrambled aptamer version as future work. Furthermore, no binding preference was detected to MDA-MB-468 (HER2-) control cells (Figure 2.13B).

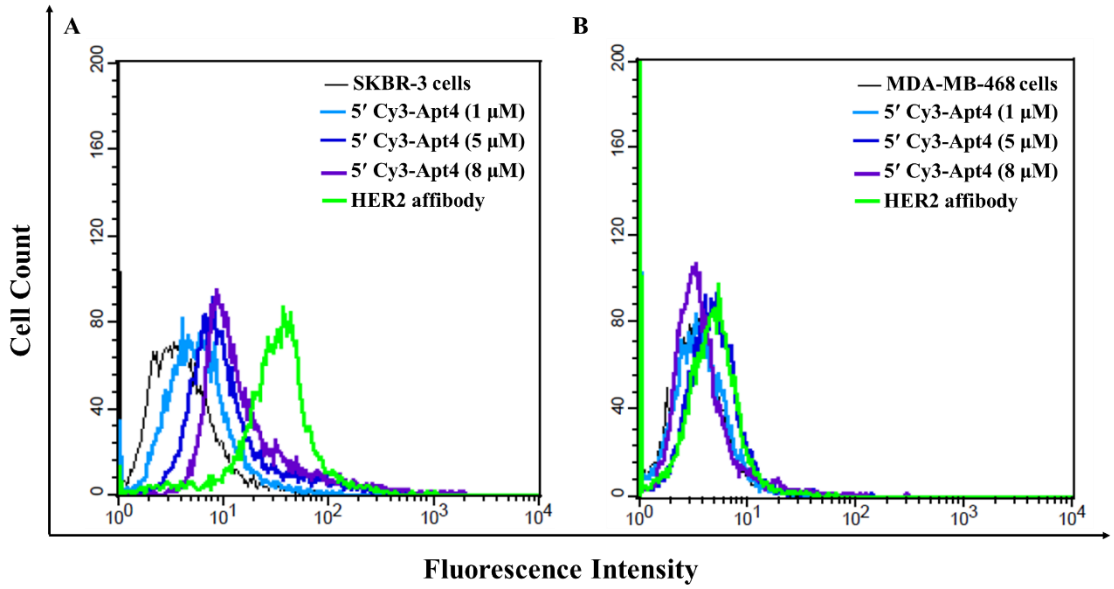


Figure 2.13. Assessment of aptamer binding properties by flow cytometry. SKBR-3 cells (A) and MDA-MB-468 cells (B) were incubated with various concentrations of 5′ Cy3-Apt4 or FITC-labelled affibody for 40 min at 4 °C in the dark.

2.3.5.3 Investigating the effect of incubation temperature on HER2 binding using fluorescence-associated cell sorting

It is known that aptamers can internalise into cells at 37 °C *via* receptor mediated endocytosis, making them useful for delivery of therapeutic agents.[219-223] Based on this, we further compared the binding assays at both 4 °C and 37 °C, respectively. Cell lines SKBR-3 (HER2+) and MDA-MB-468 (HER2-) were used and aptamers of 5' Cy3-Apt1, 5′ Cy3-Apt4, 5' Cy3-Apt5 and 5′ Cy3-Ap6 were evaluated in this study.

As presented in Figure 2.14A, the 5' Cy3-Apt1 bound to SKBR-3 (HER2+) cells to a

higher extent at 37 °C when compared to 4 °C, whilst no shift in fluorescence intensity was detected for MDA-MB-468 (HER2-) cells (Figure 2.14B). This could be because the aptamer preferentially internalised into SKBR-3 (HER2+) cells, which can also be detected by FACS.

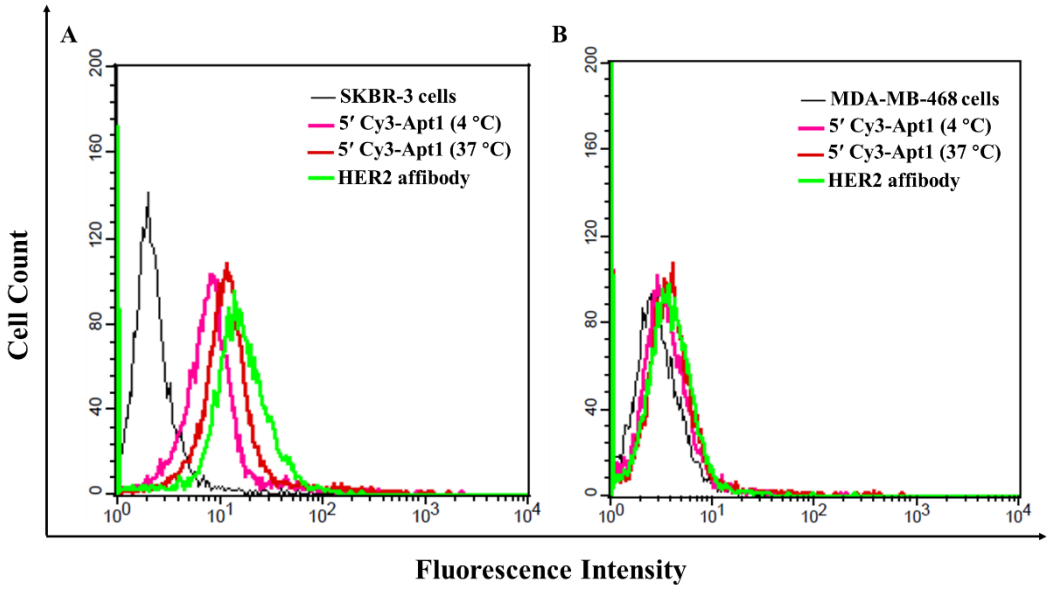


Figure 2.14. Assessment of aptamer binding properties by flow cytometry. SKBR-3 cells (A) and MDA-MB-468 cells (B) were incubated with 5' Cy3-Apt1 or FITC-labelled affibody for 40 min at both 4 °C and 37 °C in the dark. The concentration of the aptamer was 1 μM.

In addition, the negative control aptamer 5′ Cy3-Apt4 did not produce a significant increase in fluorescence intensity in either HER2+ or HER2- cell lines at 4 °C and 37 °C (Figure 2.15).

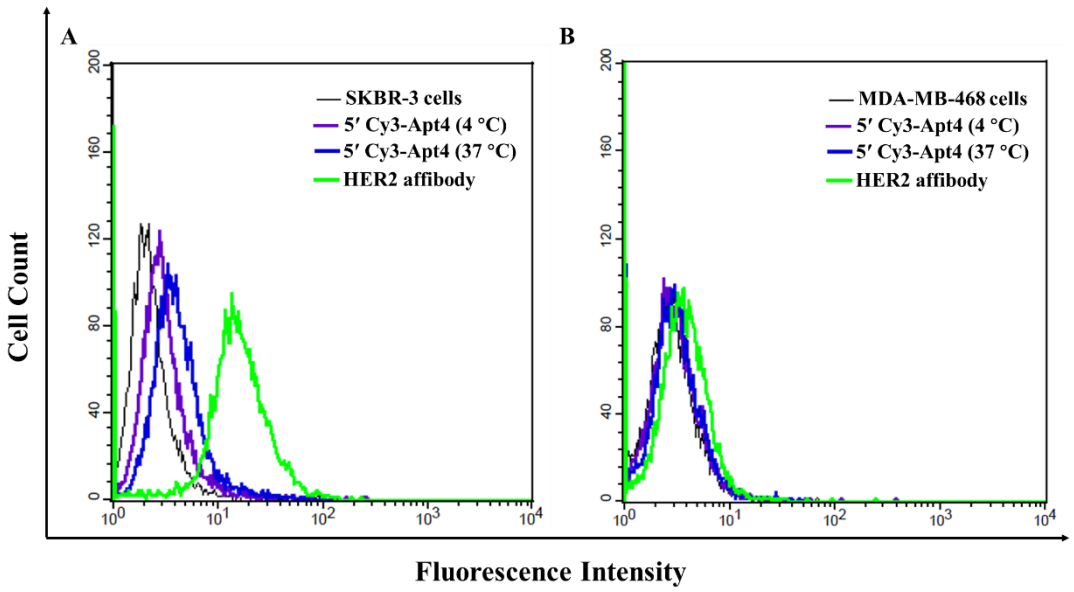


Figure 2.15. Assessment of aptamer binding properties by flow cytometry. SKBR-3 cells (A) and MDA-MB-468 cells (B) were incubated with 5′ Cy3-Apt4 or FITC-labelled affibody for 40 min at both 4 °C and 37 °C in the dark. The concentration of the aptamer was 1 μM.

We observed that 5' Cy3-Apt5 required a higher concentration of 8 μM compared with 5' Cy3-Apt1 which required 1 μM for strong positive binding to SKBR-3 (HER2+) cells at 37 °C (Figure 2.16A). However, at 8 μM a high background fluorescence from 5' Cy3-Apt5 was observed for MDA-MB-468 (HER2-) control cells (Figure 2.16B). Furthermore, the negative control 5′ Cy3-Apt6 used in this study also gave positive fluorescent signals when incubated with SKBR-3 (HER2+) cells, and lower fluorescence intensity for MDA-MB-468 (HER2-) control cells (Figure 2.17).

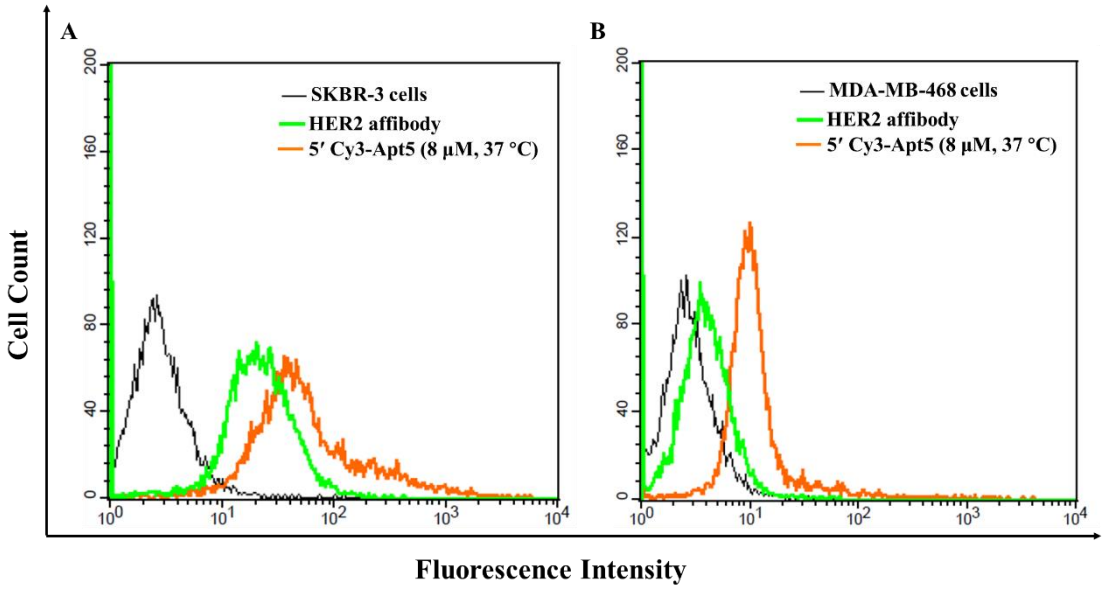


Figure 2.16. Assessment of aptamer binding properties by flow cytometry. SKBR-3 cells (A) and MDA-MB-468 cells (B) were incubated with 5' Cy3-Apt5 (8 µM) or FITC-labelled affibody for 40 min at 37 °C in the dark.

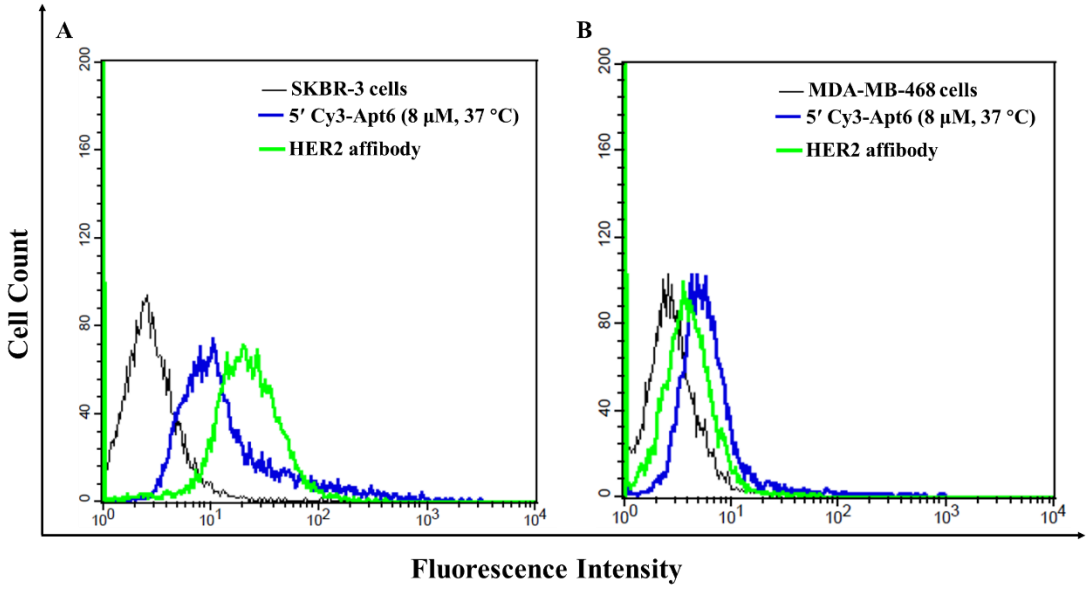


Figure 2.17. Assessment of aptamer binding properties by flow cytometry. SKBR-3 cells (A) and MDA-MB-468 cells (B) were incubated with 5' Cy3-Apt6 (8 µM) or FITC-labelled affibody for 40 min at 37 °C in the dark.

Due to higher background fluorescence observed for 5' Cy3-Apt5, we further optimised the washing step to reduce non-specific binding. This was done by varying the number of

washing steps after incubation with aptamer.

As shown in Figure 2.18, the high background fluorescence from 5' Cy3-Apt5 was not significantly reduced even after washing the control cells 10 times with DPBS. Because of the above results, the 5' Cy3-Apt5 was not investigated further due to its non-specific binding.

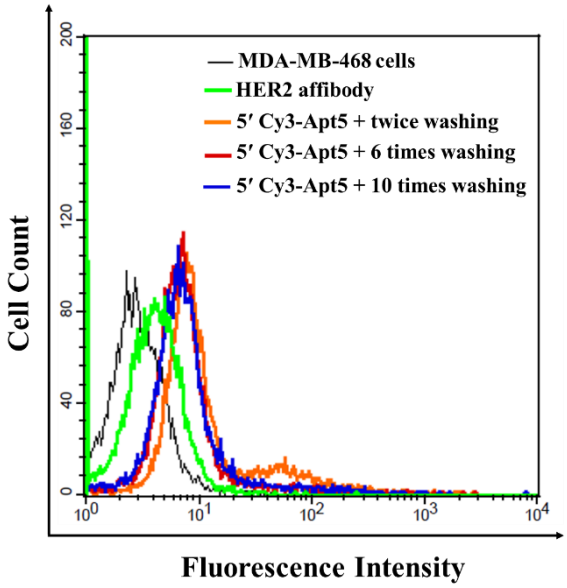


Figure 2.18. Assessment of aptamer binding properties by flow cytometry. SKBR-3 cells were incubated with 5' Cy3-Apt5 (8 μM) or FITC-labelled affibody for 40 min at 37 °C in the dark. After incubation, the cells were washed twice, 6 times or 10 times with DPBS.

2.3.5.4 Comparing new and old batches of MDA-MB-468 cell line

As the previous batch of MDA-MB-468 had been passaged over 60 times, we obtained a new batch of MDA-MB-468 cell line from Dr Jyothi Menon (Department of Oncology, University of Oxford) for further studies. Immunophenotyping, performed by Abigail R Guillermo within our group, confirmed that the old batch of MDA-MB-468 cells did not overexpress HER1 or HER2. To confirm whether the new batch of cells behaved the same, we repeated the FACS experiments. The binding ability of 5' Cy3-Apt1 to MDA-MB-468

(new batch) cells was evaluated at both 4 °C and 37 °C.

Surprisingly, 5' Cy3-Apt1 showed a higher degree of fluorescence intensity when incubated with the new batch of MDA-MB-468 cells at both 4 °C and 37 °C (Figure 2.19) compared with the old batch (Figure 2.14B), whereas reference Anti-HER2 affibody did not. We then consulted the literature and found that MDA-MB-468 is reported to be HER1+. Immunophenotyping of the new batch MDA-MB-468 cell line was then performed by Megan Grundy (The Institute of Biomedical Engineering, University of Oxford) confirming its HER1+ nature. This result led us to believe that the aptamer 5' Cy3-Apt1 binds both HER1 and HER2 receptors, which is in disagreement with the literature.[202]

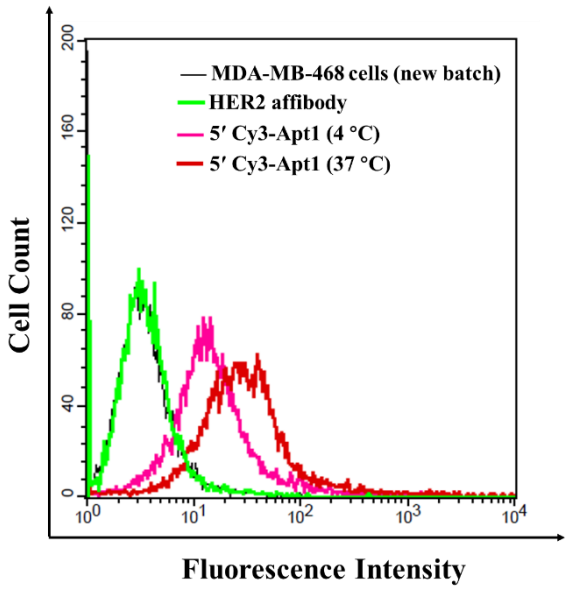


Figure 2.19. Assessment of aptamer binding properties by flow cytometry. MDA-MB-468 cells (new batch) were incubated with 5' Cy3-Apt1 (1 μM) or FITC-labelled affibody for 40 min at 4 °C and 37 °C in the dark.

2.3.5.5 Investigating aptamer binding properties for MCF-7 cell line (HER1-/HER2-) using fluorescence-associated cell sorting

As 5' Cy3-Apt1 showed high binding ability to MDA-MB-468 (HER1+) cells, we then switched to use a MCF-7 cell line that is both HER1- and HER2- as a negative control in our study. Immunophenotyping tests confirmed that the MCF-7 cell line did not overexpress HER1 or HER2 (Figure 2.20).

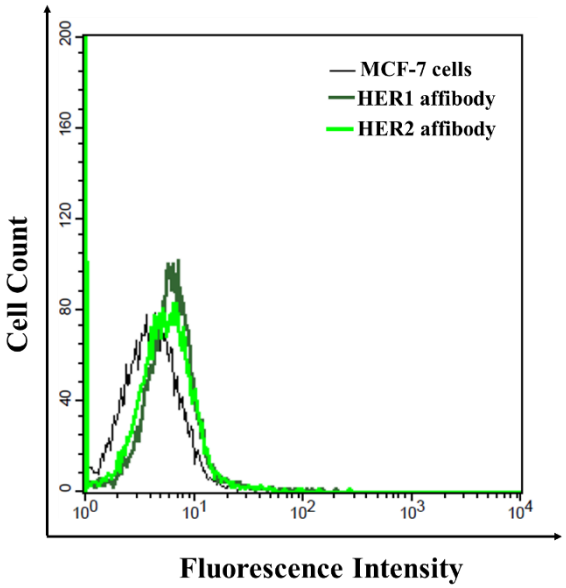


Figure 2.20. Immunophenotyping test for MCF-7 cell line by flow cytometry.

The binding affinities of 5' Cy3-Apt1 and 5′ Cy3-Apt4 were then evaluated at both 4 °C and 37 °C. Preliminary results demonstrated that no shift in fluorescence intensity was detected when both 5' Cy3-Apt1 and 5′ Cy3-Apt4 were incubated with MCF-7 (HER1-/HER2-) cells at 4 °C and 37 °C, respectively (Figure 2.21). The MCF-7 (HER1-/HER2-) cell line was then used as a negative control in the following studies.

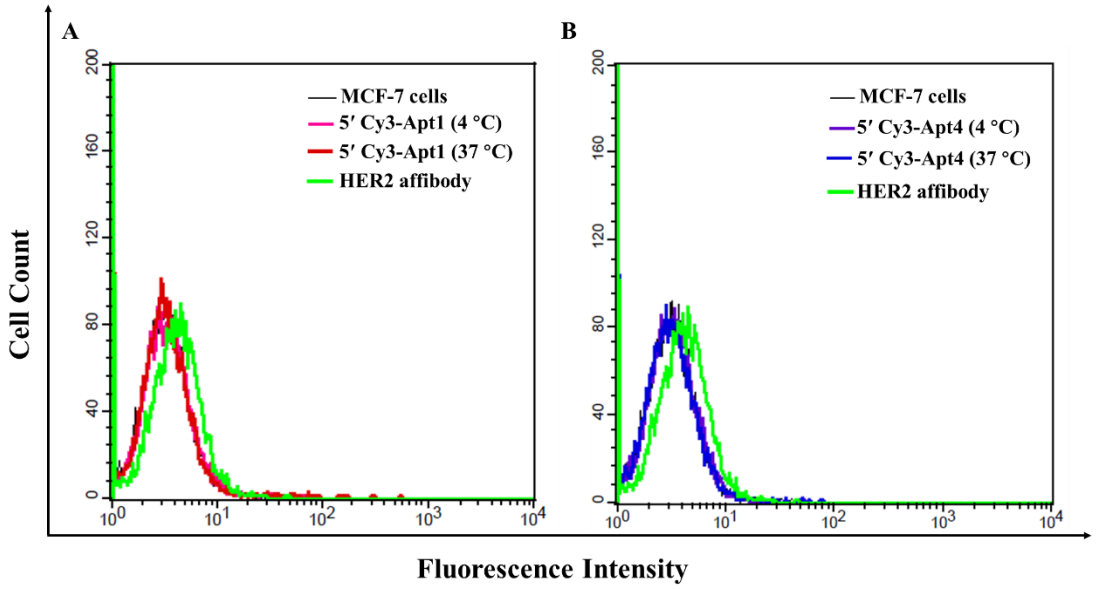


Figure 2.21. Assessment of aptamer binding properties by flow cytometry. MCF-7 cells were incubated with 5' Cy3-Apt1 and 5' Cy3-Apt4 (1 μM) or FITC-labelled affibody for 40 min at 4 °C and 37 °C in the dark.

2.3.6 Investigating aptamer cellular uptake using confocal microscopy

As mentioned above, cell specific internalisation of aptamers is crucial in the delivery of therapeutic agents to targeted cells. Confocal microscopy was used to determine if the bound aptamers were internalised into the cancer cells.

Preliminary results indicated that the fluorescence intensity for SKBR-3 cells (HER2+) increased with increasing aptamer concentrations (Figure 2.22). Fluorescence signals were mostly localised in the perinuclear area. Furthermore, no obvious fluorescence signals were detected for MCF-7 (HER1-/HER2-) control cells.

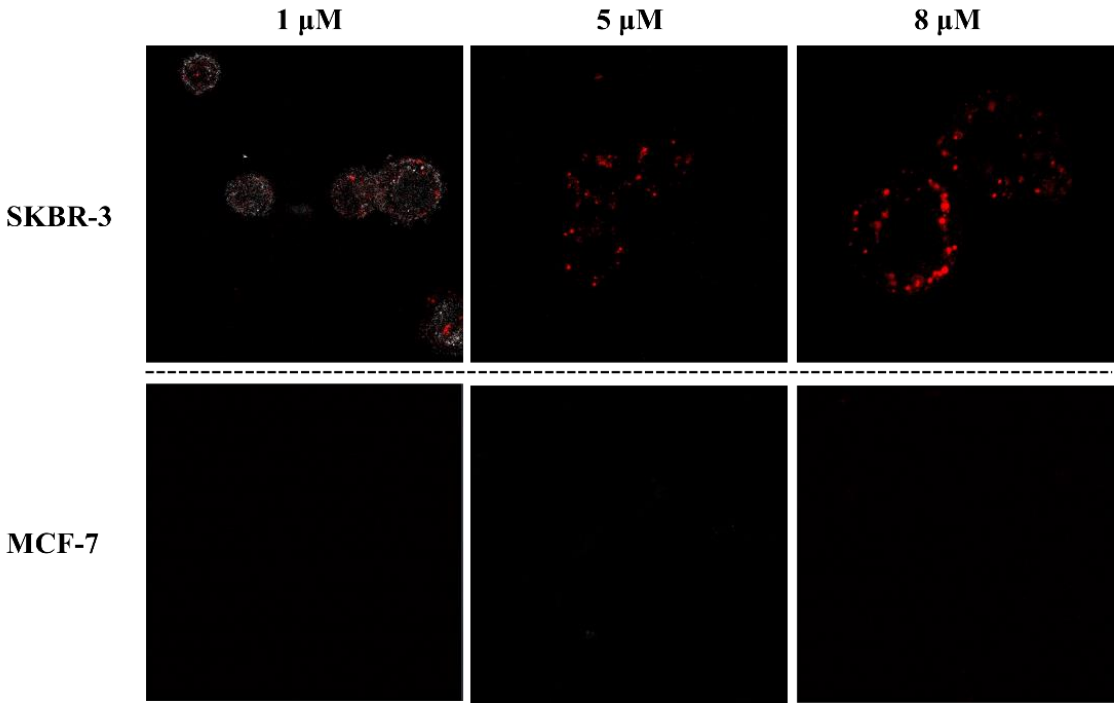
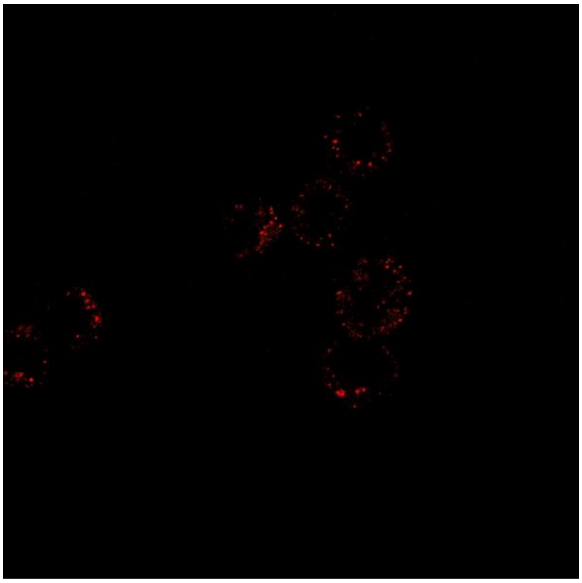


Figure 2.22. Assessment of aptamer internalisation into SKBR-3 and MCF-7 cells by confocal microscopy. Cells were incubated with various concentrations of 5' Cy3-Apt1 (1 μM, 5 μM and 8 μM) for 40 min at 37 °C in the dark.

In addition, as shown in Figure 2.23, 5' Cy3-Apt1 also internalises into MDA-MB-468 (HER1+) cells. This is consistent with the FACS results, which support the hypothesis that the aptamer also binds to HER1.



MDA-MB-468

Figure 2.23. Assessment of aptamer internalisation into MDA-MB-468 cells by confocal microscopy. Cells were incubated with 5' Cy3-Apt1 (1 μM) for 40 min at 37 °C in the dark.

As mentioned above, both FACS and confocal studies indicated that 5' Cy3-Apt1 can internalise into both HER1+ and HER2+ cancer cells. Therefore, work with Apt1 was continued and it was used to construct aptamer-based DNA-NFs in Chapter 4.

2.4 Conclusions

Six reported aptamers with Cy3 labelling were synthesised, and have been characterised using various techniques including CD, native PAGE, UV melting and FACS. Preliminary FACS studies indicated that Cy3-Apt1 and 5' Cy3-Apt5 were the most promising candidates and these were investigated further.

The structures of Cy3-Apt1 and 5' Cy3-Apt5 were successfully characterised using CD. With regards to Apt1, no significant differences were observed in the presence of Na^+ when the Cy3 dye was labelled at the either 5' end or 3' end and different annealing conditions did not result in conformation changes or the formation of a G-quadruplex. However, an external loop parallel G-quadruplex structure for 5' Cy3-Apt1 was detected in the presence of K^+. The 5' Cy3-Apt5 generated a double-stranded A-form conformation under both Na^+ and K^+ conditions.

An intramolecular G-quadruplex structure for 5' Cy3-Apt1 in the presence of K^+ was successfully characterised using native PAGE technique. Moreover, this compact structure preferentially formed at the lower concentration of K^+. In addition, UV melting study corroborated the results from the native PAGE. The T_m value did not depend on the concentration of 5' Cy3-Apt1, indicating intramolecular G-quadruplex formation. For 5' Cy3-Apt5, no intra- or intermolecular G-quadruplex or other compact structure was observed in the presence of Na^+ and K^+.

The binding properties of the two aptamers were successfully evaluated and we observed that a G-quadruplex structure was necessary for 5' Cy3-Apt1 binding to HER-positive cancer cells. Furthermore, fluorescence intensity was detected for the new batch of MDA-MB-468 cells (HER1+) suggesting that the aptamer 5' Cy3-Apt1 binds both HER1 and

HER2. For 5' Cy3-Apt5, high background fluorescence was observed for negative control cells.

Confocal microscopy was used to evaluate the internalisation of 5' Cy3-Apt1 and indicated that fluorescence signals were mostly localised in the perinuclear area of SKBR-3 (HER2+) cells. Internalisation of 5' Cy3-Apt1 to MDA-MB-468 (HER1+) cells was also detected, which supports the hypothesis that this aptamer also binds to the HER1 biomarker. No obvious fluorescence intensity was observed for MCF-7 (HER1-/HER2-) control cells.

Chapter 3

Preparation and characterisation of manganese and cobalt DNA nanoflowers

Chapter 3 – Preparation and characterisation of manganese and cobalt DNA nanoflowers

3.1 Preface

The work presented in this chapter was published in Nucleic Acids Research.[224] It was carried out in collaboration with Dr. Ysobel R. Baker who imaged the precipitated DNA nanoconstructs.

3.2 Introduction and aims

Advanced materials with increasingly sophisticated properties are at the forefront of modern technology and scientific research. Hybrid materials, that are materials formed of two or more constituents at the molecular or nanometer level, aim to merge the best properties of the biological, inorganic and organic components whilst instilling new functionalities.[225] It is possible to circumvent the limitations associated with the individual materials such as instability and lack of biocompatibility by combination of inorganic and biological materials.[226] For instance, hybrid materials coupling magnetic materials with biological properties have an expansive range of biomedical applications.[227,228] They can be utilised to generate heat locally, to direct them to a particular site using an external magnetic field to deliver therapeutics or to conjugate with antibodies, allowing for isolation of materials and magnetic capture.[229-232] In addition, magnetic materials can be combined with enzymes to prepare enzyme nanogels that are catalytically active, thermally stable, and can be readily recovered and reused.[233]

DNA-NFs are an excellent example of inorganic hybrid materials. They are composite materials consisting of long single-stranded DNA and crystalline magnesium

pyrophosphate ($Mg_2P_2O_7$) assembled into hierarchical structures with flower-shaped morphology. DNA-NFs are generated by RCA under mild reaction conditions using a DNA polymerase and circularised DNA template. In an RCA reaction, the DNA polymerase repeatedly traverses the circular template generating long single-stranded DNA composed of repeating units complementary to the circular template.[174,234] During this process, a pyrophosphate anion ($P_2O_7^{4-}$) is released when the polymerase incorporates each nucleotide. The pyrophosphate anion by-products then co-crystallise with both the growing DNA strands and Mg^{2+} ions present in the amplification buffer to produce the DNA-NFs (Figure 3.1).[235] A similar phenomenon has also be observed during rolling circle transcription (RCT), with the resulting similar materials being called RNA microsponges (RNA-MSs).[236]

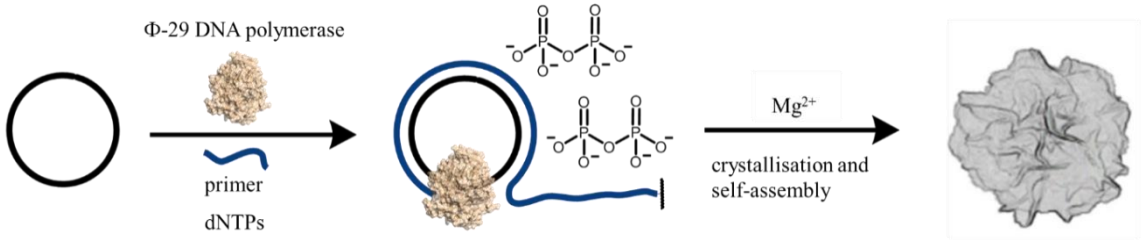


Figure 3.1. DNA-NFs self-assembly using DNA polymerase enzyme. The black circle refers to a circular DNA template and the primer that is elongated is represented in blue.

Both DNA-NFs and RNA-MSs combine the structure and stability of $Mg_2P_2O_7$ with the biological and programmable advantages of DNA or RNA. They have a variety of biomedical applications including bioimaging, targeted delivery of chemotherapeutics by incorporating aptamers into the DNA products, delivery of small interfering RNA (siRNA) for effective RNA interference therapy, delivery of DNAzymes and cellular delivery of proteins, to mention a few.[174,234,235,237-239] From this, it is evident that they exhibit many advantageous properties including sequence programmability, high stability, automated controllable synthesis and water solubility.[234,237]

Recently, researchers have focused on modifying the organic components to alter the functions of these DNA-based hybrids using methods such as incorporating modified nucleoside triphosphates, condensing the particles with cationic polymers, incorporating functional moieties through the cyclic template and loading doxorubicin and functional proteins.[174,234,239-241] We envisaged that it could be possible to obtain additional functionalities by altering the inorganic component. Literature has reported that pyrophosphates and metal phosphates have been utilised in electrochemical detection, catalysis and in supercapacitors.[242-244] They also have a wide range of biomedical applications including magnetic resonance imaging (MRI) contrast agents, therapeutics, photoluminescent probes and artificial bone scaffolds.[245-248] Therefore, we envisioned that it would be possible to broaden the versatility and applicability of DNA-NFs by altering the metal ion component of the pyrophosphate salts.

The aim of the work in this chapter was to prepare DNA-NFs with added magnetic properties. To achieve this, we replaced the most widely used magnesium ions (Mg^{2+}) with other divalent ions such as manganese ions (Mn^{2+}) and cobalt ions (Co^{2+}) during the DNA polymerisation step. During these studies, we observed that the DNA-NFs formed with Mn^{2+} and Co^{2+} had drastically different size and morphology to the Mg^{2+} DNA-NFs, which was an unexpected result. As a result, we also investigated conditions to control the morphology and size of these particles.

3.3 Manganese DNA nanoflowers

Due to the similar chemical and biochemical properties to Mg^{2+}, Mn^{2+} has been utilised as a metal activator for many DNA polymerases.[249] Furthermore, these DNA polymerases can maintain their catalytic functions when the physiologically relevant Mg^{2+} is replaced with Mn^{2+}. Compared with Mg^{2+}, Mn^{2+} possesses five unpaired d electrons, which give

rise to its magnetic properties. In order to fabricate novel DNA-based inorganic nanomaterials using DNA polymerisation, we replaced the Mg^{2+} with Mn^{2+} in the amplification buffer during the RCA process, and investigated the effect of Mn^{2+} on DNA-NFs formation when using both Φ-29 and Bst 2.0 DNA polymerases.

Preliminary results in our group suggested that metal ion concentration, pH and temperature have an effect on the particle morphology, DNA levels within particles and particle size.[224] Herein, screening conditions were carried out in collaboration with Dr. Ysobel R. Baker to evaluate this hypothesis. The process is described in detail below.

3.3.1 Variables for controlling morphology and DNA levels within the manganese DNA nanoflowers

In our studies, two templates were randomly generated and chosen to test this hypothesis (Table 3.1). The majority of the work was performed using template 1. Template 2 was included to confirm that the results were not sequence dependent.

Table 3.1. Sequences of the oligonucleotides used in this study (mass spectra data of oligonucleotides showed in Section 6.2.1, Chapter 6).

Oligonucleotide name	Sequence of linear precursor[a] (5′→3′)	length
Template 1 (T1)	[P]TATAGCCCATGTGCTGCTGCTGCAGCGATA CGCGTATGCTATGGCATATCGTACGATATGC CGCAGCAGCATTACCGTCGTT	82
Template 2 (T2)	[P]ATAGTGAGTCGTATTAGCTCGAGCTCGAGC AGCCGCGCCCTACCCTATCCCTCCCCTCGCG GCTGCTCGAGCTCGAGCATCCCT	84
Splint 1 (S1, cyclisation splint and RCA primer for T1)	GCACATGGGCTATAAACGACGGTAA	25
Splint 2 (S2, cyclisation splint and RCA primer for T2)	TAATACGACTCACTATAGGGAT	22

[a] P = 5′-PO_4.

We first investigated the formation of DNA-NFs using Mn^{2+} instead of Mg^{2+}. Based on preliminary results within the group, we investigated three variables: Mn^{2+} concentration, pH and temperature. As polymerases typically function best in a narrow temperature range, two polymerases with different amplification temperatures were used to investigate the effect of temperature: Φ-29 (a mesophilic polymerase with an optimum temperature range of 25 - 35 °C) and Bst 2.0 (a thermostable polymerase with an optimum temperature range of 55 - 65 °C).

It was first necessary to prepare the cyclic templates for this study. The linear templates modified with a 5′ phosphate group were synthesised using automated solid-phase phosphoramidite chemistry as presented in Section 6.2.1 (Chapter 6). T4 DNA ligase was used to circularise the linear oligonucleotides (linear T1 and linear T2). The resulting circularised templates were then purified by denaturing PAGE to remove potential batch-

to-batch variability related with the efficiency of enzymatic cyclisation. Prior to use, the circularised products were further desalted thoroughly in order to eliminate Mg^{2+} remaining from the ligation buffer.

For both Φ-29 and Bst 2.0 DNA polymerases, Mn^{2+} concentrations ranging from 5 - 15 mM in the pH range of 7.0 - 9.0 were investigated. The RCA reactions using Φ-29 DNA polymerase were carried out at 30 °C for 20 h, and 61.5 °C for Bst 2.0 DNA polymerase for 14 h. These incubation times and temperatures were identified during preliminary work by Dr. Ysobel R. Baker. The RCA reactions were stopped by heat denaturation of the enzyme and the DNA-NFs were collected by centrifugation and washed with MilliQ water. Both the supernatants and the precipitate containing the DNA-NFs were analysed by agarose gel electrophoresis (Appendix Figure 8.2.1 - 8.2.4).

Gel electrophoresis analysis of the supernatants demonstrated that elongated DNA products were generated by both DNA polymerases in Mn^{2+} RCA reactions, with the efficiency of Φ-29 decreasing with increasing pH whereas Bst 2.0 performed more effectively at higher pH. Moreover, more free DNA was produced at lower Mn^{2+} concentrations and more DNA was captured in the precipitates at the higher concentrations. It is noteworthy that although the long DNA products present in the particles were retarded in the wells of the gel, a second band between the 1 kb marker and the well of the gel was observed when analysing the Φ-29 precipitates. This band was also present in the corresponding supernatant. This is in agreement with a previous report and this band was assigned to a double-stranded amplification product.[250] However, this band was not observed in Bst 2.0 catalysed RCA reactions.

Precipitates identified to contain significant amounts of DNA by agarose gel electrophoresis were imaged using scanning electron microscopy (SEM). SEM imaging

indicated that Mn^{2+} concentration has a significant effect on the morphology of the particles (Figure 3.2). Each RCA reaction was performed in triplicate at specified concentration and the standard deviations of particle size are given. More specifically, at 5 mM, RCA catalysed by Bst 2.0 generated large shell-like particles with a layered structure with an average length of ~15.8 ± 2.7 μm. At 10 mM Mn^{2+}, smaller particles with the size of ~1.4 ± 0.5 μm were formed in a mesh, and individual small DNA-NFs can be obtained after sonication. At 15 mM Mn^{2+}, manganese DNA-NFs (MnDNA-NFs) of ~2.6 ± 0.3 μm in size were generated with similar morphology to the reported magnesium DNA-NFs (MgDNA-NFs).[174,234,239] In each case the average size of the particles formed was determined using ImageJ software, measuring the longest distance in at least 26 particles.

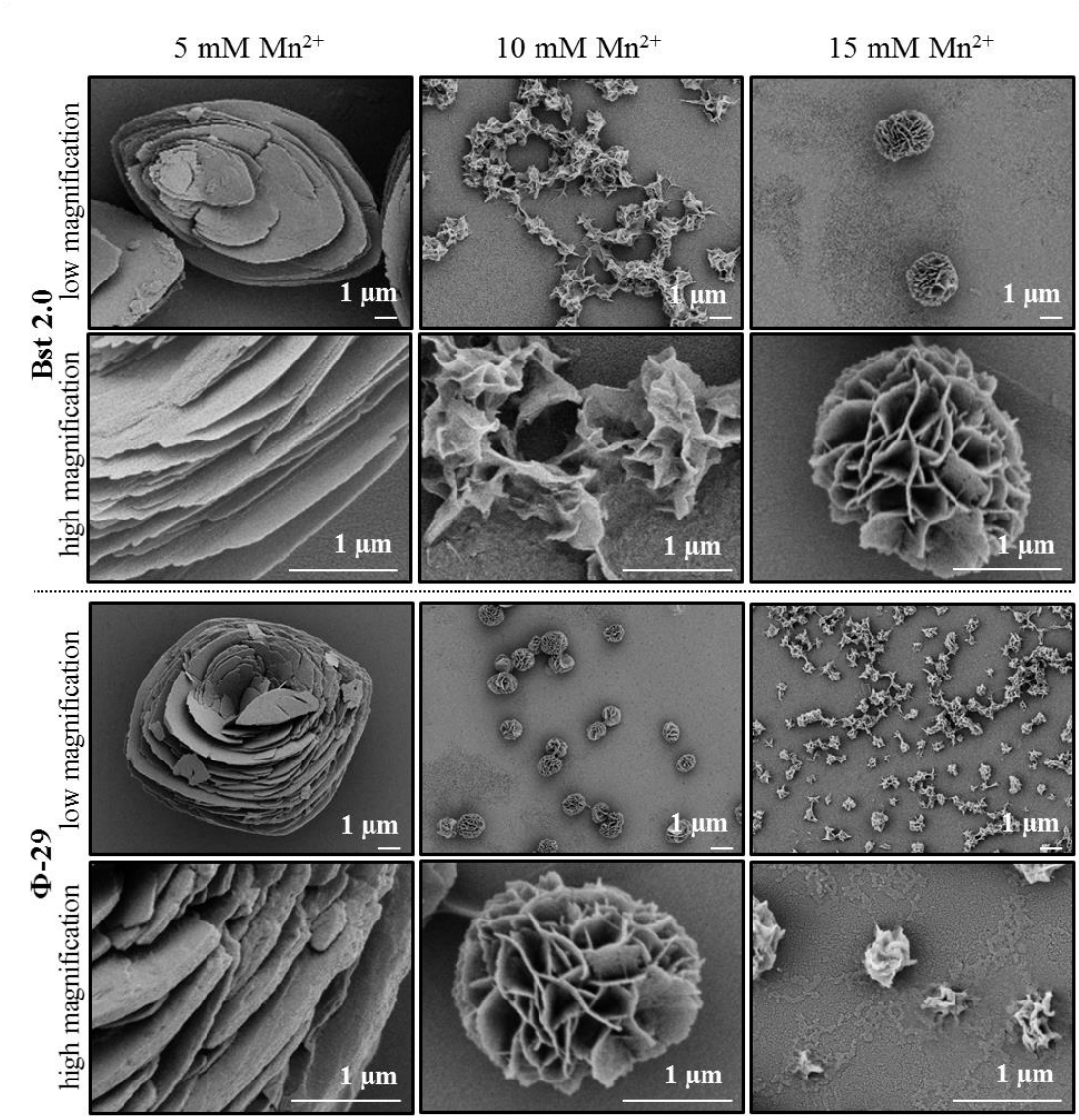


Figure 3.2. SEM images demonstrating the effect of Mn^{2+} concentration and DNA polymerases on the morphology and size of the particles that generated in RCA reactions using cyclic T1 and S1. The RCA reactions were performed using Φ-29 DNA polymerase for 20 h at pH 8.0, and Bst 2.0 DNA polymerase for 14 h at pH 7.5.

A similar trend in morphology was observed for the particles generated in the Φ-29 catalysed RCA reactions. Each RCA reaction was carried out in triplicate at specified concentration and the standard deviations of particle size are given. At 5 mM Mn^{2+}, Φ-29 produced large particles with a layered structure which were more square-like than that of those produced by Bst 2.0. The average length of these particles was ~8.8 $\pm$ 1.2 µm. At 10 mM, particles with petal-like surface morphology were formed with an average

diameter of ~1.3 ± 0.2 μm, which was similar to the particles generated by Bst 2.0 at 15 mM Mn^{2+} and the morphology of the reported MgDNA-NFs.[174,234,239] Interestingly, as the Mn^{2+} concentration increased, smaller particles with ~0.312 ± 0.006 μm in size were produced. In each case the average size of the particles formed was determined using ImageJ software, measuring the longest distance in at least 20 particles.

In order to further investigate the effect of pH on both the DNA levels present in the particles and polymerase efficiency, SYBR Gold was used to allow semi-quantitative comparison of DNA present in both the precipitates and supernatants. SYBR Gold is a DNA binding dye which has an ability to bind to both single- and double-stranded DNA. After the RCA reactions, the samples were incubated in Tris-Borate-EDTA (TBE) buffer overnight to break down any precipitate and also to sequester Mn^{2+} cations prior to incubation with the DNA binding dye and measurement. Based on the earlier electrophoresis results, 15 mM concentration of Mn^{2+} was chosen to investigate the effect of pH. We identified that the DNA levels present in the particles were significantly affected by the pH at which the RCA reactions were performed. For all pH conditions, precipitation was observed when using 15 mM Mn^{2+} in the reaction, and pH 7.0 resulted in the highest levels of precipitated DNA for both Φ-29 and Bst 2.0 DNA polymerases (Figure 3.3).

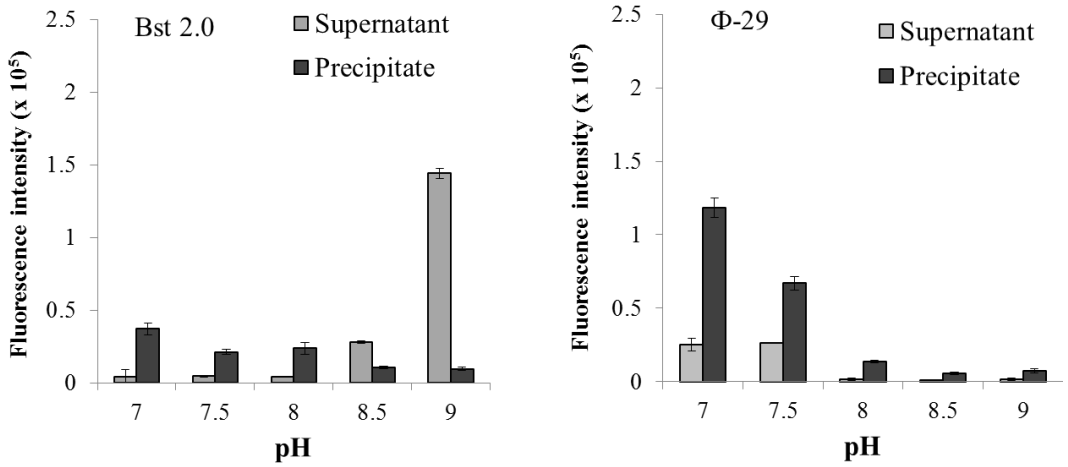


Figure 3.3. Comparing the levels of free DNA and DNA incorporated into the particles using fluorescence-based analysis. RCA reactions were carried out using cyclic T1 and S1. TBE buffer was added to the samples in order to break down the particles and release the DNA products prior to incubation with SYBR Gold and measurement. The effect of pH on both Bst 2.0 and Φ-29 DNA polymerases catalysed RCA was determined at 15 mM Mn^{2+}.

Next, the effect of Mn^{2+} concentration was investigated. Combining the earlier gel electrophoresis experiments and above fluorescence-based analysis results, pH 7.0 was chosen for Bst 2.0 experiments and pH 8.0 for the Φ-29 experiments. Here, we observed that both DNA polymerases generated the highest amount of free DNA at lower Mn^{2+} concentrations ranging from 2 - 5 mM, and the levels of DNA produced in the supernatant were greatly reduced with increasing concentration of Mn^{2+} (Figure 3.4). We hypothesise that this is a result of the DNA products becoming trapped within the precipitates, preventing further extension.

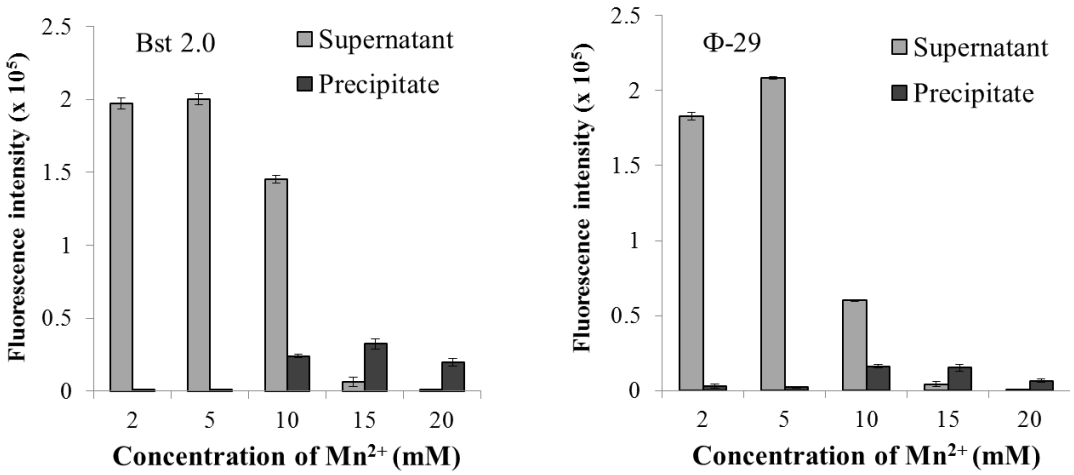


Figure 3.4. Comparing the levels of free DNA and DNA incorporated into the particles using fluorescence-based analysis. RCA reactions were carried out using cyclic T1 and S1. TBE buffer was added to the samples in order to break down the particles and release the DNA products prior to incubation with SYBR Gold and measurement. The effect of cation concentration for Bst 2.0 DNA polymerase catalysed RCA was assessed at pH 7.0. The effect of cation concentration for Φ-29 DNA polymerase catalysed RCA was assessed at pH 8.0.

To conclude, both Bst 2.0 and Φ-29 can be utilised to prepare MnDNA-NFs in a range of shapes. A second band between 1 kb marker and the well of the gel was observed for MnDNA-NFs formed by Φ-29 but not for Bst 2.0, suggesting that Bst 2.0 did not produce a significant amount of double-stranded DNA products during RCA.[250]

3.4 Cobalt DNA nanoflowers

After constructing MnDNA-NFs, we confirmed that Co^{2+} was also utilised in the RCA process to produce DNA-NFs, proving that divalent cations other than Mg^{2+} and Mn^{2+} can be used. As with Mn^{2+}, Co^{2+} also has unpaired d electrons, making Co^{2+} an interesting alternative to construct nanoconstructs with magnetic properties. Like Mn^{2+}, Co^{2+} is also known to support catalysis for many different DNA polymerases.[249] Dithiothreitol (DTT) present in the amplification buffer was found to be incompatible with Co^{2+}, resulting in dark precipitate formation in the absence of a polymerase. We found that it was necessary

to omit DTT when preparing cobalt DNA-NFs (CoDNA-NFs). This is a salient observation as literature published during the course of this study did not report this problem.[251]

Different RCA conditions were screened using the methods described above and those containing nanomaterials were identified. Precipitates containing a DNA component were confirmed using gel electrophoresis and then imaged using SEM. As with Mn^{2+} we found that CoDNA-NFs formed petal-like structures at 10 mM Co^{2+} using both Bst 2.0 and Φ-29 DNA polymerases. It is noteworthy that the volume of RCA reaction significantly altered the morphology of the materials that were generated (Figure 3.5). The reason for this is not clear, and possibly associated with the high DNA levels and precipitate settling.

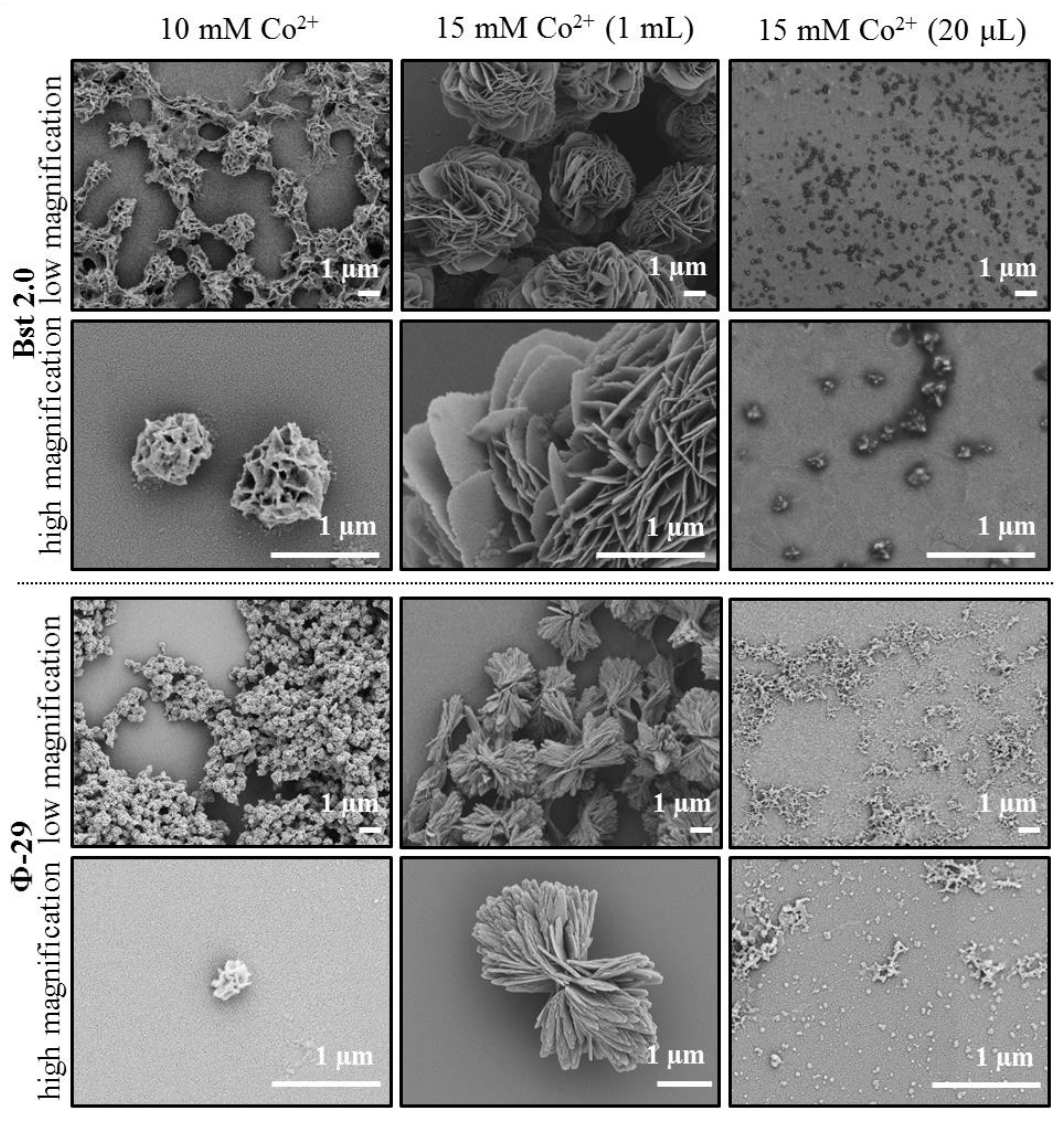


Figure 3.5. SEM images demonstrating the effect of Co^{2+} concentration and reaction scale on the morphology and size of the particles that generated in RCA reactions at pH 7.0 using cyclic T1 and S1. The RCA reactions were performed using Φ-29 DNA polymerase for 20 h, and Bst 2.0 DNA polymerase for 14 h.

As with the earlier Mn^{2+} studies, the DNA produced by the polymerases and the DNA levels present in the particles were evaluated using SYBR Gold. The results demonstrated that DNA can be efficiently incorporated into the nanomaterials at pH 7 - 8 for Bst 2.0 and pH 7 - 7.5 for Φ-29. As with RCA catalysed by Mn^{2+}, more free DNA was produced at lower concentrations of Co^{2+} and more DNA was captured within the precipitates at the higher metal cation concentrations (Figure 3.6). Interestingly, Φ-29 with Co^{2+}

produced more DNA than with Mn^{2+} if the total free DNA was combined with the total DNA present in the precipitate.

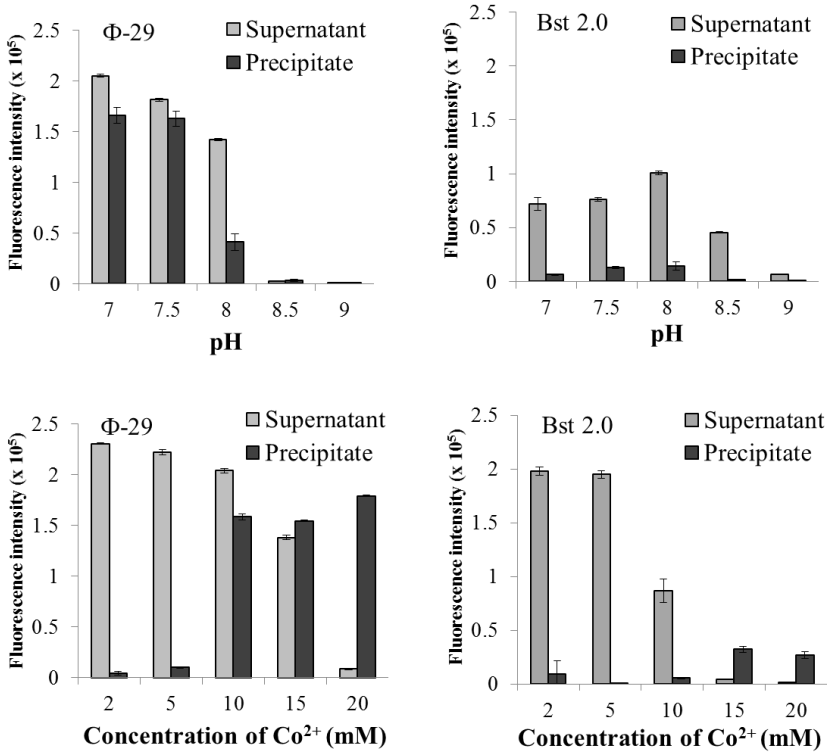


Figure 3.6. Comparing the levels of free DNA and DNA incorporated into the particles using fluorescence-based analysis. RCA reactions were carried out using cyclic T1 and S1. TBE buffer was added to the samples in order to break down the particles and release the DNA products prior to incubation with SYBR Gold and measurement. The effect of pH on Φ-29 and Bst 2.0 DNA polymerases catalysed RCA was evaluated at 10 mM Co^{2+} and the effect of cation concentration was determined at pH 7.0.

In order to determine if the trends in morphology depend upon the DNA sequence, a second template (T2) and its corresponding splint (S2) were prepared with different base composition (Table 3.1) and then utilised in RCA reactions with several conditions described above. The results indicated that the particles that were produced showed a similar trend in size and morphology to those formed using the first template T1, representative SEM images are given in the appendix (Appendix, Figure 8.3.1 - 8.3.7). The MnDNA-NFs produced at 5 mM Mn^{2+} were large with a layered structure and

increasing the concentration of Mn^{2+} resulted in the formation of flower-shaped nanomaterials. The CoDNA-NFs also generated petal-like morphology at 10 mM Co^{2+} and became smaller at 15 mM. These results suggested that the morphology mainly relies on the cation concentration rather than the nucleobase sequence.

After successfully obtaining MnDNA-NFs and CoDNA-NFs, we have also investigated their magnetic properties. Literature has reported that isothermal approaches can be utilised to synthesise nucleic acid materials that can be manipulated using a magnet.[252,253] It is also interesting that transmission electron microscopy (TEM) images showed that materials produced using RCT possessed a similar morphology to MgDNA-NFs.[253] This is possibly because these materials were RNA-NFs or RNA-MSs produced from magnesium pyrophosphate and RNA with magnetic particles embedded in the structure rather than RNA coated magnetic particles; however, the authors of the paper did not mention this. Unlike the reported studies, the magnetic materials prepared in our studies during RCA were significantly larger, and the synthesis method did not rely on using modified nucleic acids or streptavidin coated magnetic particles during the preparation. Here, we showed that both MnDNA-NFs and CoDNA-NFs could be manipulated using a magnet and captured on a commercial magnetic rack (Figure 3.7).

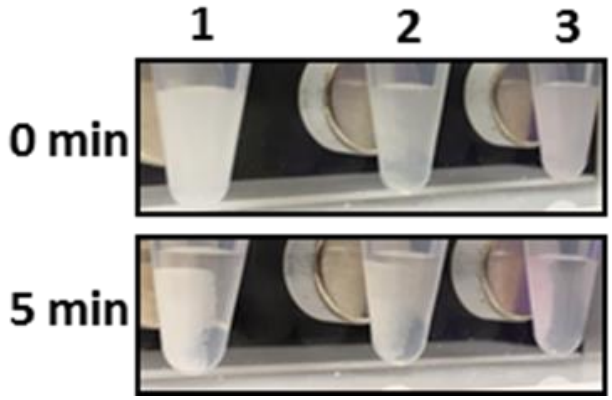


Figure 3.7. Capture of MnDNA-NFs and CoDNA-NFs using a commercial magnetic rack. The suspended particles were attracted to the magnet and the solution became clear after 5 min. (1) MnDNA-NFs produced using Bst 2.0 DNA polymerase with 15 mM Mn^{2+}; (2) MnDNA-NFs produced using Φ-29 DNA polymerase with 15 mM Mn^{2+}; (3) CoDNA-NFs produced using Φ-29 DNA polymerase with 15 mM Co^{2+}. All RCA reactions were carried out using cyclic T1 and S1.

3.5 Serum stability of DNA nanoflowers

Following the successful preparation of MnDNA-NFs and CoDNA-NFs, we were interested to know whether the DNA component present in the DNA-NFs retained high serum stability compared to previously observed for MgDNA-NFs.[239] MnDNA-NFs and CoDNA-NFs were incubated in cell culture medium substituted with 10% fetal bovine serum (FBS) and the DNA component was then analysed at different time courses using agarose gel electrophoresis, after the experiment the nanoflowers were imaged by SEM to check for degradation to the structure. The stability of the DNA present in the particles was evaluated and compared with the stability of λ-DNA incubated under the same experimental conditions as a control. The results demonstrated that the original morphology of the particles formed in all cases remained intact, even after 36 h incubation (Figure 3.9 - 3.14). Although the DNA component present in the MnDNA-NFs produced using Φ-29 DNA polymerase with 10 mM Mn^{2+} was significantly digested after 24 h, the DNA component in all DNA-NFs were more stable than the λ-DNA control (Figure 3.8).

The smaller particles showed higher serum stability than the larger micron-sized particles. The results also indicated that the CoDNA-NFs proved more stable than the MnDNA-NFs. In addition, the particles treated with 10% FBS became less aggregated. This is possibly because the individual particles might be joined together by extended long DNA strands, and the naked DNA between the particles was degraded.

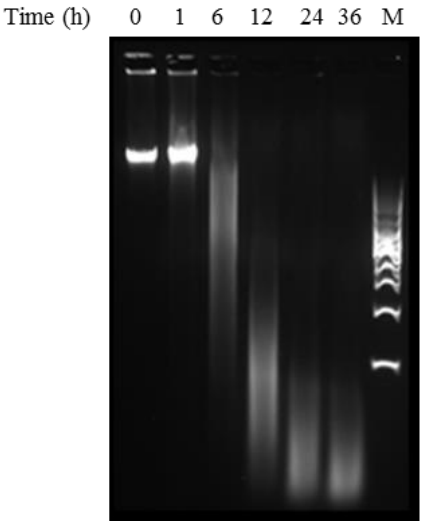


Figure 3.8. Double-stranded λ-DNA stability in Dulbecco's Modified Eagle Medium (DMEM) supplemented with 10% FBS at 37 °C. 0.8% agarose gel electrophoresis analysis after the specified incubation times. M: 1kb DNA ladder.

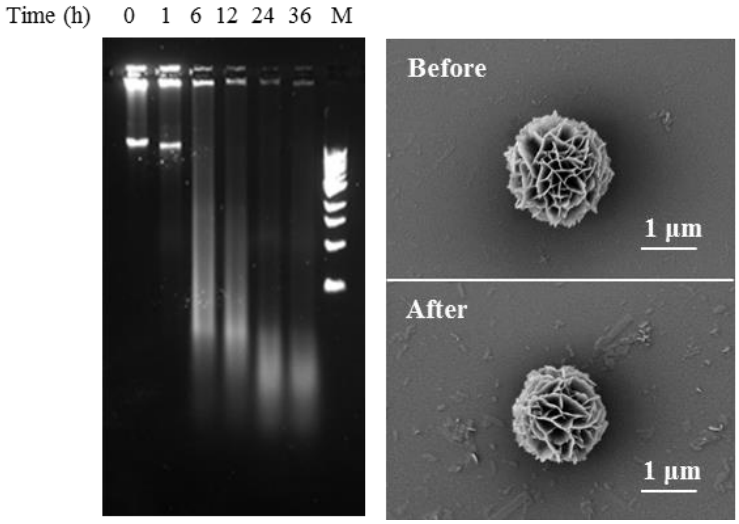


Figure 3.9. The stability of MnDNA-NFs produced using Φ-29 DNA polymerase with 10 mM Mn^{2+} in DMEM medium supplemented with 10% FBS at 37 °C. RCA reactions were carried out using cyclic T1 and S1. (left) 0.8% agarose gel electrophoresis analysis after the specified incubation times; (right) SEM images of MnDNA-NFs before and after 36 h incubation. M: 1kb DNA ladder.

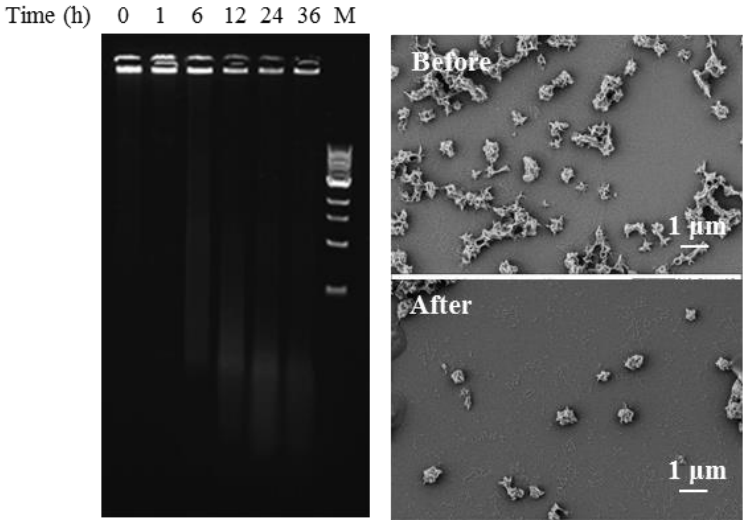


Figure 3.10. The stability of MnDNA-NFs produced using Φ-29 DNA polymerase with 15 mM Mn^{2+} in DMEM medium supplemented with 10% FBS at 37 °C. RCA reactions were carried out using cyclic T1 and S1. (left) 0.8% agarose gel electrophoresis analysis after the specified incubation times; (right) SEM images of MnDNA-NFs before and after 36 h incubation. M: 1kb DNA ladder.

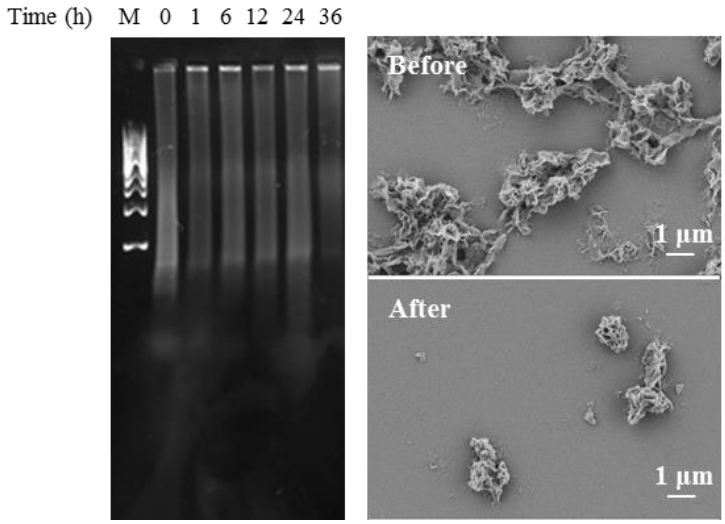


Figure 3.11. The stability of MnDNA-NFs produced using Bst 2.0 DNA polymerase with 10 mM Mn^{2+} in DMEM medium supplemented with 10% FBS at 37 °C. RCA reactions were carried out using cyclic T1 and S1. (left) 0.8% agarose gel electrophoresis analysis after the specified incubation times; (right) SEM images of MnDNA-NFs before and after 36 h incubation. M: 1kb DNA ladder.

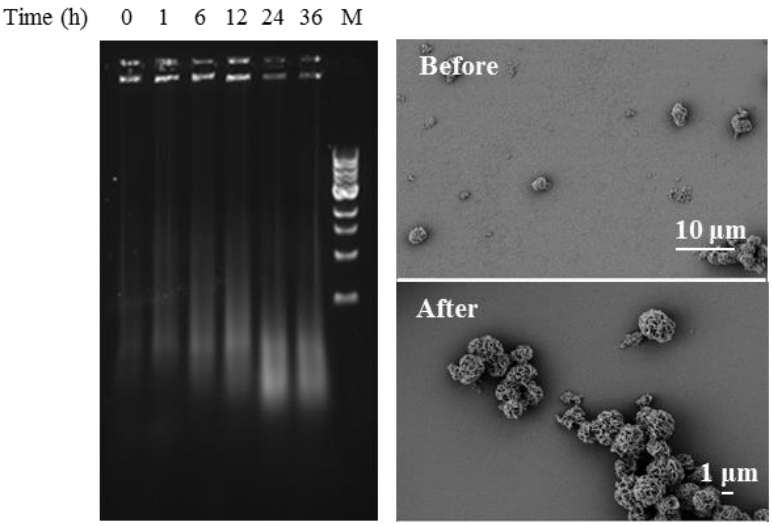


Figure 3.12. The stability of MnDNA-NFs produced using Bst 2.0 DNA polymerase with 15 mM Mn^{2+} in DMEM medium supplemented with 10% FBS at 37 °C. RCA reactions were carried out using cyclic T1 and S1. (left) 0.8% agarose gel electrophoresis analysis after the specified incubation times; (right) SEM images of MnDNA-NFs before and after 36 h incubation. M: 1kb DNA ladder.

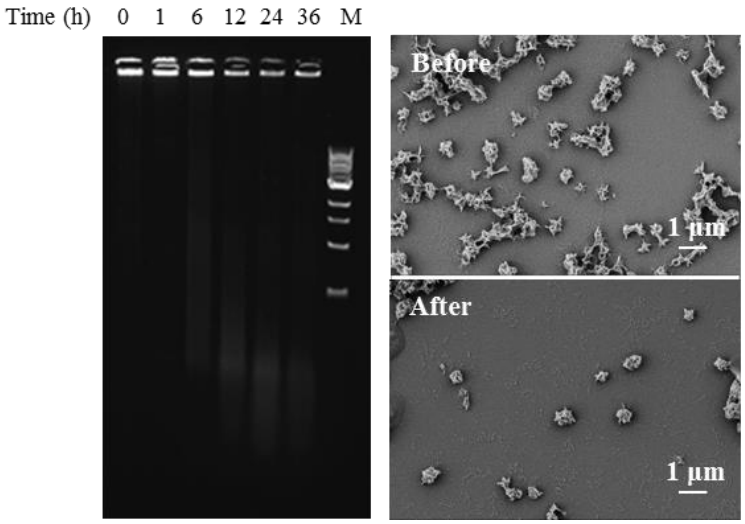


Figure 3.13. The stability of CoDNA-NFs produced using Φ-29 DNA polymerase with 10 mM Co^{2+} in DMEM medium supplemented with 10% FBS at 37 °C. RCA reactions were carried out using cyclic T1 and S1. (left) 0.8% agarose gel electrophoresis analysis after the specified incubation times; (right) SEM images of CoDNA-NFs before and after 36 h incubation. M: 1Kb DNA ladder.

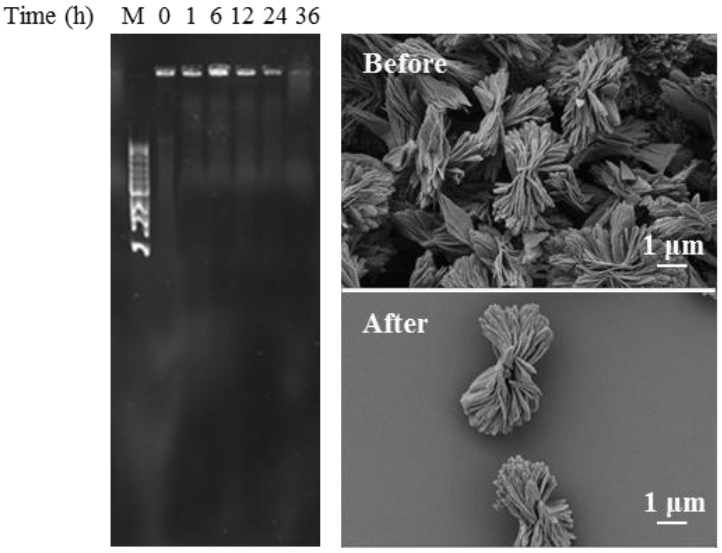


Figure 3.14. The stability of CoDNA-NFs produced using Φ-29 DNA polymerase with 15 mM Co^{2+} in DMEM medium supplemented with 10% FBS at 37 °C. RCA reactions were carried out using cyclic T1 and S1. (left) 0.8% agarose gel electrophoresis analysis after the specified incubation times; (right) SEM images of CoDNA-NFs before and after 36 h incubation. M: 1kb DNA ladder.

3.6 Hybridisation properties

For the use of DNA-NFs described above in targeted delivery through incorporation of an aptamer moiety or for bio-separation based applications, it is important that the DNA component in the DNA-NFs is functional, i.e. has the ability to interact with its specific DNA or RNA targets. To test this, the ability of the different DNA-NFs to selectively hybridise with the complementary probe was evaluated and a scrambled control was also prepared (probe sequences are given in the Table 3.2).

Table 3.2. Fluorescence probes used for hybridisation with DNA-NFs (mass spectra data of linear oligonucleotide given in Section 6.2.1, Chapter 6).

Oligonucleotide name	Sequence of oligonucleotide (5′→3′)	length
Match probe	TTACCGTCGTTTATAGC-Cy3	17
Mismatch probe	GTTGTCACTTAGTCCTA-Cy3	17

After RCA reaction, the resultant DNA-NFs were incubated with either Cy3 labelled complementary probe or a scrambled control for 1h at RT. The particles were then collected by centrifugation and the ability of different DNA-NFs to capture the matched sequence was assessed by measuring the percentage of probe left in the solution. We found that the incubation conditions significantly affected the ability of the DNA-NFs to selectively hybridise with the matched target over the scrambled control sequence (Figure 3.15). The greatest discrimination was observed when incubation of the DNA-NFs with the probe was carried out in 200 mM NaCl. This result suggested that the DNA-NFs could be utilised in magnetic assisted bio-separation or targeted delivery applications. In addition, the hypothesis we propose for enhanced selectivity in saline over water is that the negative charges on the phosphate backbone in the probe are screened by Na^+,

preventing ionic interaction between the probes and inorganic component and allowing specific base pairing to dominate relative to non-specific charge-charge interactions.

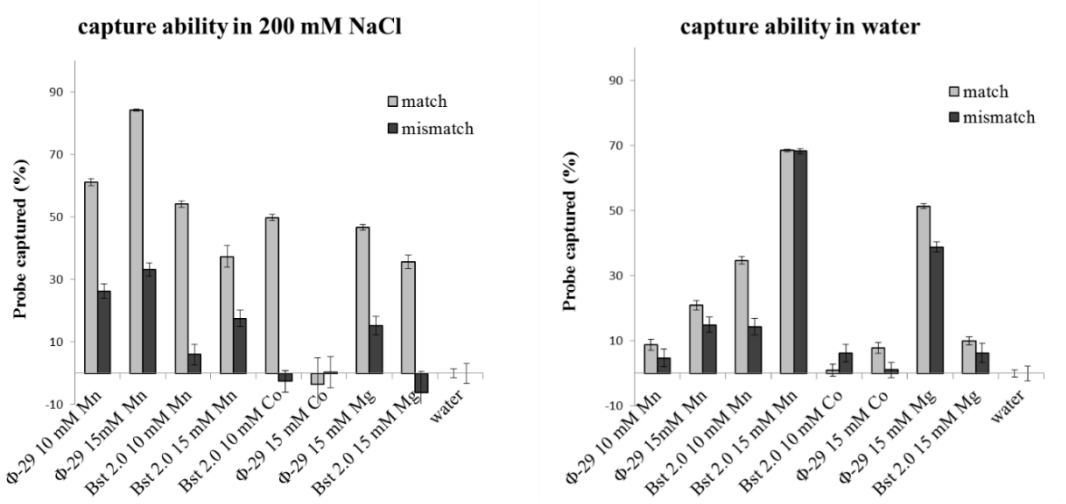


Figure 3.15. The ability of DNA-NFs produced using cyclic T1 and S1 to hybridise with and capture complementary DNA strand. DNA-NFs were incubated with either Cy3 labelled complementary DNA probe (match) or a scrambled control (mismatch) in the presence of 200 mM NaCl (left) or water (right). The percentage of probe left in solution was detected using fluorescence plate reader.

3.7 Conclusions

DNA-metal hybrid particles have been successfully prepared in a range of shapes by replacing Mg^{2+} with other divalent metal ions such as Mn^{2+} and Co^{2+} in the RCA process. Both Mn^{2+} and Co^{2+} as metal activator showed their compatibility with enzymatic DNA polymerisation.

During preparation of DNA-Mn materials, Mn^{2+} concentration significantly affected the size and morphology of the particles when using different DNA polymerases (Φ-29 and Bst 2.0). Large shell-like particles were observed at 5 mM Mn^{2+} using Bst 2.0 DNA polymerase, whilst Φ-29-catalysed RCA produced large layered structures that were more square-like. Flower-shaped superstructures were generated at 15 mM of Mn^{2+} when the RCA was carried out using Bst 2.0 DNA polymerase, whereas similar particles were produced by Φ-29 DNA polymerase at 10 mM of Mn^{2+}.

Co^{2+} was also successfully utilised in the RCA reaction to construct DNA-Co materials. DTT was found to be incompatible with Co^{2+} and was therefore excluded from the amplification buffer. CoDNA-NFs formed petal-like structures at 10 mM Co^{2+} using both Bst 2.0 and Φ-29 DNA polymerases.

We have shown that by replacing the Mg^{2+} with Mn^{2+} or Co^{2+} in RCA reactions, it can produce DNA-Mn or DNA-Co particles. Both Mn^{2+} and Co^{2+} could endow the particles with unique magnetic properties, which would broaden the application of DNA-based inorganic materials.

Under specific conditions, we have shown that these resulting DNA-NFs have the ability to selectively bind to their intended complementary target sequence, suggesting that the DNA is free to interact, rather than being tied up within the nanostructures.

Chapter 4

Synthesis of cyclic single-stranded DNA constructs and their application

Chapter 4 – Synthesis of cyclic single-stranded DNA constructs and their application

4.1 Preface

The work presented in this chapter was published in Chemical Science.[254] It was carried out in collaboration with Dr. Asha Brown who synthesised and cyclised linear phosphoramidate and amide oligonucleotides and Dr. Ysobel R. Baker who imaged the precipitated DNA nanoconstructs.

4.2 Introduction and aims

Cyclic oligonucleotides possess an expansive range of potential applications spanning molecular biology[131,132,141-143] and nanotechnology.[144-147] One of the most important applications is their role as substrate templates in RCA reactions. The cyclic template is most commonly obtained *via* enzymatic cyclisation of a linear oligonucleotide using DNA ligase enzymes such as T4 DNA ligase or CircLigase. The cyclisation efficiency significantly relies on the length of the linear precursor, and is inefficient when the linear sequence has potential secondary structures.[255,256] In addition, the scale of the cyclisation reaction is limited by the cost of the ligase enzyme. In principle, employing chemical cyclisation methods could circumvent these limitations (Figure 4.1). Chemical cyclisation reactions are readily scalable and allow the use of a wide range of buffers, including those in which oligonucleotide secondary structures are denatured. However, the creation of a natural phosphodiester backbone linkage by the use of chemical approaches in aqueous solution is extremely difficult. This is because the nucleophilicity of the attacking hydroxyl group is similar to that of the surrounding water molecules, which exist in a

great excess. Although chemical strategies have been utilised to create the canonical phosphodiester linkage, these methods often depend upon using toxic reagents such as cyanogen bromide.[257] Therefore, artificial backbone linkages that are less challenging to form offer an attractive alternative.[128] Prevalent amongst these are triazole, phosphoramidate and amide backbone linkages (Figure 4.1(ii)).[124-127,258,259] Literature has reported that these three artificial backbones incorporated into linear oligonucleotides can be read through by DNA polymerases during both PCR and linear copying to accurately transfer genetic information.[122,125,128] Inspired by these results, chemically modified backbone linkages could potentially be incorporated into cyclic RCA templates and be read through by DNA polymerases that are compatible with efficient RCA (Figure 4.1(i)). However, the use of modified backbones in cyclic templates for RCA requires the DNA polymerase to repeatedly read through the artificial backbone linkage, which is particularly demanding. In contrast, during PCR the polymerase only needs to copy the chemically modified templates once in the first cycle, after which the reaction proceeds in an exponential manner and the polymerase copies mostly unmodified backbone products in following cycles.

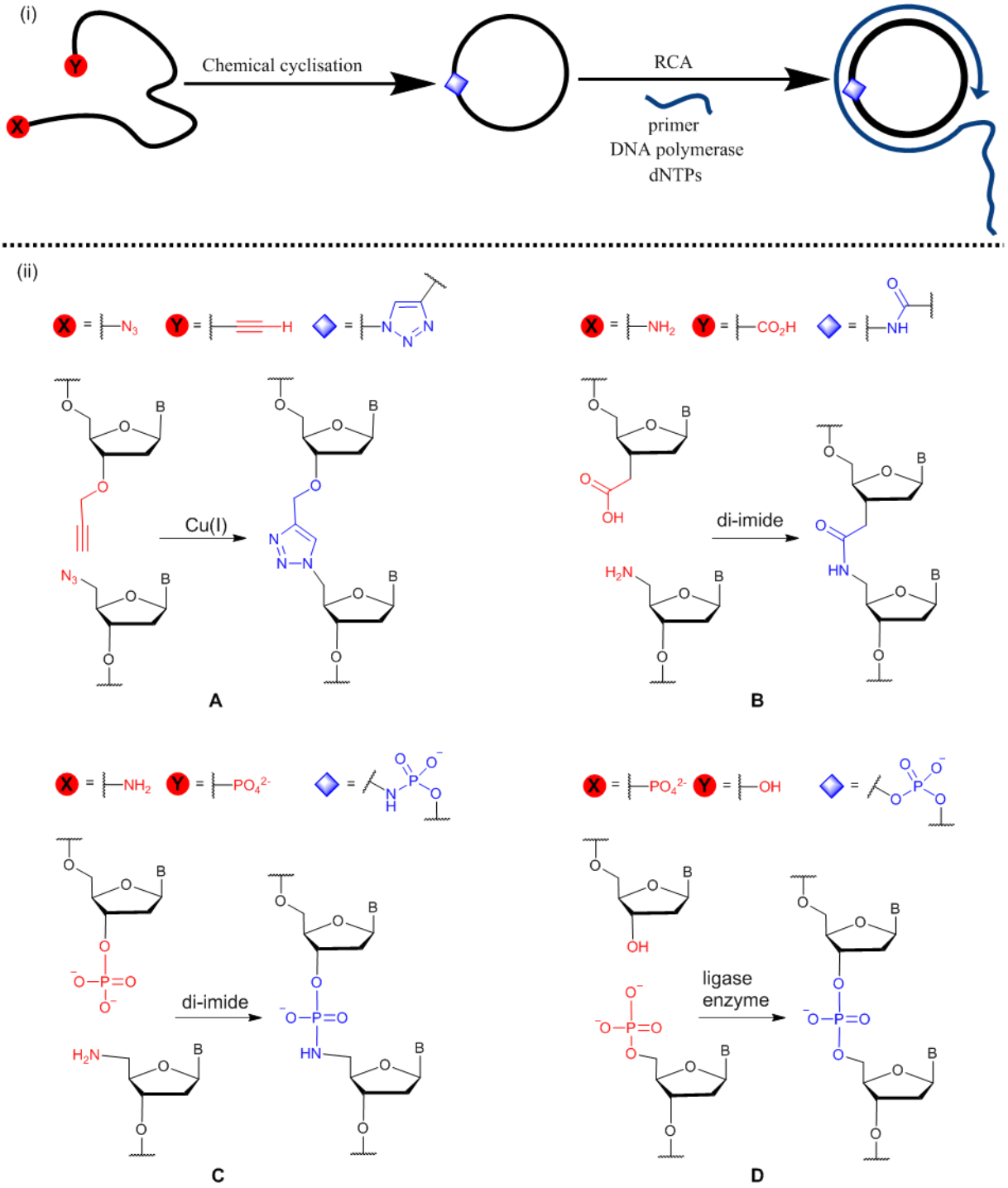


Figure 4.1. (i) Cyclisation of single-stranded oligonucleotide using chemical cyclisation methods and rolling circle amplification through artificial backbone linkage. (ii) Details of the chemical and enzymatic cyclisation strategies investigated in this study: (A) formation of an artificial triazole backbone linkage (Tz) *via* the CuAAC reaction; (B) formation of an artificial amide backbone linkage (Am) *via* di-imide coupling reaction; (C) formation of an artificial phosphoramidate backbone linkage (PA) *via* di-imide coupling reaction; (D) enzyme-catalysed formation of a natural phosphodiester backbone linkage (PO_4). B = nucleobase.

One of the important applications of RCA is to synthesise functional DNA nanomaterials. Specifically, the extended single-stranded DNA building blocks generated during the RCA processes can further self-assemble into DNA-inorganic hybrid nanoflower structures in the presence of magnesium pyrophosphate crystals. Nanoflower self-assembly is driven by crystallisation and formed without depending on Watson-Crick base paring between DNA strands. Therefore, conventional complex sequence design is not necessary. By incorporating therapeutic aptamer sequences in the cyclic template, the resulting DNA-NFs can be endowed with multivalent binding properties for selectively recognising target cells.[234]

The aims of the work in this chapter were to synthesise cyclic templates by incorporating three PCR-compatible backbone modifications and to examine their suitability as substrate templates for RCA (e.g. reaction rates, product distribution and product yields). In addition, we also identified a need for scalable generation of cyclic templates for the synthesis of DNA-NFs with a wide range of applications.

4.3 Choice of backbone linkages and template sequences

In this chapter, RCA of cyclic templates containing a single triazole, phosphoramidate or amide analogue of the natural DNA phosphodiester backbone will be systematically evaluated. All three artificial backbone linkages have been reported and successfully used in PCR amplification of linear DNA.[119,121,122,125,128,260,261] Of the three, the triazole-modified backbone linkage (Figure 4.1(ii)A) generated through click chemistry is the most thoroughly studied and can be read through by both DNA and RNA polymerases.[258] Moreover, it has been used to construct genes by chemical ligation, and Next-Gen DNA sequencing assays demonstrated that the click-linked gene has been correctly replicated in the bacteria without any mutations compared to the canonical analogue.[122]

Two reports have showed that the linear oligonucleotides bearing 5′-azide and 3′-alkyne functional groups were circularised by click reaction and subsequently served as substrate template in the RCA reaction. For example, El-Sagheer *et al*. in 2011 reported that a structure-free 100-mer linear oligonucleotide was cyclised by click reaction, and that the cyclic product can be used in RCA reaction to generate long DNA.[119] Afterwards, Li *et al*. employed a cyclic template with triazole-modified backbone linkage to construct an "off-on" switch system based on RCA for fluorescence sensing of microRNA, but the authors did not compare the RCA efficiency with unmodified natural backbone linkage.[262] In this study, another two artificial backbone linkages containing phosphoramidate and amide (Figure 4.1(ii)B and C) were also investigated, both of which can be generated by di-imide coupling chemistry. Of particular interest is phosphoramidate backbone linkage, which closely mimics the electronic and steric properties of the natural phosphodiester backbone.

With the aim of studying these non-canonical artificial backbone linkages, we designed four cyclic templates (**1** - **4**) in order to investigate the effects of length of the template, base composition and secondary structure of the template on both cyclisation reaction and acting as substrate template in RCA reaction. These templates are predicted to incorporate secondary structures, and two of them are complementary to the aptamer sequences. All cyclic oligonucleotide sequences are given in Table 4.1, and their corresponding splint oligonucleotides for cyclisation and RCA are listed in Table 4.2. The secondary structures of cyclic templates are shown in Figure 4.2.

Table 4.1. Sequences of the cyclic templates used in this chapter (mass spectra data of linear and cyclic oligonucleotides showed in Section 6.2.1, Chapter 6).

Cyclic oligonucleotide code	Sequence of linear precursor[a] (5′→3′)	length
Cyclic **1**_PO_4	^{P}TCCCAATTGGGTACGCAGTACCCACAGCAGA TGTGACTGTGAATCGTGAC	50
Cyclic **1**_Tz	^{Z}TCCCAATTGGGTACGCAGTACCCACAGCAGA TGTGACTGTGAATCGTGAC^{K}	50
Cyclic **1**_Am	^{M}TCCAATTGGGTACGCAGTACCCACAGCAGAT GTGACTGTGAATCGTGACT^{X}	50
Cyclic **1**_PA	^{M}TCCCAATTGGGTACGCAGTACCCACAGCAGA TGTGACTGTGAATCGTGAC^{P}	50
Cyclic **2**_PO_4	^{P}TGTCGTTTTACCCATGTGCTATAGCCACTACT GTCGTTTTACCCATGTGCTATAGCCACTAC	62
Cyclic **2**_Tz	^{Z}TGTCGTTTTACCCATGTGCTATAGCCACTACT GTCGTTTTACCCATGTGCTATAGCCACTAC^{K}	62
Cyclic **2**_Am	^{M}TGTCGTTTTACCCATGTGCTATAGCCACTACT GTCGTTTTACCCATGTGCTATAGCCACTAT^{X}	62
Cyclic **2**_PA	^{M}TGTCGTTTTACCCATGTGCTATAGCCACTACT GTCGTTTTACCCATGTGCTATAGCCACTAC^{P}	62
Cyclic **3**_PO_4	^{P}TTACCCCACACCGCTGCCCCCACACCGCTGCC CCCACACCGCTGCCTTAC	50
Cyclic **3**_Tz	^{Z}TTACCCCACACCGCTGCCCCCACACCGCTGCC CCCACACCGCTGCCTTAC^{K}	50
Cyclic **3**_Am	^{M}TACCCCACACCGCTGCCCCCACACCGCTGCC CCCACACCGCTGCCTTACT^{X}	50
Cyclic **3**_PA	^{M}TTACCCCACACCGCTGCCCCCACACCGCTGC CCCCACACCGCTGCCTTAC^{P}	50
Cyclic **4**_PO_4	^{P}GTTAATATTATTCGACGGGCCTGCTCGAGCTC GAGCTTGCATCGTGCAGCCGAAGCTTGCACGC GTGCTATTAAT	75
Cyclic **4**_Tz	^{Z}TTGCACGCGTGCTATTAATGTTAATATTATTC GACGGGCCTGCTCGAGCTCGAGCTTGCATCGT GCAGCCGAAG^{Me}C^{K}	75

[a] P = 5′-PO_4; M = 5′-amine; X = 3′-carboxy; Z = 5′-azide; K = 3′-propargyl; ^{Me}C = methyl cytosine.

Table 4.2. Corresponding splint oligonucleotides used for cyclisation and RCA (mass spectra data of linear oligonucleotides given in Section 6.2.1, Chapter 6).

Oligonucleotide code	Sequence of oligonucleotide (5′→3′)	length
ODN4-1 (Cyclisation splint for Cyclic **1**_PO_4; RCA primer for Cyclic **1**_PO_4, Cyclic **1**_Tz and Cyclic **1**_PA)	CAATTGGGAGTCACGATT	18
ODN4-2 (Cyclisation splint for Cyclic **2**_PO_4; RCA primer for Cyclic **2**_PO_4, Cyclic **2**_Tz and Cyclic **2**_PA)	AAACGACAGTAGTGGC	16
ODN4-3 (Cyclisation splint for Cyclic **3**_PO_4; RCA primer for Cyclic **3**_PO_4, Cyclic **3**_Tz and Cyclic **3**_PA)	TGGGGTAAGTAAGGCA	16
ODN4-4 (Cyclisation splint for Cyclic **4**_PO_4; RCA primer for Cyclic **4**_PO_4 and Cyclic **4**_Tz)	ATAATATTAACATTAATAGCA	21
ODN4-5 (Cyclisation splint and RCA primer for Cyclic **1**_Am)	CCAATTGGAAGTCACGAT	18
ODN4-6 (RCA primer for Cyclic **2**_Am)	AAAACGACAATAGTGGCT	18
ODN4-7 (RCA primer for Cyclic **3**_Am)	TGTGGGGTAAGTAAGGCA	18

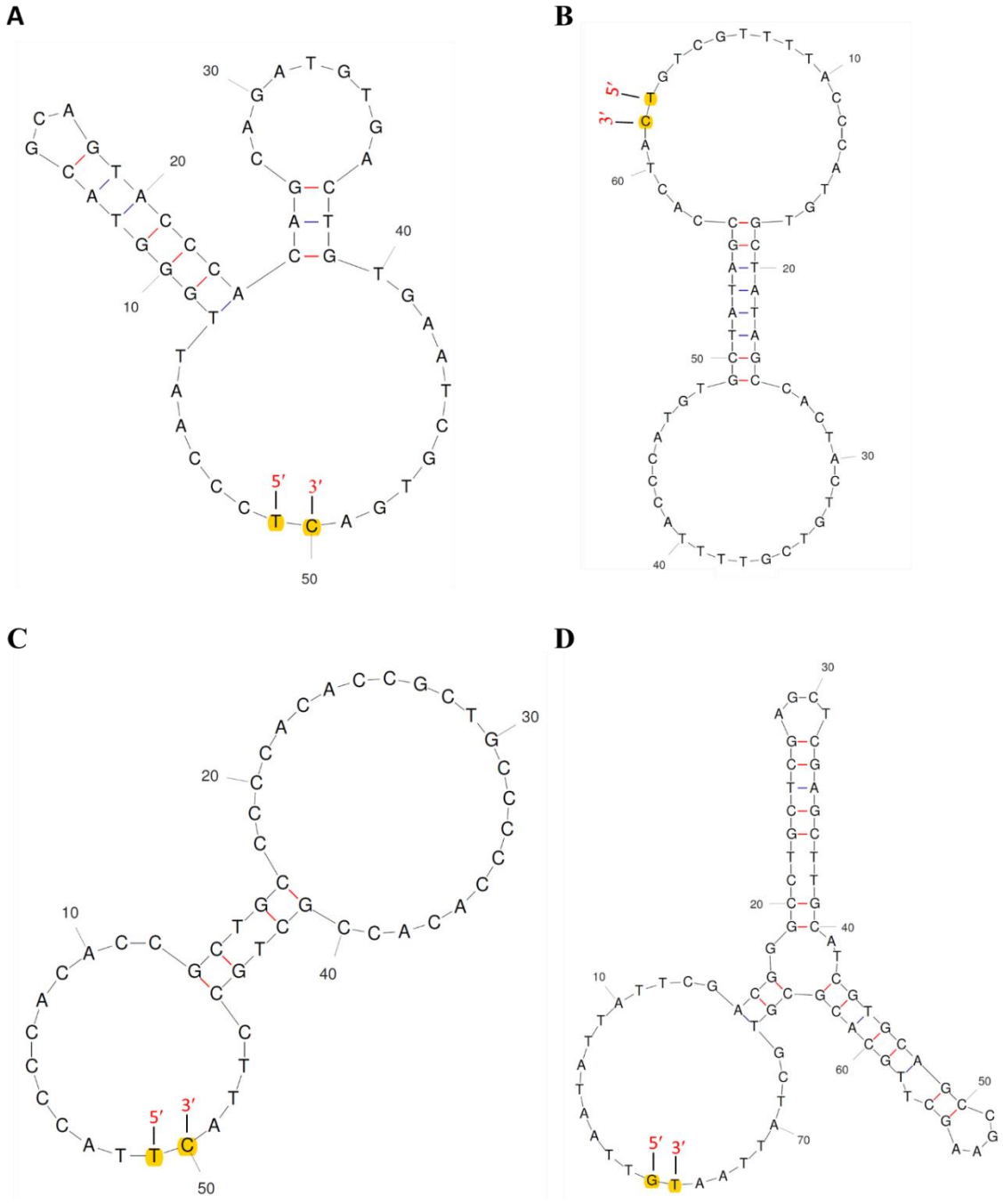


Figure 4.2. Predicted secondary structures of the cyclic template oligonucleotides used in this chapter. (A) template **1**; (B) template **2**; (C) template **3** and (D) template **4**. All structures were predicted by using the Mfold web server software.[263] The highlighted bases represent the point of ligation.

Template **1** is a 50-mer that was randomly generated with approximately 50% GC base content. Template **2** encoded a dumbbell-shaped double hairpin structure and served as a template for an aptamer sequence which is specific for targeting the mucin 1 (MUC1)

glycoprotein.[264] The MUC1 glycoprotein is overexpressed on cancer cells surface and has become an attractive molecular target. The sequence of template **3** is complementary to the trimeric G-quadruplex aptamer that specifically recognising the HER2 biomarker.[202] As such, it encodes for an RCA product formed of repeating HER2 aptamers. This aptamer sequence is guanine-rich with an intramolecular G-quadruplex secondary structure and was previously characterised as described in Chapter 2. Each template (**1** - **3**) was made containing a single unmodified natural phosphodiester (PO_4) backbone and analogues of triazole (Tz), phosphoramidate (PA) and amide (Am) artificial linkages at the point of cyclisation. The chemistry is discussed further below (Section 4.4). In addition, a fourth template (template **4**) which incorporates a palindromic sequence was investigated and two versions of this comprising unmodified and triazole-modified cyclic templates (**4**_PO_4 and **4**_Tz) were prepared. It has been reported that the RCA products generated from the corresponding cyclic template (**4**_PO_4) self-assembled into a three-dimensional interwoven "cocoon-like nanoclew" structure by intramolecular hybridisation, which was further used to deliver anticancer drugs.[265]

4.4 Synthesis of cyclic oligonucleotides

4.4.1 Enzymatic cyclisation with a canonical phosphodiester backbone linkage

We first prepared the unmodified cyclic control templates. To enable cyclisation using DNA ligase enzyme, linear oligonucleotides bearing 5′-phospate/3′-hydroxyl modifications were synthesised using automated solid-phase phosphoramidite chemistry as presented in Section 6.2.1 (Chapter 6). The unmodified linear oligonucleotides were first annealed with a bridging oligonucleotide (splint) and then circularised using T4 DNA ligase to give the cyclic templates with a natural phosphodiester backbone linkage. The short splint acts as complementary cyclisation template positioning the two reacting ends

of the participating linear oligonucleotide in close proximity which is necessary for the enzyme (Figure 4.3). The enzymatic cyclisation was carried out following the supplier's conditions in commercially available T4 DNA ligase buffer (1×), and the cyclic products were purified by denaturing PAGE. The mechanism of enzymatic cyclisation is detailed in Section 1.4.1 (Chapter 1).

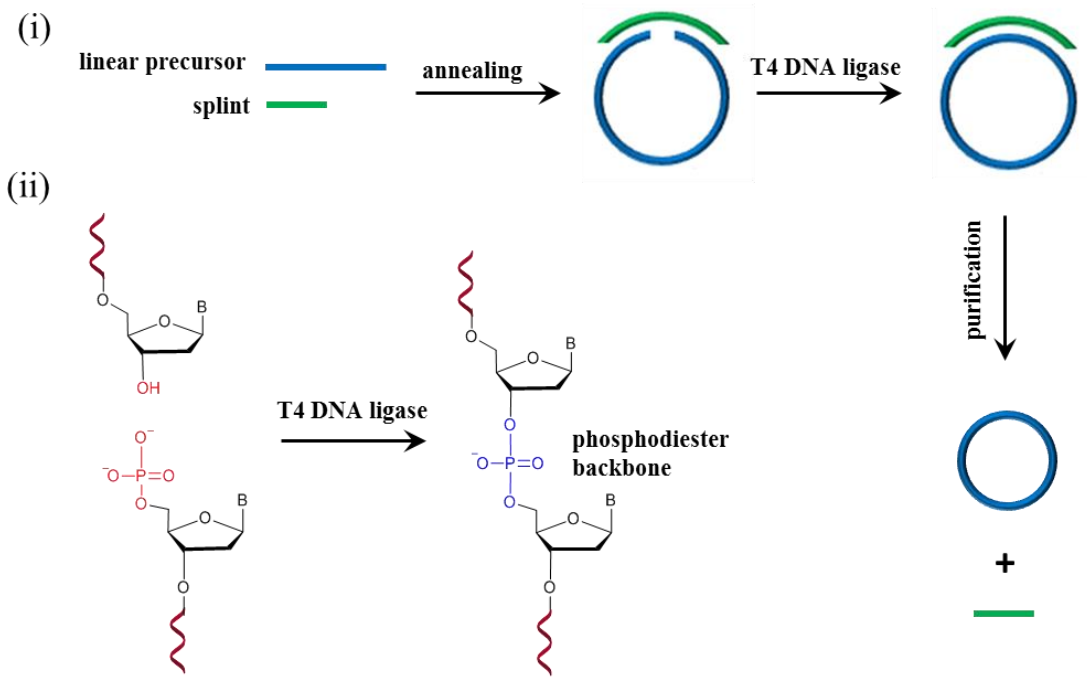


Figure 4.3. (i) Splint-mediated enzymatic cyclisation using T4 DNA ligase. (ii) Formation of a natural phosphodiester backbone linkage. 'B' refers to DNA bases.

The effect of the linear precursor to splint ratio on cyclisation efficiency was investigated for all four designed templates, varying from 1:1 to 1:10 (linear precursor: splint). Circular products were obtained from all four linear templates in varying efficiency. More specifically, the intramolecular cyclisation of linear **2**_PO_4 and linear **3**_PO_4 was relatively successful with little to no polymeric by-products, with a single band observed by denaturing PAGE post-stained with SYBR Gold (Figure 4.4). A significant amount of slow-migrating polymeric side-product was observed in the cyclisation reaction of linear

1_PO_4, which was further identified as a cyclic dimer by mass spectrometry (Figure 4.7 and Appendix Figure 8.4.1).

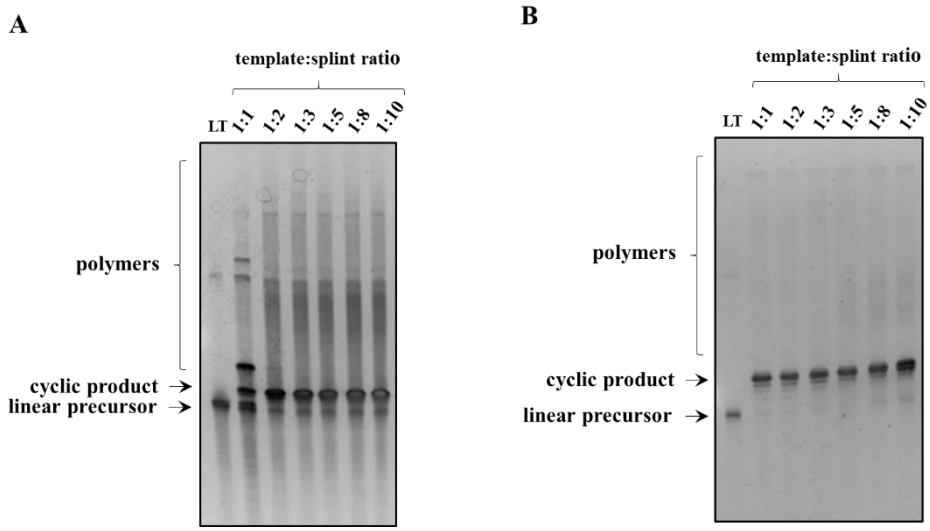


Figure 4.4. Splint-mediated enzymatic cyclisation of linear **2**_PO_4 and linear **3**_PO_4 to give cyclic **2**_PO_4 (A) and cyclic **3**_PO_4 (B), respectively. Samples were imaged after staining with SYBR Gold. LT: linear oligonucleotide precursor. The enzymatic cyclisation reaction was carried out with different ratios of template oligonucleotide and splint at RT overnight using T4 DNA ligase and Bio-Rad T100^{TM} thermocycler. (A) The crude reaction mixtures for cyclisation of linear **2**_PO_4 were analysed by an 8% denaturing PAGE gel. (B) The crude reaction mixtures for cyclisation of linear **3**_PO_4 were analysed by a 12% denaturing PAGE gel.

Cyclisation of linear **4**_PO_4 proved challenging, and intermolecular polymeric side-products of varying size as the major cyclisation products were formed (Figure 4.5). Changing the linear substrate to splint ratio did not result in significant improvement in yield of cyclisation product. Moreover, increasing the amount of enzyme appeared to reduce the cyclisation efficiency (Figure 4.6). This is possibly due to the linear substrate containing a complicated secondary structure at RT, which is unfavourable for the enzymatic cyclisation. Recently, Liang *et al.* have also reported that both Taq and T4 DNA ligases were inefficient in converting the linear precursors to their corresponding cyclic products when the linear substrates involved complex secondary structures.[256]

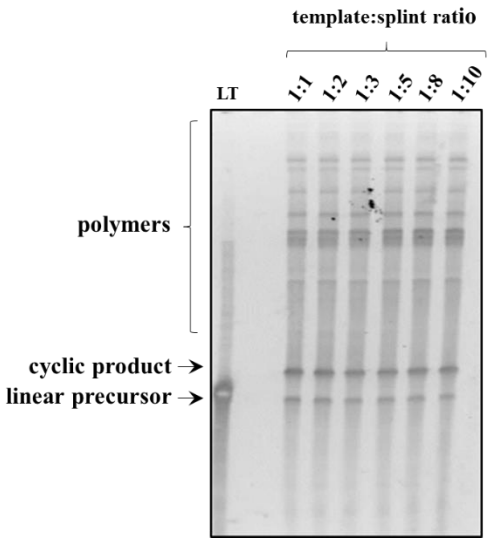


Figure 4.5. Splint-mediated enzymatic cyclisation of linear **4**_PO_4 to give cyclic **4**_PO_4. The crude reaction mixtures were analysed by an 8% denaturing PAGE gel. Samples were imaged after staining with SYBR Gold. LT: linear oligonucleotide precursor. The enzymatic cyclisation reaction was carried out with different ratios of template oligonucleotide and splint at RT overnight using T4 DNA ligase and Bio-Rad T100^{TM} thermocycler.

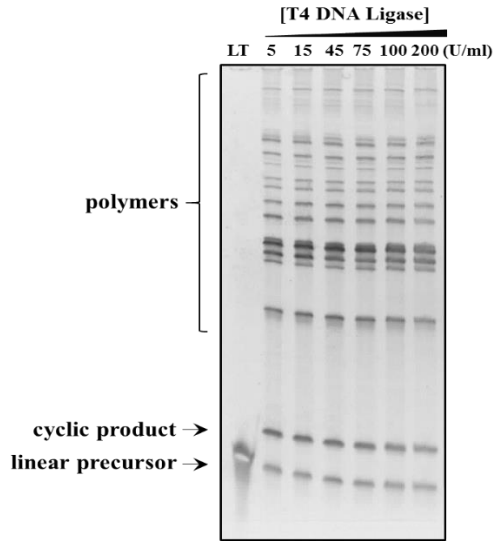


Figure 4.6. Splint-mediated enzymatic cyclisation of linear **4**_PO_4 to give cyclic **4**_PO_4. The crude reaction mixtures were analysed by an 8% denaturing PAGE gel. Samples were imaged after staining with SYBR Gold. LT: linear oligonucleotide precursor. The splint-mediated enzymatic cyclisation was carried out in the presence of an increasing concentration of T4 DNA ligase at RT overnight using Bio-Rad T100^{TM} thermocycler.

It is worth noting that we also found that the gel mobility of circular products varies depending on the percentage of acrylamide used to make the denaturing PAGE gel. For example, compared with linear precursor, the circular products from **1**_PO_4 migrated faster on an 8% denaturing PAGE gel than that of the same sample on a 15% denaturing PAGE gel (Figure 4.7 and Appendix Figure 8.4.1). In the case of template **3**, there was no obvious separation between circular products and linear precursor on an 8% denaturing PAGE gel (Appendix Figure 8.4.2). However, an improved separation was observed when using 12% denaturing PAGE gel (Figure 4.4B). This difference of migration was possibly caused by the structure of template.

Based on the above results, a 1:3 ratio of linear precursor to splint for **1**_PO_4, **2**_PO_4 and **3**_PO_4 and 1:2 for **4**_PO_4 were chosen when scaling up the cyclisation reaction. The acrylamide percentage in the denaturing PAGE gel used to purify each of the circular products and approximate isolated yields were as follows: cyclic **1**_PO_4: 15% PAGE with 12% yield; cyclic **2**_PO_4: 8% PAGE with 23% yield; cyclic **3**_PO_4: 12% PAGE with 24% yield; cyclic **4**_PO_4: 8% PAGE with a yield of less than 10%. The crude cyclisation reaction mixture of each template was analysed, and the masses of their corresponding cyclic products are given below (Figure 4.7 - Figure 4.10).

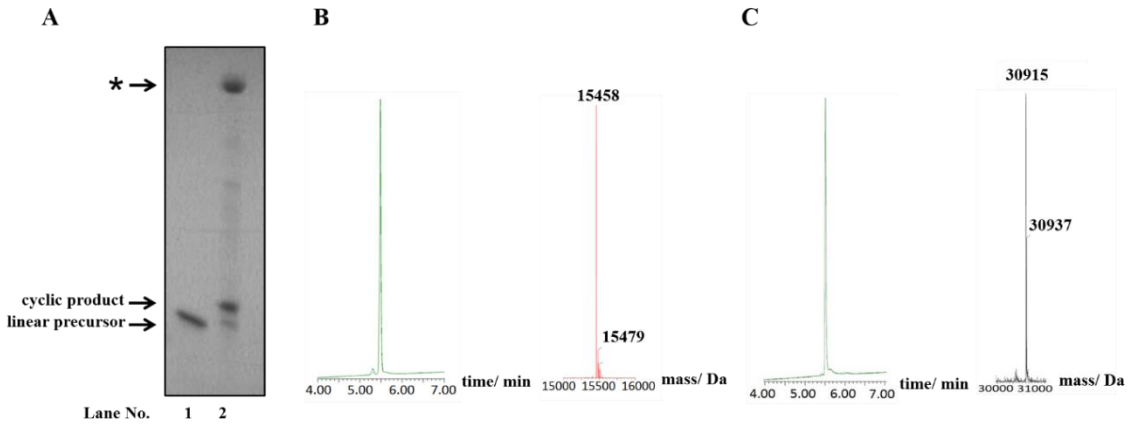


Figure 4.7. Splint-mediated enzymatic cyclisation reaction to give cyclic **1**_PO_4. (A) The crude reaction mixture was analysed by a 15% denaturing PAGE gel. The gel was imaged under UV shadowing. Lane 1: linear oligonucleotide precursor; Lane 2: crude cyclisation reaction; *: Slow-migrating side-product observed in the crude reaction mixture for the enzymatic cyclisation was identified as cyclic dimer. (B) Reverse-phase UPLC (UV abs at 260 nm) and mass spectrum (ES^-) of cyclic **1**_PO_4, required 15456 Da, found 15458 Da. The peaks show the product and its Na^+ adduct. (C) Reverse-phase UPLC (UV abs at 260 nm) and mass spectrum (ES^-) of the slow-migrating side-product extracted from the gel during PAGE purification. The side-product was identified as a cyclic dimer: required 30912 Da, found 30915 Da. The mass peaks show the product and its Na^+ adduct.

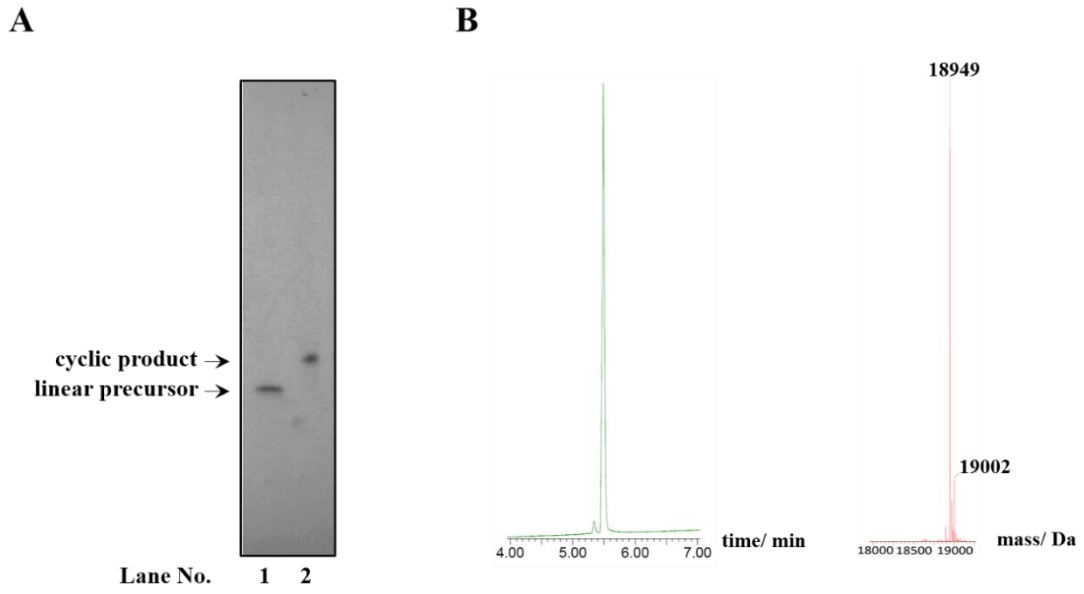


Figure 4.8. Splint-mediated enzymatic cyclisation reaction to give cyclic **2**_PO_4. (A) The crude reaction mixture was analysed by an 8% denaturing PAGE gel. The gel was imaged under UV shadowing. Lane 1: linear oligonucleotide precursor; Lane 2: crude cyclisation reaction. (B) Reverse-phase UPLC (UV abs at 260 nm) and mass spectrum (ES^-) of cyclic **2**_PO_4, required 18947 Da, found 18949 Da. The mass peaks show the product and its Na^+ adduct.

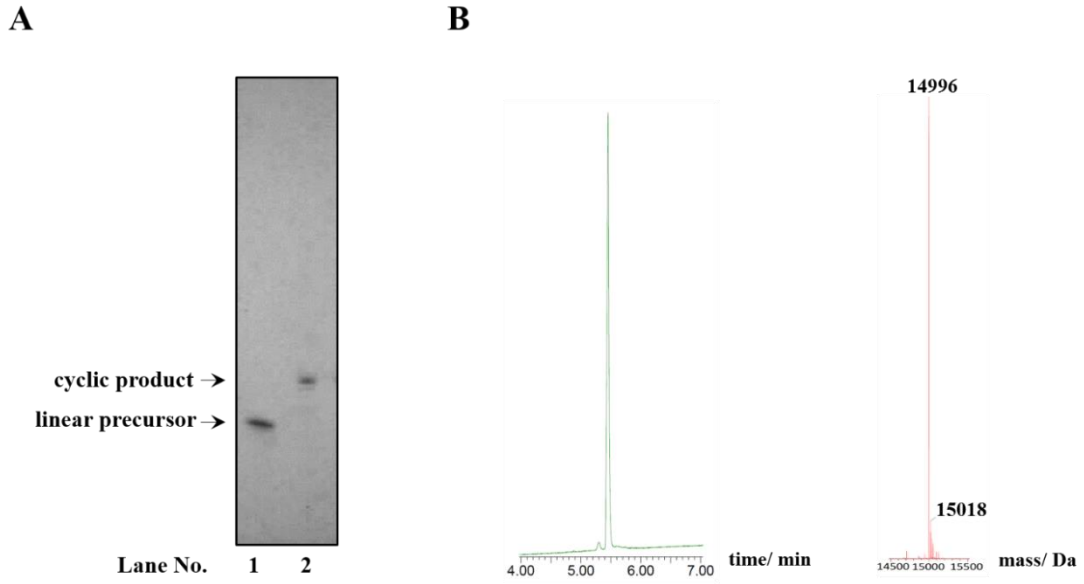


Figure 4.9. Splint-mediated enzymatic cyclisation reaction to give cyclic **3**_PO_4. (A) The crude reaction mixture was analysed by a 12% denaturing PAGE gel. The gel was imaged under UV shadowing. Lane 1: linear oligonucleotide precursor; Lane 2: crude cyclisation reaction. (B) Reverse-phase UPLC (UV abs at 260 nm) and mass spectrum (ES^-) of cyclic **3**_PO_4, required 14995 Da, found 14996 Da. The mass peaks show the product and its Na^+ adduct.

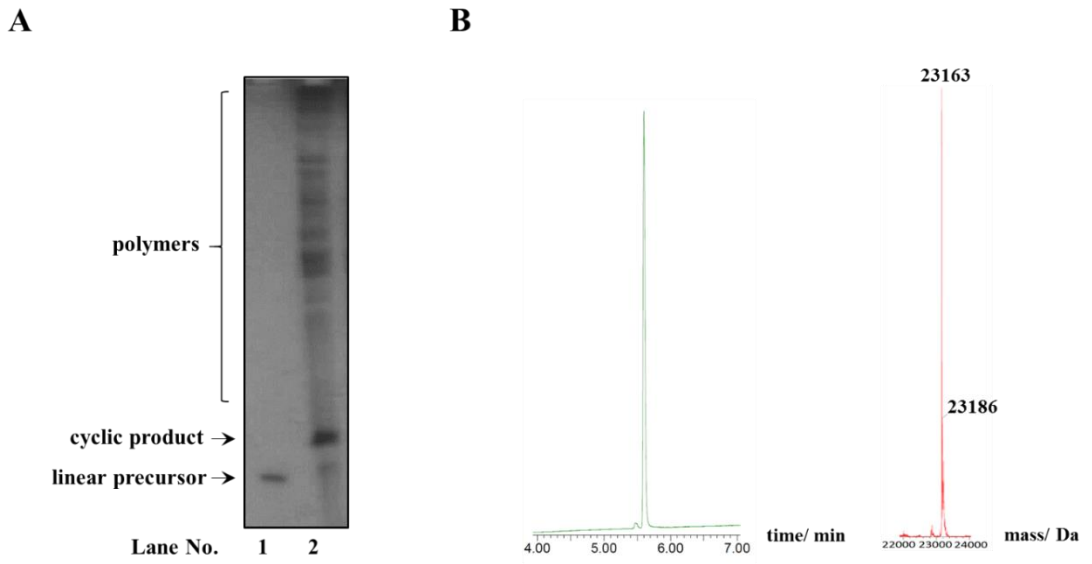


Figure 4.10. Splint-mediated enzymatic cyclisation reaction to give cyclic **4**_PO_4. (A) The crude reaction mixture was analysed by an 8% denaturing PAGE gel. The gel was imaged under UV shadowing. Lane 1: linear oligonucleotide precursor; Lane 2: crude cyclisation reaction. (B) Reverse-phase UPLC (UV abs at 260 nm) and mass spectrum (ES^-) of cyclic **4**_PO_4, required 23163 Da, found 23163 Da. The mass peaks show the product and its Na^+ adduct.

As the circularisation of linear **4**_PO_4 was low yielding, the reaction concentration of linear oligonucleotide substrate was further investigated. This was based on previous reports that a lower concentration of DNA substrate used in enzymatic preparation of single-stranded DNA rings increases yields.[255,266-270] As expected, the formation of polymeric side-products was significantly suppressed when the cyclisation reaction was carried out at lower concentration of linear precursor such as 60 nM (Figure 4.11); however, lower conversion efficiency of the desired cyclic products was also observed.

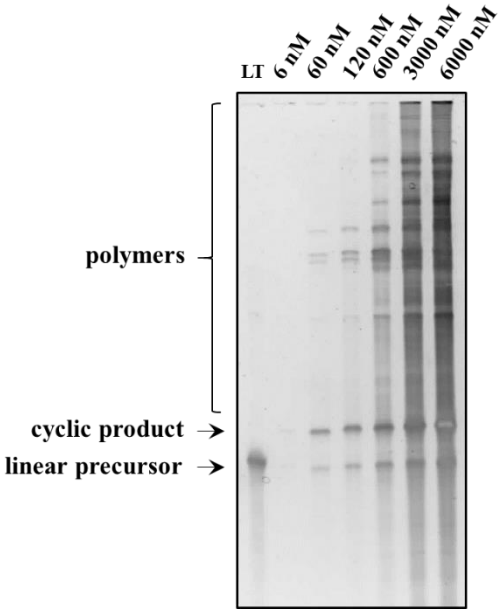


Figure 4.11. Splint-mediated enzymatic cyclisation reaction to give cyclic **4**_PO_4 in the presence of an increasing concentration of linear precursor. The crude reaction mixture was analysed by an 8% denaturing PAGE gel, which was visualised by post-staining with SYBR Gold. LT: linear oligonucleotide precursor.

For practical reasons, a 0.6 μM concentration of linear oligonucleotide substrate was used in order to obtain enough cyclic products to use in further experiments. No further optimisation was carried out for enzymatic cyclisations as sufficient quantities of the desired circular products were obtained for their further studies.

4.4.2 Chemical cyclisation by introducing chemically modified backbone linkages

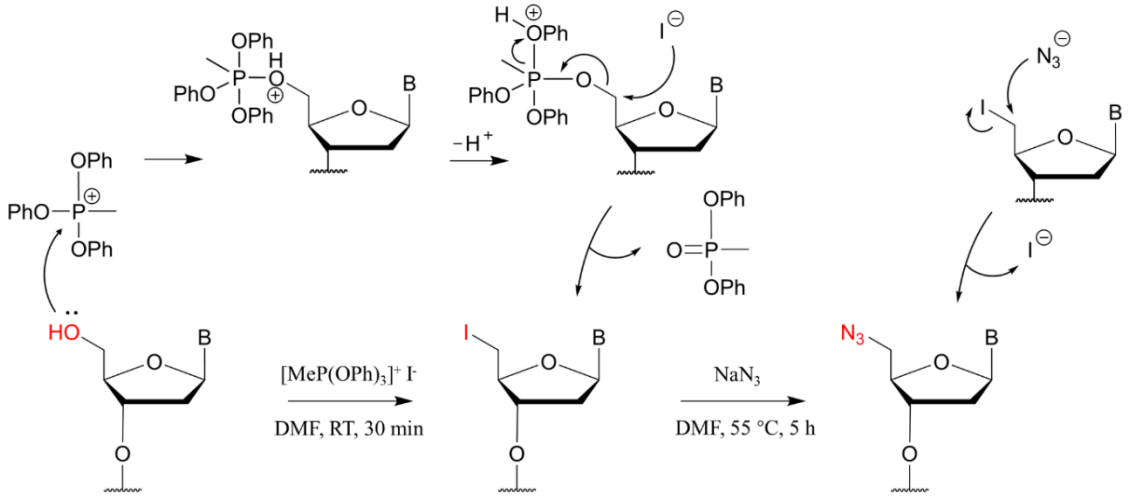
Due to the limitation of enzymatic cyclisation, an alternative strategy is still in demand. Chemical cyclisation has attracted attention with several potential advantages compared to enzymatic cyclisation, for example: (i) large scale on which the cyclisation reaction can be achieved by organic synthesis at lower costs is possible, (ii) highly efficient chemical reactions can be chosen, (iii) the cyclisation reaction can be carried out in the absence of a bridging splint. Moreover, this strategy can be used to incorporate a

potentially biocompatible artificial backbone linkage which mimics the natural phosphodiester backbone allowing us to study their biocompatibility. We envisage that using chemical methods to cyclise the linear oligonucleotides would overcome the above-mentioned enzymatic limitations (Section 4.4.1).

Here, three different chemical cyclisation methods were studied for the preparation of single-stranded cyclic DNA constructs. The resulting circular oligonucleotide template each contains a single non-canonical backbone linkage at the ligation point, named triazole, amide or phosphoramidate, respectively.

4.4.2.1 Modified backbone with triazole linkage

To enable cyclisation using the CuAAC reaction, 5′-azide/3′-alkyne modifications on the linear oligonucleotides were required. A 3′-alkyne modification was achieved by using 5′-*O*-(4,4′-dimethoxytrityl)-3′-*O*-propargyl-deoxycytidine or 5′-*O*-(4,4′-dimethoxytrityl)-3′-*O*-propargyl-5-methyldeoxycytidinepolystyrene solid support. The 5′-azide modification was obtained by post-synthetic conversion of the 5′-hydroxyl group to an 5′-iodo intermediate, which was then converted to 5′-azide (Scheme 4.1). The linear oligonucleotides with 5′-OH and 3′-alkyne modifications were synthesised using automated solid-phase phosphoramidite chemistry as presented in Chapter 6 (Section 6.2.1).



Scheme 4.1. Conversion of 5′-hydroxyl group to 5′-azide modification and the mechanism of the reactions. "B" refers to DNA bases, which were still protected during the conversion process.

The modified linear oligonucleotides were then circularised to give their corresponding cyclic versions using click chemistry. The CuAAC reaction is detailed in Chapter 1 (See Section 1.4.2.1). The linear 5′-azide/3′-alkyne oligonucleotides (linear **1**_Tz, linear **2**_Tz, linear **3**_Tz and linear **4**_Tz) were cyclised by treatment with $CuSO_4$ in the presence of sodium ascorbate and THPTA ligand in 0.2 M aqueous NaCl (Figure 4.12). The molar ratio of reagents $CuSO_4$, sodium ascorbate and THPTA ligand was 1:10:7, which was optimised by previous work in our group.[119] In most cases, the click cyclisation reaction proceeded smoothly in the absence of a splint. All the resulting single-stranded cyclic DNA products containing a single triazole linkage were purified by denaturing PAGE gel.

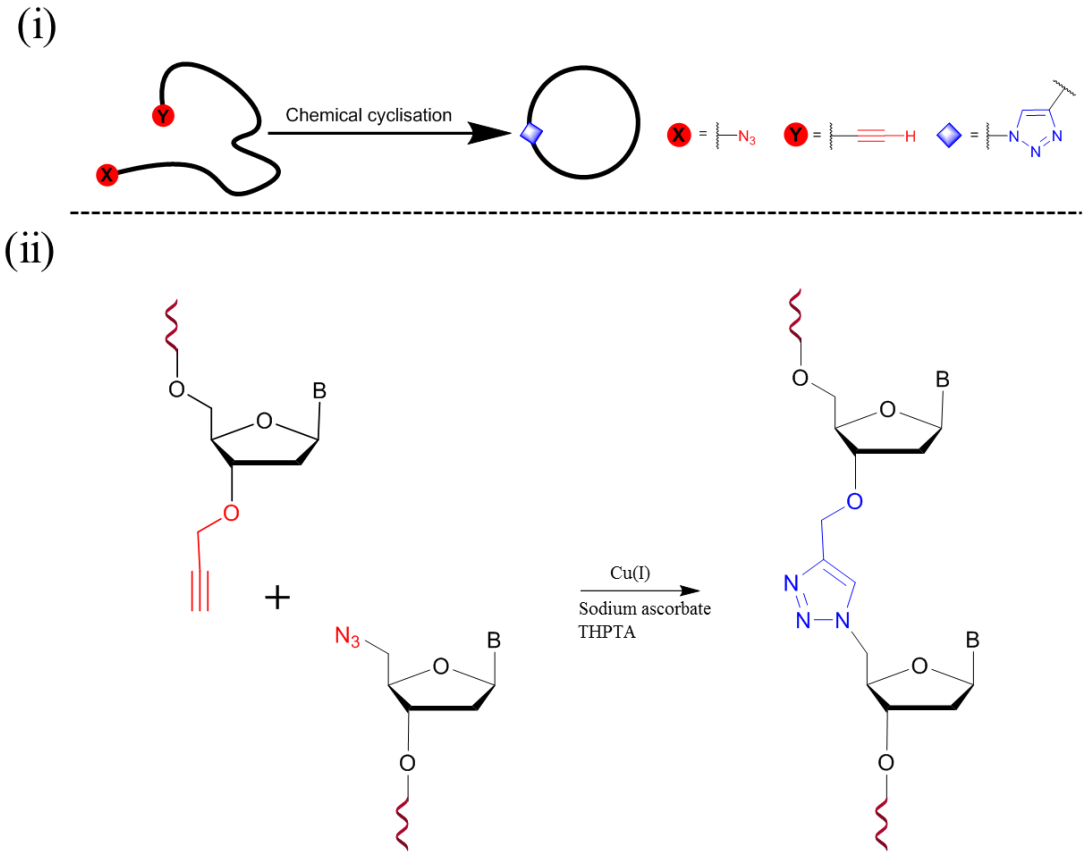


Figure 4.12. (i) Chemical cyclisation of single-stranded DNA by introducing a triazole backbone linkage. (ii) Formation of an artificial triazole backbone linkage *via* the CuAAC reaction. "B" refers to DNA bases.

In accordance with previous observations on the enzymatic cyclisation, here we first investigated the effect of concentration of linear oligonucleotide substrate on the click cyclisation reaction. For linear oligonucleotides linear **1**_Tz, linear **2**_Tz, linear **3**_Tz, the results indicated that the chemical cyclisation was efficient with high yields obtained using untemplated CuAAC cyclisation. Moreover, no significant polymeric by-products were observed even though the chemical cyclisation reaction was carried out at relatively high concentration of linear oligonucleotide precursor such as 5 μM (Appendix Figure 8.4.3 - 8.4.5). The resulting cyclic oligonucleotide constructs containing a single triazole backbone linkage were further investigated for their applications in Section 4.5. The crude reaction mixture of each template using CuAAC-mediated click chemistry was analysed

by denaturing PAGE gel and the isolated yields were as follows: cyclic **1**_Tz: 15% PAGE with 21% yield; cyclic **2**_Tz: 8% PAGE with 21% yield; cyclic **3**_Tz: 12% PAGE with 22% yield. Their corresponding cyclic products were identified by LC-MS (Figure 4.13 - Figure 4.15).

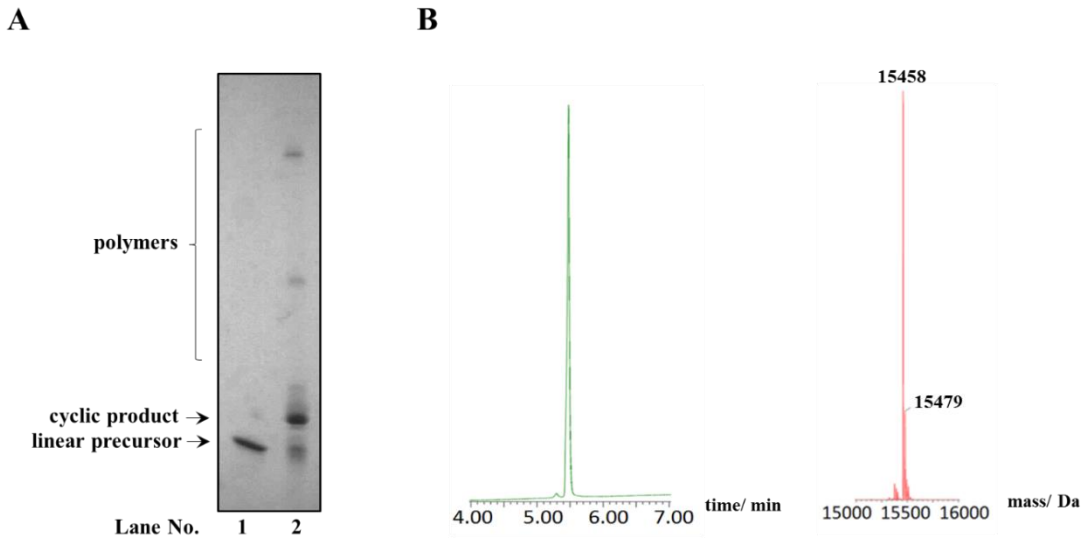


Figure 4.13. Non-templated CuAAC-mediated click cyclisation reaction to give cyclic **1**_Tz. (A) The crude reaction mixture was analysed by a 15% denaturing PAGE gel. The gel was imaged under UV shadowing. Lane 1: linear oligonucleotide precursor; Lane 2: crude cyclisation reaction. (B) Reverse-phase UPLC (UV abs at 260 nm) and mass spectrum (ES^-) of cyclic **1**_Tz, required 15457 Da, found 15458 Da. The mass peaks show the product and the Na^+ adduct.

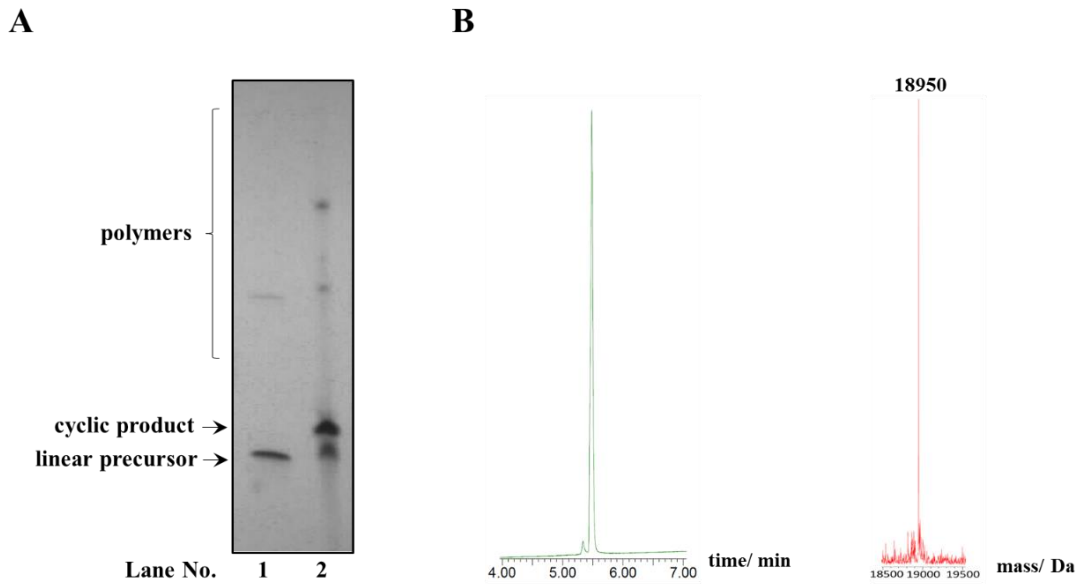


Figure 4.14. Non-templated CuAAC-mediated click cyclisation reaction to give cyclic **2**_Tz. (A) The crude reaction mixture was analysed by an 8% denaturing PAGE gel. The gel was imaged under UV shadowing. Lane 1: linear oligonucleotide precursor; Lane 2: crude cyclisation reaction. (B) Reverse-phase UPLC (UV abs at 260 nm) and mass spectrum (ES^-) of cyclic **2**_Tz, required 18948 Da, found 18950 Da.

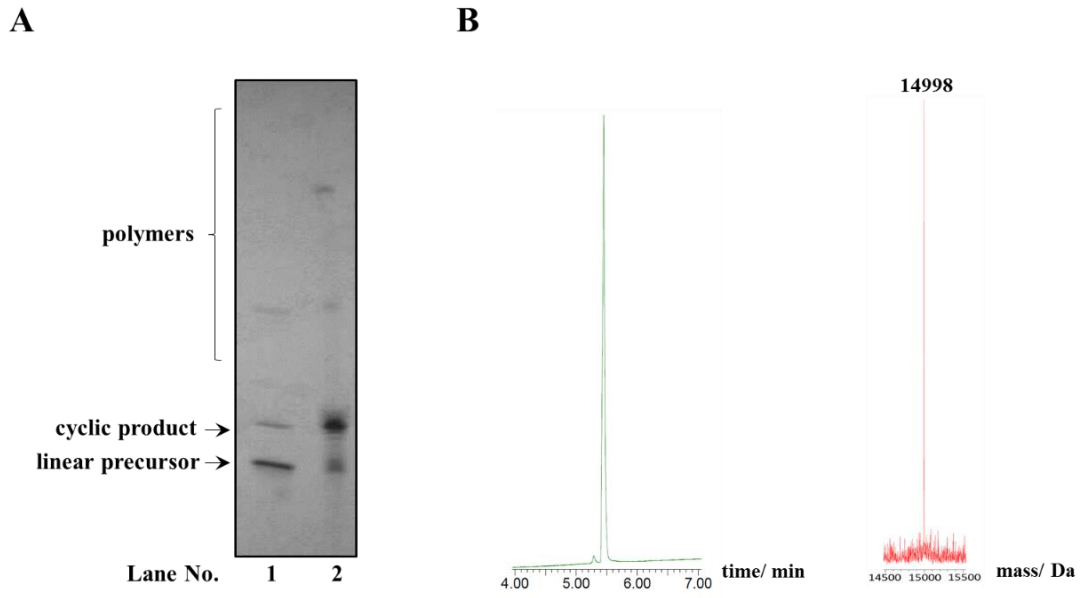


Figure 4.15. Non-templated CuAAC-mediated click cyclisation reaction to give cyclic **3**_Tz. (A) The crude reaction mixture was analysed by a 12% denaturing PAGE gel. The gel was imaged under UV shadowing. Lane 1: linear oligonucleotide precursor; Lane 2: crude cyclisation reaction. (B) Reverse-phase UPLC (UV abs at 260 nm) and mass spectrum (ES^-) of cyclic **3**_Tz, required 14997 Da, found 14998 Da.

However, a low conversion of linear to cyclic product (yield < 10%) was again observed for template **4** (linear **4**_Tz). A number of intermolecular polymeric side-products with higher molecular weight were generated as the major cyclisation products (Appendix Figure 8.4.6). We reasoned that this was due to secondary structures forming in the linear oligonucleotide, reducing the cyclisation efficiency. Based on this hypothesis, the CuAAC click reaction was repeated in the presence of organic solvents (formamide, DMSO or acetonitrile). These are known to denature oligonucleotides, removing secondary structures. Pleasingly, the CuAAC-mediated click reaction then proceeded more cleanly, generating fewer oligomeric by-products (Figure 4.16). Moreover, the isolated yield was remarkably improved up to 22%. According to the results from the click reaction under these denaturing conditions, the efficiency of the CuAAC click cyclisation appears comparable to that of the reported CircLigase II-mediated cyclisation

of the same template.[265] In addition, the CuAAC click cyclisation strategy is not limited in scale by the high cost associated with the CircLigase enzyme.

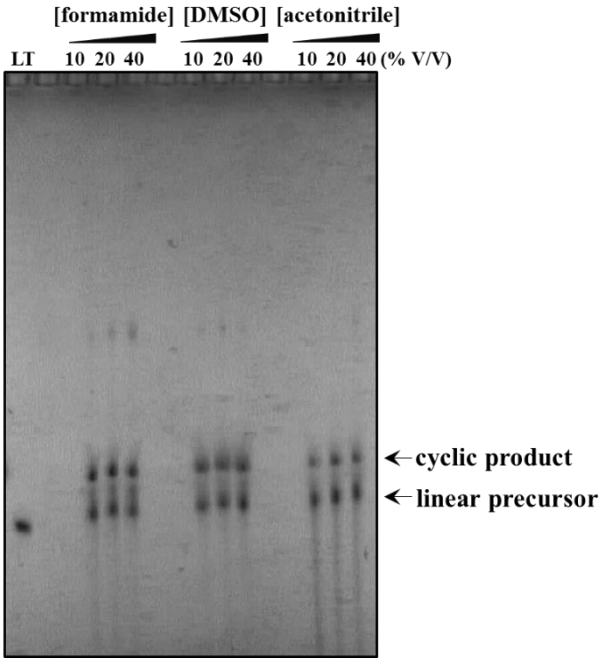


Figure 4.16. Non-template CuAAC click cyclisation of the linear **4**_Tz to prepare the circularised constructs cyclic **4**_Tz in the presence of denaturing organic solvents. The crude cyclisation products were analysed using an 8% denaturing PAGE gel, which was visualised under UV shadowing. LT: linear 5′-azide/3′-alkyne modified oligonucleotide precursor. The sequence of template **4** incorporated a complex secondary structure (See Figure 4.2D).

4.4.2.2 Modified backbone with phosphoramidate linkage

To enable cyclisation using di-imide coupling reaction, linear oligonucleotides incorporating the required 5′-amine/3′-phosphate modifications were synthesised using automated solid-phase phosphoramidite chemistry, as mentioned in Section 6.2.1 (Chapter 6). These chemically modified linear oligonucleotides were circularised under aqueous di-imide coupling conditions to give the non-canonical artificial phosphoramidate backbone linkage (Figure 4.17).

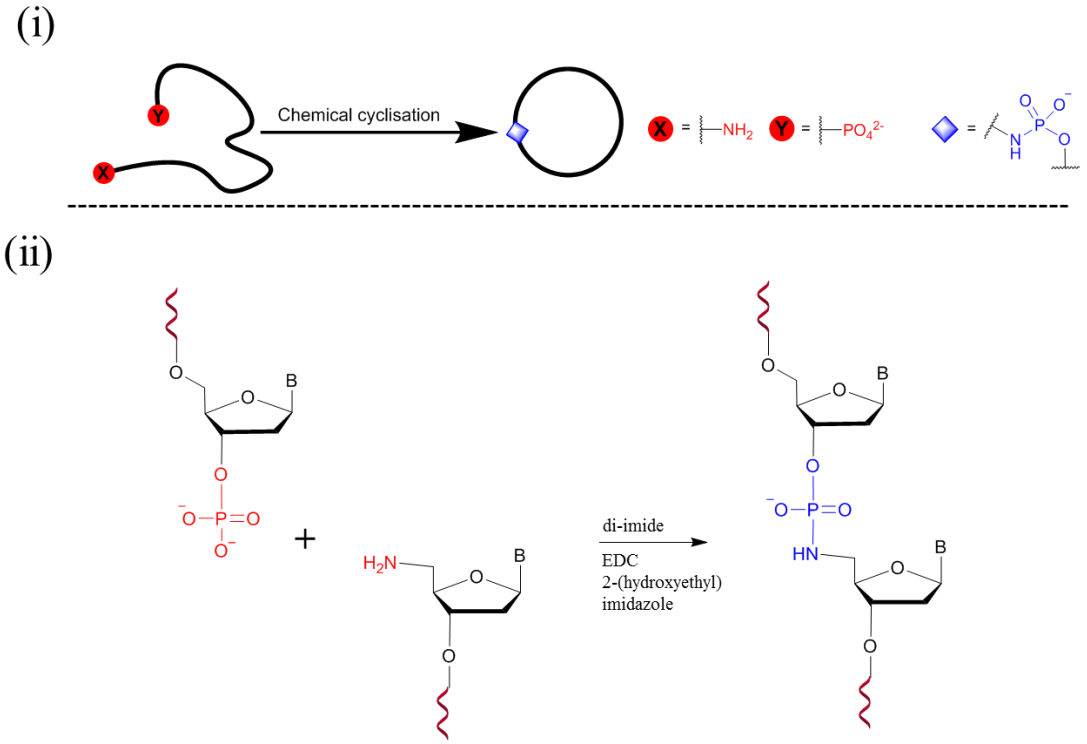


Figure 4.17. (i) Chemical cyclisation of single-stranded DNA by introducing a phosphoramidate backbone linkage. (ii) di-imide-mediated formation of an artificial phosphoramidate backbone linkage. "B" refers to DNA bases.

The chemical cyclisation of linear 5′-amine/3′-phosphate oligonucleotide was carried out using EDC·HCl and 2-(hydroxyethyl)imidazole in aqueous 0.2 M HEPES buffer (pH 7.2) by using an adaptation of reported phosphoramidate ligation method from our group.[125] The linear **1**_PA construct was converted to the cyclic template readily in the absence of a templating splint oligonucleotide. Compared to the enzymatic cyclisation, the di-imide-mediated cyclisation reaction was efficient and produced the phosphoramidate-modified cyclic product in higher yield of 22%. Moreover, no polymeric by-products were observed in the cyclisation reaction confirmed by denaturing PAGE gel (Figure 4.18). In order to achieve more efficient circularisation, the cyclisation reactions of **2**_PA and **3**_PA were carried out by Dr. Asha Brown under templating conditions with 26% and 11% yield, respectively (data not shown here).

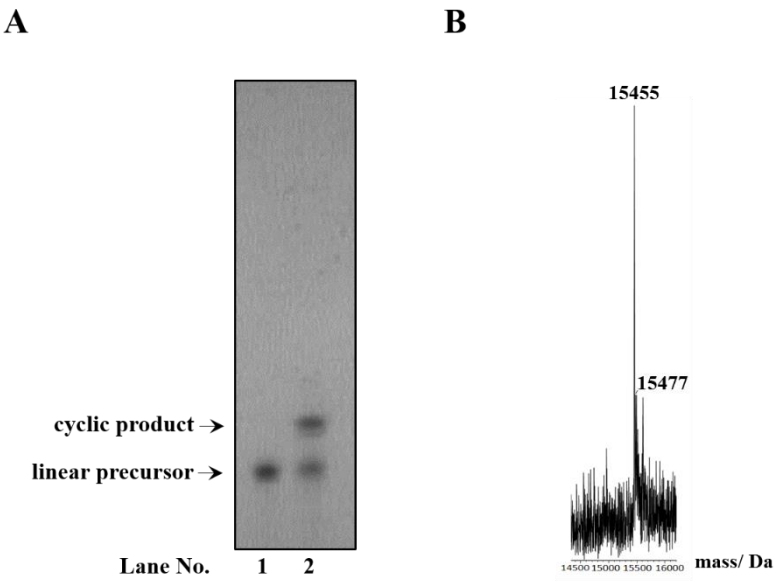
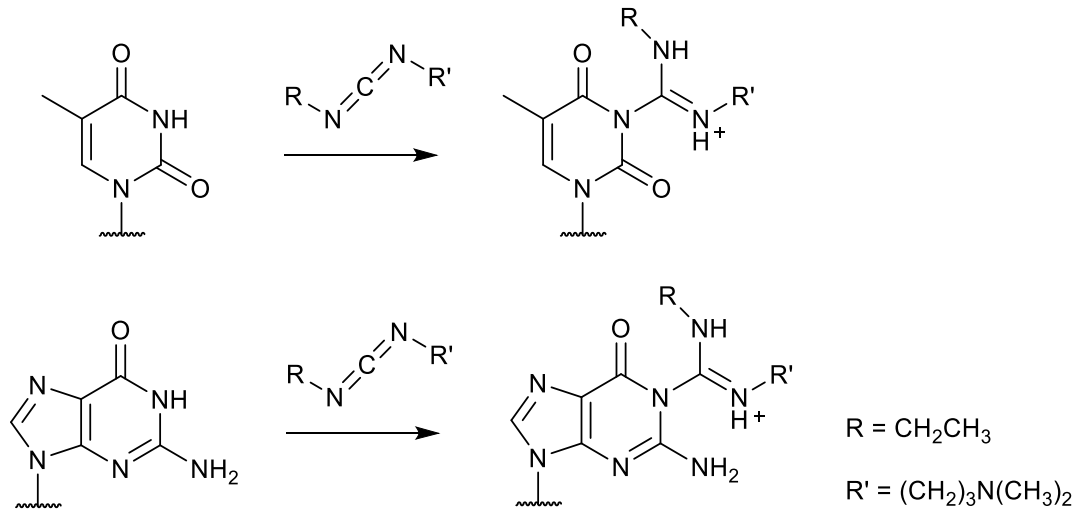


Figure 4.18. Non-templated di-imide-mediated cyclisation reaction to give cyclic **1**_PA. (A) The crude reaction mixture was analysed by a 15% denaturing PAGE gel. The gel was imaged under UV shadowing. Lane 1: linear oligonucleotide precursor; Lane 2: crude cyclisation reaction. (B) Mass spectrum (ES^-) of cyclic **1**_PA, required 15457 Da, found 15455 Da. The mass peaks show the product and the Na^+ adduct.

Despite a clean conversion being observed, the use of EDC during cyclisation led to the formation of a by-product with a molecular weight +155 than the expected product as confirmed by UPLC-mass spectrometry. This is consistent with the chemical addition of EDC to the oligonucleotide. A similar phenomenon has been also reported previously.[271-275] This addition adduct is proposed to arise from a chemical reaction between the di-imide coupling reagent and the N3 imide group of thymine and N1 imide of guanine bases (Scheme 4.2).



Scheme 4.2. Proposed formation of covalent adducts between di-imide coupling reagent and DNA bases (guanine and thymine).

Fortunately, this unwanted side-reaction could be reversed by gently heating the crude product mixture in 0.1 M NaOH after conducting the phosphoramidate cyclisation reaction. The crude reaction mixture of cyclic **1**_PA using di-imide-mediated cyclisation was analysed by denaturing PAGE gel. The corresponding cyclic product was identified by LC-MS (Figure 4.18). The resulting cyclic oligonucleotide construct with an artificial phosphoramidate backbone linkage was further investigated for its applications (Section 4.5).

4.4.2.3 Modified backbone with amide linkage

To enable amide cyclisation using the di-imide coupling reaction, linear oligonucleotides with 5′-amide/3′-carboxylate were required and synthesised using automated solid-phase phosphoramidite chemistry, as described in Section 6.2.1 (Chapter 6). Cyclisation of the chemically modified linear oligonucleotides was performed under aqueous di-imide coupling conditions (Figure 4.19).

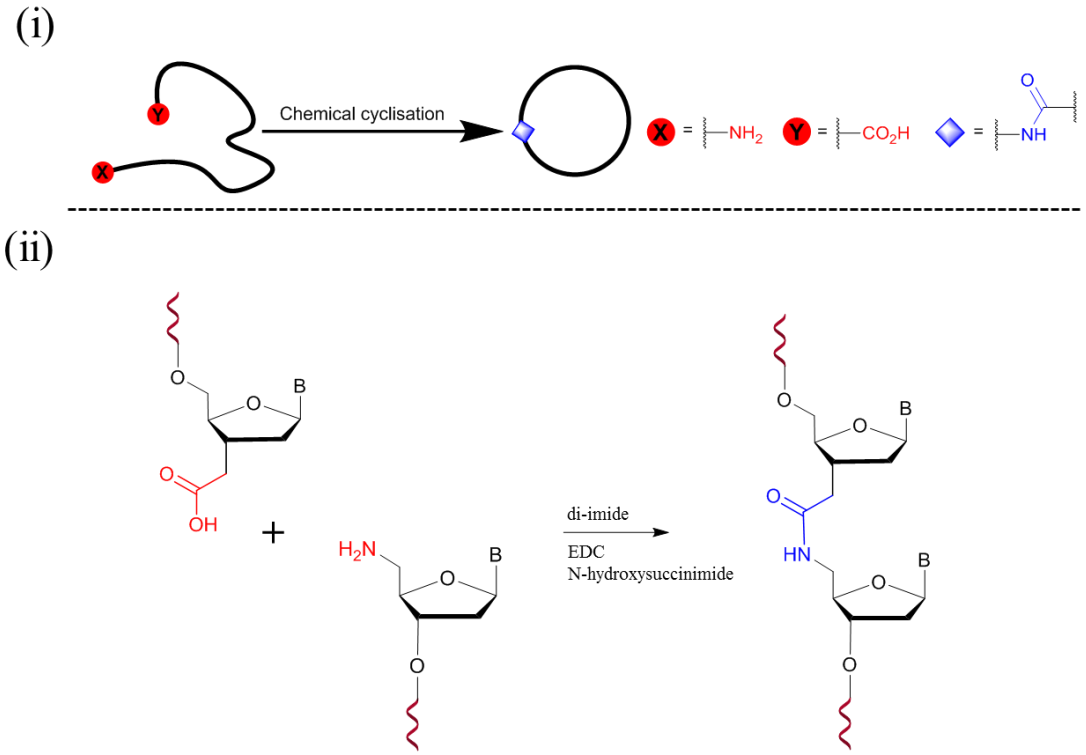


Figure 4.19. (i) Chemical cyclisation of single-stranded DNA by introducing an amide backbone linkage. (ii) di-imide-mediated formation of an artificial amide backbone linkage. "B" refers to DNA bases.

Similar to phosphoramidate cyclisation, the linear oligonucleotide with 5′-amide/3′-carboxylate modifications was cyclised by treatment with EDC·HCl in combination with NHS in aqueous NaCl, an adaptation of the method reported previously from our group.[128] The chemical cyclisation of **1**_Am was carried out in the absence of a templating splint oligonucleotide. The linear oligonucleotide precursor was successfully converted to the desired cyclic product with high efficiency in 16% yield. Compared with enzymatic cyclisation, there was no intermolecular side-product observed during this chemical cyclisation process (Figure 4.20). In terms of **2**_Am and **3**_Am, the cyclisation reactions were performed by Dr. Asha Brown in the presence of a splint oligonucleotide with relatively lower yield of 9% and 5%, respectively (data not shown here).

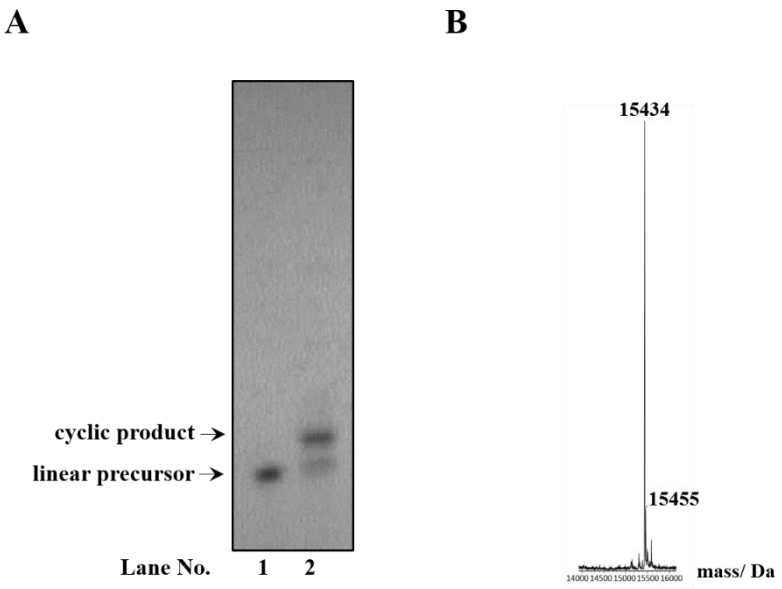


Figure 4.20. Non-templated di-imide-mediated cyclisation reaction to give cyclic **1**_Am. (A) The crude reaction mixture was analysed by a 15% denaturing PAGE gel. The gel was imaged under UV shadowing. Lane 1: linear oligonucleotide precursor; Lane 2: crude cyclisation reaction. (B) Mass spectrum (ES^-) of cyclic **1**_Am, required 15433 Da, found 15434 Da. The mass peaks show the product and the Na^+ adduct.

Interestingly, during the cyclisation reaction for preparing the amide-modified cyclic constructs, we did not observe any evidence of the formation of the EDC addition adducts. A possible explanation is that the cyclisation reaction was performed under slightly different conditions and required a lower concentration of the di-imide coupling reagent. The crude reaction mixture of cyclic **1**_Am using di-imide-mediated cyclisation was analysed by denaturing PAGE gel. The corresponding cyclic product was identified by LC-MS (Figure 4.20). The resulting cyclic oligonucleotide constructs with an artificial amide backbone linkage were further investigated for its applications (Section 4.5).

4.5 Rolling circle amplification of the cyclic oligonucleotides

One particularly important application of cyclic oligonucleotides is as substrate templates in RCA reaction. As described in Chapter 1 (Section 1.5), RCA is a simple and efficient

isothermal enzymatic technique that is widely used to make very long single-stranded DNA or RNA of repeated sequence.[154,155]

It is worth noting that phosphodiester backbone analogues (triazole, amide and phosphoramidate) incorporated into the linear oligonucleotides can be read through by DNA polymerases during linear copying and PCR, with accurate transfer of genetic information.[122,125,128] Under this context, the cyclic oligonucleotides with modified backbone linkages serving as RCA templates could be potentially read through by the specific DNA polymerases that are compatible with efficient RCA (Figure 4.21).

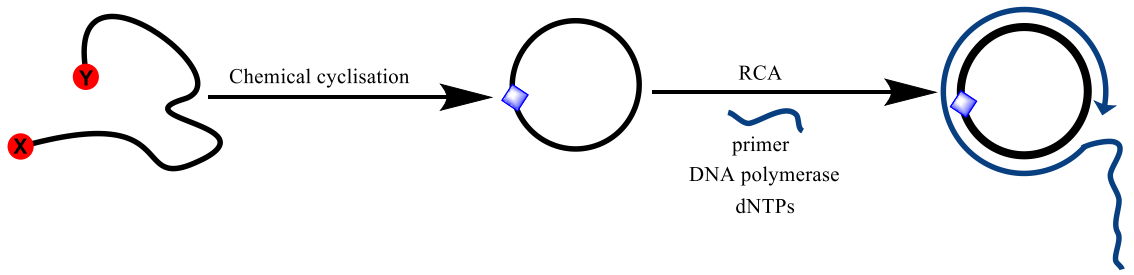


Figure 4.21. The circularised oligonucleotide with non-canonical backbone linkage acts as template in the rolling circle amplification reaction.

4.5.1 RCA using the Φ-29 DNA polymerase

After success in obtaining the desired cyclic oligonucleotides containing an artificial triazole, phosphoramidate or amide backbone linkage, the next step was to explore their use as substrate templates in RCA. The RCA reaction was carried out at 30 °C using Φ-29 DNA polymerase, a highly processive polymerase with strand displacement activity.[276] Mg^{2+} serves as a cofactor for DNA polymerases, and its concentration has a big influence on the interaction between DNA polymerase and substrate. Therefore, the effect of concentration of Mg^{2+} on RCA was first investigated. After the RCA reaction,

the sample mixtures were centrifuged removing any precipitate, and the resulting supernatants were analysed to evaluate RCA efficiency by agarose gel electrophoresis.

Our experiments demonstrated that the RCA reactions from tested cyclic templates proceeded efficiently over a wide Mg^{2+} concentration ranging from 10 - 25 mM. However, the extent of DNA present in the precipitate at 10 mM Mg^{2+} concentration is often negligible, whereas 20 mM Mg^{2+} concentration showed higher and more consistent levels of DNA in the precipitates (Appendix Figure 8.5.1 - 8.5.6). Taking this into account, we therefore chose to use 20 mM Mg^{2+} concentration for the subsequent RCA experiments.

After determining the optimised Mg^{2+} concentration for RCA, all fourteen cyclic templates (template **1 - 3**: four versions of each template containing an unmodified natural phosphodiester (PO_4), triazole (Tz), phosphoramidate (PA) or amide (Am) backbone linkage; template **4**: two versions of unmodified and triazole-modified backbone linkage) were evaluated into the RCA reaction and their efficiency as substrate templates was systematically evaluated (e.g. overall yield, product distribution and reaction rate). In all cases, the RCA reactions were analysed using agarose gel electrophoresis. However, significant differences in the quantities and size distributions of the RCA products were observed depending on the nature of the modified backbone linkage in the cyclic templates.

The agarose gel results indicated that each reaction generated a detectable quantity of very slow-migrating products, which were retarded in the wells of the gel. A second discrete band with higher gel mobility in some cases was also observed and formed a substantial proportion of the products (Figure 4.22). A similar phenomenon was also observed by Ducani *et al*. who reported that this faster-running band is double-stranded DNAs that form during RCA, whilst the products retarded in the wells are as very long

single-stranded products.[250] In their assays, the produced amplicons were digested by restriction enzyme, and the digestion products were further analysed by agarose electrophoresis. The gel results indicated that the slow-migrating products retarded in the wells are not digested, while only the band with higher gel mobility is completely digested into predicted discrete fragments based upon a map sequence analysis, confirming the double-stranded nature of the fast-running band.

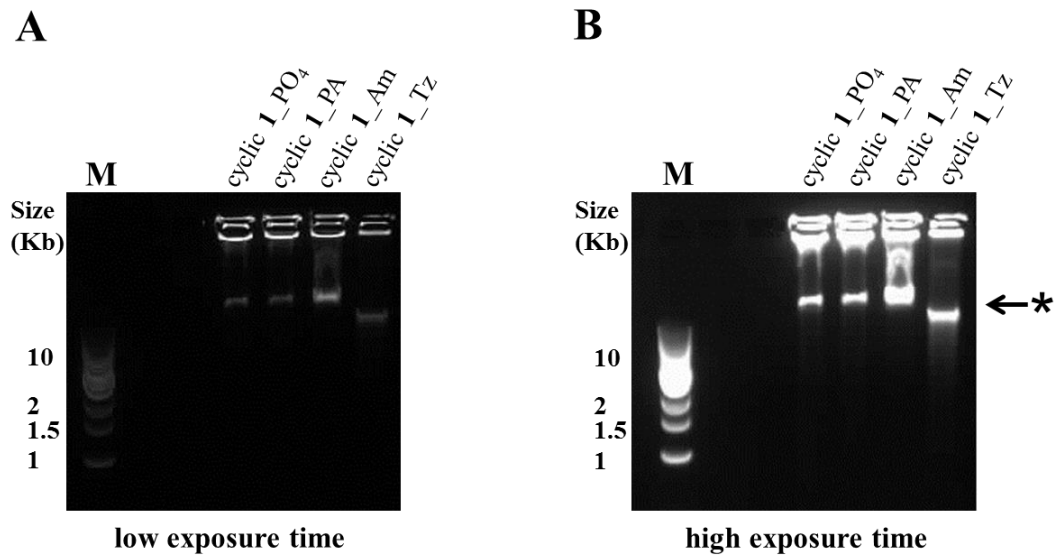


Figure 4.22. 0.8% agarose gel analysis of the RCA products generated using Φ-29 DNA polymerase and cyclic **1**_PO_4, cyclic **1**_PA, cyclic **1**_Am and cyclic **1**_Tz (8 h amplification time). The RCA products were visualised by pre-casting the gel with 0.5× concentration of SYBR Gold nucleic acid gel stain. (A) Gel image using a short exposure time. (B) The same gel was imaged using a longer exposure time, allowing visualisation of all RCA products. M: 1 kb DNA ladder; *: the band is assigned to double-stranded DNA by-products.[250]

Based on above findings, a possible mechanism for the formation of double-stranded side-products during the RCA process is illustrated below. In the normal RCA process (Figure 4.23A), the elongated single-stranded product is continuously displaced from the cyclic template, leading to the formation of very long single-stranded products. However, for triazole- and amide-modified cyclic templates, we hypothesise that the DNA

polymerase dissociates from the cyclic template and copies the emerging single-stranded products, resulting in the formation of double-stranded by-products (Figure 4.23B). During this process, the cyclic template is sequestered, and the RCA reaction is also inhibited. This alternative mechanism might be favoured by the artificial amide- or triazole-modified backbone linkage, which the DNA polymerase has difficulty in reading through.

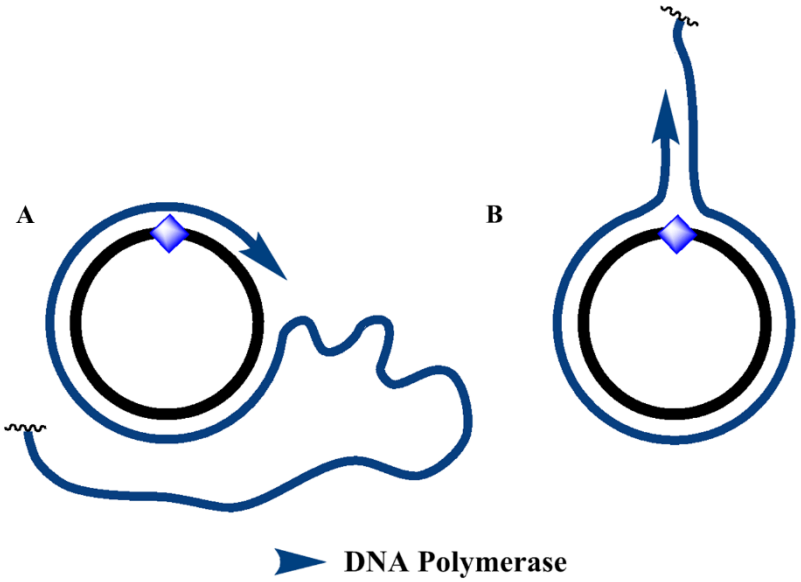
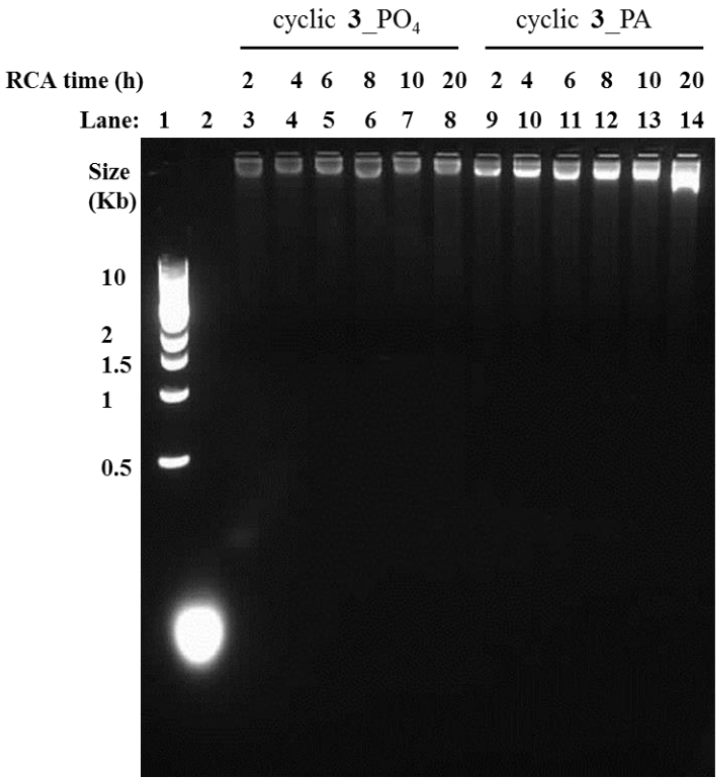
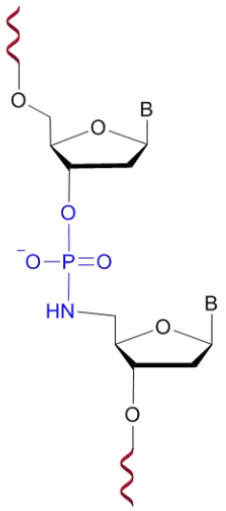


Figure 4.23. Possible mechanism for the generation of double-stranded products in the RCA reaction. (A) Normal RCA mechanism for natural phosphodiester backbone linkage. (B) An alternative mechanism for unnatural modified amide- or triazole-backbone linkage.

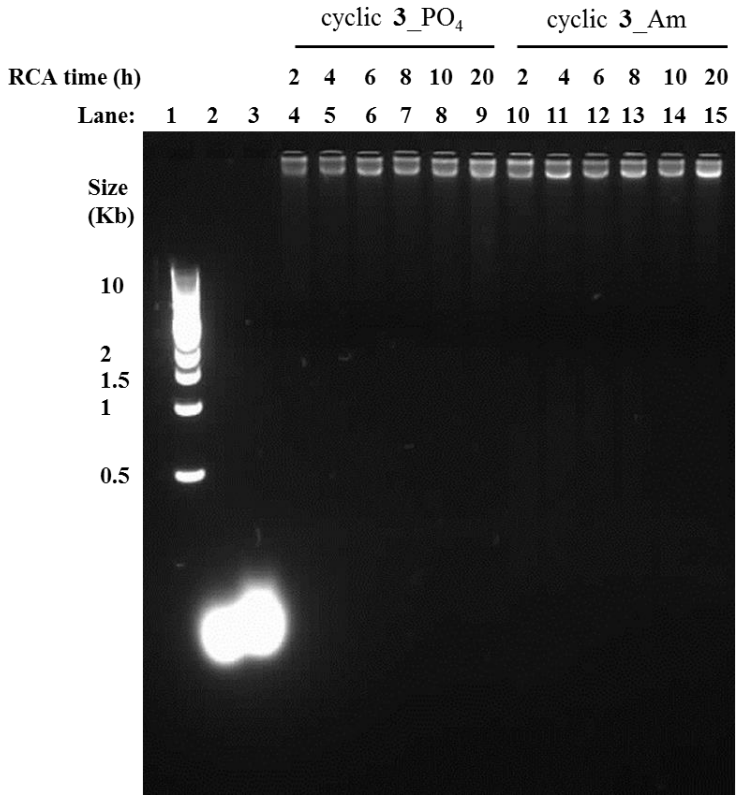
In addition, the faster-running band assigned to the double-stranded RCA side-products was not observed for the cyclic templates cyclic **3**_PO_4, cyclic **3**_PA, cyclic **3**_Am and cyclic **3**_Tz, in which were incorporated a complementary trimeric G-quadruplex aptamer sequence (Figure 4.24 - Figure 4.26). One possible explanation is that the formation of double-stranded side-products is suppressed by the emerging RCA products which further fold into a G-quadruplex secondary structure.

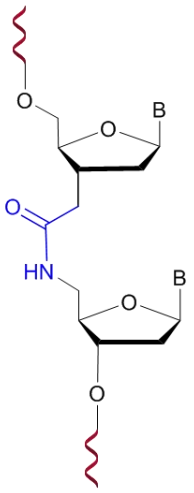




Phosphoramidate (PA) backbone

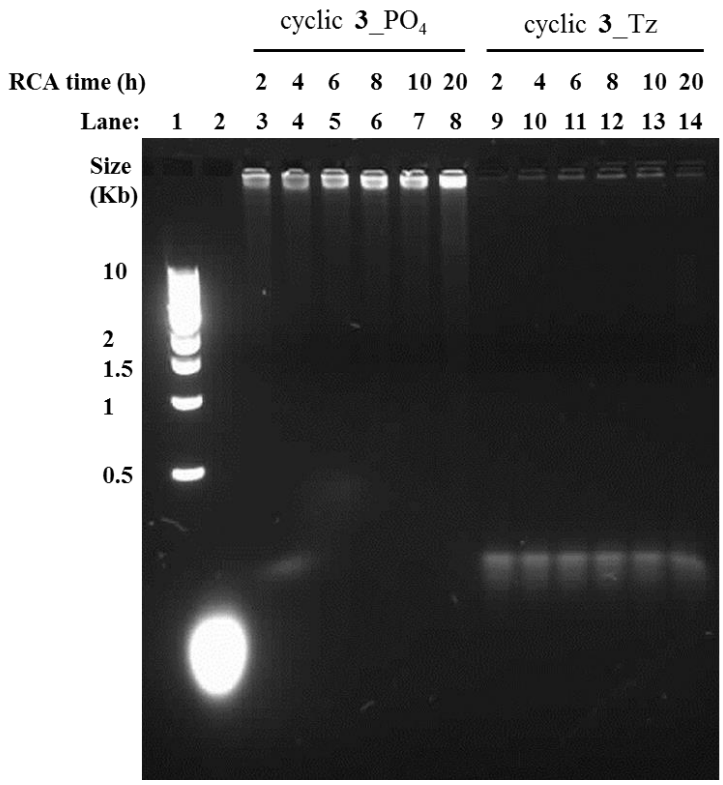
Figure 4.24. 0.8% agarose gel analysis of RCA supernatant from cyclic **3**_PO_4 and cyclic **3**_PA. The RCA reaction was carried out in the presence of 20 mM Mg^{2+} at different time courses using Φ-29 DNA polymerase. After finishing the RCA reactions, EDTA (20 mM final concentration) was added to the reaction mixture in an attempt to break down the precipitate releasing the very long RCA products. However, the precipitate was still observed. Lane 1: 1kb DNA ladder; Lane 2: RCA primer ODN4-3.

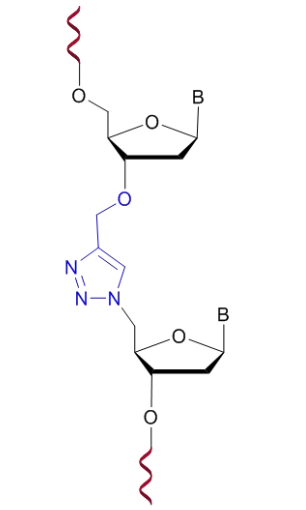




Amide (Am) backbone

Figure 4.25. 0.8% agarose gel analysis of RCA supernatant from cyclic **3**_PO_4 and cyclic **3**_Am. The RCA reaction was carried out in the presence of 20 mM Mg^{2+} at different time courses using Φ-29 DNA polymerase. After finishing the RCA reactions, EDTA (20 mM final concentration) was added to the reaction mixture in an attempt to break down the precipitate releasing the very long RCA products. However, the precipitate was still observed. Lane 1: 1kb DNA ladder; Lane 2: RCA primer ODN4-3; Lane 3: RCA primer ODN4-7 for cyclic **3**_Am.





Triazole (Tz) backbone

Figure 4.26. 0.8% agarose gel analysis of RCA supernatant from cyclic **3**_PO_4 and cyclic **3**_Tz. The RCA reaction was carried out in the presence of 20 mM Mg^{2+} at different time courses using Φ-29 DNA polymerase. After finishing the RCA reactions, EDTA (20 mM final concentration) was added to the reaction mixture in an attempt to break down the precipitate releasing the very long RCA products. However, the precipitate was still observed. Lane 1: 1kb DNA ladder; Lane 2: RCA primer ODN4-3.

For template **1** - **3**, all the cyclic oligonucleotide templates modified with phosphoramidate backbone linkage gave efficient RCA, and the product distributions were indistinguishable from those of the unmodified controls with natural phosphodiester backbone linkage (Figure 4.22 and Figure 4.24; Appendix Figure 8.6.1 - 8.6.2). The amide-modified cyclic templates also appeared to be well-tolerated by the Φ-29 DNA polymerase, generating similar product distributions in comparison with the unmodified control sequences (Figure 4.22 and Figure 4.25; Appendix Figure 8.6.3 - 8.6.4).

In contrast, cyclic templates with the incorporated triazole-modified backbone linkage showed weaker and more variable results. The RCA reaction from triazole-modified

cyclic **1**_Tz proceeded moderately compared with its counterparts containing unmodified and phosphoramidate-modified analogues (Figure 4.22; Appendix Figure 8.6.5). Cyclic templates containing cyclic **2**_Tz and cyclic **3**_Tz consistently produced much lower yields of very long, slow-migrating RCA products (Figure 4.26; Appendix Figure 8.6.6).

Based on above results, the overall performance of the triazole-modified cyclic templates appears to be compromised compared with those of the unmodified and phosphoramidate-modified analogues. This is an important observation given a recent publication where a triazole-modified cyclic template was employed in an RCA-based fluorescent switch-based diagnostic assay for microRNA detection using Φ-29 DNA polymerase.[262] Interestingly, the proportion of double-stranded by-products in RCA from the amide- and triazole-containing cyclic **1**_Am, cyclic **1**_Tz and cyclic **2**_Am appeared to increase with extended amplification time. In contrast, for all of the unmodified and phosphoramidate-containing cyclic templates, the relative proportion of the bands assigned to single- and double-stranded RCA products remained approximately constant through the time course of the RCA reactions (Figure 4.24; Appendix Figure 8.6.1 - 8.6.2).

We also investigated the effect of using single-stranded DNA binding protein (T4 gene 32 protein) on the formation of double-stranded side-products during the RCA process. A recent paper has reported that this protein can promote RCA in the single-stranded form and dramatically reduce the amplification of DNA in the double-stranded form.[250] In order to examine whether the presence of T4 gene 32 protein reduces the formation of double-stranded side-products and thus enhances the RCA reaction, we repeated the reported conditions. However, no significant differences were observed in the product distribution in the presence or absence of the single-stranded binding protein when the

RCA reactions carried out using cyclic **1**_PO_4 and cyclic **1**_PA and Φ-29 DNA polymerase (Figure 4.27).

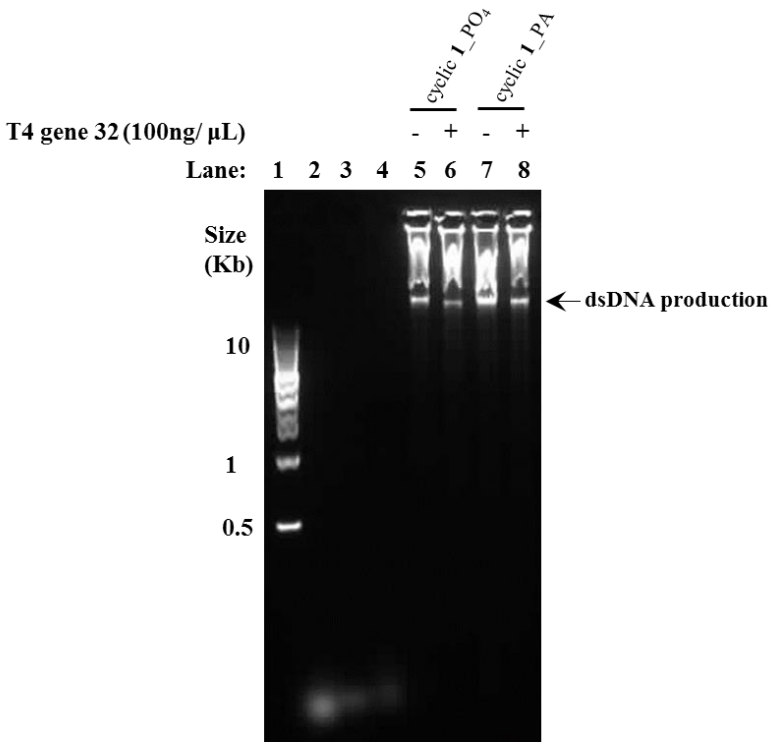


Figure 4.27. 0.8% agarose gel analysis of the reaction mixtures of RCA reactions conducted in the presence of single-stranded binding protein. The RCA reactions were performed in the presence of 10 mM Mg^{2+} using cyclic **1**_PO_4 and cyclic **1**_PA and Φ-29 DNA polymerase. Lane 1: 1 kb DNA ladder; Lane 2: RCA primer ODN4-1; Lane 3: cyclic unmodified template cyclic **1**_PO_4; Lane 4: cyclic phosphoramidate-modified template cyclic **1**_PA. Arrow shows the band which is assigned to the double-stranded DNA.

4.5.1.1 Probing the single-stranded RCA products with complementary fluorescent oligonucleotides

In an attempt to obtain further information about the nature of the RCA products from the cyclic templates containing phosphoramidate-, amide- and triazole artificial backbone linkages, we designed a fluorescent probe assay to enable us to differentiate the single- and double-stranded RCA products by agarose gel electrophoresis analysis.

Here, we designed a single-stranded Cy3 labelled fluorescent hybridisation probe. Its sequence is complementary to those of the single-stranded RCA products generated from the cyclic **1**_PO_4, cyclic **1**_Tz, cyclic **1**_Am and cyclic **1**_PA (template **1** used as an example here). To validate the assay, a scrambled version of the fluorescent probe was also synthesised (probe sequences are given in Table 4.3). The preliminary results demonstrated that the complementary fluorescent probe specifically hybridised to the RCA products formed from the cyclic **1**_PO_4 through base paring (Figure 4.28).

Table 4.3. Fluorescence probes used for hybridisation with single-stranded RCA product (mass spectra data of linear oligonucleotide given in Section 6.2.1, Chapter 6).

Oligonucleotide code	Sequence of oligonucleotide (5′→3′)	length
ODN4-8 (fluorescent probe)	AATTGGGTACGCAGTACC-Cy3	18
ODN4-9 (scrambled version of OND4-8)	ATGTCAGACCTCGAAGGT-Cy3	18

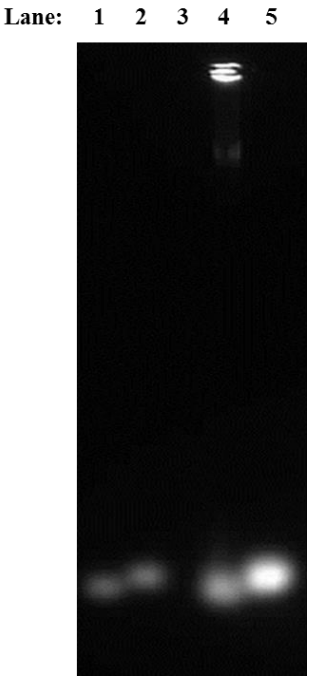


Figure 4.28. 0.8% agarose gel analysis of probing the amplified products from Φ-29 DNA polymerase catalysed RCA using cyclic **1**_PO_4 after incubation with fluorescent probes. Lane 1: fluorescent probe ODN4-8; Lane 2: fluorescent probe ODN4-9 (scrambled version of ODN4-8); Lane 3: RCA products without probes; Lane 4: after hybridisation of RCA products with complementary fluorescent probe ODN4-8; Lane 5: after hybridization of RCA products with scrambled fluorescent probe ODN4-9. The gel was visualised using a G:Box (Syngene) with excitation at 520 nm under the Cy3 fluorescence channel.

RCA reactions from four templates cyclic **1**_PO_4, cyclic **1**_Tz, cyclic **1**_Am and cyclic **1**_PA were carried out using Φ-29 DNA polymerase. After incubation, the individual sample was heated to inactivate the polymerase at two-hour intervals over a period of twenty hours. The reaction mixtures were then incubated with the fluorescent hybirdisation probe for two hours at RT prior to analysis by agarose gel electrophoresis. The gels were visualised under the Cy3 fluorescence channel with an excitation at 520 nm (Figure 4.29). The same gels were subsequently stained with SYBR Gold, which can sensitively detect both single- and double-stranded DNA. The gels were imaged with an excitation at 302 nm (Appendix Figure 8.7.1).

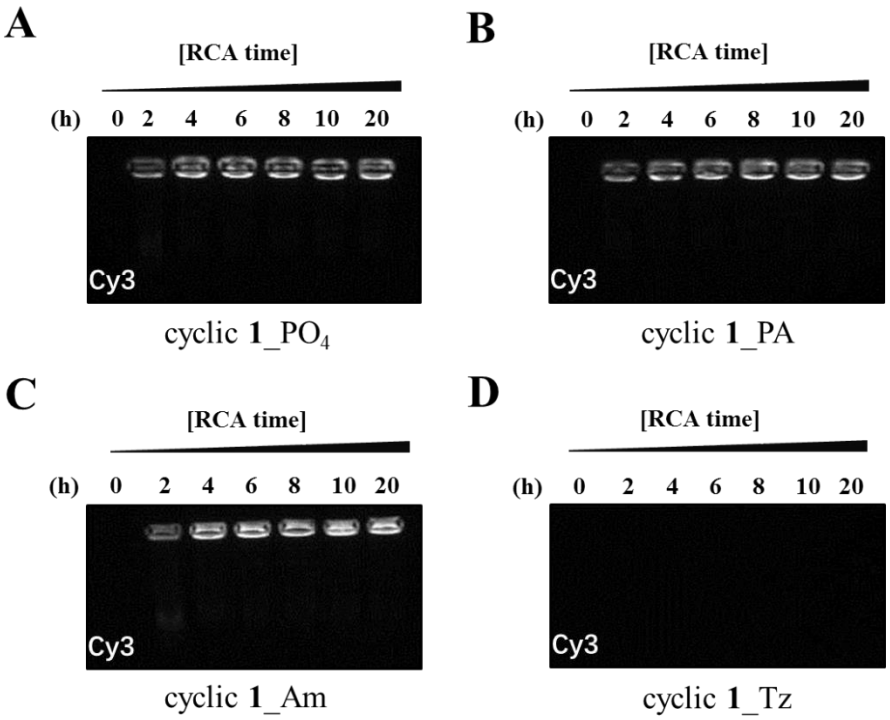


Figure 4.29. Probing the nature of the amplified products from Φ-29 DNA polymerase catalysed RCA of cyclic **1**_PO_4 (A), cyclic **1**_PA (B), cyclic **1**_Am (C) and cyclic **1**_Tz (D) using a fluorescent probe hybridisation assay. A Cy3 labelled fluorescent probe used with a sequence which is complementary to the RCA products was added to the individual aliquot and the mixtures were then analysed by 0.8% agarose gel electrophoresis. The gels were visualised under the Cy3 fluorescence channel. The same gels were post-stained with SYBR Gold (Appendix Figure 8.7.1).

A strong fluorescent signal was detected from the bound Cy3 labelled probe after amplification of the unmodified, phosphoramidate-modified and amide-modified cyclic **1**_PO_4, cyclic **1**_PA and cyclic **1**_Am. This suggests that the RCA products were single-stranded in nature. However, when amplifying triazole-modified cyclic **1**_Tz, there was no appreciable fluorescent signal from the Cy3 fluorophore, although some slow-migrating RCA products were weakly detected in the wells of the gel after staining with SYBR Gold. This indicates that the triazole-modified cyclic template generated a significantly lower quantity of RCA products containing both single- and double-stranded DNA.

4.5.1.2 Probing the nature and quantity of the RCA products *via* a fluorometric plate-reading assay

To further support above results from gel imaging, we developed a fluorometric plate-reading assay to allow a semi-quantitative comparison of the RCA rates and total DNA yields. The RCA reactions were carried out using Φ-29 DNA polymerase and cyclic **1**_PO_4, cyclic **1**_Tz, cyclic **1**_Am and cyclic **1**_PA over a ten-hour time period. Aliquots were taken at 2 h intervals and heated to inactivate the DNA polymerase. The samples were then measured using three different DNA-binding dyes containing SYBR Gold, SYBR Green I and SYBR Green II. All three dyes are capable of selectivity of single- or double-stranded DNA and could be used to detect the nature of the RCA products.

In each reaction mixture, the intensities of the measured fluorescent signals were approximately proportional to the total concentration of formed DNA products. There were some deviations observed due to the different proportions of single- and double-stranded DNA amplification products. As expected, the total product yield and RCA reaction rate from the phosphoramidate-modified cyclic **1**_PA were essentially the same as unmodified cyclic **1**_PO_4 (Figure 4.30), which is consistent with the previous agarose gel-imaging results (Figure 4.22). In addition, the amide-modified cyclic **1**_Am performed almost as well as the natural phosphodiester backbone. However, the measured fluorescence intensities at each time-course given by the triazole-modified cyclic **1**_Tz were weaker than that of those involving other backbone linkage analogues. This suggests that a relatively lower quantity of DNA was produced when using triazole-containing cyclic template as RCA substrate.

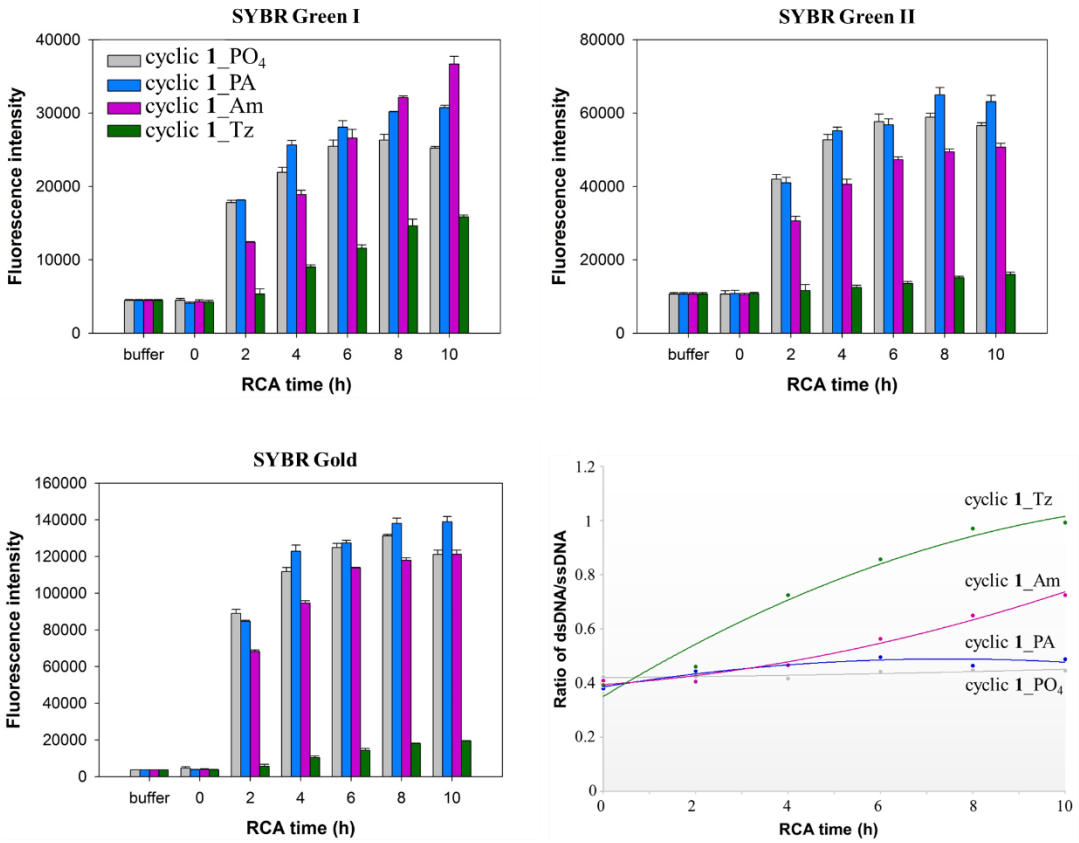


Figure 4.30. Fluorescence quantification of amplified DNA products from RCA reactions using cyclic **1**_PO_4, cyclic **1**_PA, cyclic **1**_Am and cyclic **1**_Tz and the Φ-29 DNA polymerase over a 10-hour time course. EDTA was added to break down the precipitate releasing the extended RCA products before incubation with DNA binding dyes. Error bars show the standard deviation of three measurements taken from a single RCA reaction. The ratio of dsDNA/ssDNA for four types of cyclic template was calculated using the fluorescence value obtained from SYBR Green I and SYBR Green II. The reactions were also repeated, and the same trends were observed.

Although all three DNA binding dyes are known to bind both single- and double-stranded DNA to some extent, SYBR Green I has been reported to specifically select double-stranded DNA rather than single-stranded DNA.[277-279] The plate-reading results showed that the measured fluorescence intensities from the triazole-containing cyclic template were significantly higher in the presence of SYBR Green I than in the presence of the SYBR Green II and SYBR Gold dyes compared with unmodified and phosphoramidate modified backbone linkages (Figure 4.30). This clearly demonstrates that a significant amount of double-stranded DNA was generated when using triazole-modified cyclic

template in RCA reaction (see ratio of dsDNA/ssDNA), which agrees with previous agarose gel-imaging results (Figure 4.22). In addition, the same phenomenon was also observed for the amide-modified cyclic **1**_Am but to a much lower extent referring to the ratio of dsDNA/ssDNA. This is probably because when the DNA polymerase encounters the modified backbone linkage in the cyclic template each time, it can either read through the modified backbone linkage or dissociate from the cyclic template, copying the emerging RCA products resulting in formation of the double-stranded products (Figure 4.23).[250]

The above results agree with our hypothesis that the triazole backbone linkage leads to an alternative amplification mechanism described earlier (Figure 4.23).

4.5.2 RCA using the Bst 2.0 DNA polymerase

Taking into consideration the disappointing performances of the triazole-modified cyclic templates in the Φ-29 DNA polymerase catalysed RCA reactions, we further investigated the RCA reaction using another commonly used thermostable polymerase, named Bst 2.0 DNA polymerase. In order to examine whether this alternative DNA polymerase can read through the triazole-modified backbone linkage more efficiently, the triazole-containing templates cyclic **1**_Tz and cyclic **4**_Tz and their corresponding unmodified controls cyclic **1**_PO_4 and cyclic **4**_PO_4 were used as positive controls. Bst 2.0 DNA polymerase has been previously used to construct DNA "nanoclews" in the RCA reaction using the cyclic **4**_PO_4.[265] It also has been shown to efficiently incorporate the modified dNTPs during the RCA process.[280,281] However, its capability to read through the modified backbone linkages has not yet been thoroughly studied.

The RCA reactions here were carried out in the presence of 20 mM Mg^{2+} concentration at 61.5 °C. This chosen temperature was utilised based upon the previous work from our group.[224] The results from agarose gel analysis showed that Φ-29 DNA polymerase consistently exhibited high efficiency in the RCA reaction for the unmodified cyclic **1**_PO_4 and cyclic **4**_PO_4 compared to triazole-modified cyclic **1**_Tz and cyclic **4**_Tz, whereas Bst 2.0 DNA polymerase appeared to process the triazole-modified cyclic templates more efficiently (Figure 4.31). More specifically, the RCA reactions carried out using the Bst 2.0 DNA polymerase generated similar product distributions and yields for the unmodified and triazole-containing cyclic **1**_PO_4 and cyclic **1**_Tz (Figure 4.31 B). When using the "nanoclew" cyclic **4**_PO_4 and cyclic **4**_Tz in the RCA reactions, the Bst 2.0 DNA polymerase was able to produce a markedly greater quantity of very long, slow-migrating RCA products from the triazole-modified cyclic **4**_Tz than that produced from the unmodified control with natural phosphodiester backbone linkage cyclic **4**_PO_4. This important observation suggests a promising alternative chemical cyclisation method in cases where the cyclisation or RCA amplification of a specific template sequence with natural phosphodiester backbone linkage is problematic or inefficient.

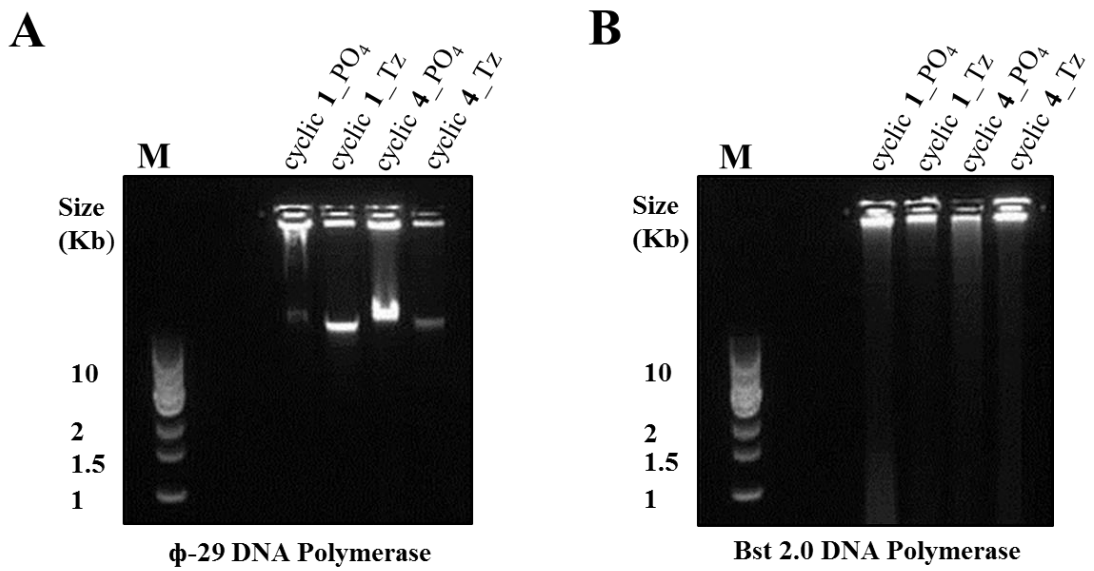


Figure 4.31. 0.8% agarose gel analysis of the product distributions from RCA (20 h amplification time) of the unmodified control cyclic **1**_PO_4 and cyclic **4**_PO_4 and the triazole-containing cyclic **1**_Tz and cyclic **4**_Tz using Φ-29 DNA polymerase (A) and Bst 2.0 DNA polymerase (B). M: 1 kb DNA ladder. The gel was pre-cast containing 0.5× concentrated solution of SYBR Gold nucleic acid gel stain.

Encouraged by the above findings, the performances of the amide- and phosphoramidate-containing cyclic **1**_Am and cyclic **1**_PA were further evaluated in the RCA reactions using Bst 2.0 DNA polymerase. All the versions of the other two templates (template **2** - **3**) were also investigated as RCA substrate templates using this alternative DNA polymerase. The products of the RCA reactions were analysed after different incubation times using the same reaction conditions as mentioned above. After incubation, the samples were heated to inactivate the enzyme, and the reaction mixtures were then analysed using agarose gel electrophoresis to evaluate the RCA efficiency.

The same trends were observed for Bst 2.0 DNA polymerase when compared with the RCA efficiencies using modified backbone linkages and Φ-29 DNA polymerase (see Section 4.5.1). The gel results demonstrated that the phosphoramidate backbone linkage again performed particularly well, with product yields and reaction rates which were

indistinguishable from those of the unmodified control with all natural phosphodiester backbone linkages (Figure 4.32; Appendix Figure 8.8.1 and Figure 8.8.4).

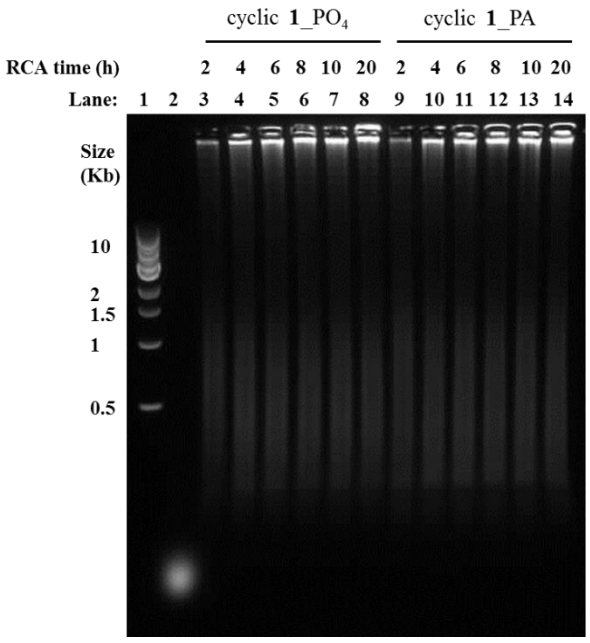


Figure 4.32. 0.8% agarose gel analysis of original RCA reaction mixtures from cyclic **1**_PO_4 and cyclic **1**_PA. The RCA was carried out in the presence of 20 mM Mg^{2+} at different time courses using Bst 2.0 DNA polymerase. Lane 1: 1 kb DNA ladder; Lane 2: RCA primer ODN4-1.

The triazole-modified backbone linkage was observed to slow down the RCA reaction rate in the beginning of the amplification, suggesting that the Bst 2.0 DNA polymerase also had difficulty reading through this modified backbone linkage (Figure 4.33; Appendix Figure 8.8.3 and Figure 8.8.6). The products distribution and yields appeared to be similar at twenty-hour time point of amplification time for triazole-containing cyclic **1**_Tz and unmodified control cyclic **1**_PO_4 (Figure 4.33).

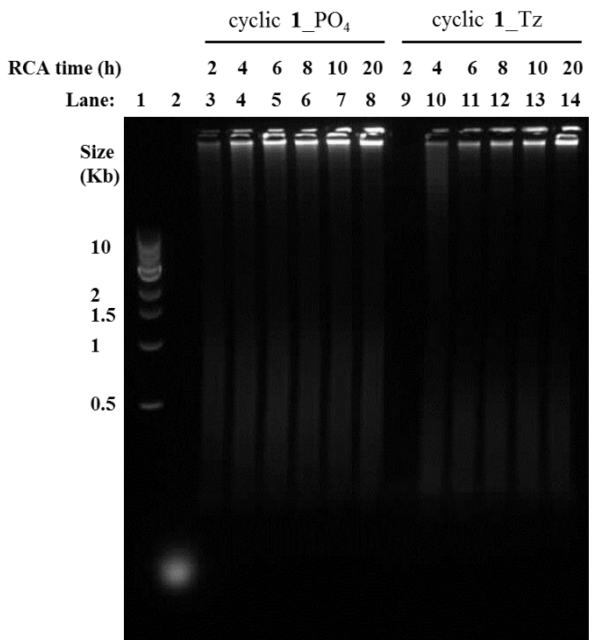


Figure 4.33. 0.8% agarose gel analysis of original RCA reaction mixtures from cyclic **1**_PO_4 and cyclic **1**_Tz. The RCA was carried out in the presence of 20 mM Mg^{2+} at different time courses using Bst 2.0 DNA polymerase. Lane 1: 1 kb DNA ladder; Lane 2: RCA primer ODN4-1.

The amide-modified backbone linkage also appeared to be compatible with Bst 2.0 DNA polymerase, producing similar product distributions and yields compared with unmodified control (Appendix Figure 8.8.2 and Figure 8.8.5). Moreover, the performance in the RCA reaction was between those of the phosphoramidate and triazole backbone linkages. However, RCA products generated from cyclic **1**_Am with size distribution between 1 - 2 kb were observed. This is possibly due to the lower processivity and strand displacement activity of the Bst 2.0 DNA polymerase which led to it producing shorter DNA strands (Figure 4.34).

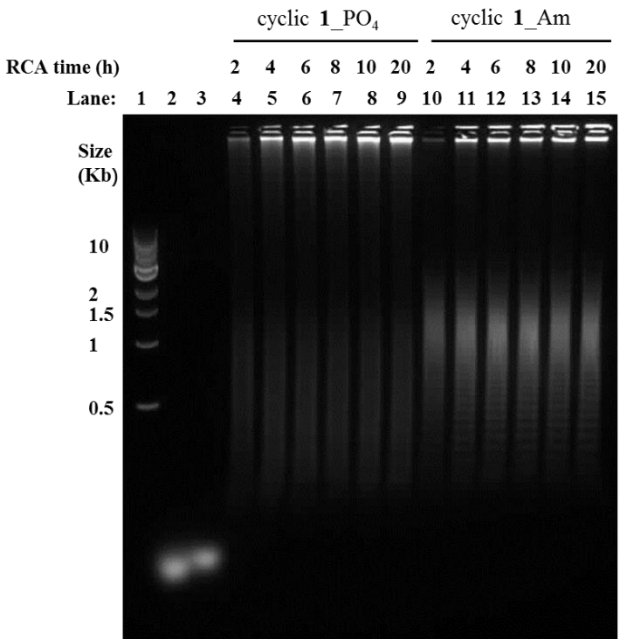


Figure 4.34. 0.8% agarose gel analysis of original RCA reaction mixtures from cyclic **1**_PO_4 and cyclic **1**_Am. The RCA was carried out in the presence of 20 mM Mg^{2+} at different time courses using Bst 2.0 DNA polymerase. Lane 1: 1 kb DNA ladder; Lane 2: RCA primer ODN4-1 for cyclic **1**_PO_4; Lane 3: RCA primer ODN4-5 for cyclic **1**_Am.

After that, we also employed the complementary fluorescent oligonucleotide method to probe the single-stranded RCA products generated from Bst 2.0 DNA polymerase catalysed RCA reactions. Template **1** (all four versions) was used as an example here. Unfortunately, there was no fluorescent signal observed under the Cy3 fluorescence channel. One possible explanation is that a lower quantity of single-stranded RCA products was generated when the RCA reactions performed using this alternative DNA polymerase. Based on above results, we therefore only carried out further investigations on the findings presented in Figure 4.31 using the fluorometric plate-reading assay (see Section 4.5.2.1 below).

4.5.2.1 Probing the nature and quantity of the RCA products *via* a fluorometric plate-reading assay

In order to corroborate the above findings from the gel images (Figure 4.31), we again carried out fluorometric plate-reading experiments to compare the RCA rates and product yields. The RCA reactions were performed using cyclic **1**_PO_4, cyclic **1**_Tz, cyclic **4**_PO_4 and cyclic **4**_Tz over a ten-hour time course. After the desired amplification time, the RCA reactions were stopped by heat inactivation of the DNA polymerase using a recommended temperature provided by the supplier. The samples from each time point were then measured using three DNA-binding dyes: SYBR Gold, SYBR Green I and SYBR Green II.

In the Bst 2.0 DNA polymerase catalysed RCA reactions, the measured fluorescence intensities from triazole-modified cyclic **4**_Tz were significantly stronger than from the unmodified control cyclic **4**_PO_4 after six hours amplification time in the presence of all three DNA-binding dyes, but weaker than its unmodified control at the beginning of RCA reaction (Figure 4.35A). This result revealed that a relatively higher quantity of DNA was generated after a longer amplification time when using the triazole-modified cyclic template, which is consistent with the previous gel results (Figure 4.31).

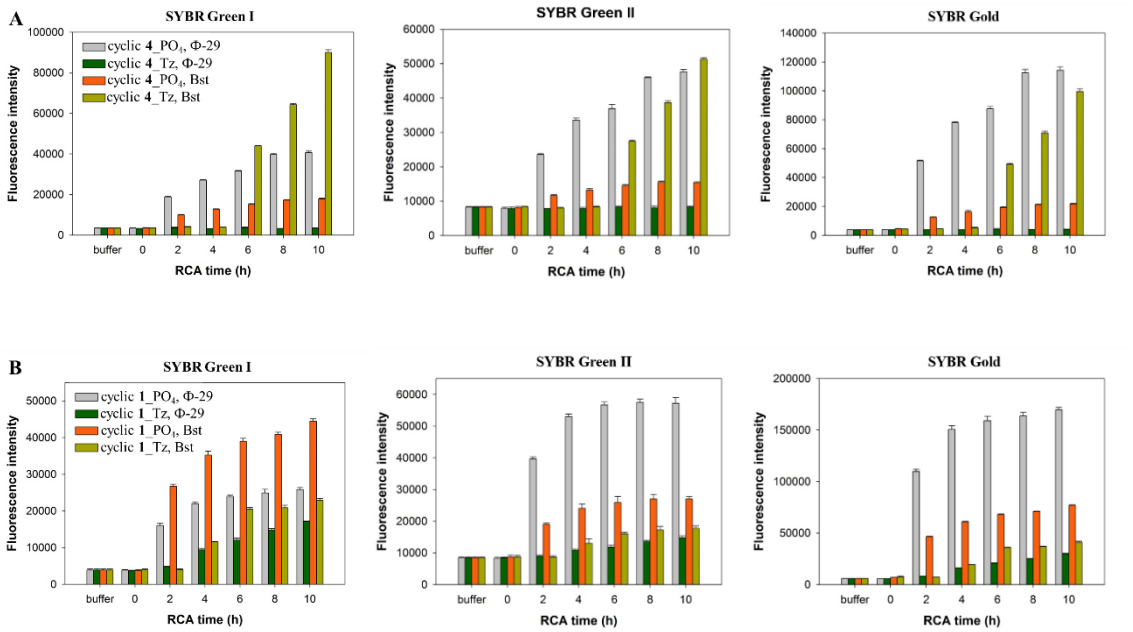


Figure 4.35. Fluorescence quantification of amplified DNA products from RCA reactions using cyclic templates ((A) cyclic **4**_PO_4 and cyclic **4**_Tz; (B) cyclic **1**_PO_4 and cyclic **1**_Tz) and DNA polymerase over a 10-hour time course. The performance of the Bst 2.0 and Φ-29 DNA polymerases were compared. EDTA was added to break down the precipitate releasing the extended RCA products before incubation with three different DNA-binding dyes: SYBR Green I, SYBR Green II and SYBR Gold. Error bars indicate the standard deviation of three measurements taken from a single RCA reaction. The reactions were also repeated, and the same trends were observed.

Moreover, the modified triazole backbone linkage slowed the reaction rate at the beginning of RCA reaction suggesting that the Bst 2.0 DNA polymerase has greater difficulty repeatedly reading through this artificial backbone linkage. In terms of the unmodified control and triazole-containing cyclic **1**_PO_4 and cyclic **1**_Tz, the measured fluorescence intensities given by cyclic **1**_PO_4 were consistently higher than that of from the cyclic **1**_Tz at each time course for the RCA reactions performed using Bst 2.0 DNA polymerase (Figure 4.35B).

It is noteworthy that in all four RCA reactions the Bst 2.0 DNA polymerase produced a higher proportion of double-stranded side-products than the Φ-29 DNA polymerase, suggesting inferior processivity and strand displacement activity of Bst 2.0 DNA

polymerase. In addition, the results also demonstrated that all unmodified cyclic templates again gave higher fluorescence intensities than their triazole-containing cyclic template counterparts when the RCA reactions were performed using Φ-29 DNA polymerase.

4.6 Nanoflower formation

It is well known that the long RCA products can spontaneously self-assemble into densely-packed DNA-inorganic hybrid nanoflower structures in the presence of magnesium pyrophosphate crystals.[174,234,235,238,282] During the RCA process, a pyrophosphate anion is released when the polymerase incorporates each nucleotide. The pyrophosphate anions then co-crystallise with both the growing DNA strands and magnesium ions to generate the DNA-NFs. These DNA-NFs structures have several advantages which have driven research into their application as potential diagnostic and therapeutic agents, including (1) they are readily to prepare compared with other DNA nanostructures relying on Watson-Crick base paring between short DNA building blocks; (2) they are size-tuneable; (3) they are biodegradable, but the DNA component is more stable than a free oligonucleotide against digestion by exonuclease enzymes; (4) they can be fabricated to incorporate functionalities such as aptamers, restriction enzymes, siRNA, DNAzymes or drug-loading moieties for targeted recognition and drug delivery; (5) they are capable of cellular transfection.[234,238,239,241,265,283] However, the scale on preparing the DNA-NFs is a major limitation, as the enzymatic cyclisation of the linear DNA strand can be inefficient or problematic. We investigated whether the cyclic templates generated using chemical cyclisation methods, incorporating an artificial backbone linkage, would address this limitation. Here, we showed for the first time that cyclic oligonucleotide

templates containing artificial backbone linkages can be used as substrates in the RCA process to prepare DNA-NFs (Figure 4.36).

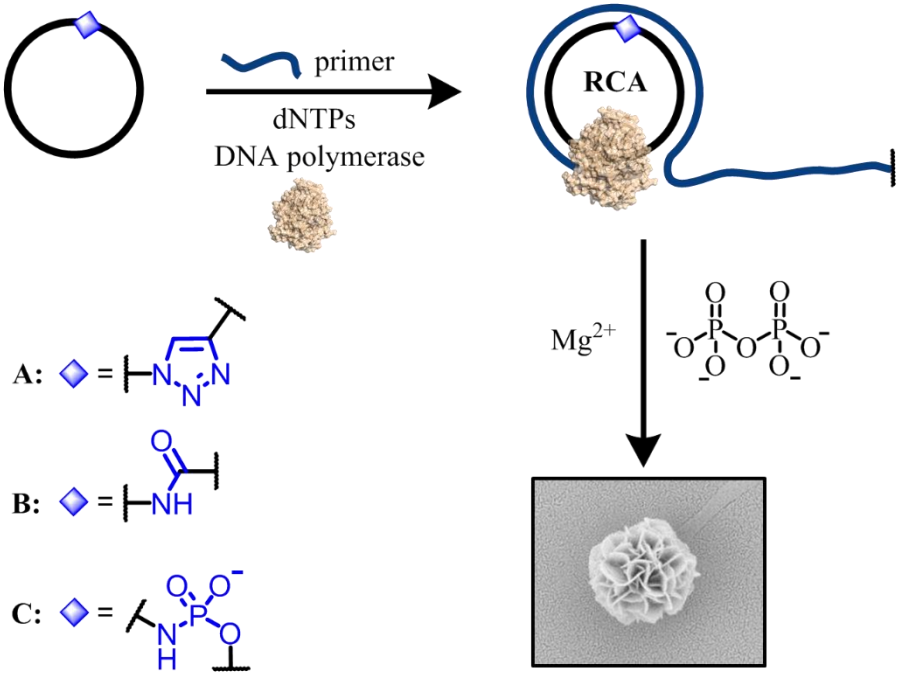


Figure 4.36. The cyclic templates containing three artificial backbone linkages (triazole, amide or phosphoramidate) were used in rolling circle amplification and DNA nanoflower formation.

We investigated the effect of backbone modification on DNA-NF formation. In order to determine whether the slower rate of read through would affect the morphology of the resulting products, DNA-NFs were isolated from RCA reactions, which were carried out using Φ-29 DNA polymerase and cyclic **1**_PO_4, cyclic **1**_Tz, cyclic **1**_Am and cyclic **1**_PA after an eight- or twenty-hour incubation times. The samples were heated to inactivate the DNA polymerase, the precipitates were collected by centrifugation, thoroughly washed with MilliQ water, and dried prior to analysis. SEM imaging experiments were then used to map the size and morphology of the formed DNA-NFs.

SEM imaging revealed no significant differences in the size and morphology of the DNA-NFs generated from the four types of the cyclic template, even though the RCA reaction

with the triazole-containing cyclic template was less efficient. The diameters of the DNA-NFs in all cases were over 1 μm with petal-like surface morphologies. As expected, the size of the DNA-NFs significantly increased after a twenty-hour RCA reaction in comparison with eight hours amplification time (Figure 4.37).

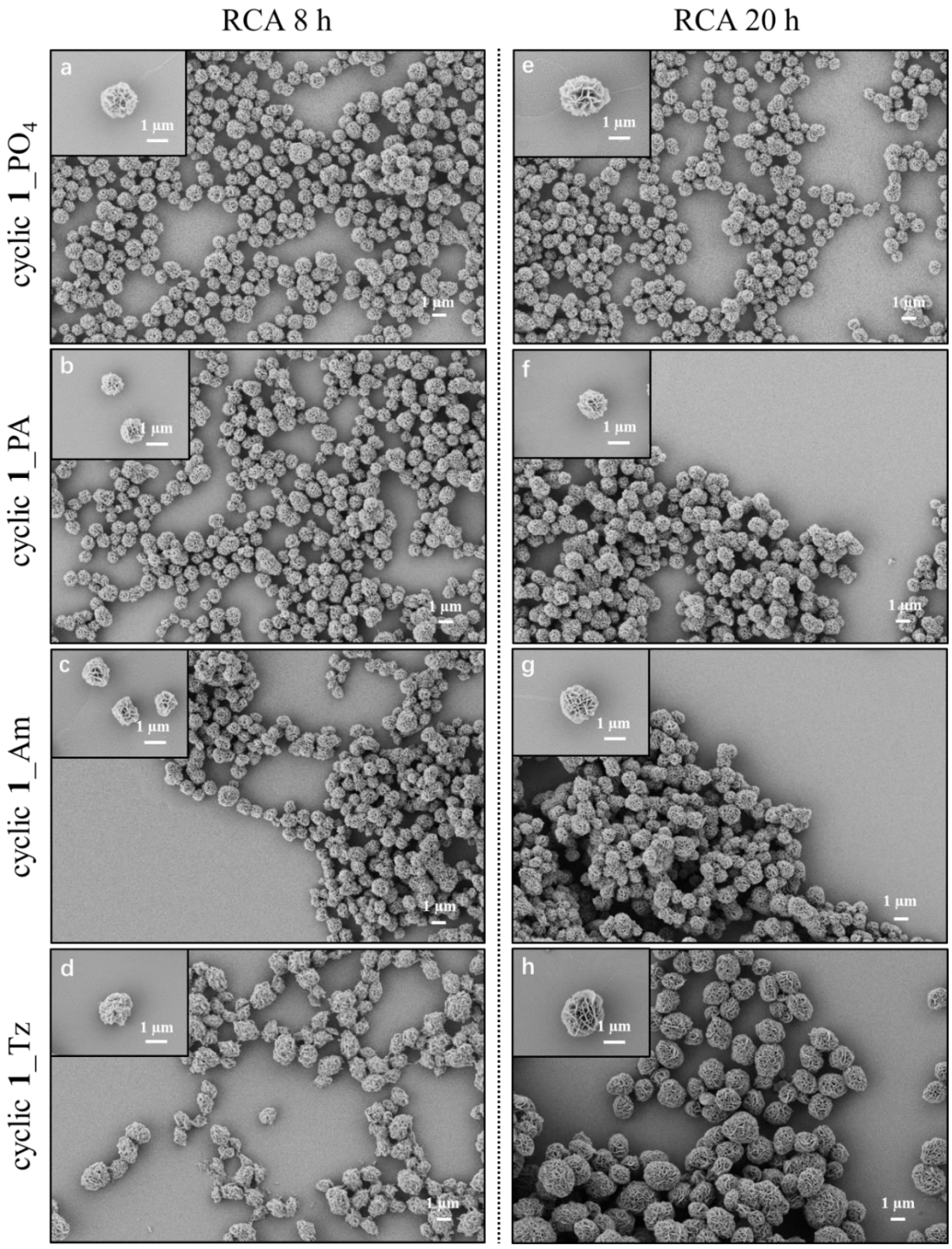


Figure 4.37. SEM images of the DNA-NFs generated from RCA of cyclic **1**_PO_4, cyclic **1**_PA, cyclic **1**_Am and cyclic **1**_Tz using the Φ-29 DNA polymerase in the presence of 20 mM Mg^{2+} after 8 h and 20 h amplification time.

In addition, we also found that the Mg^{2+} concentration has a remarkable effect on the size of the particles. As the Mg^{2+} concentration increased from 10 - 25 mM, the size of the

particles reduced from ~3 μm to ~0.8 μm (Figure 4.38, Appendix Figure 8.9.1 - 8.9.4). Although the reason for the reduction of the DNA-NFs with increasing Mg^{2+} concentration is not clear, we hypothesise that this is due to the higher metal ion concentration, which increases the rate of nucleation, resulting in formation of a higher number of particles with a smaller average diameter.

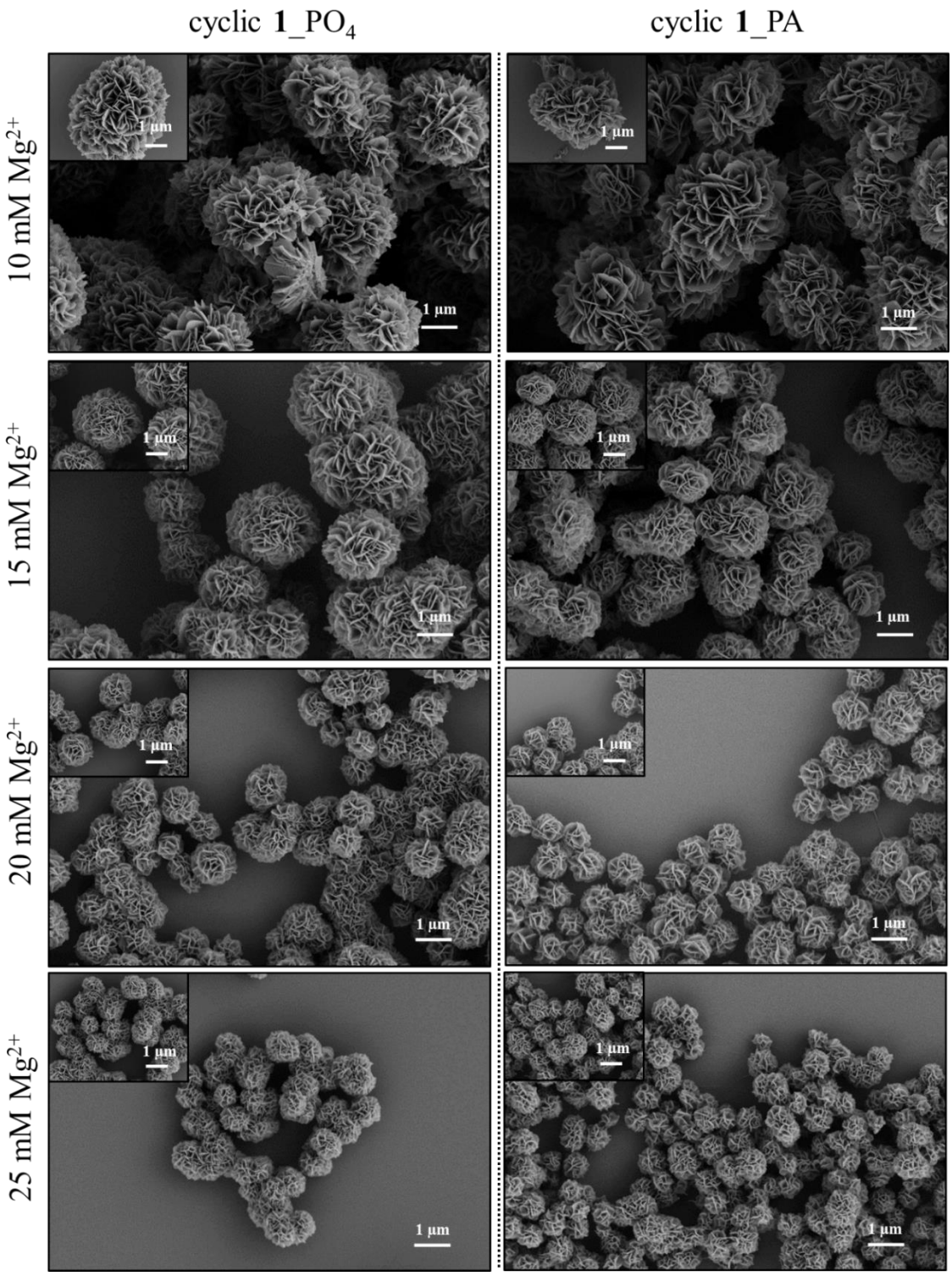


Figure 4.38. SEM images of the DNA-NFs generated from RCA of the cyclic **1**_PO_4 (left) and cyclic **1**_PA (right) using the Φ-29 DNA polymerase in the presence of varying concentration of Mg^{2+}. The RCA reactions were carried out for 20 hours amplification time and the Mg^{2+} concentrations ranged from 10 to 25 mM.

4.7 Conclusions

We have shown that carefully designed linear single-stranded DNA templates can be cyclised using three different chemical cyclisation methods with moderate to excellent efficiency in aqueous solution at RT. The resulting circularised templates contain a single triazole, phosphoramidate or amide unnatural backbone linkage at the ligation point. These chemical ligation methods show several advantages over the more commonly used enzymatic ligation, addressing some of the limitations: (1) they are cheaper to carry out than the enzymatic reaction; (2) they can be performed under mild reaction conditions on a larger scale than enzymatic cyclisation; (3) they can be conducted in the absence of a splint oligonucleotide compared with enzymatic ligation using T4 DNA ligase; (4) they can be carried out under denaturing conditions, solving problems associated with complicated secondary structures.

All four types of cyclic templates were successfully used in RCA, generating long single-stranded DNA. The cyclic templates modified with the phosphoramidate backbone linkage exhibited excellent polymerisation efficiency during RCA. The overall product yields, size distribution and reaction rates were essentially the same as those of the unmodified cyclic templates. In contrast to the phosphoramidate backbone linkage, the triazole-modified cyclic templates showed lower RCA efficiency, varying overall product yields, and were less well tolerated by Φ-29 DNA polymerase. However, for one of the cyclic templates, the Bst 2.0 DNA polymerase was found to read through the template containing the triazole-modified backbone linkage with greater efficiency in comparison to the unmodified control. Furthermore, during the RCA reaction, more double-stranded side-products were generated for the template containing the triazole-modified linkage and this was further confirmed by fluorometric plate-reading assay. In comparison, the

performances of the cyclic templates containing the amide-modified backbone linkage lay between those of the phosphoramidate and triazole linkages.

Having confirmed the biocompatibility of the modified templates, we then showed that these could be successfully used to prepare DNA-NFs. There were no significant differences observed in the size and morphology of the nanoflowers. The Mg^{2+} concentration was found to not only affect the extent of DNA loading in the particles but also to significantly influence the size of the DNA-NFs.

Chapter 5

Conclusions and future work

Chapter 5 – Conclusions and future work

The development of aptamer-functionalised nanostructures is creating new diagnostic and therapeutic opportunities for cancer treatment with the promise of enhanced efficacy and potentially low toxicity. The eventual aim of this work presented herein was to construct DNA superstructures functionalised with aptamer moieties for selective cancer cell recognition, intracellular imaging, anticancer drug delivery and sensing specific mRNAs in cancer cells.

To fabricate the aptamer-integrated superstructures, previously reported HER2 DNA and RNA aptamers were initially evaluated (Chapter 2). In our characterisation studies, only the DNA aptamer (Apt 1) showed specific binding to cancer cells. Moreover, we observed that the binding affinity of 5' Cy3-Apt1 varied between synthetic batches. CD studies were therefore carried out and showed that 5' Cy3-Apt1 forms a parallel G-quadruplex structure in the presence of K^+, but not in Na^+ buffer. Likewise, both UV melting and native PAGE analysis corroborated the results from the CD assays (quadruplex formation). The binding ability of this aptamer was re-assessed by FACS, and the results confirmed that the structure of 5' Cy3-Apt1 affected its binding efficiency to positive cancer cells. Confocal microscopy studies confirmed that 5' Cy3-Apt1 internalised into cells, and fluorescence signals were mostly localised in the perinuclear area. Unexpectedly, this aptamer also exhibited binding affinity for HER1+ cancer cells, suggesting the aptamer studied here binds to both HER1 and HER2 biomarkers, which is in disagreement with the literature.[202]

To expand the functionality of DNA-NFs, we prepared DNA-metal hybrid superstructures in a range of morphologies (Chapter 3). These particles were endowed

with magnetic properties and showed enhanced stability against DNA degradation. They could be enzymatically prepared using different divalent cations such as Mn^{2+} and Co^{2+}. During the RCA process, the metal ions co-crystallised with both pyrophosphate anions and the growing DNA, creating a novel class of nanomaterials. By substituting more commonly used Mg^{2+} with Mn^{2+} or Co^{2+} in the amplification buffer, we showed that it is possible to change the inorganic core of DNA-NFs and control their size and morphology. By altering the polymerase enzyme, it is also possible to further control the morphology of the particles. In addition, under certain conditions, the resulting nanomaterials have the ability to selectively bind to their intended complementary target sequence. Having now developed modified DNA-metal hybrid superstructures, future studies will focus on the applications of these DNA-metal hybrid particles, for example, DNA-Mn hybrid particles could possibly be utilised as MRI contrast agent for cell tracking.

After successful characterisation of several aptamers in chapter 2, Apt1 was chosen for further studies. Its complementary sequence was introduced into a cyclic DNA construct, which served as a substrate template in RCA reactions to generate DNA-NFs (Chapter 4). In order to obtain the cyclic template in high yield for utilisation in RCA reactions, we designed a variety of linear single-stranded DNA templates functionalised with reactive groups at the 5'-and 3'-ends and successfully cyclised them with moderate to excellent efficiency using three different chemical methods. The resulting circularised templates contained a single unnatural triazole, phosphoramidate or amide linkage at the point of ligation. These chemical ligation approaches have several advantages over the more limited enzymatic method; they are cheaper and easier to carry out, allowing for the large-scale synthesis and purification of the cyclic products; the cyclisation reactions can be performed under mild conditions in the absence of a splint oligonucleotide and under denaturing conditions, solving problems associated with complicated secondary

structures. The chemical cyclisation methods therefore provide a versatile expanded toolkit for the preparation of cyclic oligonucleotides. We also investigated the use of the chemically modified cyclic products as templates for the generation of long single-stranded DNA concatamers *via* the RCA reaction. The cyclic templates containing a phosphoramidate backbone linkage exhibited excellent copying efficiency during RCA – with overall yields, nanoconstruct size distribution and reaction rates indistinguishable from those of the unmodified cyclic controls. In contrast to the phosphoramidate backbone linkage, triazole-modified cyclic templates showed lower RCA efficiency, varying overall product yields, and were less well tolerated by the Φ-29 DNA polymerase. However, for one of the cyclic templates, Bst 2.0 DNA polymerase was found to read through the triazole-containing template with greater efficiency compared to the unmodified analogue, suggesting that combining chemical cyclisation approaches and polymerase enzymatic copying might find application where RCA proves challenging. In comparison, the performance of the cyclic templates containing an amide-modified backbone linkage lay in between those of the phosphoramidate and triazole linkages. Having confirmed the biocompatibility of the modified cyclic templates, we then successfully employed them to prepare DNA-NFs. The results confirmed that there were no significant differences observed in the size and morphology of the nanoparticles generated from the different cyclic templates. Future studies on the applications of DNA-NFs such as modifying the nanoflowers with various functional moieties including fluorescent tags, drugs and photosensitisers are planned. The obtained multivalent DNA-NFs have the potential for selective cancer cell recognition, intracellular imaging and anticancer drug delivery.

Chapter 6

Experimental

Chapter 6 – Experimental

6.1 General information

All chemicals were purchased from Sigma-Aldrich, Alfa Aesar and Fisher Scientific unless otherwise specified and used without further purification. SKBR-3 (HER2+, human breast cancer) cell line was purchased from American Type Cell Culture (ATCC, USA). MDA-MB-468 (HER1+, human breast cancer) and MCF-7 (HER1- and HER2-, human breast cancer) cell lines were kindly provided by Prof. Robert Carlisle (The Institute of Biomedical Engineering, University of Oxford). Cell culture medium, Dulbecco's Phosphate Buffered Saline (DPBS) and fetal bovine serum (FBS) were purchased from Gibco. T4 DNA ligase was purchased from Promega. NxGen Φ-29 DNA polymerase was purchased from Lucigen. Bst 2.0 DNA polymerase, T4 gene 32 protein, deoxynucleotides (dNTPs) solution mix and Quick-Load® Purple 1 kb DNA ladder were purchased from New England Biolabs (UK). Scanning electron microscopy (SEM) consumables were purchased from Agar scientific and used without further treatment. NAP-10 and NAP-25 columns were purchased from G.E. Healthcare Life Sciences. 96-well black, polystyrene, microplates were purchased from Greiner Bio-one. SYBR Gold Nucleic Acid Gel Stain, SYBR Green I Nucleic Acid Gel Stain and SYBR Green II RNA Gel Stain were purchased from ThermoFisher.

RP-HPLC columns used in oligonucleotides purification:

Phenomenex Luna® 10 μm C8 100Å, 10 × 250 mm

ACE® 10 μm C8 100Å, 10 × 250 mm

General biological buffers and solutions

Table 6.1. The buffers and solutions used were as follows:

Buffer	Composition
10× Tris/borate/EDTA (TBE, 1 L)	Tris base (108 g, 0.9 M), boric acid (55 g, 0.9 M), ethylenediaminetetraacetic acid (9.2 g, 31 mM)
10× Potassium phosphate buffer	PO_4^{3-} (100 mM), potassium chloride (1 M), pH 7.2
10× PBS	Sodium chloride (80 g), potassium chloride (2 g), disodium hydrogen phosphate (11.5 g), dihydrogen potassium phosphate (2 g), total volume 1 L, pH 7.3
Tris-HCl buffer	Tris base (200 mM), pH 7.0 - 9.0
PIPES-NaOH buffer	PIPES (200 mM), pH 7.5
HEPES-NaOH buffer	HEPES (200 mM), pH 7.0 and pH 7.5
Solution I	Sucrose (40% w/v) in MilliQ water
10× T4 ligase reaction buffer (Promega)	Tris-HCl (300 mM), magnesium chloride (100 mM), dithiothreitol (100 mM), adenosine triphosphate (10 mM), pH 7.8 at 25 °C
10× phi29 DNA polymerase reaction buffer (Lucigen)	Tris-HCl (500 mM), magnesium chloride (100 mM), ammonium sulfate (100 mM), dithiothreitol (40 mM), pH 7.5 at 25 °C
10× Bst 2.0 DNA polymerase reaction buffer (NEB)	Tris-HCl (200 mM), ammonium sulfate (100 mM), potassium chloride (500 mM), magnesium sulfate (20 mM), 1% Tween 20, pH 8.8 at 25 °C

6.2 Oligonucleotides synthesis and purification

6.2.1 General methods for synthesis and purification of linear oligonucleotides

Linear DNA oligonucleotides synthesis

DNA oligonucleotides were synthesised on an Applied Biosystems 394 automated DNA/RNA synthesiser using a standard 0.2 μmol or 1.0 μmol phosphoramidite cycle of acid-catalysed detritylation, coupling, capping and iodine oxidation. DNA phosphoramidites and reagents were purchased from Link Technologies, Applied Biosystems Ltd or Glen Research. Unless otherwise stated the syntheses were performed using 1000 Å controlled pore glass (CPG) solid supports with a particle size of 110 μm and nucleoside loading of 25 - 40 μm/g, purchased from Link technologies. Except where stated, standard β-cyanoethyl phosphoramidite monomers (benzoyl-dA, isobutylryl-dG, benzoyl-dC and dT) were used throughout. During the synthesis of the 3′-carboxy functionalised oligonucleotides, acetyl-dC was used in place of benzoyl-dC. Terminal 5′ phosphate modification was added using the commercially available phosphoramidite monomer 2-[2-(4,4′-dimethoxytrityloxy)ethylsulfonyl]ethyl-(2- cyanoethyl)-(N,N-diisopropyl)-phosphoramidite. Terminal 5′ amino dT modifications were added using the commercially available phosphoramidite monomer 5′-monomethoxytritylamino-2′-deoxythymidine,3′-[(2-cyanoethyl)-(N,N-diisopropyl)]-phosphoramidite, purchased from Glen research. Terminal 5′-azide functionality was introduced by post-synthetic modification of 5′-iodo dT containing oligonucleotides. Terminal 3′ phosphate modifications were incorporated using commercially available, pre-packed 3′ phosphate SynBase^{TM} CPG 1000/110 columns, purchased from Link technologies. Terminal 3′ alkyne functionality was introduced using a 3′ propargyl dC or 3′ propargyl 5-methyl dC functionalised CPG resin, prepared as described in the literature reported previously in

our group.[119] Terminal 5′ or 3′ Cyanine 3 modifications were incorporated using commercially available Cyanine 3 phosphoramidite or Cyanine 3 CPG, respectively. The coupling time for addition of standard A, G, C and T monomers was set to 60 seconds. For addition of above-mentioned modified monomers, the coupling time was extended to 600 seconds or 10 min. Stepwise coupling efficiencies and overall yields were monitored using the instrument's in-built automated trityl cation conductivity measurement facility, and in all cases were >98%.

Except where stated the oligonucleotides were cleaved from the solid support and deprotected by exposure to concentrated aqueous ammonia solution at RT for 60 min followed by heating in a sealed glass vial at 55 °C for 5 h. The aqueous solution of ammonia was then removed by evaporation prior to oligonucleotide purification.

Linear RNA oligonucleotides synthesis

RNA oligonucleotides were synthesised on an Applied Biosystems 394 automated DNA/RNA synthesiser using a standard 0.2 μmol or 1.0 μmol RNA phosphoramidite cycle of acid-catalysed detritylation, coupling, capping and iodine oxidation. The building blocks for RNA analogues were prepared using 2′-*O*-*tert*-butyldimethysilyl (TBDMS) protected RNA phosphoramidite monomers with *t*-butylphenoxyacetyl protection of the A, G and C nucleobases and unprotected uracil. A solution of 0.3 M benzylthiotetrazole in acetonitrile (Link Technologies) was used as the coupling agent, *t*-butylphenoxyacetic anhydride as the capping agent and 0.1 M iodine as the oxidising agent. All RNA phosphoramidite monomers were dissolved in anhydrous acetonitrile to a concentration of 0.1 M immediately prior to use, and the coupling time for all monomers was 6 min. Stepwise coupling efficiencies and overall yields were monitored using the instrument's in-built automated trityl cation conductivity measurement facility, and in all

cases were >97%. Cleavage of oligonucleotides from the solid support and deprotection were performed by exposure to concentrated aqueous ammonia/ethanol (3:1 v/v) and heated at 55 °C for 2 - 4 h in a sealed glass vial. RNA oligonucleotide solutions were concentrated using CentriVap Concentrator and then lyophilised. The dry RNA was dissolved in DMSO (300 μL) and triethylamine trihydrofluoride (300 μL) was then added. The reaction mixture was incubated at 65 °C for 2.5 h, after which sodium acetate (3 M, 50 μL) and butanol (3 mL) were added with vortexing. The mixed solution was kept at -80 °C for at least 1 h, and then centrifuged for 30 min at 4 °C and 8500 RPM. The supernatant was discarded, and the RNA precipitate was washed twice with ethanol (2 × 0.75 mL) followed by freeze drying prior to oligonucleotide purification.

Linear oligonucleotide purification and characterisation

The oligonucleotides were purified by reverse-phase high performance liquid chromatography (RP-HPLC). All 5′ amino functionalised oligonucleotides were purified on a Shimadzu LC-20AP HPLC system with a Waters XBridge OST C18 column (particle size: 2.5 μm; pore size: 100 Å; column dimensions: 1.9 × 50 mm). The following elution buffers were used: buffer A: 0.1 M triethylammonium acetate$_{(aq)}$; buffer B: 0.1 M triethylammonium acetate$_{(aq)}$ containing 20% CH_3CN; gradient 30 - 70% buffer B over 9 min. The flow rate was 15 mL/min. The elution of oligonucleotides was monitored by UV absorption at 260 nm. The pure fractions were combined, evaporated and desalted using a NAP-25 column followed by a NAP-10 column. All other oligonucleotides were purified on a Gilson system using a Luna or ACE 10 μm C8 100 Å pore Phenomenex 10 × 250 mm column with a gradient of acetonitrile in triethylammonium bicarbonate (TEAB) increasing from 0% to 50% buffer B over 20 min with a flow rate of 4 mL/min (buffer A: 0.1 M TEAB, pH 7.5, buffer B: 0.1 M TEAB, pH 7.5 with 50% acetonitrile).

The elution of oligonucleotides was monitored by UV absorption at 298 nm. After HPLC purification, the oligonucleotides were freeze dried and then re-dissolved in MilliQ water without the need for further de-salting.

All oligonucleotides were characterised by negative-mode UPLC-mass spectrometry using either a Bruker micrOTOFTM II focus ESI-TOF mass spectrometer with an Acquity UPLC system, equipped with a Ethylene Bridged Hybrid (BEH) C18 column (particle size: 1.7 μm; pore size: 130 Å; column dimensions: 2.1 × 50 mm; Waters) or a Waters Xevo G2-XS QT of mass spectrometer with an Acquity UPLC system, equipped with an Acquity UPLC oligonucleotide BEH C18 column (particle size: 1.7 μm; pore size: 130 Å; column dimensions: 2.1 × 50 mm). Data were analysed using Waters MassLynx software or Waters UNIFI Scientific Information System software.

Further details of the syntheses of the linear chemically modified DNA oligonucleotides are detailed below.

Synthesis of 5′-phosphate oligonucleotides. Terminal 5′ phosphate modifications were added using a commercially available 2-[2-(4,4′-dimethoxytrityloxy)ethylsulfonyl]ethyl-(2-cyanoethyl)-(N,N-diisopropyl)-phosphoramidite, purchased from Link technologies, using an extended coupling time of 600 seconds. The oligonucleotides were cleaved from the solid support, deprotected and purified as described above.

Synthesis of 3′-alkyne-5′-azide oligonucleotides. 5′-*O*-(4,4′-Dimethoxytrityl)-3′-*O*-propargyl-deoxycytidine or 5′-*O*-(4,4′-dimethoxytrityl)-3′-*O*-propargyl-5-methyldeoxycytidine on polystyrene solid support, prepared as described above,[119] was packed into a twist column (Glen Research) and used to synthesise the required sequences in the 3′- to 5′-direction (standard phosphoramidite oligonucleotide synthesis) with 5′-

iodo dT as the final nucleotide. The 5′-iodo dT modification was introduced either using a commercially available 5′-iodo-2′-deoxythymidine, 3′-[(2-cyanoethyl)-(N,N-diisopropyl)]-phosphoramidite, purchased from Glen research or through converting 5′-hydroxyl to 5′-iodo. For conversion of 5′-hydroxyl to 5′-iodo, a solution of methyltriphenoxyphosphonium iodide ($[MeP(OPh)_3]^+I^-$， 0.5 M) in dry DMF (1 mL) was prepared before periodically passing the reagent solution through the oligonucleotide synthesis column using two 1 mL syringes over 30 min at RT. The column was then washed with dry DMF (3 × 1 mL). To convert the 5′-iodo dT to 5′-azido dT, sodium azide (20 mg) was suspended in dry DMF (1 mL) and heated at 70 °C for 20 min followed by cooling down to RT. The supernatant was taken up into a 1 mL syringe, passed back and forth through the column periodically, and then left at 55 °C for 5 h. The column was washed with DMF (3 × 1 mL) followed by acetonitrile (3 × 1 mL) and dried by the passage of a stream of argon gas. The resultant 5′-azide oligonucleotide was cleaved from the solid support, deprotected and purified as described above.

Synthesis of 5′-amino-3′-phosphate oligonucleotides. Oligonucleotides were synthesised on commercially available, pre-packed 3′ phosphate SynBaseTM CPG 1000/110 columns, purchased from Link technologies. The terminal 5′ amino dT modification was added using the commercially available phosphoramidite monomer 5′-monomethoxytritylamino-2′-deoxythymidine,3′-[(2-cyanoethyl)-(N,N-diisopropyl)]-phosphoramidite, purchased from Glen research, using an extended coupling time of 600 seconds. During addition of the final 5′ amino dT nucleotide the acetic anhydride capping step was omitted from the synthesis cycle in order to avoid acetylation of the amino group. The oligonucleotide was cleaved from the solid support, deprotected and purified according to the general procedure described above.

Synthesis of 5′-amino-3′-carboxy oligonucleotides. In order to introduce the terminal 3′ carboxylic acid functionality, oligonucleotides were synthesised on a 3′ carboxy dT functionalised polystyrene resin, prepared as described above.[128] During oligonucleotide synthesis the use of benzoyl-protected dC phosphoramidite was avoided in favour of acetyl-dC, because benzoyl dC is known to undergo a deamination side-reaction under the sodium hydroxide mediated deprotection conditions used in this procedure. The terminal 5′ amino dT modification was added using the commercially available phosphoramidite monomer 5′-monomethoxytritylamino-2′-deoxythymidine,3′-[(2-cyanoethyl)-(N,N-diisopropyl)]-phosphoramidite, purchased from Glen research, using an extended coupling time of 600 seconds. Prior to the addition of this final nucleotide the resin was treated with a 20% v/v solution of di-isopropylethylamine in acetonitrile for 15 min, washed three times with acetonitrile and dried under a stream of argon. During addition of the final 5′ amino dT nucleotide the acetic anhydride capping step was omitted from the synthesis cycle in order to avoid acetylation of the amino group. The resin was then treated with 0.5 mL of a solution 0.4 M of NaOH in MeOH:H_2O 4:1 v/v for 6 h at RT. At this point 0.5 mL of a solution 0.4 M of NaOH in MeOH:H_2O 1:4 v/v was added, to give a 0.4 M solution of NaOH in MeOH:H_2O 1:1 v/v. The mixture was allowed to stand at RT for a further 40 h before being neutralized by addition of 1 mL of triethylammonium acetate buffer (1 M, pH 7.4), concentrated on a rotary evaporator and desalted using a NAP-25 column. To ensure complete cleavage of all isobutyryl protecting groups, the product was taken up in concentrated aqueous ammonia and heated at 55 °C for 2 - 5 h in a sealed glass vial. After concentration of the aqueous ammonia solution in vacuo the oligonucleotide was purified according to the general procedure described above.

Synthesis of 5′-Cyanine 3 oligonucleotides. Terminal 5′-Cyanine 3 modification was added using a commercially available 2-((1E,3E)-3-(1-(3-(((2-cyanoethoxy)(diisopropylamino)-phosphino)oxy)propyl)- 3,3-dimethylindolin-2-ylidene)prop-1-en-1-yl)- 1-(3-((4-methoxyphenyl)diphenylmethoxy)propyl)-3,3-dimethyl- 3H-indol-1-ium chloride–phosphoramidite monomer, purchased from Link technologies, using an extended coupling time of 10 min. The oligonucleotides were cleaved from the solid support, deprotected and purified as described above.

Synthesis of 3′-Cyanine 3 oligonucleotides. Terminal 3′-Cyanine 3 modification was incorporated using commercially available, pre-packed 3′ Cyanine 3 SynBase^{TM} CPG 1000/110 columns, purchased from Link technologies, using an extended coupling time of 10 min. The oligonucleotides were cleaved from the solid support, deprotected and purified as described above.

Further details of the syntheses of the linear chemically modified RNA oligonucleotides are provided below.

Synthesis of 5′-Cyanine 3 oligonucleotides. Terminal 5′-Cyanine 3 modification was added using a corresponding phosphoramidite monomer, purchased from Link technologies, on the solid-phase oligonucleotide synthesiser. The oligonucleotides were cleaved from the solid support, deprotected and purified as described above.

Synthesis of 2′-fluorine oligonucleotides. 2′-fluorine modification was added using corresponding phosphoramidites (dC and dU), purchased from Glen Research, on the solid-phase oligonucleotide synthesiser. The oligonucleotides were cleaved from the solid support, deprotected and purified as described above.

Quantification of oligonucleotides

The concentration of oligonucleotides was calculated by measuring absorbance at 260 nm with a Varian Cary 50 Bio UV-Vis spectrophotometer (Agilent) at RT in MilliQ water and using the Lambert-Beer equation A (absorbance) = OD (optical density) = εcl (molar extinction coefficient ε obtained from the database of DNA/RNA synthesiser, cuvette length l = 1 cm).

The sequences and length of oligonucleotides used in the following studies are detailed in the appropriate chapters. The mass data of the oligonucleotides are listed below (Table 6.2 and Table 6.3).

Table 6.2. The mass data of the linear oligonucleotides are as follows:

Linear oligonucleotide code	Calc. Mass	Found Mass
Apt1	13326	13326
5′ Cy3-Apt1	13833	13834
3′ Cy3-Apt1	13833	13833
5′ Cy3-Apt2	26777	26779
5′ Cy3-Apt3	17235	17236
5′ Cy3-Apt4	13737	13737
3′ Cy3-Apt4	13737	13737
5′ Cy3-Apt5	11746	11744
5′ Cy3-Apt6	11371	11371
Template 1 (T1)	25597	25598
Template 2 (T2)	25690	25692
Splint (S1)	7724	7723
Splint 2 (S2)	6742	6742
Match probe	5658	5658
Mismatch probe	5658	5659
1_PO_4	15473	15474
1_Tz	15457	15458
1_Am	15451	15450
1_PA	15474	15474
2_PO_4	18964	18966
2_Tz	18948	18949
2_Am	18942	18942
2_PA	18965	18967
3_PO_4	15012	15014
3_Tz	14997	14998
3_Am	14976	14975

3_PA	15014	15013
4_PO_4	23180	23182
4_Tz	23180	23182
ODN4-1	5539	5540
ODN4-2	4939	4941
ODN4-3	5010	5012
ODN4-4	6420	6421
ODN4-5	5507	5507
ODN4-6	5540	5540
ODN4-7	5643	5643
ODN4-8	6030	6030
ODN4-9	6030	6031

Table 6.3. The mass data of the cyclic oligonucleotides are as follows:

Cyclic oligonucleotides codes	Calc. Mass	Found Mass
Cyclic T1	51160	51163
Cyclic T2	51346	51349
Cyclic **1**_PO_4	15456	15458
Cyclic **1**_Tz	15457	15458
Cyclic **1**_Am	15433	15434
Cyclic **1**_PA	15457	15455
Cyclic **2**_PO_4	18947	18949
Cyclic **2**_Tz	18948	18950
Cyclic **2**_Am	18924	18924
Cyclic **2**_PA	18948	18949
Cyclic **3**_PO_4	14995	14996
Cyclic **3**_Tz	14997	14998
Cyclic **3**_Am	14958	14959
Cyclic **3**_PA	14997	14997
Cyclic **4**_PO_4	23163	23163
Cyclic **4**_Tz	23180	23180

6.3 Biophysical studies of aptamers

6.3.1 Structural study of aptamers using circular dichroism

CD spectra were recorded on a Chirascan-plus spectrometer (Applied Photophysics) equipped with a temperature controller (Series 800) using a quartz optical cell with a path length of 2 mm. Oligonucleotides (Apt1 and Apt5, Table 2.1 and Table 2.2, Chapter 2) were prepared at 10 μM in following buffers: PBS containing 153 mM NaCl at pH 7.3

and 10 mM potassium phosphate with 100 mM KCl at pH 7.2. The samples were annealed by heating at 95 °C for 5 min using a block heater and then fast-cooled to RT using ice or by heating at 95 °C for 5 min and then annealing at a cooling rate of 0.5 °C/min to RT. Prior to measurement, the samples were filtered with Kinesis regenerated cellulose 13 mm, 0.45 μm syringe filters. CD spectra were collected at 25 °C, scanning from 200 - 320 nm with a bandwidth of 2.0 nm and a response time of 1.5 seconds. The spectra were obtained by taking the average of four scans with 0.5 nm wavelength increments. A blank sample containing only buffer was used for the baseline correction and the signal contributions of the buffer were subtracted. The molar ellipticity [θ] was calculated according to the equation $[\theta] = \theta/Cl$, where θ is the ellipticity value, C is the molar concentration of oligonucleotides, and l is the path length of the cell in centimetres. Δε was calculated and interconverted using the relationship $[\theta] = 3298.2\ \Delta\varepsilon$, where Δε is the difference in the extinction coefficients for left- and right-handed circularly polarised light.

6.3.2 Structural study of aptamers using native polyacrylamide gel electrophoresis

Aptamer samples (5′ Cy3-Apt1 and 5′ Cy3-Apt5, Table 2.3 and Table 2.4, Chapter 2) were prepared for native PAGE analysis as follows. The samples in MilliQ water were first heated at 95 °C for 5 min using block heater, followed by rapidly cooling on ice for 10 min. Afterwards, the samples were diluted further with various buffers; different conditions investigated are listed below.

Table 6.4. Various conditions investigated for aptamers. In annealing step, 'Fast' corresponds to fast annealing; 'Slow' represents slow annealing. Fast annealing refers to heating at 95 °C for 5 min followed by rapid cooling on ice for 10 min. Slow annealing corresponds to heating at 95 °C for 5 min, followed by cooling at a rate of 0.5 °C/min to RT using a thermal cycler (Bio-Rad, T100^{TM}). Once annealed, samples were kept at 4 °C.

Condition	Aptamer concentration (μM)	Annealing	Buffer
1	40	None	PBS
2	40	Fast	PBS
3	40	Slow	PBS
4	40	None	K_3PO_4
5	40	Fast	K_3PO_4
6	40	Slow	K_3PO_4
7	20	None	PBS
8	20	Fast	PBS
9	20	Slow	PBS
10	20	None	K_3PO_4
11	20	Fast	K_3PO_4
12	20	Slow	K_3PO_4
13	10	None	PBS
14	10	Fast	PBS
15	10	Slow	PBS
16	10	None	K_3PO_4
17	10	Fast	K_3PO_4
18	10	Slow	K_3PO_4

The samples were then diluted to 1 μM using the same buffer as in the annealing step and analysed by native PAGE. 2.5 μL of each sample supplemented with 0.5 μL of 40% (w/v) sucrose in MilliQ water was then loaded onto a 16% polyacrylamide gel (acrylamide: bisacrylamide 19:1, 40% acrylamide solution, prepared using 1× Tris-Borate-EDTA (TBE) buffer supplemented with 20 mM KCl). The gel was run for 100 min at 4 °C using a constant voltage of 120 V and a TBE running buffer supplemented with 20 mM KCl.

The bands of gels were visualised using a G:BOX (Syngene) after staining with SYBR Gold. Band migration and intensities were determined using Genesnap software.

6.3.3 Thermal stability study of aptamers using UV melting

UV melting measurements were carried out on a Varian Cary 4000 UV-VIS spectrophotometer fitted with a Cary temperature controller using a 1 cm path length (Hellma Precision cuvettes made of synthetic quartz glass, QG). Oligonucleotides (5′ Cy3-Apt1, Table 2.3, Chapter 2) were prepared at 2 μM in 10 mM potassium phosphate buffer with 100 mM KCl at pH 7.2. Prior to measurement, all buffers and samples were filtered using Kinesis regenerated cellulose 13 mm, 0.45 μm syringe filters. The samples were initially denatured by heating to 95 °C for 5 min and then allowed to cool to RT over 2 h before measurement. For 5′ Cy3-Apt1 with G-rich sequence, the experiments were conducted by increasing the temperature from 20 °C to 85 °C at a heating rate of 0.2 °C/min with absorbance monitoring at both wavelengths 260 nm and 295 nm recorded every 0.5 °C. The T_m of oligonucleotides were determined through using Cary Win UV thermal application software, and the first derivative of absorption with respect to temperature (dA / dT) of the melting curve was generated and used to calculate the value of T_m. The experiment was performed in four stages. The thermal protocol used was as follows:

Table 6.5. The thermal protocol used for UV melting studies.

Stage	Data Interval (°C)	Rate (°C/min)	End Temp(°C)	Hold Time (min)
1 (Melt 1)	0.50	0.20	85.00	5.00
2 (Anneal 1)	0.50	0.20	20.00	5.00
3 (Melt 2)	0.50	0.20	85.00	5.00
4 (Anneal 2)	0.50	0.20	20.00	5.00

6.4 Cell biology

Tumor cell lines and cultivation

SKBR-3 (HER2+, human breast cancer) cell line was maintained in McCoy′s 5A medium supplemented with 15% (v/v) FBS, whereas MDA-MB-468 (HER1+, human breast cancer) and MCF-7 (HER1- and HER2-, human breast cancer) cell lines were maintained in Dulbecco′s Modified Eagle Medium (DMEM) supplemented with 10% (v/v) FBS. The cell lines were incubated at 37 °C under a humidified atmosphere of 5% CO_2. Experiments were conducted on cells in the exponential growth phase.

Freezing, thawing and long-term storage of cell lines

Cells were harvested with trypsin-EDTA solution in DPBS buffer and resuspended in freezing medium containing 40% DMEM, 50% FBS and 10% DMSO for the MDA-MB-468 cell line or 70% DMEM, 20% FBS and 10% DMSO for the MCF-7 cell line or 90% FBS and 10% DMSO for the SKBR-3 cell line. The cell suspension was immediately transferred into 1 mL cryovials, gradually cooled to -80 °C at a rate of -1 °C/min using isopropanol container overnight and then kept at -80 °C for long-term storage. Cryovials containing cells were rapidly thawed in a 37 °C water bath and then added into 9 mL of growth medium dropwise to reduce exposure to DMSO during the process of cell thawing. The cells were collected by centrifugation (1000 RPM, 5 min, RT) and the supernatant removed prior to resuspending in 15 mL of fresh complete growth medium. The cells were counted and further cultured for experimental use.

Cell counting

50 μL of Trypan-Blue, 100 μL of DPBS and 50 μL of cell suspension were gently mixed. 10 μL of mixed cell solution was then loaded onto a haemocytometer and counted using microscopy. The number of non-blue visible cells was used to calculate the cell concentration using the following formula: cell concentration (cells/mL) = dilution factor × (number of cells in total 4 × 4 grids/4) × 10^4. The final concentration of cells was adjusted to 20 × 10^4 cells/mL or 100 × 10^4 cells/mL diluting with complete growth medium for further experimental use.

6.4.1 Fluorescence-associated cell sorting analysis (FACS)

FACS general method 1

The binding affinity of aptamers was analysed using a BD FACS Calibur cytometer. Prior to the FACS experiment, the cell lines were prepared as follows. Cell lines were split and grown in 15 mL of fresh complete growth medium for 24 h. Afterwards, the medium was removed, and the cells were washed with 5 mL of pre-warmed DPBS. Cells were incubated with 2.5 mL of trypsin-EDTA dissociation solution for 2 min at 37 °C and then gently removed. 10 mL of complete growth medium was added to the cell culture flask and the cells were pelleted by centrifugation (1000 RPM, 5 min, RT). The cells were then resuspended in complete growth medium, counted as outlined above and diluted using cold complete growth medium to give the desired cell suspension density (20 × 10^4 cells/mL). Prior to the FACS experiment, stock solutions of aptamers were prepared as follows. The aptamers were prepared at 20 μM using DPBS containing 1% BSA without any annealing step. 26 μL of 20 μM aptamers were then incubated with 494 μL of cell suspension containing 1% BSA (cell concentration: 20 × 10^4 cells/mL) for 40 min at 4 °C

in the dark. Here, the final incubation concentration of aptamer was 1μM. As a control, 5 μL of the reference Anti-HER2 affibody (FITC) (Abcam, supplied as a 0.38 mg/mL solution in storage buffer), was used in the incubation step in place of the aptamers for each experiment. The supernatant was then removed by centrifugation (2500 RPM, 5 min, RT), the cell pellet was washed once with 500 μL of ice-cold DPBS and collected by centrifugation as presented before. The cells were then resuspended in 500 μL of ice-cold DPBS containing 1% BSA. The fluorescence intensity was measured by counting 10000 events, and data were analysed using CellQuest software. All experiments for the binding assay were repeated at least three times.

Optimising experimental conditions based on FACS general method 1

HER2 aptamers of 5′ Cy3-Apt1 and 5′ Cy3-Apt4 (Table 2.3, Chapter 2), anti-HER2 affibody (FITC) and cell lines (SKBR-3 and MDA-MB-468) were used when optimising the FACS experiments here. The conditions were investigated as described below.

Investigating the binding ability of aptamers with an annealing step

FACS experiments were performed as described in the FACS general method 1. Prior to FACS experiment, aptamers were annealed in the K^+ buffer by heating at 95 °C for 5 min and then annealing at a cooling rate of 0.5 °C/min to RT. The final concentration of the aptamers was adjusted accordingly using DPBS containing 1% BSA in the incubation step. These changes are outlined in Table 6.6.

Table 6.6. Conditions used to investigate the binding affinity of aptamers with an annealing step.

Experiment	Concentration of stock solution used in annealing step	Buffer
A	10 μM	K_3PO_4

FACS general method 2

The binding affinity of the aptamers was quantified by flow cytometry. FACS analysis was performed using a BD FACS Calibur cytometer. Prior to the FACS experiment, the cell lines were prepared as follows. Cell lines were split and grown in 15 mL of fresh complete growth medium for 24 h. Afterwards, the medium was removed. The cells were detached using 2.5 mL of non-enzymatic cell dissociation solution (1×) for 40 min at 37 °C and then gently removed. 10 mL of complete growth medium was added to the cell culture flask and the cells were pelleted by centrifugation (1000 RPM, 5 min, RT). The cells were then resuspended in complete growth medium, counted as outlined above and diluted using cold complete growth medium to give the desired cell suspension density (20×10^4 cells/mL or 100×10^4 cells/mL). Prior to the FACS experiment, stock solutions of aptamers were prepared as follows. The aptamers were prepared at 10 μM in potassium phosphate buffer (1×), heated to 95 °C for 5 min and cooled to RT at a cooling rate of 0.5 °C/min. The desired concentration of aptamers in the incubation step was adjusted accordingly using DPBS. As a control, 5 μL of the reference Anti-HER2 affibody (FITC) (Abcam, supplied as a 0.38 mg/mL solution in storage buffer), was used in the incubation step in place of the aptamers for each experiment. Cells were then incubated with the aptamers at either 4 °C or 37 °C for 40 min in the dark. After incubation with aptamers, the supernatant was then removed by centrifugation (2500 RPM, 5 min, RT). The cell pellet was washed twice with 500 μL of ice-cold DPBS and collected by centrifugation as presented before. The cells were then resuspended in 500 μL of ice-cold DPBS containing 1% BSA. The fluorescence intensity was measured by counting 10000 events, and data were analysed using CellQuest software. All experiments for the binding assay were repeated at least three times.

Optimising experimental conditions based on FACS general method 2

HER2 aptamers of 5′ Cy3-Apt1, 5′ Cy3-Apt4, 5′ Cy3-Apt5 and 5′ Cy3-Apt6 (Table 2.3 and Table 2.4, Chapter 2), anti-HER2 affibody (FITC) and cell lines (SKBR-3 and MDA-MB-468) were used when optimising the FACS experiments here. The conditions were investigated as described below.

Investigating the effect of aptamer concentration on HER2 binding

FACS experiments were performed as described in the FACS general method 2, varying the concentration of the aptamers. The desired concentration of aptamers was adjusted accordingly using DPBS containing 1% BSA in the incubation step. Cells were incubated with the aptamers at 4 °C for 40 min in the dark. The cell incubation mixtures were then gently shaken every 5 min. These changes are outlined in Table 6.7.

Table 6.7. Conditions used to investigate the effect of aptamer incubation concentration.

Experiment	Final concentration of aptamers
B	1 μM
C	5 μM
D	8 μM

Investigating the effect of incubation temperature on FACS experiments

FACS experiments were performed as described in the FACS general method 2. Cells were incubated with the aptamers at a concentration of 8 μM and at either 4 °C or 37 °C for 40 min in the dark. The cell incubation mixtures were then gently shaken every 5 min. The conditions are described in the Table 6.8.

Table 6.8. Conditions used to investigate the effect of incubation temperature.

Experiment	Temperature
E	4 °C
F	37 °C

Investigating the optimum washing step on FACS experiments

FACS experiments were performed as described in the FACS general method 2. Cells were incubated with the aptamers at the concentration of 8 μM and 37 °C for 40 min in the dark. The cell incubation mixtures were then gently shaken every 5 min. After incubation, the cells were washed 2, 6 or 10 times using 500 μL of ice-cold DPBS, pelleting the cells by centrifugation (2500 RPM, 5 min, RT) each time (Table 6.9).

Table 6.9. Investigating the effect of number of washing steps on FACS experiments.

Experiment	Number of washing steps
G	2
H	6
I	10

Comparing new and old batches of MDA-MB-468 cell line

FACS experiments were performed as described in the FACS general method 2. MDA-MB-468 (new batch) cell line was used. Cells were incubated with 5′ Cy3-Apt1 (Table 2.3, Chapter 2) at the concentration of 1 μM and temperature either 4 °C or 37 °C for 40 min in the dark. This was experiment J.

Investigating aptamer binding properties for MCF-7 cell line

FACS experiments were performed as described in the FACS general method 2. HER2 aptamers of 5′ Cy3-Apt1 and 5′ Cy3-Apt4 (Table 2.3, Chapter 2), and cell line (MCF-7) were used. Cells were incubated with aptamers (1 μM of final concentration) at temperature either 4 °C or 37 °C for 40 min in the dark. This was experiment K.

6.4.2 Confocal microscopy imaging of cancer cells bound with Cy3 labelled aptamer

Cells were seeded in 35 mm glass bottom culture dishes (Greiner Bio-One). After 48 h of cell growth (30 - 40% confluence), the cells were washed with pre-warmed DPBS, and then incubated with various concentrations of aptamer (1 μM, 5 μM or 8 μM) in complete growth media at 37 °C for 40 min. After incubation, the cells were washed three times with 500 μL of ice-cold DPBS to remove unbound aptamer followed by adding 500 μL of ice-cold DPBS containing 1% BSA. Confocal imaging was performed on a Zeiss LSM 780 confocal microscope using a 63× oil objective (laser 543 for Cy3). The images were obtained using ZEN 2.1 acquisition software.

6.5 Preparation of manganese and cobalt DNA nanoflowers

General procedure for denaturing PAGE

The DNA samples were mixed with an equal volume of formamide and denatured by heating at 95 °C for 5 min. The mixture was cooled quickly on ice, and then loaded onto denaturing PAGE gel (acrylamide:bisacrylamide 19:1, 40% acrylamide solution, 7 M urea, prepared in a 1× TBE buffer). The gel was run at 20 W for the desired time period (2 - 3 h) in 1× TBE buffer at RT. Gels were visualised using a G:Box gel documentation

system (Syngene). The cyclised oligonucleotide bands were excised, crushed and soaked in MilliQ water (10 - 15 mL) overnight at 37 °C with shaking. After filtration and evaporation of the MilliQ water, the cyclised oligonucleotides were desalted using NAP-25, followed by a NAP-10 column. The concentration of cyclised oligonucleotides was measured by using a UV-Vis spectrophotometer (Cary, model 50 Bio, Varian, Australia).

General procedure for agarose gel electrophoresis

The RCA products were analysed using a 0.8% (w/v) agarose gel with the addition of 0.5× SYBR Gold. 7.5 μL of sample was mixed with 2.5 μL of 5× GoTaq® Green buffer (Promega) before loading onto the gel. The gel was run at RT (126 V) in 1× TBE buffer and imaged using a G:Box (Syngene).

6.5.1 Screening experiments

Prior to experiments, 200 mM buffer stock solutions were prepared including PIPES pH 7.5, HEPES pH 7.0, HEPES pH 7.5, Tris pH 7.0, Tris pH 7.5, Tris pH 8.0, Tris pH 8.5, Tris pH 9.0. Stock solutions of $MnCl_2$ including 16.7 mM, 33.3 mM and 50 mM in MilliQ water were prepared by diluting a 1 M solution of $MnCl_2$ using MilliQ water. The same concentrations were also prepared for $CoCl_2$ by diluting a 1 M solution of $CoCl_2$ with MilliQ water.

Φ-29 DNA polymerase screening with $MnCl_2$

The $MnCl_2$ stock solution (6 μL) and buffer stock solution (5 μL) were first added to a 200 μL PCR tube. A solution of cyclic template T1 (Table 3.1, Chapter 3; 0.67 μM), S1 (Table 3.1, Chapter 3; 1.33 μM), ammonium sulfate (22.2 mM), DTT (8.89 mM), dNTPs (4.44 mM) and Φ-29 DNA polymerase (0.57 U/μL) in MilliQ water was then prepared,

adding the DNA polymerase last. The solution was briefly mixed by vortexing, and 9 μL was then added to each PCR tube. The samples were incubated at 30 °C for 20 h using a Bio-Rad T100^{TM} thermocycler. The enzyme was then inactivated by heating the samples at 65 °C for 10 min before cooling to 4 °C. The samples were centrifuged, and the supernatant was analysed by 0.8% agarose gel electrophoresis. Any precipitates that formed were washed 3 times with MilliQ water followed by resuspending in 20 μL of MilliQ water. 7.5 μL of the samples were then analysed by 0.8% agarose gel electrophoresis. The samples were imaged by SEM if DNA was observed.

Φ-29 DNA polymerase screening with $CoCl_2$

The $CoCl_2$ stock solution (6 μL) and buffer stock solution (5 μL) were first added to a 200 μL PCR tube. A solution of cyclic template T1 (Table 3.1, Chapter 3; 0.67 μM), S1 (Table 3.1, Chapter 3; 1.33 μM), ammonium sulfate (22.2 mM), dNTPs (4.44 mM) and Φ-29 DNA polymerase (0.57 U/μL) in MilliQ water was then prepared, adding the DNA polymerase last. The solution was vortexed, and 9 μL was then added to each PCR tube. The samples were incubated at 30 °C for 20 h using a Bio-Rad T100^{TM} thermocycler. The enzyme was then inactivated by heating the samples at 65 °C for 10 min before cooling to 4 °C. The samples were centrifuged, and the supernatant was analysed by 0.8% agarose gel electrophoresis. Any precipitates that formed were washed 3 times with MilliQ water followed by resuspending in 20 μL of MilliQ water. 7.5 μL of the samples were then analysed by 0.8% agarose gel electrophoresis.

Bst 2.0 DNA polymerase screening

The divalent cation stock solution (6 μL) and buffer stock solution (2 μL) were first added to a 200 μL PCR tube. A solution of cyclic template T1 (Table 3.1, Chapter 3; 0.5 μM),

S1 (Table 3.1, Chapter 3; 1 μM), ammonium sulfate (16.7 mM), KCl (83.3 mM), 0.17% Tween 20, dNTPs (3.33 mM) and Bst 2.0 DNA polymerase (0.27 U/μL) in MilliQ water was then prepared, adding the DNA polymerase last. The solution was vortexed, and 12 μL was then added to each PCR tube. The samples were incubated at 61.5 °C for 14 h using a Bio-Rad T100^{TM} thermocycler. The enzyme was then inactivated by heating the samples at 85 °C for 20 min before cooling to 4 °C. The samples were centrifuged, and the supernatant was analysed by 0.8% agarose gel electrophoresis. Any precipitates that formed were washed 3 times with MilliQ water followed by resuspending in 20 μL of MilliQ water. 7.5 μL of the samples were then analysed by 0.8% agarose gel electrophoresis. The samples were imaged by SEM if DNA was observed.

6.5.2 Comparison of DNA levels using SYBR Gold

RCA reactions were carried out as described above using cyclic template T1 and S1 (Table 3.1, Chapter 3). After heat inactivation of the polymerase enzyme, the samples were diluted 5 times by adding 80 μL of MilliQ water. The precipitate was then collected by centrifugation and the supernatant was carefully removed and kept. The precipitates were washed 3 times with 100 μL of MilliQ water, and then incubated in 100 μL of TBE buffer overnight at RT to break down the formed particles. 100 μL of buffer (1× TBE, 0.1% triton X-100, 1× SYBR Gold) was added into a 96-well plate followed by adding 5 μL of either supernatant or the particle solution. Before each measurement the 96-well plate was shaken three times 10 min apart (1 min, 300 RPM). The fluorescence intensity of the solution was then measured using a CLARIOstar microplate reader (BMG LABTECH, Ortenberg, Germany). All samples were performed in triplicate and the standard deviations of these are given. For SYBR Gold measurements the parameters used were Excitation: 495-8; Dichroic filter: 514.2; Emission: 537-15.

6.5.3 Preparation of manganese and cobalt particles using cyclic T2

Preparation of the cyclic T2 using T4 DNA ligase

A 5′-phosphorylated linear oligonucleotide (T2, Table 3.1, Chapter 3; 6 nmol, 1 eq) and a templating splint oligonucleotide (S2, Table 3.1, Chapter 3; 12 nmol, 2 eq) were annealed in 4.9 mL of 1× T4 DNA ligase buffer (30 mM Tris-HCl, pH 7.8 @ 25 °C, 10 mM $MgCl_2$, 10 mM DTT, and 1 mM ATP) by heating to 95 °C for 5 min, followed by cooling to RT at a rate of 0.5 °C/min. T4 DNA ligase (125μL, 3U/μL) was then added to the solution which was incubated at 25 °C overnight. The sample was heated to 95 °C for 5 min to denature the enzyme. The volume of reaction mixture was then reduced to approximately 1 mL using a CentriVap centrifugal concentrator at 55 °C after which purified by 8% denaturing PAGE gel. After filtration and evaporation of the MilliQ water, the cyclised oligonucleotides were desalted using two NAP-25 columns. The concentration of cyclised oligonucleotides was measured by using a Nanodrop 2000C spectrometer (Thermo Scientific).

Preparation of manganese particles using Φ-29 DNA polymerase with 5 mM Mn^{2+}

A solution of cyclic template (T2, Table 3.1, Chapter 3; 6 pmol), primer (S2, Table 3.1, Chapter 3; 12 pmol), Tris-HCl buffer (5 μL, 200 mM, pH 7.5), $MnCl_2$ (1 μL, 100 mM), ammonium sulfate (0.2 μL, 1 M), DTT (0.8 μL, 0.1 M) and MilliQ water (8.5 μL) with a final volume of 15.5 μL was first annealed by heating the mixture to 95 °C for 5 min followed by cooling to RT at a rate of 0.5 °C/min. Φ-29 DNA polymerase (0.5 μL, 10,000 U/ mL) and dNTPs (4 μL, 10 mM) were added to the above mixture and briefly vortexed. The sample was incubated at 30 °C for 20 h using a Bio-Rad T100^{TM} thermocycler. The enzyme was then inactivated by heating the samples at 65 °C for 10 min before cooling

to 4 °C. The sample was centrifuged, and the supernatant was carefully collected. The resultant precipitate was collected by centrifugation and washed 5 times with MilliQ water followed by resuspending in 20 μL of MilliQ water. 10 μL of the precipitate suspension in MilliQ water was added onto a silicon wafer chip followed by drying at 55 °C for 15 min and then imaged by SEM.

Preparation of manganese particles using Φ-29 DNA polymerase with 10 mM Mn^{2+}

A solution of cyclic template (T2, Table 3.1, Chapter 3; 6 pmol), primer (S2, Table 3.1, Chapter 3; 12 pmol), Tris-HCl buffer (5 μL, 200 mM, pH 7.5), $MnCl_2$ (2 μL, 100 mM), ammonium sulfate (0.2 μL, 1 M), DTT (0.8 μL, 0.1 M), and MilliQ water (7.5 μL) with a final volume of 15.5 μL was first annealed by heating the mixture to 95 °C for 5 min followed by cooling to RT at a rate of 0.5 °C/min. Φ-29 DNA polymerase (0.5 μL, 10,000 U/ mL) and dNTPs (4 μL,10 mM) were added to the above mixture and briefly vortexed. The sample was incubated at 30 °C for 20 h using a Bio-Rad T100^{TM} thermocycler. The enzyme was then inactivated by heating the samples at 65 °C for 10 min before cooling to 4 °C. The sample was centrifuged, and the supernatant was carefully collected. The resultant precipitate was collected by centrifugation and washed 5 times with MilliQ water followed by resuspending in 20 μL of MilliQ water. 10 μL of the precipitate suspension in MilliQ water was added onto a silicon wafer chip followed by drying at 55 °C for 15 min and then imaged by SEM.

Preparation of manganese particles using Bst 2.0 DNA polymerase with 5 mM Mn^{2+}

A solution of cyclic template (T2, Table 3.1, Chapter 3; 6 pmol), primer (S2, Table 3.1, Chapter 3; 12 pmol), Tris-HCl buffer (2 μL, 200 mM, pH 7.5), $MnCl_2$ (6 μL, 16.7 mM), ammonium sulfate (0.2 μL, 1 M), Tween 20 (0.2 μL, 10% v/v), KCl (1 μL, 1 M) and

MilliQ water (6.2 μL) with a final volume of 15.6 μL was first annealed by heating the mixture to 95 °C for 5 min followed by cooling to RT at a rate of 0.5 °C/min. Bst 2.0 DNA polymerase (0.4 μL, 8,000 U/ mL) and dNTPs (4 μL, 10 mM) were added to the above mixture and briefly vortexed. The sample was incubated at 61.5 °C for 14 h using a Bio-Rad T100^{TM} thermocycler. The enzyme was then inactivated by heating the samples at 85 °C for 20 min before cooling to 4 °C. The sample was centrifuged, and the supernatant was carefully collected. The resultant precipitate was collected by centrifugation and washed 5 times with MilliQ water followed by resuspending in 20 μL of MilliQ water. 10 μL of the precipitate suspension in MilliQ water was added onto a silicon wafer chip followed by drying at 55 °C for 15 min and then imaged by SEM.

Preparation of manganese particles using Bst 2.0 DNA polymerase with 10 mM Mn^{2+}

A solution of cyclic template (T2, Table 3.1, Chapter 3; 6 pmol), primer (S2, Table 3.1, Chapter 3; 12 pmol), Tris-HCl buffer (2 μL, 200 mM, pH 7.5), $MnCl_2$ (4 μL, 50 mM), ammonium sulfate (0.2 μL, 1 M), Tween 20 (0.2 μL, 10% v/v), KCl (1 μL, 1 M) and MilliQ water (8.2 μL) with a final volume of 15.6 μL was first annealed by heating the mixture to 95 °C for 5 min followed by cooling to RT at a rate of 0.5 °C/min. Bst 2.0 DNA polymerase (0.4 μL, 8,000 U/ mL) and dNTPs (4 μL, 10 mM) were added to the above mixture and briefly vortexed. The sample was incubated at 61.5 °C for 14 h using a Bio-Rad T100^{TM} thermocycler. The enzyme was then inactivated by heating the samples at 85 °C for 20 min before cooling to 4 °C. The sample was centrifuged, and the supernatant was carefully collected. The resultant precipitate was collected by centrifugation and washed 5 times with MilliQ water followed by resuspending in 20 μL

of MilliQ water. 10 μL of the precipitate suspension in MilliQ water was added onto a silicon wafer chip followed by drying at 55 °C for 15 min and then imaged by SEM.

Preparation of manganese particles using Bst 2.0 DNA polymerase with 15 mM Mn^{2+}

A solution of cyclic template (T2, Table 3.1, Chapter 3; 6 pmol), primer (S2, Table 3.1, Chapter 3; 12 pmol), Tris-HCl buffer (2 μL, 200 mM, pH 7.5), $MnCl_2$ (6 μL, 50 mM), ammonium sulfate (0.2 μL, 1 M), Tween 20 (0.2 μL, 10% v/v), KCl (1 μL, 1 M) and MilliQ water (6.2 μL) with a final volume of 15.6 μL was first annealed by heating the mixture to 95 °C for 5 min followed by cooling to RT at a rate of 0.5 °C/min. Bst 2.0 DNA polymerase (0.4 μL, 8,000 U/ mL) and dNTPs (4 μL, 10 mM) were added to the above mixture and briefly vortexed. The sample was incubated at 61.5 °C for 14 h using a Bio-Rad T100^{TM} thermocycler. The enzyme was then inactivated by heating the samples at 85 °C for 20 min before cooling to 4 °C. The sample was centrifuged, and the supernatant was carefully collected. The resultant precipitate was collected by centrifugation and washed 5 times with MilliQ water followed by resuspending in 20 μL of MilliQ water. 10 μL of the precipitate suspension in MilliQ water was added onto a silicon wafer chip followed by drying at 55 °C for 15 min and then imaged by SEM.

Preparation of cobalt particles using Φ-29 DNA polymerase with 10 mM Co^{2+}

A solution of cyclic template (T2, Table 3.1, Chapter 3; 6 pmol), primer (S2, Table 3.1, Chapter 3;12 pmol), Tris-HCl buffer (5 μL, 200 mM, pH 7.0), $CoCl_2$ (6 μL, 33.33 mM), ammonium sulfate (0.2 μL, 1 M), and MilliQ water (4.3 μL) with a final volume of 15.5 μL was first annealed by heating the mixture to 95 °C for 5 min followed by cooling to RT at a rate of 0.5 °C/min. Φ-29 DNA polymerase (10,000 U/ mL, 0.5 μL) and dNTPs

(10 mM, 4 μL) were added to the above mixture and briefly vortexed. The sample was incubated at 30 °C for 30 h using a Bio-Rad T100^{TM} thermocycler. The enzyme was then inactivated by heating the samples at 65 °C for 10 min before cooling to 4 °C. The sample was centrifuged, and the supernatant was carefully collected. The resultant precipitate was collected by centrifugation and washed 5 times with MilliQ water followed by resuspending in 20 μL of MilliQ water. 10 μL of the precipitate suspension in MilliQ water was loaded onto a silicon wafer chip followed by drying at 55 °C for 15 min and then imaged by SEM.

Preparation of cobalt particles using Φ-29 DNA polymerase with 15 mM Co^{2+}

A solution of cyclic template (T2, Table 3.1, Chapter 3; 6 pmol), primer (S2, Table 3.1, Chapter 3; 12 pmol), Tris-HCl buffer (5 μL, 200 mM, pH 7.0), $CoCl_2$ (6 μL, 50 mM), ammonium sulfate (0.2 μL, 1 M), and MilliQ water (4.3 μL) with a final volume of 15.5 μL was first annealed by heating the mixture to 95 °C for 5 min followed by cooling to RT at a rate of 0.5 °C/min. Φ-29 DNA polymerase (10,000 U/ mL, 0.5 μL) and dNTPs (10 mM, 4 μL) were added to the above mixture and briefly vortexed. The sample was incubated at 30 °C for 30 h using a Bio-Rad T100^{TM} thermocycler. The enzyme was then inactivated by heating the samples at 65 °C for 10 min before cooling to 4 °C. The sample was centrifuged, and the supernatant was carefully collected. The resultant precipitate was collected by centrifugation and washed 5 times with MilliQ water followed by resuspending in 20 μL of MilliQ water. 10 μL of the precipitate suspension in MilliQ water was loaded onto a silicon wafer chip followed by drying at 55 °C for 15 min and then imaged by SEM.

6.5.4 Preparation of manganese and cobalt particles for magnetic studies

Preparation of particles using Bst 2.0 DNA polymerase with 15 mM Mn^{2+}

A solution of cyclic template (T1, Table 3.1, Chapter 3; 0.3 nmol), primer (S1, Table 3.1, Chapter 3; 0.6 nmol), Tris-HCl buffer (100 μL, 200 mM, pH 7.5), $MnCl_2$ (300 μL, 50 mM), ammonium sulfate (10 μL, 1 M), Tween 20 (10 μL, 10% v/v), KCl (50 μL, 1 M) and MilliQ water (310 μL) with a final volume of 780 μL was first annealed by heating the mixture to 95 °C for 5 min followed by cooling to RT at a rate of 1 °C/min. Bst 2.0 DNA polymerase (20 μL, 8,000 U/ mL) and dNTPs (200 μL, 10 mM) were added to the above mixture and briefly vortexed. The sample was incubated at 61.5 °C for 14 h. The enzyme was then inactivated by heating the samples at 85 °C for 20 min before cooling to RT. The sample was centrifuged, and the supernatant was carefully removed. The resultant precipitate was collected by centrifugation and washed 5 times with MilliQ water followed by resuspending in MilliQ water. The precipitate was dried under vacuum for 12 h and used in magnetic studies.

Preparation of particles using Φ-29 DNA polymerase with 15 mM Mn^{2+}

A solution of cyclic template (T1, Table 3.1, Chapter 3; 0.3 nmol), primer (S1, Table 3.1, Chapter 3; 0.6 nmol), Tris-HCl buffer (250 μL, 200 mM, pH 8.0), $MnCl_2$ (300 μL, 50 mM), ammonium sulfate (10 μL, 1 M), and MilliQ water (215 μL) with a final volume of 775 μL was first annealed by heating the mixture to 95 °C for 5 min followed by cooling to RT at a rate of 1 °C/min. Φ-29 DNA polymerase (25 μL, 10,000 U/ mL) and dNTPs (200 μL,10 mM) were added to the above mixture and briefly vortexed. The sample was incubated at 30 °C for 20 h. The enzyme was then inactivated by heating the samples at 65 °C for 10 min before cooling to RT. The sample was centrifuged, and the supernatant

was carefully removed. The resultant precipitate was collected by centrifugation and washed 5 times with MilliQ water followed by resuspending in MilliQ water. The precipitate was dried under vacuum for 12 h and used in magnetic studies.

Preparation of particles using Φ-29 DNA polymerase with 15 mM Co^{2+}

A solution of cyclic template (T1, Table 3.1, Chapter 3; 0.3 nmol), primer (S1, Table 3.1, Chapter 3; 0.6 nmol), Tris-HCl buffer (250 μL, 200 mM, pH 7.0), $CoCl_2$ (300 μL, 50 mM), ammonium sulfate (10 μL, 1 M), and MilliQ water (215 μL) with a final volume of 775 μL was first annealed by heating the mixture to 95 °C for 5 min followed by cooling to RT at a rate of 1 °C/min. Φ-29 DNA polymerase (25 μL, 10,000 U/ mL) and dNTPs (200 μL, 10 mM) were added to the above mixture and briefly vortexed. The sample was incubated at 30 °C for 20 h. The enzyme was then inactivated by heating the samples at 65 °C for 10 min before cooling to RT. The sample was centrifuged, and the supernatant was carefully removed. The resultant precipitate was collected by centrifugation and washed 5 times with MilliQ water followed by resuspending in MilliQ water. The precipitate was dried under vacuum for 12 h and used in magnetic studies.

6.5.5 Enzymatic stability studies

Particle solutions (10 μL) were centrifuged and the water was removed. The precipitates were then resuspended in 20 μL of DMEM containing 10% FBS followed by incubating at 37 °C for different time points (1 h, 6 h, 12 h, 24 h and 36 h). According to the literature, double-stranded λ-DNA (1 μL, 500 μg/mL, NEB) as control was incubated under the same conditions.[239] After incubation, the samples were then analysed by 0.8% agarose gel electrophoresis. Particles from the 36 h incubation were collected by centrifugation, washed 3 times with MilliQ water and imaged using SEM to evaluate structural integrity.

6.5.6 Hybridisation studies

DNA-NFs generated from the equivalent of 20 μL RCA volume were incubated with 100 μL of either 50 nM Cy3 labelled complementary DNA probe (match, Table 3.2, Chapter 3) or 50 nM of a scrambled version (mismatch, Table 3.2, Chapter 3) at RT for 1 h in the presence of 200 mM NaCl or MilliQ water. After incubation, the particles were collected by centrifugation and the percentage of probe left in solution was determined using a fluorescence plate reader.

6.6 Synthesis of cyclic oligonucleotides using enzymatic and chemical methods

6.6.1 Enzymatic cyclisation of the linear oligonucleotides

Preparation of the cyclic oligonucleotide 1_PO_4, 2_PO_4 and 3_PO_4 using T4 DNA ligase

A 5′-phosphorylated linear oligonucleotide **1**_PO_4, **2**_PO_4 and **3**_PO_4 (Table 4.1, Chapter 4; 2.4 nmol, 1 eq) and a templating splint oligonucleotide (ODN4-1, ODN4-2 or ODN4-3, Table 4.2, Chapter 4; 7.2 nmol, 3 eq) were annealed in 3.9 mL of 1× T4 DNA ligase buffer (30 mM Tris-HCl, pH 7.8 @ 25 °C, 10 mM $MgCl_2$, 10 mM DTT, and 1 mM ATP) by heating to 95 °C for 5 min, followed by cooling to RT at a rate of 0.5 °C/min. T4 DNA ligase (100 μL, 3U/μL) was then added to the solution which was incubated at RT overnight. The sample was heated to 70 °C for 15 min to denature the enzyme. The volume of reaction mixture was then reduced to 2.5 mL using a CentriVap centrifugal concentrator at 55 °C followed by de-salting using NAP-25 column. The cyclised oligonucleotides was purified by denaturing PAGE gel (cyclic **1**_PO_4: 15% PAGE; cyclic **2**_PO_4: 8% PAGE and cyclic **3**_PO_4: 12% PAGE) as described above.

Preparation of the cyclic oligonucleotide 4_PO$_4$ using T4 DNA ligase

The 5′-phosphorylated linear oligonucleotide **4**_PO$_4$ (Table 4.1, Chapter 4; 2.4 nmol, 1 eq) and the templating splint oligonucleotide ODN4-4 (Table 4.2, Chapter 4; 4.8 nmol, 2 eq) were annealed in 3.9 mL of 1× T4 DNA ligase buffer (30 mM Tris-HCl, pH 7.8 @ 25 °C, 10 mM $MgCl_2$, 10 mM DTT, and 1 mM ATP) by heating to 95 °C for 5 min, followed by cooling to RT at a rate of 0.5 °C/min. T4 DNA ligase (100 μL, 3U/μL) was then added and the solution was incubated at RT overnight. The sample was heated to 70 °C for 15 minutes to denature the enzyme. The volume of reaction mixture was reduced to 2.5 mL using a CentriVap centrifugal concentrator at 55 °C followed by desalting using NAP-25 column. The cyclised oligonucleotides was purified by 8% denaturing PAGE gel as described above.

6.6.2 Chemical cyclisation of the linear oligonucleotides

Preparation of Cu(I) click catalyst solution

To prepare a solution of Cu(I) click catalyst, THPTA (3.6 mg) was dissolved into a solution of sodium ascorbate (12 μmol in MilliQ water, 24 μL) followed by degassing by bubbling with argon gas (~ 3 min). $CuSO_4 \cdot 5H_2O$ (1.2 μmol in MilliQ water, 12 μL) was added and the solution was degassed again.

Preparation of the cyclic oligonucleotides 1_Tz, 2_Tz and 3_Tz containing triazole linkages through CuAAC 'click ligation'

Cu(I) click catalyst solution (36 μL, prepared as described above) was added to 2.364 mL of the linear 5′-azide-3′-propargyl oligonucleotide (linear **1**_Tz, linear **2**_Tz and linear **3**_Tz, Table 4.1, Chapter 4; 12 nmol in 0.2 M $NaCl_{(aq)}$). The reaction mixture was kept

at RT for 2.5 h after which reagents were removed by NAP-25 gel filtration. The volume of reaction mixture was concentrated using a CentriVap centrifugal concentrator at 55 °C. The cyclised DNA products were analysed and purified by denaturing PAGE gel (cyclic **1**_Tz: 15% PAGE; cyclic **2**_Tz: 8% PAGE and cyclic **3**_Tz: 12% PAGE) as described above.

Preparation of the cyclic oligonucleotide 4_Tz containing a triazole linkage through CuAAC 'click' ligation under denaturing condition

1.2 nmol of the linear 5′-azide-3′-propargyl oligonucleotide (linear **4**_Tz, Table 4.1, Chapter 4) was first dissolved in 236 μL of the organic solvent/MilliQ water solution (9:1, 4:1 or 3:2 v/v of MilliQ water:formamide, DMSO or acetonitrile) and heated to 95 °C for 5 min followed by cooling rapidly on ice. A solution of Cu(I) click catalyst (3.6 μL, prepared as described above) was added to the reaction, and the solution was kept at RT for 2.5 h after which reagents were removed by NAP-10 gel filtration. The volume of reaction mixture was concentrated using a CentriVap centrifugal concentrator at 55 °C. The cyclised DNA products were analysed and purified by 8% denaturing PAGE gel as described above.

Preparation of the cyclic oligonucleotide 1_PA containing a phosphoramidate linkage

The linear 3′-phosphate/5′-amino dT oligonucleotide (linear **1**_PA, Table 4.1, Chapter 4; 10 nmol, 4 μM) was dissolved in 2.5 mL of 0.2 M HEPES buffer (pH 7.2). 1-(2-Hydroxyethyl)imidazole (0.25 mmol, 0.1 M) was added as a solid, followed by EDC·HCl (0.19 mmol, 0.075 M). The solution was allowed to stand at RT for 3 h. An additional portion of EDC·HCl (0.19 mmol) was then added and the solution was left at RT for a

further 13 h, before removal of the small molecule reagents and buffer by gel-filtration, using a NAP-25 column, followed by a NAP-10 column. The crude product was taken up in 1 mL of 0.1 M $NaOH_{(aq)}$ and the solution was heated at 55 °C for 6 h, then cooled to RT and desalted using a NAP-25 column followed by a NAP-10 column. The crude product mixture was analysed and purified by 15% denaturing PAGE gel as described above.

Non-templated cyclisation to give the modified circular template 1_Am containing an amide linkage

The linear 3′-carboxy/5′-amino dT oligonucleotide (linear **1**_Am, Table 4.1, Chapter 4; 5 nmol) was dissolved in 1.0 mL of 0.125 M $NaCl_{(aq)}$. N-Hydroxysuccinimide (125 μL of a 25 mM solution in MilliQ water) and EDC·HCl (125 μL of a 100 mM solution in MilliQ water) were added. The reaction mixture was allowed to stand at RT for 2 h, before removal of reagents and salt using a NAP-25 column. The product mixture was analysed and purified by 15% denaturing PAGE gel as described above.

6.7 Rolling circle amplification

Comparing the effect of Mg^{2+} concentration on RCA catalysed by Φ-29 DNA polymerase

A solution of cyclic template (cyclic **1**_PO_4, cyclic **1**_PA, cyclic **2**_PO_4, cyclic **2**_PA, cyclic **3**_PO_4 and cyclic **3**_PA, Table 4.1, Chapter 4; 3 pmol), primer (OND4-1, OND4-2, OND4-3, Table 4.2, Chapter 4; 12 pmol), $MgSO_4$ (either 0 μL, 0.5 μL, 1 μL, 2 μL or 3 μL of a 100 mM aqueous solution) and 2 μL of 10× Φ-29 DNA polymerase buffer (500 mM Tris-HCl, pH 7.5 @ 25°C, 100 mM $(NH_4)_2SO_4$, 40 mM DTT, 100 mM $MgCl_2$) in MilliQ water with a final volume of 15.2 μL was first annealed by heating the mixture to

95 °C for 5 min followed by cooling to RT at a rate of 0.5 °C/min. Φ-29 DNA polymerase (0.8 μL, 10,000 U/ mL) and dNTPs (4 μL, 10 mM) were added to the above mixture and briefly vortexed. The samples were incubated at 30 °C for 20 h using a Bio-Rad T100^{TM} thermocycler. The enzyme was then inactivated by heating the samples at 65 °C for 10 min before cooling to 4 °C. The samples were centrifuged, and the supernatant was carefully collected. The resultant precipitate was collected by centrifugation and washed 5 times with MilliQ water followed by resuspending in 20 μL of MilliQ water. 7.5 μL of the supernatant or the precipitate suspension were then analysed by 0.8% agarose gel electrophoresis.

Comparing the performance of the different templates and backbones in RCA catalysed using Φ-29 DNA polymerase

The following setup was used for each template described: The cyclic template (Table 4.1, Chapter 4; 3 pmol) and primer (Table 4.2, Chapter 4; 12 pmol) were dissolved in 11.2 μL of MilliQ water and 2 μL of $MgSO_4$ (100 mM) and 2 μL of 10× Φ-29 DNA polymerase buffer (500 mM Tris-HCl, pH 7.5 @ 25°C, 100 mM $(NH_4)_2SO_4$, 40 mM DTT, 100 mM $MgCl_2$) were added. The samples were annealed by heating the mixture to 95 °C for 5 min followed by cooling to RT at a rate of 0.5 °C/min. Φ-29 DNA polymerase (0.8 μL, 10,000 U/ mL) and dNTPs (4 μL, 10 mM) were added to the above mixture. The samples were incubated at 30 °C for the desired time period. The enzyme was then inactivated by heating the samples at 65 °C for 10 min before cooling to 4 °C. The RCA reaction mixture was diluted 5 times with MilliQ water and analysed by 0.8% agarose gel electrophoresis before centrifugation.

RCA reaction catalysed using Φ-29 DNA polymerase with 10 mM Mg^{2+} and single-stranded binding protein T4 gene 32 for cyclic templates (1_PO_4 and 1_PA)

The cyclic template (cyclic **1**_PO_4 and cyclic **1**_PA, Table 4.1, Chapter 4; 4.5 pmol) and primer (ODN4-1, Table 4.2, Chapter 4; 18 pmol) were dissolved in 19.5 μL MilliQ water and 3 μL of 10× Φ-29 DNA polymerase buffer was added. The solution was annealed by heating the mixture to 95 °C for 5 min followed by cooling to RT at a rate of 0.5 °C/min. Φ-29 DNA polymerase (1.2 μL, 10,000 U/ mL), dNTPs (6 μL, 10 mM) and T4 gene 32 protein (0.3 μL, 10 mg/ mL) were added to the above mixture (The concentration of Mg^{2+} and T4 gene 32 protein were chosen based on previous literature[250]). The RCA reactions were incubated at 30 °C for 20 h. The enzyme was then inactivated by heating the samples at 65 °C for 10 min before cooling to 4 °C. The original RCA reaction mixture was diluted to 100 μL with MilliQ water and then analysed by 0.8% agarose gel electrophoresis.

Quantification of the RCA rate with Φ-29 DNA polymerase using fluorescent probes

RCA reactions were performed as described above for different lengths of time (0 h, 2 h, 4 h, 6 h, 8 h, 10 h, or 20 h) using cyclic **1**_PO_4, cyclic **1**_PA, cyclic **1**_Am and cyclic **1**_Tz (Table 4.1, Chapter 4) and their corresponding primers (ODN4-1 and ODN4-5, Table 4.2, Chapter 4). After heat inactivation of the enzyme, the samples were diluted 5 times with 10 mM EDTA in MilliQ water. 10 μL of each sample was mixed with a 10 μL solution composed of fluorescent probe (ODN4-8, Table 4.3, Chapter 4; 100 μM) and NaCl (1 M) and incubated at RT for 2 h. 9 μL of each sample was mixed with 3 μL of 5× GoTaq® Green buffer (Promega) and analysed by 0.8% agarose gel electrophoresis (cast without SYBR Gold). The gels were run at RT (100 V) and imaged using a G:Box gel documentation system (Syngene) with excitation at 520 nm under the Cy3 fluorescence channel. Afterwards, the gels were stained with SYBR Gold (1×) at RT for 15 min, and reimaged with excitation at 302 nm.

Measurement of fluorescence intensity of the RCA products stained with SYBR Green I, SYBR Green II and SYBR Gold

RCA reactions were performed as described above. After heat inactivation of the polymerase enzyme the samples were diluted 500 times with a solution of 20 mM of EDTA in MilliQ water. 100 μL of buffer (1× TBE, 0.1% triton X-100, 1× SYBR Green I, 1× SYBR Green II or 1× SYBR Gold) was added into a 96-well plate followed by adding 5 μL of diluted RCA product. Before each measurement the 96-well plate was shaken three times 10 min apart (1 min, 300 RPM). The fluorescence intensity of the solution was then measured using a CLARIOstar microplate reader (BMG LABTECH, Ortenberg, Germany). Three independent readings were taken for each RCA sample. For SYBR Green I measurements the parameters used were Excitation: 492-8; Dichroic filter: 514.2; Emission: 526-8. For SYBR Green II measurements the parameters used were Excitation: 492-8; Dichroic filter: 514.2; Emission: 526-8. For SYBR Gold measurements the parameters used were Excitation: 495-8; Dichroic filter: 514.2; Emission: 537-15.

RCA reaction catalysed using Bst 2.0 DNA polymerase with 20 mM Mg^{2+}

The cyclic template (cyclic templates **1** - **4**, Table 4.1, Chapter 4; 3 pmol) and primer (Table 4.2, Chapter 4; 12 pmol) were dissolved in 10 μL MilliQ water and 3.6 μL of 100 mM $MgSO_4$ and 2 μL of 10× isothermal amplification buffer (200 mM Tris-HCl, pH 8.8 @ 25°C, 100 mM $(NH_4)_2SO_4$, 500 mM KCl, 20 mM $MgSO_4$, 0.1% Tween® 20) were added. The sample was annealed by heating the mixture to 95 °C for 5 min followed by cooling to RT at a rate of 0.5 °C/min. Bst 2.0 DNA polymerase (0.4 μL, 8000 U/ mL) and dNTPs (4 μL, 10 mM) were then added. The RCA reactions were carried out at 61.5 °C for 20 h. The enzyme was then inactivated by heating the samples at 80 °C for 20 min

before cooling to 4 °C. The original RCA reaction mixture was diluted 5 times by MilliQ water and then analysed by 0.8% agarose gel electrophoresis.

Quantification of the RCA rate with Bst 2.0 DNA polymerase using fluorescent probe

RCA reactions were performed as described above for different lengths of time (0 h, 2 h, 4 h, 6 h, 8 h, 10 h, or 20 h) using cyclic **1**_PO_4, cyclic **1**_PA, cyclic **1**_Am and cyclic **1**_Tz (Table 4.1, Chapter 4) and their corresponding primers (ODN4-1 and ODN4-5, Table 4.2, Chapter 4). After heat inactivation of the enzyme, the samples were diluted 5 times with 10 mM EDTA in MilliQ water. 10 μL of each sample was mixed with a 10 μL solution composed of fluorescent probe (ODN4-8, 100 μM) and NaCl (1 M) and incubated at RT for 2 h. 9 μL of each sample was mixed with 3 μL of 5× GoTaq® Green buffer (Promega) and analysed by 0.8% agarose gel electrophoresis (cast without SYBR Gold). The gels were run at RT (100 V) and imaged using a G:Box gel documentation system (Syngene) with excitation at 520 nm under the Cy3 fluorescence channel. Afterwards, the gels were stained with SYBR Gold (1×) at RT for 15 min, and reimaged with excitation at 302 nm.

6.8 DNA nanoflower experiments

Using the cyclic templates to prepare DNA-NFs

A solution of cyclic template (cyclic **1**_PO_4, cyclic **1**_PA, cyclic **1**_Am and cyclic **1**_Tz, Table 4.1, Chapter 4; 3 pmol), primer (ODN4-1 and ODN4-5, Table 4.2, Chapter 4; 12 pmol), 2 μL $MgSO_4$ (100 mM aqueous solution) and 2 μL of 10× Φ-29 DNA polymerase buffer (500 mM Tris-HCl, pH 7.5 @ 25°C, 100 mM $(NH_4)_2SO_4$, 40 mM DTT, 100 mM $MgCl_2$) in MilliQ water with a final volume of 15.2 μL was first annealed by heating the

mixture to 95 °C for 5 min followed by cooling to RT at a rate of 0.5 °C/min. Φ-29 DNA polymerase (0.8 μL, 10,000 U/ mL) and dNTPs (4 μL, 10 mM) were added to the above mixture and briefly vortexed. The samples were incubated at 30 °C for either 8 h or 20 h using a Bio-Rad T100^{TM} thermocycler. The enzyme was then inactivated by heating the samples at 65 °C for 10 min before cooling to 4 °C. 80 μL of MilliQ water was added and the samples were centrifuged. The resultant precipitate was collected by centrifugation and washed 5 times with MilliQ water followed by resuspending in 20 μL of MilliQ water. 10 μL of each of the RCA precipitate suspensions were loaded onto silicon wafer chips and dried at 55 °C for 15 min. The samples were then imaged using SEM. The resuspended precipitate solution was also analysed by agarose gel electrophoresis.

Comparing the effect of Mg^{2+} concentration on DNA-NF size

RCA was performed as described in the 'comparing the effect of Mg^{2+} concentration on DNA loading of DNA-NFs' section above using cyclic **1**_PO_4 and cyclic **1**_PA (Table 4.1, Chapter 4). 10 μL of each of the RCA precipitate suspensions were loaded onto silicon wafer chips and dried at 55 °C for 15 min. The samples were then imaged using SEM.

References

References

(1) Berg, J. M.; Tymoczko, J. L.; Stryer, L.: *Biochemistry*. *Fifth Edition*. **2002**.

(2) Blackburn, G. M.: *Nucleic acids in chemistry and biology*, *Third Edition*. **2015**.

(3) Chargaff, E. Chemical specificity of nucleic acids and mechanism of their enzymatic degradation. *Experientia*, **1950**, *6*, 201-209.

(4) Belmont, P.; Constant, J.-F.; Demeunynck, M. Nucleic acid conformation diversity: from structure to function and regulation. *Chem. Soc. Rev.*, **2001**, *30*, 70-81.

(5) Franklin, R. E.; Gosling, R. G. Molecular configuration in sodium thymonucleate. *Nature*, **1953**, *171*, 740-741.

(6) Wilkins, M. H. F.; Seeds, W. E.; Stokes, A. R.; Wilson, H. R. Helical structure of crystalline deoxypentose nucleic acid. *Nature*, **1953**, *172*, 759-762.

(7) Watson, J. D.; Crick, F. H. C. Molecular structure of nucleic acids: a structure for deoxyribose nucleic acid. *Nature*, **1953**, *171*, 737-738.

(8) Simonsson, S.; Samuelsson, T.; Elias, P. The herpes simplex virus type 1 origin binding protein: specific recognition of phosphates and methyl groups defines the interacting surface for a monomeric DNA binding domain in the major groove of DNA. *J. Biol. Chem.*, **1998**, *273*, 24633-24639.

(9) Hamilton, P. L.; Arya, D. P. Natural product DNA major groove binders. *Nat. Prod. Rep.*, **2012**, *29*, 134-143.

(10) Carole A. Bewley; Angela M. Gronenborn, a.; Clore, G. M. Minor groove-binding architectural proteins: structure, function, and DNA recognition. *Annu. Rev. Biophys. Biomol. Struct.*, **1998**, *27*, 105-131.

(11) Baraldi, P. G.; Bovero, A.; Fruttarolo, F.; Preti, D.; Tabrizi, M. A.; Pavani, M. G.; Romagnoli, R. DNA minor groove binders as potential antitumor and antimicrobial agents. *Med. Res. Rev.*, **2004**, *24*, 475-528.

(12) Dickerson, R.; Drew, H.; Conner, B.; Wing, R.; Fratini, A.; Kopka, M. The anatomy of A-, B-, and Z-DNA. *Science*, **1982**, *216*, 475-485.

(13) Leslie, A. G. W.; Arnott, S.; Chandrasekaran, R.; Ratliff, R. L. Polymorphism of DNA double helices. *J. Mol. Biol.*, **1980**, *143*, 49-72.

(14) Zhang, H.; Yu, H.; Ren, J.; Qu, X. Reversible B/Z-DNA transition under the low salt condition and non-B-form polydApolydT selectivity by a cubane-like europium-L-aspartic acid complex. *Biophys. J.*, **2006**, *90*, 3203-3207.

(15) Kaushik, M.; Kaushik, S.; Roy, K.; Singh, A.; Mahendru, S.; Kumar, M.; Chaudhary, S.; Ahmed, S.; Kukreti, S. A bouquet of DNA structures: emerging diversity. *Biochem Biophys Rep.*, **2016**, *5*, 388-395.

(16) Gowers, D. M.; Fox, K. R. Towards mixed sequence recognition by triple helix formation. *Nucleic Acids Res.*, **1999**, *27*, 1569-1577.

(17) James, P. L.; Brown, T.; Fox, K. R. Thermodynamic and kinetic stability of intermolecular triple helices containing different proportions of C+*GC and T*AT triplets. *Nucleic Acids Res.*, **2003**, *31*, 5598-5606.

(18) Williamson, J. R. G-quartet structures in telomeric DNA. *Annu. Rev. Biophys. Biomol. Struct.*, **1994**, *23*, 703-730.

(19) Davis, J. T. G-quartets 40 years later: from 5′-GMP to molecular biology and supramolecular chemistry. *Angew. Chem., Int. Ed.*, **2004**, *43*, 668-698.

(20) Williamson, J. R.; Raghuraman, M. K.; Cech, T. R. Monovalent cation-induced structure of telomeric DNA: the G-quartet model. *Cell*, **1989**, *59*, 871-880.

(21) Nagatoishi, S.; Tanaka, Y.; Tsumoto, K. Circular dichroism spectra demonstrate formation of the thrombin-binding DNA aptamer G-quadruplex under stabilizing-cation-deficient conditions. *Biochem Biophys Res Commun.*, **2007**, *352*, 812-817.

(22) Keniry, M. A. Quadruplex structures in nucleic acids. *Biopolymers*, **2000**, *56*, 123-146.

(23) Risitano, A.; Fox, K. R. Influence of loop size on the stability of intramolecular DNA quadruplexes. *Nucleic Acids Res.*, **2004**, *32*, 2598-2606.

(24) Bochman, M. L.; Paeschke, K.; Zakian, V. A. DNA secondary structures: stability and function of G-quadruplex structures. *Nat Rev Genet.*, **2012**, *13*, 770-780.

(25) Lakhin, A. V.; Tarantul, V. Z.; Gening, L. V. Aptamers: problems, solutions and prospects. *Acta Naturae.*, **2013**, *5*, 34-43.

(26) Morita, Y.; Leslie, M.; Kameyama, H.; Volk, D. E.; Tanaka, T. Aptamer therapeutics in cancer: current and future. *Cancers*, **2018**, *10*, 80.

(27) Tuerk, C.; Gold, L. Systematic evolution of ligands by exponential enrichment: RNA ligands to bacteriophage T4 DNA polymerase. *Science*, **1990**, *249*, 505-510.

(28) Ellington, A. D.; Szostak, J. W. *In vitro* selection of RNA molecules that bind specific ligands. *Nature*, **1990**, *346*, 818-822.

(29) Feigon, J.; Dieckmann, T.; Smith, F. W. Aptamer structures from A to ζ. *Chem. Biol.*, **1996**, *3*, 611-617.

(30) Patel, D. J.; Suri, A. K.; Jiang, F.; Jiang, L.; Fan, P.; Kumar, R. A.; Nonin, S. Structure, recognition and adaptive binding in RNA aptamer complexes. *J. Mol. Biol.*, **1997**, *272*, 645-664.

(31) Hermann, T.; Patel, D. J. Adaptive recognition by nucleic acid aptamers. *Science*, **2000**, *287*, 820-825.

(32) Piganeau, N.; Schroeder, R. Aptamer structures: a preview into regulatory pathways? *Chem. Biol.*, **2003**, *10*, 103-104.

(33) Ku, T.-H.; Zhang, T.; Luo, H.; Yen, T. M.; Chen, P.-W.; Han, Y.; Lo, Y.-H. Nucleic acid aptamers: an emerging tool for biotechnology and biomedical sensing. *Sensors*, **2015**, *15*, 16281-16313.

(34) Shangguan, D.; Li, Y.; Tang, Z.; Cao, Z. C.; Chen, H. W.; Mallikaratchy, P.; Sefah, K.; Yang, C. J.; Tan, W. Aptamers evolved from live cells as effective molecular probes for cancer study. *Proc. Natl. Acad. Sci. U. S. A.*, **2006**, *103*, 11838-11843.

(35) Cerchia, L.; Ducongé, F.; Pestourie, C.; Boulay, J.; Aissouni, Y.; Gombert, K.; Tavitian, B.; de Franciscis, V.; Libri, D. Neutralizing aptamers from whole-cell SELEX inhibit the RET receptor tyrosine kinase. *PLoS Biol.*, **2005**, *3*, e123-e123.

(36) Mallikaratchy, P. Evolution of complex target SELEX to identify aptamers against mammalian cell-surface antigens. *Molecules*, **2017**, *22*, 215.

(37) Nimjee, S. M.; Rusconi, C. P.; Sullenger, B. A. Aptamers: an emerging class of therapeutics. *Annu Rev Med.*, **2005**, *56*, 555-583.

(38) Sun, H.; Zu, Y. A highlight of recent advances in aptamer technology and its application. *Molecules*, **2015**, *20*, 11959.

(39) Song, K.-M.; Lee, S.; Ban, C. Aptamers and their biological applications. *Sensors*, **2012**, *12*, 612-631.

(40) Mascini, M. Aptamers and their applications. *Anal. Bioanal. Chem.*, **2008**, *390*, 987-988.

(41) Argos, P.; Rossmann, M. G.; Grau, U. M.; Zuber, H.; Frank, G.; Tratschin, J. D. Thermal stability and protein structure. *Biochemistry*, **1979**, *18*, 5698-5703.

(42) Pontius, B. W.; Berg, P. Rapid renaturation of complementary DNA strands mediated by cationic detergents: a role for high-probability binding domains in enhancing the kinetics of molecular assembly processes. *Proc. Natl. Acad. Sci. U. S. A.*, **1991**, *88*, 8237-8241.

(43) John SantaLucia, J.; Hicks, D. The thermodynamics of DNA structural motifs. *Annu. Rev. Biophys. Biomol. Struct.*, **2004**, *33*, 415-440.

(44) Ireson, C. R.; Kelland, L. R. Discovery and development of anticancer aptamers. *Mol. Cancer Ther.*, **2006**, *5*, 2957-2962.

(45) Ciesiolka, J.; Gorski, J.; Yarus, M. Selection of an RNA domain that binds Zn^{2+}. *RNA*, **1995**, *1*, 538-550.

(46) Li, S.; Xu, H.; Ding, H.; Huang, Y.; Cao, X.; Yang, G.; Li, J.; Xie, Z.; Meng, Y.; Li, X.; Zhao, Q.; Shen, B.; Shao, N. Identification of an aptamer targeting hnRNP A1 by tissue slide-based SELEX. *J. Pathol.*, **2009**, *218*, 327-336.

(47) Stoltenburg, R.; Nikolaus, N.; Strehlitz, B. Capture-SELEX: selection of DNA aptamers for aminoglycoside antibiotics. *J. Anal. Methods Chem.*, **2012**, *2012*, 14.

(48) Yang, Q.; Goldstein, I. J.; Mei, H. Y.; Engelke, D. R. DNA ligands that bind tightly and selectively to cellobiose. *Proc. Natl. Acad. Sci. U. S. A.*, **1998**, *95*, 5462-5467.

(49) Liu, Z.; Duan, J.-H.; Song, Y.-M.; Ma, J.; Wang, F.-D.; Lu, X.; Yang, X.-D. Novel HER2 aptamer selectively delivers cytotoxic drug to HER2-positive breast cancer cells *in vitro*. *J. Transl. Med.*, **2012**, *10*, 148.

(50) Birch, J. R.; Racher, A. J. Antibody production. *Adv. Drug Deliv. Rev.*, **2006**, *58*, 671-685.

(51) Layzer, J. M.; McCaffrey, A. P.; Tanner, A. K.; Huang, Z.; Kay, M. A.; Sullenger, B. A. *In vivo* activity of nuclease-resistant siRNAs. *RNA*, **2004**, *10*, 766-771.

(52) Ruckman, J.; Green, L. S.; Beeson, J.; Waugh, S.; Gillette, W. L.; Henninger, D. D.; Claesson-Welsh, L.; Janjic, N. N. 2′-Fluoropyrimidine RNA-based

aptamers to the 165-amino acid form of vascular endothelial growth factor (VEGF165): inhibition of receptor binding and VEGF-induced vascular permeability through interactions requiring the exon 7-encoded domain. *J. Biol. Chem.,* **1998**, *273*, 20556-20567.

(53) Khati, M.; Schüman, M.; Ibrahim, J.; Sattentau, Q.; Gordon, S.; James, W. Neutralization of infectivity of diverse R5 clinical isolates of human immunodeficiency virus type 1 by gp120-binding 2'F-RNA aptamers. *J. Virol.,* **2003**, *77*, 12692-12698.

(54) Kim, M. Y.; Jeong, S. *In vitro* selection of RNA aptamer and specific targeting of ErbB2 in breast cancer cells. *Nucleic Acid Ther.,* **2011**, *21*, 173-178.

(55) Dellafiore, M. A.; Montserrat, J. M.; Iribarren, A. M. Modified nucleoside triphosphates for *in vitro* selection techniques. *Front. Chem.,* **2016**, *4*, 18-18.

(56) Yan, X.; Gao, X.; Zhang, Z. Isolation and characterization of 2'-amino-modified RNA aptamers for human TNFalpha. *Genom. Proteom. Bioinform.,* **2004**, *2*, 32-42.

(57) Jellinek, D.; Green, L. S.; Bell, C.; Lynott, C. K.; Gill, N.; Vargeese, C.; Kirschenheuter, G.; McGee, D. P. C.; Abesinghe, P. Potent 2'-amino-2'-deoxypyrimidine RNA inhibitors of basic fibroblast growth factor. *Biochemistry,* **1995**, *34*, 11363-11372.

(58) Padilla, R.; Sousa, R. A Y639F/H784A T7 RNA polymerase double mutant displays superior properties for synthesizing RNAs with non-canonical NTPs. *Nucleic Acids Res.,* **2002**, *30*, e138-e138.

(59) Volk, D. E.; Lokesh, G. L. R. Development of phosphorothioate DNA and DNA thioaptamers. *Biomedicines,* **2017**, *5*, 41.

(60) Rusconi, C. P.; Scardino, E.; Layzer, J.; Pitoc, G. A.; Ortel, T. L.; Monroe, D.; Sullenger, B. A. RNA aptamers as reversible antagonists of coagulation factor IXa. *Nature,* **2002**, *419*, 90.

(61) Farokhzad, O. C.; Cheng, J.; Teply, B. A.; Sherifi, I.; Jon, S.; Kantoff, P. W.; Richie, J. P.; Langer, R. Targeted nanoparticle-aptamer bioconjugates for cancer chemotherapy *in vivo*. *Proc. Natl. Acad. Sci. U.S.A.,* **2006**, *103*, 6315-6320.

(62) Ng, E. W. M.; Shima, D. T.; Calias, P.; Cunningham Jr, E. T.; Guyer, D. R.; Adamis, A. P. Pegaptanib, a targeted anti-VEGF aptamer for ocular vascular disease. *Nat Rev Drug Discov.,* **2006**, *5*, 123.

(63) Nimjee, S. M.; White, R. R.; Becker, R. C.; Sullenger, B. A. Aptamers as therapeutics. *Annu Rev Pharmacol Toxicol.,* **2017**, *57*, 61-79.

(64) Hayat, A.; Marty, J. L. Aptamer based electrochemical sensors for emerging environmental pollutants. *Front. Chem.,* **2014**, *2*, 41-41.

(65) Förster, U.; Weigand, J. E.; Trojanowski, P.; Suess, B.; Wachtveitl, J. Conformational dynamics of the tetracycline-binding aptamer. *Nucleic Acids Res.,* **2012**, *40*, 1807-1817.

(66) Freeman, R.; Girsh, J.; Willner, I. Nucleic acid/quantum dots (QDs) hybrid systems for optical and photoelectrochemical sensing. *ACS Appl. Mater. Interfaces.,* **2013**, *5*, 2815-2834.

(67) Liu, J.; Lu, Y. Fast colorimetric sensing of adenosine and cocaine based on a general sensor design involving aptamers and nanoparticles. *Angew. Chem., Int. Ed.*, **2006**, *45*, 90-94.

(68) Wang, H.-Q.; Wu, Z.; Tang, L.-J.; Yu, R.-Q.; Jiang, J.-H. Fluorescence protection assay: a novel homogeneous assay platform toward development of aptamer sensors for protein detection. *Nucleic Acids Res.*, **2011**, *39*, e122-e122.

(69) Choi, J. H.; Chen, K. H.; Strano, M. S. Aptamer-capped nanocrystal quantum dots: a new method for label-free protein detection. *J. Am. Chem. Soc.*, **2006**, *128*, 15584-15585.

(70) Xu, G.; Hou, J.; Zhao, Y.; Bao, J.; Yang, M.; Fa, H.; Yang, Y.; Li, L.; Huo, D.; Hou, C. Dual-signal aptamer sensor based on polydopamine-gold nanoparticles and exonuclease I for ultrasensitive malathion detection. *Sensor Actuat B-Chem.*, **2019**.

(71) Feng, S.; Chen, C.; Wang, W.; Que, L. An aptamer nanopore-enabled microsensor for detection of theophylline. *Biosens. Bioelectron.*, **2018**, *105*, 36-41.

(72) Park, K. S. Nucleic acid aptamer-based methods for diagnosis of infections. *Biosens. Bioelectron.*, **2018**, *102*, 179-188.

(73) Zhao, Y.; Xu, D.; Tan, W. Aptamer-functionalized nano/micro-materials for clinical diagnosis: isolation, release and bioanalysis of circulating tumor cells. *Integr. Biol.*, **2017**, *9*, 188-205.

(74) Thiviyanathan, V.; Gorenstein, D. G. Aptamers and the next generation of diagnostic reagents. *Proteomics Clin Appl.*, **2012**, *6*, 563-573.

(75) Turner, D. J.; Tuytten, R.; Janssen, K. P. F.; Lammertyn, J.; Wuyts, J.; Pollet, J.; Eyckerman, S.; Brown, C.; Kas, K. Toward clinical proteomics on a next-generation sequencing platform. *Anal Chem.*, **2011**, *83*, 666-670.

(76) Ostroff, R. M.; Bigbee, W. L.; Franklin, W.; Gold, L.; Mehan, M.; Miller, Y. E.; Pass, H. I.; Rom, W. N.; Siegfried, J. M.; Stewart, A.; Walker, J. J.; Weissfeld, J. L.; Williams, S.; Zichi, D.; Brody, E. N. Unlocking biomarker discovery: large scale application of aptamer proteomic technology for early detection of lung cancer. *PLoS One*, **2010**, *5*, e15003.

(77) Chang, Y. M.; Donovan, M. J.; Tan, W. Using aptamers for cancer biomarker discovery. *J Nucleic Acids.*, **2013**, *2013*, 817350-817350.

(78) Chen, M.; Bi, S.; Jia, X.; He, P. Aptamer-conjugated bio-bar-code Au-Fe_3O_4 nanoparticles as amplification station for electrochemiluminescence detection of tumor cells. *Anal. Chim. Acta.*, **2014**, *837*, 44-51.

(79) Meng, X.; Liu, Z.; Cao, Y.; Dai, W.; Zhang, K.; Dong, H.; Feng, X.; Zhang, X. Fabricating aptamer-conjugated PEGylated-MoS_2/$Cu_{1.8}S$ theranostic nanoplatform for multiplexed imaging diagnosis and chemo-photothermal therapy of cancer. *Adv. Funct. Mater.*, **2017**, *27*, 1605592.

(80) Keefe, A. D.; Pai, S.; Ellington, A. Aptamers as therapeutics. *Nat Rev Drug Discov.*, **2010**, *9*, 537.

(81) Ni, X.; Castanares, M.; Mukherjee, A.; Lupold, S. E. Nucleic acid aptamers: clinical applications and promising new horizons. *Curr Med Chem.*, **2011**, *18*, 4206-4214.

(82) Parashar, A. Aptamers in therapeutics. *J Clin Diagn Res.*, **2016**, *10*, BE01-BE06.

(83) Sun, H.; Zu, Y. Aptamers and their applications in nanomedicine. *Small*, **2015**, *11*, 2352-2364.

(84) Amaya-González, S.; de-los-Santos-Alvarez, N.; Miranda-Ordieres, A. J.; Lobo-Castañón, M. J. Aptamer-based analysis: a promising alternative for food safety control. *Sensors*, **2013**, *13*, 16292-16311.

(85) Wu, J.; Zhu, Y.; Xue, F.; Mei, Z.; Yao, L.; Wang, X.; Zheng, L.; Liu, J.; Liu, G.; Peng, C.; Chen, W. Recent trends in SELEX technique and its application to food safety monitoring. *Mikrochim Acta.*, **2014**, *181*, 479-491.

(86) Liu, Q.; Jin, C.; Wang, Y.; Fang, X.; Zhang, X.; Chen, Z.; Tan, W. Aptamer-conjugated nanomaterials for specific cancer cell recognition and targeted cancer therapy. *NPG Asia Mater.*, **2014**, *6*, e95.

(87) Zhu, G.; Zheng, J.; Song, E.; Donovan, M.; Zhang, K.; Liu, C.; Tan, W. Self-assembled, aptamer-tethered DNA nanotrains for targeted transport of molecular drugs in cancer theranostics. *Proc. Natl. Acad. Sci. U.S.A.*, **2013**, *110*, 7998-8003.

(88) Ray, P.; White, R. R. Aptamers for targeted drug delivery. *Pharmaceuticals*, **2010**, *3*, 1761-1778.

(89) Liu, J.; Wei, T.; Zhao, J.; Huang, Y.; Deng, H.; Kumar, A.; Wang, C.; Liang, Z.; Ma, X.; Liang, X.-J. Multifunctional aptamer-based nanoparticles for targeted drug delivery to circumvent cancer resistance. *Biomaterials*, **2016**, *91*, 44-56.

(90) Bunka, D. H. J.; Stockley, P. G. Aptamers come of age-at last. *Nat Rev Microbiol.*, **2006**, *4*, 588.

(91) Esposito, C.; Catuogno, S.; de Franciscis, V.; Cerchia, L.: New insight into clinical development of nucleic acid aptamers. *Discov Med.*, 2011; Vol. 11.

(92) Rosenberg, J. E.; Bambury, R. M.; Van Allen, E. M.; Drabkin, H. A.; Lara, P. N., Jr.; Harzstark, A. L.; Wagle, N.; Figlin, R. A.; Smith, G. W.; Garraway, L. A.; Choueiri, T.; Erlandsson, F.; Laber, D. A. A phase II trial of AS1411 (a novel nucleolin-targeted DNA aptamer) in metastatic renal cell carcinoma. *Invest New Drugs.*, **2014**, *32*, 178-187.

(93) Ruiz Ciancio, D.; Vargas, M. R.; Thiel, W. H.; Bruno, M. A.; Giangrande, P. H.; Mestre, M. B. Aptamers as diagnostic tools in cancer. *Pharmaceuticals*, **2018**, *11*, 86.

(94) Hall, R. H.; Todd, A.; Webb, R. F. 644. Nucleotides. Part XLI. Mixed anhydrides as intermediates in the synthesis of dinucleoside phosphates. *J. Chem. Soc.*, **1957**, 3291-3296.

(95) Michelson, A. M.; Todd, A. R. Nucleotides part XXXII. Synthesis of a dithymidine dinucleotide containing a 3′: 5′-internucleotidic linkage. *J. Chem. Soc.*, **1955**, 2632-2638.

(96) Letsinger, R. L.; Mahadevan, V. Stepwise synthesis of oligodeoxyribonucleotides on an insoluble polymer support[1,2]. *J. Am. Chem. Soc.*, **1966**, *88*, 5319-5324.

(97) Beaucage, S. L.; Caruthers, M. H. Deoxynucleoside phosphoramidites–a new class of key intermediates for deoxypolynucleotide synthesis. *Tetrahedron Lett.*, **1981**, *22*, 1859-1862.

(98) Reese, C. B. Oligo- and poly-nucleotides: 50 years of chemical synthesis. *Org. Biomol. Chem.*, **2005**, *3*, 3851-3868.

(99) Finn, P. J.; Gibson, N. J.; Fallon, R.; Hamilton, A.; Brown, T. Synthesis and properties of DNA-PNA chimeric oligomers. *Nucleic Acids Res.*, **1996**, *24*, 3357-3363.

(100) Sonveaux, E. The organic chemistry underlying DNA synthesis. *Bioorg Chem.*, **1986**, *14*, 274-325.

(101) Vongsutilers, V.; Daft, J. R.; Shaughnessy, K. H.; Gannett, P. M. A general synthesis of C8-arylpurine phosphoramidites. *Molecules*, **2009**, *14*, 3339-3352.

(102) Merrifield, R. B. Automated synthesis of peptides. *Science*, **1965**, *150*, 178-185.

(103) Caruthers, Marvin H. A brief review of DNA and RNA chemical synthesis. *Biochem. Soc. Trans.*, **2011**, *39*, 575-580.

(104) Caruthers, M. H. The chemical synthesis of DNA/RNA: our gift to science. *J. Biol. Chem.*, **2013**, *288*, 1420-1427.

(105) Sproat, B. S.: RNA synthesis using 2′-O-(tert-butyldimethylsilyl) protection. *Oligonucleotide synthesis*. Humana Press, **2005**, 17-31.

(106) Xiong, A.-S.; Peng, R.-H.; Zhuang, J.; Liu, J.-G.; Gao, F.; Chen, J.-M.; Cheng, Z.-M.; Yao, Q.-H. Non-polymerase-cycling-assembly-based chemical gene synthesis: strategies, methods, and progress. *Biotechnol. Adv.*, **2008**, *26*, 121-134.

(107) Kok, S. d.; Stanton, L. H.; Slaby, T.; Durot, M.; Holmes, V. F.; Patel, K. G.; Platt, D.; Shapland, E. B.; Serber, Z.; Dean, J.; Newman, J. D.; Chandran, S. S. Rapid and reliable DNA assembly *via* ligase cycling reaction. *ACS Synth. Biol.*, **2014**, *3*, 97-106.

(108) Pawlowska, R.; Korczynski, D.; Nawrot, B.; Stec, W. J.; Chworos, A. The α-thio and/or β-γ-hypophosphate analogs of ATP as cofactors of T4 DNA ligase. *Bioorg Chem.*, **2016**, *67*, 110-115.

(109) Timson, D. J.; Singleton, M. R.; Wigley, D. B. DNA ligases in the repair and replication of DNA. *Mutat. Res.*, **2000**, *460*, 301-318.

(110) Lohman, G. J. S.; Chen, L.; Evans, T. C. Kinetic characterisation of single strand break ligation in duplex DNA by T4 DNA ligase. *J. Biol. Chem.*, **2011**, *286*, 44187-44196.

(111) Martin, I. V.; MacNeill, S. A. ATP-dependent DNA ligases. *Genome Biol.*, **2002**, *3*, reviews3005-1.

(112) Kolb, H. C.; Finn, M. G.; Sharpless, K. B. Click chemistry: diverse chemical function from a few good reactions. *Angew. Chem., Int. Ed.*, **2001**, *40*, 2004-2021.

(113) Liang, L.; Astruc, D. The copper(I)-catalyzed alkyne-azide cycloaddition (CuAAC) “click” reaction and its applications. An overview. *Coordin Chem Rev.*, **2011**, *255*, 2933-2945.

(114) Rostovtsev, V. V.; Green, L. G.; Fokin, V. V.; Sharpless, K. B. A stepwise huisgen cycloaddition process: copper(I)-catalysed regioselective "ligation" of azides and terminal alkynes. *Angew. Chem., Int. Ed.,* **2002**, *41*, 2596-2599.

(115) Fujino, T.; Yamazaki, N.; Isobe, H. Convergent synthesis of oligomers of triazole-linked DNA analogue (TLDNA) in solution phase. *Tetrahedron Lett.,* **2009**, *50*, 4101-4103.

(116) Isobe, H.; Fujino, T.; Yamazaki, N.; Guillot-Nieckowski, M.; Nakamura, E. Triazole-linked analogue of deoxyribonucleic acid (TLDNA): design, synthesis, and double-strand formation with natural DNA. *Org. Lett.,* **2008**, *10*, 3729-3732.

(117) Isobe, H.; Fujino, T.; Miyauchi, Y.; Tsunaka, N.; Okada, K.: Post-modification of triazole-linked analogues of DNA for positively charged variants. *Heterocycles,* **2013**, *87*, 1023-1028.

(118) El-Sagheer, A. H.; Brown, T. A triazole linkage that mimics the DNA phosphodiester group in living systems. *Q Rev Biophys.,* **2015**, *48*, 429-436.

(119) El-Sagheer, A. H.; Sanzone, A. P.; Gao, R.; Tavassoli, A.; Brown, T. Biocompatible artificial DNA linker that is read through by DNA polymerases and is functional in Escherichia coli. *Proc. Natl. Acad. Sci. U. S. A.,* **2011**, *108*, 11338-11343.

(120) El-Sagheer, A. H.; Brown, T. Efficient RNA synthesis by *in vitro* transcription of a triazole-modified DNA template. *Chem. Commun.,* **2011**, *47*, 12057-12058.

(121) Birts, C. N.; Sanzone, A. P.; El-Sagheer, A. H.; Blaydes, J. P.; Brown, T.; Tavassoli, A. Transcription of click-linked DNA in human cells. *Angew. Chem., Int. Ed.,* **2014**, *53*, 2362-2365.

(122) Kukwikila, M.; Gale, N.; El-Sagheer, A. H.; Brown, T.; Tavassoli, A. Assembly of a biocompatible triazole-linked gene by one-pot click-DNA ligation. *Nat. Chem.,* **2017**, *9*, 1089.

(123) Taemaitree, L.; Shivalingam, A.; El-Sagheer, A. H.; Brown, T. An artificial triazole backbone linkage provides a split-and-click strategy to bioactive chemically modified CRISPR sgRNA. *Nat Commun.,* **2019**, *10*, 1610.

(124) Kalinowski, M.; Haug, R.; Said, H.; Piasecka, S.; Kramer, M.; Richert, C. Phosphoramidate ligation of oligonucleotides in nanoscale structures. *ChemBioChem,* **2016**, *17*, 1150-1155.

(125) El-Sagheer, A. H.; Brown, T. Single tube gene synthesis by phosphoramidate chemical ligation. *Chem. Commun.,* **2017**, *53*, 10700-10702.

(126) De Mesmaeker, A.; Waldner, A.; Lebreton, J.; Hoffmann, P.; Fritsch, V.; Wolf, R. M.; Freier, S. M. Amides as a new type of backbone modification in oligonucleotides. *Angew Chem Int Ed Engl.,* **1994**, *33*, 226-229.

(127) Kuwahara, M.; Takeshima, H.; Nagashima, J.-i.; Minezaki, S.; Ozaki, H.; Sawai, H. Transcription and reverse transcription of artificial nucleic acids involving backbone modification by template-directed DNA polymerase reactions. *Bioorganic Med. Chem.,* **2009**, *17*, 3782-3788.

(128) Shivalingam, A.; Tyburn, A. E. S.; El-Sagheer, A. H.; Brown, T. Molecular requirements of high-fidelity replication-competent DNA backbones for orthogonal chemical ligation. *J. Am. Chem. Soc.,* **2017**, *139*, 1575-1583.

(129) Wang, S.; Kool, E. T. Circular RNA oligonucleotides. Synthesis, nucleic acid binding properties, and a comparison with circular DNAs. *Nucleic Acids Res.*, **1994**, *22*, 2326-2333.

(130) Pedroso, E.; Escaja, N.; Frieden, M.; Grandas, A.: Solid-phase synthesis of circular oligonucleotides. *Oligonucleotide synthesis*. Humana Press, **2005**, 101-125.

(131) Kool, E. T. Recognition of DNA, RNA, and proteins by circular oligonucleotides. *Acc. Chem. Res.*, **1998**, *31*, 502-510.

(132) Kool, E. T. Circular oligonucleotides: new concepts in oligonucleotide design. *Annu. Rev. Biophys. Biomol. Struct.*, **1996**, *25*, 1-28.

(133) Rowley, P. T.; Kosciolek, B. A.; Kool, E. T. Circular antisense oligonucleotides inhibit growth of chronic myeloid leukemia cells. *Mol Med.*, **1999**, *5*, 693-700.

(134) Rumney, S. t.; Kool, E. T. DNA recognition by hybrid oligoether-oligodeoxynucleotide macrocycles. *Angew. Chem., Int. Ed.*, **1992**, *31*, 1617-1619.

(135) Roulon, T.; Hélène, C.; Escudé, C. A ligand-modulated padlock oligonucleotide for supercoiled plasmids. *Angew. Chem., Int. Ed.*, **2001**, *40*, 1523-1526.

(136) Nilsson, M.; Krejci, K.; Koch, J.; Kwiatkowski, M.; Gustavsson, P.; Landegren, U. Padlock probes reveal single-nucleotide differences, parent of origin and in situ distribution of centromeric sequences in human chromosomes 13 and 21. *Nat Genet.*, **1997**, *16*, 252-255.

(137) Mazumder, A.; Uchida, H.; Neamati, N.; Sunder, S.; Jaworska-Maslanka, M.; Wickstrom, E.; Zeng, F.; Jones, R. A.; Mandes, R. F.; Chenault, H. K.; Pommier, Y. Probing interactions between viral DNA and human immunodeficiency virus type 1 integrase using dinucleotides. *Mol Pharmacol.*, **1997**, *51*, 567-575.

(138) Lizardi, P. M.; Huang, X.; Zhu, Z.; Bray-Ward, P.; Thomas, D. C.; Ward, D. C. Mutation detection and single-molecule counting using isothermal rolling-circle amplification. *Nat Genet.*, **1998**, *19*, 225.

(139) Abe, T.; Takai, K.; Nakada, S.; Yokota, T.; Takaku, H. Specific inhibition of influenza virus RNA polymerase and nucleoprotein gene expression by circular dumbbell RNA/DNA chimeric oligonucleotides containing antisense phosphodiester oligonucleotides. *FEBS Lett.*, **1998**, *425*, 91-96.

(140) Clusel, C.; Ugarte, E.; Enjolras, N.; Vasseur, M.; Blumenfeld, M. Ex vivo regulation of specific gene expression by nanomolar concentration of double-stranded dumbbell oligonucleotides. *Nucleic Acids Res.*, **1993**, *21*, 3405-3411.

(141) Kuai, H.; Zhao, Z.; Mo, L.; Liu, H.; Hu, X.; Fu, T.; Zhang, X.; Tan, W. Circular bivalent aptamers enable *in vivo* stability and recognition. *J. Am. Chem. Soc.*, **2017**, *139*, 9128-9131.

(142) Yang, L.; Kim, H. B.; Sul, J.-Y.; Yeldell, S. B.; Eberwine, J. H.; Dmochowski, I. J. Efficient synthesis of light-triggered circular antisense oligonucleotides targeting cellular protein expression. *ChemBioChem*, **2018**, *19*, 1250-1254.

(143) Jiang, Y.; Pan, X.; Chang, J.; Niu, W.; Hou, W.; Kuai, H.; Zhao, Z.; Liu, J.; Wang, M.; Tan, W. Supramolecularly engineered circular bivalent aptamer for enhanced functional protein delivery. *J. Am. Chem. Soc.*, **2018**, *140*, 6780-6784.

(144) Lu, C.-H.; Cecconello, A.; Elbaz, J.; Credi, A.; Willner, I. A three-station DNA catenane rotary motor with controlled directionality. *Nano Lett.,* **2013**, *13*, 2303-2308.

(145) Lu, C.-H.; Cecconello, A.; Qi, X.-J.; Wu, N.; Jester, S.-S.; Famulok, M.; Matthies, M.; Schmidt, T.-L.; Willner, I. Switchable reconfiguration of a seven-ring interlocked DNA catenane nanostructure. *Nano Lett.,* **2015**, *15*, 7133-7137.

(146) Valero, J.; Pal, N.; Dhakal, S.; Walter, N. G.; Famulok, M. A bio-hybrid DNA rotor–stator nanoengine that moves along predefined tracks. *Nat. Nanotechnol.,* **2018**, *13*, 496-503.

(147) Li, T.; Lohmann, F.; Famulok, M.: Interlocked DNA nanostructures controlled by a reversible logic circuit. *Nat Commun.,* **2014**, *5*, 4940.

(148) Zhao, Y.; Chen, F.; Li, Q.; Wang, L.; Fan, C. Isothermal amplification of nucleic acids. *Chem. Rev.,* **2015**, *115*, 12491-12545.

(149) Fire, A.; Xu, S. Q. Rolling replication of short DNA circles. *Proc. Natl. Acad. Sci. U.S.A.*, **1995**, *92*, 4641-4645.

(150) Liu, D.; Daubendiek, S. L.; Zillman, M. A.; Ryan, K.; Kool, E. T. Rolling circle DNA synthesis: small circular oligonucleotides as efficient templates for DNA polymerases. *J. Am. Chem. Soc.,* **1996**, *118*, 1587-1594.

(151) Kobori, T.; Takahashi, H. Expanding possibilities of rolling circle amplification as a biosensing platform. *Anal Sci.,* **2014**, *30*, 59-64.

(152) Demidov, V. V.; A. G.: Rolling circle amplification (RCA) toward new clinical diagnostics and therapeutics, *Springer*, **2018**.

(153) Yan, L.; Zhou, J.; Zheng, Y.; Gamson, A. S.; Roembke, B. T.; Nakayama, S.; Sintim, H. O. Isothermal amplified detection of DNA and RNA. *Mol Biosyst.,* **2014**, *10*, 970-1003.

(154) Mohsen, M. G.; Kool, E. T. The discovery of rolling circle amplification and rolling circle transcription. *Acc. Chem. Res.,* **2016**, *49*, 2540-2550.

(155) Ali, M. M.; Li, F.; Zhang, Z.; Zhang, K.; Kang, D.-K.; Ankrum, J. A.; Le, X. C.; Zhao, W. Rolling circle amplification: a versatile tool for chemical biology, materials science and medicine. *Chem. Soc. Rev.,* **2014**, *43*, 3324-3341.

(156) Lin, C.; Xie, M.; Chen, J. J. L.; Liu, Y.; Yan, H. Rolling-circle amplification of a DNA nanojunction. *Angew. Chem., Int. Ed.,* **2006**, *45*, 7537-7539.

(157) Lin, C.; Wang, X.; Liu, Y.; Seeman, N. C.; Yan, H. Rolling circle enzymatic replication of a complex multi-crossover DNA nanostructure. *J. Am. Chem. Soc.,* **2007**, *129*, 14475-14481.

(158) Zhang, D. Y.; Brandwein, M.; Hsuih, T.; Li, H. B. Ramification amplification: a novel isothermal DNA amplification method. *Mol Diagn.,* **2001**, *6*, 141-150.

(159) Kaocharoen, S.; Wang, B.; Tsui, K. M.; Trilles, L.; Kong, F.; Meyer, W. Hyperbranched rolling circle amplification as a rapid and sensitive method for species identification within the cryptococcus species complex. *Electrophoresis,* **2008**, *29*, 3183-3191.

(160) Ma, C.; Wang, W.; Yang, Q.; Shi, C.; Cao, L. Cocaine detection *via* rolling circle amplification of short DNA strand separated by magnetic beads. *Biosens. Bioelectron.,* **2011**, *26*, 3309-3312.

(161) Mikawa, T.; Inoue, J.; Shigemori, Y. Single-stranded DNA binding protein facilitates specific enrichment of circular DNA molecules using rolling circle amplification. *Anal. Biochem.,* **2009**, *391*, 81-84.

(162) Xu, W.; Xie, X.; Li, D.; Yang, Z.; Li, T.; Liu, X. Ultrasensitive colorimetric DNA detection using a combination of rolling circle amplification and nicking endonuclease-assisted nanoparticle amplification (NEANA). *Small,* **2012**, *8*, 1846-1850.

(163) Chapin, S. C.; Doyle, P. S. Ultrasensitive multiplexed microRNA quantification on encoded gel microparticles using rolling circle amplification. *Anal Chem.,* **2011**, *83*, 7179-7185.

(164) Li, J.; Deng, T.; Chu, X.; Yang, R.; Jiang, J.; Shen, G.; Yu, R. Rolling circle amplification combined with gold nanoparticle aggregates for highly sensitive identification of single-nucleotide polymorphisms. *Anal Chem.,* **2010**, *82*, 2811-2816.

(165) Cao, A.; Zhang, C.-y. Sensitive and label-free DNA methylation detection by ligation-mediated hyperbranched rolling circle amplification. *Anal Chem.,* **2012**, *84*, 6199-6205.

(166) Ding, C.; Liu, H.; Wang, N.; Wang, Z. Cascade signal amplification strategy for the detection of cancer cells by rolling circle amplification and nanoparticles tagging. *Chem. Commun.,* **2012**, *48*, 5019-5021.

(167) Larsson, C.; Koch, J.; Nygren, A.; Janssen, G.; Raap, A. K.; Landegren, U.; Nilsson, M. In situ genotyping individual DNA molecules by target-primed rolling-circle amplification of padlock probes. *Nat Methods.,* **2004**, *1*, 227.

(168) Zhao, W.; Ali, M. M.; Brook, M. A.; Li, Y. Rolling circle amplification: applications in nanotechnology and biodetection with functional nucleic acids. *Angew. Chem., Int. Ed.,* **2008**, *47*, 6330-6337.

(169) Ma, Y.; Zheng, H.; Wang, C.; Yan, Q.; Chao, J.; Fan, C.; Xiao, S.-J. RCA strands as scaffolds to create nanoscale shapes by a few staple strands. *J. Am. Chem. Soc.,* **2013**, *135*, 2959-2962.

(170) Hamblin, G. D.; Carneiro, K. M. M.; Fakhoury, J. F.; Bujold, K. E.; Sleiman, H. F. Rolling circle amplification-templated DNA nanotubes show increased stability and cell penetration ability. *J. Am. Chem. Soc.,* **2012**, *134*, 2888-2891.

(171) Zhang, K.; Deng, R.; Sun, Y.; Zhang, L.; Li, J. Reversible control of cell membrane receptor function using DNA nano-spring multivalent ligands. *Chem. Sci.,* **2017**, *8*, 7098-7105.

(172) Qi, H.; Ghodousi, M.; Du, Y.; Grun, C.; Bae, H.; Yin, P.; Khademhosseini, A. DNA-directed self-assembly of shape-controlled hydrogels. *Nat Commun.,* **2013**, *4*, 2275.

(173) Wilner, O. I.; Shimron, S.; Weizmann, Y.; Wang, Z.-G.; Willner, I. Self-assembly of enzymes on DNA scaffolds: en route to biocatalytic cascades and the synthesis of metallic nanowires. *Nano Lett.,* **2009**, *9*, 2040-2043.

(174) Hu, R.; Zhang, X.; Zhao, Z.; Zhu, G.; Chen, T.; Fu, T.; Tan, W. DNA nanoflowers for multiplexed cellular imaging and traceable targeted drug delivery. *Angew. Chem., Int. Ed.,* **2014**, *53*, 5821-5826.

(175) Meng, H.-M.; Liu, H.; Kuai, H.; Peng, R.; Mo, L.; Zhang, X.-B. Aptamer-integrated DNA nanostructures for biosensing, bioimaging and cancer therapy. *Chem. Soc. Rev.*, **2016**, *45*, 2583-2602.

(176) Zhao, W.; Gao, Y.; Kandadai, S. A.; Brook, M. A.; Li, Y. DNA polymerization on gold nanoparticles through rolling circle amplification: towards novel scaffolds for three-dimensional periodic nanoassemblies. *Angew. Chem., Int. Ed.,* **2006**, *45*, 2409-2413.

(177) Nilsen, T. W.; Grayzel, J.; Prensky, W. Dendritic nucleic acid structures. *J. Theor. Biol.,* **1997**, *187*, 273-284.

(178) Li, Y.; Tseng, Y. D.; Kwon, S. Y.; d'Espaux, L.; Bunch, J. S.; McEuen, P. L.; Luo, D. Controlled assembly of dendrimer-like DNA. *Nat. Mater.,* **2003**, *3*, 38.

(179) Meng, H.-M.; Zhang, X.; Lv, Y.; Zhao, Z.; Wang, N.-N.; Fu, T.; Fan, H.; Liang, H.; Qiu, L.; Zhu, G.; Tan, W. DNA dendrimer: an efficient nanocarrier of functional nucleic acids for intracellular molecular sensing. *ACS Nano,* **2014**, *8*, 6171-6181.

(180) Zhu, G.; Zhang, S.; Song, E.; Zheng, J.; Hu, R.; Fang, X.; Tan, W. Building fluorescent DNA nanodevices on target living cell surfaces. *Angew. Chem., Int. Ed.,* **2013**, *52*, 5490-5496.

(181) Li, Q.; Zhao, D.; Shao, X.; Lin, S.; Xie, X.; Liu, M.; Ma, W.; Shi, S.; Lin, Y. Aptamer-modified tetrahedral DNA nanostructure for tumor-targeted drug delivery. *ACS Appl. Mater. Interfaces.,* **2017**, *9*, 36695-36701.

(182) Lei, Y.; Qiao, Z.; Tang, J.; He, X.; Shi, H.; Ye, X.; Yan, L. a.; He, D.; Wang, K. DNA nanotriangle-scaffolded activatable aptamer probe with ultralow background and robust stability for cancer theranostics. *Theranostics,* **2018**, *8*, 4062-4071.

(183) Sun, W.; Lu, Y.; Gu, Z. Rolling circle replication for engineering drug delivery carriers. *Ther. Delivery.,* **2015**, *6*, 765-768.

(184) Kwak, M.; Herrmann, A. Nucleic acid amphiphiles: synthesis and self-assembled nanostructures. *Chem. Soc. Rev.*, **2011**, *40*, 5745-5755.

(185) Pei, H.; Zuo, X.; Zhu, D.; Huang, Q.; Fan, C. Functional DNA nanostructures for theranostic applications. *Acc. Chem. Res.,* **2014**, *47*, 550-559.

(186) Dentinger, P. M.; Simmons, B. A.; Cruz, E.; Sprague, M. DNA-mediated delivery of lipophilic molecules *via* hybridization to DNA-based vesicular aggregates. *Langmuir,* **2006**, *22*, 2935-2937.

(187) Wu, Y.; Sefah, K.; Liu, H.; Wang, R.; Tan, W. DNA aptamer–micelle as an efficient detection/delivery vehicle toward cancer cells. *Proc. Natl. Acad. Sci. U. S. A.,* **2010**, *107*, 5-10.

(188) Shieh, Y.-A.; Yang, S.-J.; Wei, M.-F.; Shieh, M.-J. Aptamer-based tumor-targeted drug delivery for photodynamic therapy. *ACS Nano,* **2010**, *4*, 1433-1442.

(189) Han, D.; Zhu, G.; Wu, C.; Zhu, Z.; Chen, T.; Zhang, X.; Tan, W. Engineering a cell-surface aptamer circuit for targeted and amplified photodynamic cancer therapy. *ACS Nano*, **2013**, *7*, 2312-2319.

(190) Liu, X.; Xu, Y.; Yu, T.; Clifford, C.; Liu, Y.; Yan, H.; Chang, Y. A DNA nanostructure platform for directed assembly of synthetic vaccines. *Nano Lett.*, **2012**, *12*, 4254-4259.

(191) Krieg, A. M. CpG motifs in bacterial DNA and their immune effects. *Annu Rev Immunol.*, **2002**, *20*, 709-760.

(192) Lv, Y.; Peng, R.; Zhou, Y.; Zhang, X.; Tan, W. Catalytic self-assembly of a DNA dendritic complex for efficient gene silencing. *Chem. Commun.*, **2016**, *52*, 1413-1415.

(193) Wang, Y.-M.; Wu, Z.; Liu, S.-J.; Chu, X. Structure-switching aptamer triggering hybridization chain reaction on the cell surface for activatable theranostics. *Anal Chem.*, **2015**, *87*, 6470-6474.

(194) Nahta, R.; Esteva, F. J. Trastuzumab: triumphs and tribulations. *Oncogene*, **2007**, *26*, 3637.

(195) Monsuez, J.-J.; Charniot, J.-C.; Vignat, N.; Artigou, J.-Y. Cardiac side-effects of cancer chemotherapy. *Int J Cardiol.*, **2010**, *144*, 3-15.

(196) Sun, H.; Zhu, X.; Lu, P. Y.; Rosato, R. R.; Tan, W.; Zu, Y. Oligonucleotide aptamers: new tools for targeted cancer therapy. *Mol Ther Nucleic Acids.*, **2014**, *3*, e182-e182.

(197) Prakash, J. S.; Rajamanickam, K. Aptamers and their significant role in cancer therapy and diagnosis. *Biomedicines*, **2015**, *3*, 248-269.

(198) Thiel, K. W.; Hernandez, L. I.; Dassie, J. P.; Thiel, W. H.; Liu, X.; Stockdale, K. R.; Rothman, A. M.; Hernandez, F. J.; McNamara, J. O., 2nd; Giangrande, P. H. Delivery of chemo-sensitizing siRNAs to HER2+-breast cancer cells using RNA aptamers. *Nucleic Acids Res.*, **2012**, *40*, 6319-6337.

(199) McNamara, J. O.; Kolonias, D.; Pastor, F.; Mittler, R. S.; Chen, L.; Giangrande, P. H.; Sullenger, B.; Gilboa, E. Multivalent 4-1BB binding aptamers costimulate CD8+ T cells and inhibit tumor growth in mice. *J Clin Invest.*, **2008**, *118*, 376-386.

(200) Wang, R.; Zhu, G.; Mei, L.; Xie, Y.; Ma, H.; Ye, M.; Qing, F.-L.; Tan, W. Automated modular synthesis of aptamer – drug conjugates for targeted drug delivery. *J. Am. Chem. Soc.*, **2014**, *136*, 2731-2734.

(201) Wu, C.; Han, D.; Chen, T.; Peng, L.; Zhu, G.; You, M.; Qiu, L.; Sefah, K.; Zhang, X.; Tan, W. Building a multifunctional aptamer-based DNA nanoassembly for targeted cancer therapy. *J. Am. Chem. Soc.*, **2013**, *135*, 18644-18650.

(202) Mahlknecht, G.; Maron, R.; Mancini, M.; Schechter, B.; Sela, M.; Yarden, Y. Aptamer to ErbB-2/HER2 enhances degradation of the target and inhibits tumorigenic growth. *Proc. Natl. Acad. Sci. U. S. A.*, **2013**, *110*, 8170-8175.

(203) Niazi, J. H.; Verma, S. K.; Niazi, S.; Qureshi, A. *In vitro* HER2 protein-induced affinity dissociation of carbon nanotube-wrapped anti-HER2 aptamers for HER2 protein detection. *Analyst*, **2015**, *140*, 243-249.

(204) Mahlknecht, G.; Maron, R.; Schechter, B.; Yarden, Y.; Sela, M. Multimerization of ERBB2/HER2 specific aptamer leads to improved receptor binding. *Biochem Biophys Res Commun.,* **2015**, *465*, 218-224.

(205) Iqbal, N.; Iqbal, N. Human epidermal growth factor receptor 2 (HER2) in cancers: overexpression and therapeutic implications. *Mol Biol Int.,* **2014**, *2014*, 852748-852748.

(206) Hu, Y.; Duan, J.; Cao, B.; Zhang, L.; Lu, X.; Wang, F.; Yao, F.; Zhu, Z.; Yuan, W.; Wang, C.; Yang, X.-D. Selection of a novel DNA thioaptamer against HER2 structure. *Clin Transl Oncol.,* **2015**, *17*, 647-656.

(207) Mahlknecht, G.; Maron, R.; Mancini, M.; Schechter, B.; Sela, M.; Yarden, Y. Aptamer to ErbB-2/HER2 enhances degradation of the target and inhibits tumorigenic growth. *Proc. Natl. Acad. Sci. U. S. A.,* **2013**, *110*, 8170-8175.

(208) Paramasivan, S.; Rujan, I.; Bolton, P. H. Circular dichroism of quadruplex DNAs: applications to structure, cation effects and ligand binding. *Methods,* **2007**, *43*, 324-331.

(209) Vorlíčková, M.; Kejnovská, I.; Bednářová, K.; Renčiuk, D.; Kypr, J. Circular dichroism spectroscopy of DNA: from duplexes to quadruplexes. *Chirality,* **2012**, *24*, 691-698.

(210) Yu, H.-Q.; Miyoshi, D.; Sugimoto, N. Characterisation of structure and stability of long telomeric DNA G-quadruplexes. *J. Am. Chem. Soc.,* **2006**, *128*, 15461-15468.

(211) Bhattacharyya, D.; Mirihana Arachchilage, G.; Basu, S. Metal cations in G-quadruplex folding and stability. *Front. Chem.,* **2016**, *4*, 38-38.

(212) Rujan, I. N.; Meleney, J. C.; Bolton, P. H. Vertebrate telomere repeat DNAs favor external loop propeller quadruplex structures in the presence of high concentrations of potassium. *Nucleic Acids Res.,* **2005**, *33*, 2022-2031.

(213) Kypr, J.; Kejnovská, I.; Renciuk, D.; Vorlícková, M. Circular dichroism and conformational polymorphism of DNA. *Nucleic Acids Res.,* **2009**, *37*, 1713-1725.

(214) Rangan, A.; Fedoroff, O. Y.; Hurley, L. H. Induction of duplex to G-quadruplex transition in the c-myc promoter region by a small molecule. *J. Biol. Chem.,* **2001**, *276*, 4640-4646.

(215) Li, Q.-J.; Tong, X.-J.; Duan, Y.-M.; Zhou, J.-Q. Characterization of the intramolecular G-quadruplex promoting activity of Est1. *FEBS Lett.,* **2013**, *587*, 659-665.

(216) Oganesian, L.; Moon, I. K.; Bryan, T. M.; Jarstfer, M. B. Extension of G-quadruplex DNA by ciliate telomerase. *EMBO J.,* **2006**, *25*, 1148-1159.

(217) Rachwal, P. A.; Fox, K. R. Quadruplex melting. *Methods,* **2007**, *43*, 291-301.

(218) Tran, P. L. T.; Mergny, J.-L.; Alberti, P. Stability of telomeric G-quadruplexes. *Nucleic Acids Res.,* **2011**, *39*, 3282-3294.

(219) Zhou, J.; Rossi, J. Aptamers as targeted therapeutics: current potential and challenges. *Nat Rev Drug Discov.,* **2017**, *16*, 181-202.

(220) Philippou, S.; Mastroyiannopoulos, N. P.; Makrides, N.; Lederer, C. W.; Kleanthous, M.; Phylactou, L. A. Selection and identification of skeletal-muscle-targeted RNA aptamers. *Mol Ther Nucleic Acids.,* **2018**, *10*, 199-214.

(221) Hernandez, L. I.; Flenker, K. S.; Hernandez, F. J.; Klingelhutz, A. J.; McNamara, J. O., 2nd; Giangrande, P. H. Methods for evaluating cell-specific, cell-internalising RNA aptamers. *Pharmaceuticals,* **2013**, *6*, 295-319.

(222) Macdonald, J.; Henri, J.; Roy, K.; Hays, E.; Bauer, M.; Veedu, R. N.; Pouliot, N.; Shigdar, S. EpCAM immunotherapy versus specific targeted delivery of drugs. *Cancers,* **2018**, *10*, 19.

(223) Wan, L.-Y.; Yuan, W.-F.; Ai, W.-B.; Ai, Y.-W.; Wang, J.-J.; Chu, L.-Y.; Zhang, Y.-Q.; Wu, J.-F. An exploration of aptamer internalization mechanisms and their applications in drug delivery. *Expert Opin. Drug Deliv.*, **2019**, *16*, 207-218.

(224) Baker, Y. R.; Chen, J.; Brown, J.; El-Sagheer, A. H.; Wiseman, P.; Johnson, E.; Goddard, P.; Brown, T. Preparation and characterization of manganese, cobalt and zinc DNA nanoflowers with tuneable morphology, DNA content and size. *Nucleic Acids Res.,* **2018**, *46*, 7495-7505.

(225) Sanchez, C.; Belleville, P.; Popall, M.; Nicole, L. Applications of advanced hybrid organic–inorganic nanomaterials: from laboratory to market. *Chem. Soc. Rev.,* **2011**, *40*, 696-753.

(226) Darder, M.; Aranda, P.; Ruiz-Hitzky, E. Bionanocomposites: a new concept of ecological, bioinspired, and functional hybrid materials. *Adv. Mater.*, **2007**, *19*, 1309-1319.

(227) Mohammed, L.; Gomaa, H. G.; Ragab, D.; Zhu, J. Magnetic nanoparticles for environmental and biomedical applications: A review. *Particuology,* **2017**, *30*, 1-14.

(228) Yoo, D.; Lee, J.-H.; Shin, T.-H.; Cheon, J. Theranostic magnetic nanoparticles. *Acc. Chem. Res.,* **2011**, *44*, 863-874.

(229) Hauser, A. K.; Wydra, R. J.; Stocke, N. A.; Anderson, K. W.; Hilt, J. Z. Magnetic nanoparticles and nanocomposites for remote controlled therapies. *J. Control. Release.,* **2015**, *219*, 76-94.

(230) Felfoul, O.; Becker, A. T.; Fagogenis, G.; Dupont, P. E. Simultaneous steering and imaging of magnetic particles using MRI toward delivery of therapeutics. *Sci. Rep,.* **2016**, *6*, 33567.

(231) Périgo, E. A.; Hemery, G.; Sandre, O.; Ortega, D.; Garaio, E.; Plazaola, F.; Teran, F. J. Fundamentals and advances in magnetic hyperthermia. *Appl. Phys. Rev.*, **2015**, *2*, 041302.

(232) Iranmanesh, M.; Hulliger, J. Magnetic separation: its application in mining, waste purification, medicine, biochemistry and chemistry. *Chem. Soc. Rev.,* **2017**, *46*, 5925-5934.

(233) Lin, M.; Lu, D.; Zhu, J.; Yang, C.; Zhang, Y.; Liu, Z. Magnetic enzyme nanogel (MENG): a universal synthetic route for biocatalysts. *Chem. Commun.*, **2012**, *48*, 3315-3317.

(234) Zhu, G.; Hu, R.; Zhao, Z.; Chen, Z.; Zhang, X.; Tan, W. Noncanonical self-assembly of multifunctional DNA nanoflowers for biomedical applications. *J. Am. Chem. Soc.*, **2013**, *135*, 16438-16445.

(235) Shopsowitz, K. E.; Roh, Y. H.; Deng, Z. J.; Morton, S. W.; Hammond, P. T. RNAi-microsponges form through self-assembly of the organic and inorganic products of transcription. *Small,* **2014**, *10*, 1623-1633.

(236) Lee, J. B.; Hong, J.; Bonner, D. K.; Poon, Z.; Hammond, P. T. Self-assembled RNA interference microsponges for efficient siRNA delivery. *Nat. Mater.,* **2012**, *11*, 316.

(237) Roh, Y. H.; Deng, J. Z.; Dreaden, E. C.; Park, J. H.; Yun, D. S.; Shopsowitz, K. E.; Hammond, P. T. A multi-RNAi microsponge platform for simultaneous controlled delivery of multiple small interfering RNAs. *Angew. Chem., Int. Ed.,* **2016**, *55*, 3347-3351.

(238) Jin, Y.; Li, Z.; Liu, H.; Chen, S.; Wang, F.; Wang, L.; Li, N.; Ge, K.; Yang, X.; Liang, X.-J.; Zhang, J. Biodegradable, multifunctional DNAzyme nanoflowers for enhanced cancer therapy. *NPG Asia Mater.,* **2017**, *9*, e365.

(239) Kim, E.; Zwi-Dantsis, L.; Reznikov, N.; Hansel, C. S.; Agarwal, S.; Stevens, M. M. One-pot synthesis of multiple protein-encapsulated DNA flowers and their application in intracellular protein delivery. *Adv. Mater.,* **2017**, *29*, 1701086.

(240) Roh, Y. H.; Lee, J. B.; Shopsowitz, K. E.; Dreaden, E. C.; Morton, S. W.; Poon, Z.; Hong, J.; Yamin, I.; Bonner, D. K.; Hammond, P. T. Layer-by-layer assembled antisense DNA microsponge particles for efficient delivery of cancer therapeutics. *ACS Nano,* **2014**, *8*, 9767-9780.

(241) Lv, Y.; Hu, R.; Zhu, G.; Zhang, X.; Mei, L.; Liu, Q.; Qiu, L.; Wu, C.; Tan, W. Preparation and biomedical applications of programmable and multifunctional DNA nanoflowers. *Nat. Protoc.,* **2015**, *10*, 1508-1524.

(242) Zhang, Z.; Zhang, Y.; Song, R.; Wang, M.; Yan, F.; He, L.; Feng, X.; Fang, S.; Zhao, J.; Zhang, H. Manganese(II) phosphate nanoflowers as electrochemical biosensors for the high-sensitivity detection of ractopamine. *Sensor Actuat B-Chem.,* **2015**, *211*, 310-317.

(243) Kim, H.; Park, J.; Park, I.; Jin, K.; Jerng, S. E.; Kim, S. H.; Nam, K. T.; Kang, K. Coordination tuning of cobalt phosphates towards efficient water oxidation catalyst. *Nat Commun.,* **2015**, *6*, 8253.

(244) Pang, H.; Yan, Z.; Ma, Y.; Li, G.; Chen, J.; Zhang, J.; Du, W.; Li, S. Cobalt pyrophosphate nano/microstructures as promising electrode materials of supercapacitor. *J. Solid State Electrochem.,* **2013**, *17*, 1383-1391.

(245) Dumont, M. F.; Baligand, C.; Li, Y.; Knowles, E. S.; Meisel, M. W.; Walter, G. A.; Talham, D. R. DNA surface modified gadolinium phosphate nanoparticles as MRI contrast agents. *Bioconjugate Chem.,* **2012**, *23*, 951-957.

(246) Fishbane, S. N.; Singh, A. K.; Cournoyer, S. H.; Jindal, K. K.; Fanti, P.; Guss, C. D.; Lin, V. H.; Pratt, R. D.; Gupta, A. Ferric pyrophosphate citrate (Triferic™) administration *via* the dialysate maintains hemoglobin and iron balance in chronic hemodialysis patients. *Nephrol Dial Transplant.,* **2015**, *30*, 2019-2026.

(247) Doat, A.; Pellé, F.; Lebugle, A. Europium-doped calcium pyrophosphates: allotropic forms and photoluminescent properties. *J. Solid State Chem.,* **2005**, *178*, 2354-2362.

(248) Wang, P.; Zhao, L.; Liu, J.; Weir, M. D.; Zhou, X.; Xu, H. H. K. Bone tissue engineering *via* nanostructured calcium phosphate biomaterials and stem cells. *Bone Res.*, **2014**, *2*, 14017-14017.

(249) Vashishtha, A. K.; Wang, J.; Konigsberg, W. H. Different divalent cations alter the kinetics and fidelity of DNA polymerases. *J Biol Chem.*, **2016**, *291*, 20869-20875.

(250) Ducani, C.; Bernardinelli, G.; Högberg, B. Rolling circle replication requires single-stranded DNA binding protein to avoid termination and production of double-stranded DNA. *Nucleic Acids Res.*, **2014**, *42*, 10596-10604.

(251) Lee, J. S.; Kim, H.; Jo, C.; Jeong, J.; Ko, J.; Han, S.; Lee, M. S.; Lee, H.-Y.; Han, J. W.; Lee, J.; Lee, J. B. Enzyme-driven hasselback-like DNA-based inorganic superstructures. *Adv. Funct. Mater.*, **2017**, *27*, 1704213.

(252) Guo, Y.; Wang, Y.; Li, S.; Niu, L.; Wei, D.; Zhang, S. DNA-spheres decorated with magnetic nanocomposites based on terminal transfer reactions for versatile target detection and cellular targeted drug delivery. *Chem. Commun.*, **2017**, *53*, 4826-4829.

(253) Guo, Y.; Li, S.; Wang, Y.; Zhang, S. Diagnosis-therapy integrative systems based on magnetic RNA nanoflowers for co-drug delivery and targeted therapy. *Anal Chem.*, **2017**, *89*, 2267-2274.

(254) Chen, J.; Baker, Y. R.; Brown, A.; El-Sagheer, A. H.; Brown, T. Enzyme-free synthesis of cyclic single-stranded DNA constructs containing a single triazole, amide or phosphoramidate backbone linkage and their use as templates for rolling circle amplification and nanoflower formation. *Chem. Sci.*, **2018**, *9*, 8110-8120.

(255) An, R.; Li, Q.; Fan, Y.; Li, J.; Pan, X.; Komiyama, M.; Liang, X. Highly efficient preparation of single-stranded DNA rings by T4 ligase at abnormally low Mg(II) concentration. *Nucleic Acids Res.*, **2017**, *45*, e139-e139.

(256) Cui, Y.; Han, X.; An, R.; Zhou, G.; Komiyama, M.; Liang, X. Cyclization of secondarily structured oligonucleotides to single-stranded rings by using Taq DNA ligase at high temperatures. *RSC Adv.*, **2018**, *8*, 18972-18979.

(257) Prakash, G.; Kool, E. T. Structural effects in the recognition of DNA by circular oligonucleotides. *J. Am. Chem. Soc.*, **1992**, *114*, 3523-3527.

(258) El-Sagheer, A. H.; Brown, T. Click nucleic acid ligation: applications in biology and nanotechnology. *Acc. Chem. Res.*, **2012**, *45*, 1258-1267.

(259) Gryaznov, S. M.; Letsinger, R. L. Synthesis and properties of oligonucleotides containing aminodeoxythymidine units. *Nucleic Acids Res.*, **1992**, *20*, 3403-3409.

(260) Sanzone, A. P.; El-Sagheer, A. H.; Brown, T.; Tavassoli, A. Assessing the biocompatibility of click-linked DNA in Escherichia coli. *Nucleic Acids Res.*, **2012**, *40*, 10567-10575.

(261) Shivalingam, A.; Brown, T. Synthesis of chemically modified DNA. *Biochem. Soc. Trans.*, **2016**, *44*, 709-715.

(262) Li, Y.; Pu, Q.; Li, J.; Zhou, L.; Tao, Y.; Li, Y.; Yu, W.; Xie, G. An "off-on" fluorescent switch assay for microRNA using nonenzymatic ligation-rolling circle amplification. *Microchim. Acta*, **2017**, *184*, 4323-4330.

(263) Zuker, M. Mfold web server for nucleic acid folding and hybridization prediction. *Nucleic Acids Res.*, **2003**, *31*, 3406-3415.

(264) Ferreira, C. S. M.; Cheung, M. C.; Missailidis, S.; Bisland, S.; Gariépy, J. Phototoxic aptamers selectively enter and kill epithelial cancer cells. *Nucleic Acids Res.*, **2009**, *37*, 866-876.

(265) Sun, W.; Jiang, T.; Lu, Y.; Reiff, M.; Mo, R.; Gu, Z. Cocoon-like self-degradable DNA nanoclew for anticancer drug delivery. *J. Am. Chem. Soc.*, **2014**, *136*, 14722-14725.

(266) Liu, Y.; Kuzuya, A.; Sha, R.; Guillaume, J.; Wang, R.; Canary, J. W.; Seeman, N. C. Coupling across a DNA helical turn yields a hybrid DNA/organic catenane doubly tailed with functional termini. *J. Am. Chem. Soc.*, **2008**, *130*, 10882-10883.

(267) Liang, X.; Kuhn, H.; Frank-Kamenetskii, M. D. Monitoring single-stranded DNA secondary structure formation by determining the topological state of DNA catenanes. *Biophys. J.*, **2006**, *90*, 2877-2889.

(268) Billen, L. P.; Li, Y. Synthesis and characterization of topologically linked single-stranded DNA rings. *Bioorg Chem.*, **2004**, *32*, 582-598.

(269) Wu, Z.-S.; Shen, Z.; Tram, K.; Li, Y. Engineering interlocking DNA rings with weak physical interactions. *Nat Commun.*, **2014**, *5*, 4279.

(270) Liu, M.; Zhang, Q.; Li, Z.; Gu, J.; Brennan, J. D.; Li, Y. Programming a topologically constrained DNA nanostructure into a sensor. *Nat Commun.*, **2016**, *7*, 12074.

(271) Gilham, P. T. An addition reaction specific for uridine and guanosine nucleotides and its application to the modification of ribonuclease action. *J. Am. Chem. Soc.*, **1962**, *84*, 687-688.

(272) Ho, N. W. Y.; Gilham, P. T. The reversible chemical modification of uracil, thymine, and guanine nucleotides and the modification of the action of ribonuclease on ribonucleic acid*. *Biochemistry*, **1967**, *6*, 3632-3639.

(273) Shabarova, Z. A.; Dolinnaya, N. G.; Drutsa, V. L.; Mehiikova, N. P.; Purmal, A. A. DNA-like duplexes with repetitions. III. efficient template-guided chemical polymerization of d(TGGCCAAGCTp). *Nucleic Acids Res.*, **1981**, *9*, 5747-5761.

(274) Dolinnaya, N. G.; Sokolova, N. I.; Gryaznova, O. I.; Shabarova, Z. A. Site-directed modification of DNA duplexes by chemical ligation. *Nucleic Acids Res.*, **1988**, *16*, 3721-3738.

(275) Franzini, R. M.; Samain, F.; Abd Elrahman, M.; Mikutis, G.; Nauer, A.; Zimmermann, M.; Scheuermann, J.; Hall, J.; Neri, D. Systematic evaluation and optimisation of modification reactions of oligonucleotides with amines and carboxylic acids for the synthesis of DNA-encoded chemical libraries. *Bioconjugate Chem.*, **2014**, *25*, 1453-1461.

(276) Dean, F. B.; Nelson, J. R.; Giesler, T. L.; Lasken, R. S. Rapid amplification of plasmid and phage DNA using Phi 29 DNA polymerase and multiply-primed rolling circle amplification. *Genome Res.*, **2001**, *11*, 1095-1099.

(277) Ririe, K. M.; Rasmussen, R. P.; Wittwer, C. T. Product differentiation by analysis of DNA melting curves during the polymerase chain reaction. *Anal. Biochem.*, **1997**, *245*, 154-160.

(278) Tuma, R. S.; Beaudet, M. P.; Jin, X.; Jones, L. J.; Cheung, C.-Y.; Yue, S.; Singer, V. L. Characterization of SYBR Gold nucleic acid gel stain: a dye optimized for use with 300-nm ultraviolet transilluminators. *Anal. Biochem.*, **1999**, *268*, 278-288.

(279) Battaglia, C.; Salani, G.; Consolandi, C.; Bernardi, L. R.; Bellis, G. D. Analysis of DNA microarrays by non-destructive fluorescent staining using SYBR® Green II. *BioTechniques*, **2000**, *29*, 78-81.

(280) Kielkowski, P.; Fanfrlík, J.; Hocek, M. 7-Aryl-7-deazaadenine 2′-deoxyribonucleoside triphosphates (dNTPs): better substrates for DNA polymerases than dATP in competitive incorporations. *Angew. Chem., Int. Ed.*, **2014**, *53*, 7552-7555.

(281) Cahová, H.; Panattoni, A.; Kielkowski, P.; Fanfrlík, J.; Hocek, M. 5-substituted pyrimidine and 7-substituted 7-deazapurine dNTPs as substrates for DNA polymerases in competitive primer extension in the presence of natural dNTPs. *ACS Chem. Biol.*, **2016**, *11*, 3165-3171.

(282) Lee, J. H.; Ku, S. H.; Kim, M. J.; Lee, S. J.; Kim, H. C.; Kim, K.; Kim, S. H.; Kwon, I. C. Rolling circle transcription-based polymeric siRNA nanoparticles for tumor-targeted delivery. *J. Control. Release.*, **2017**, *263*, 29-38.

(283) Zhang, L.; Zhu, G.; Mei, L.; Wu, C.; Qiu, L.; Cui, C.; Liu, Y.; Teng, I. T.; Tan, W. Self-assembled DNA immunonanoflowers as multivalent CpG nanoagents. *ACS Appl. Mater. Interfaces.*, **2015**, *7*, 24069-24074.

Appendix

Appendix

8.1 Authority permission for figure reuse

Copyright Clearance Center

Note: Copyright.com supplies permissions but not the copyrighted content itself.

1 PAYMENT 2 REVIEW 3 CONFIRMATION

Step 3: Order Confirmation

Thank you for your order! A confirmation for your order will be sent to your account email address. If you have questions about your order, you can call us 24 hrs/day, M-F at +1.855.239.3415 Toll Free, or write to us at info@copyright.com. This is not an invoice.

Confirmation Number: 11804346
Order Date: 04/03/2019

If you paid by credit card, your order will be finalized and your card will be charged within 24 hours. If you choose to be invoiced, you can change or cancel your order until the invoice is generated.

Payment Information

Jinfeng Chen
jinfeng.chen@stx.ox.ac.uk
+44 7526814876
Payment Method: n/a

Order Details

Chemical Society reviews

Order detail ID:	71868325
Order License Id:	4561280469451
ISSN:	0306-0012
Publication Type:	Journal
Volume:	
Issue:	
Start page:	
Publisher:	ROYAL SOCIETY OF CHEMISTRY, ETC.]
Author/Editor:	CHEMICAL SOCIETY (GREAT BRITAIN)

Permission Status: Granted

Permission type: Republish or display content
Type of use: Thesis/Dissertation

View details

Creative Commons License Deed

Attribution 4.0 International (CC BY 4.0)

This is a human-readable summary of (and not a substitute for) the license.

You are free to:

Share — copy and redistribute the material in any medium or format

Adapt — remix, transform, and build upon the material

for any purpose, even commercially.

The licensor cannot revoke these freedoms as long as you follow the license terms.

Under the following terms:

Attribution — You must give appropriate credit, provide a link to the license, and indicate if changes were made. You may do so in any reasonable manner, but not in any way that suggests the licensor endorses you or your use.

No additional restrictions — You may not apply legal terms or technological measures that legally restrict others from doing anything the license permits.

8.2 Agarose gel analysis for Mn^{2+} screening experiments

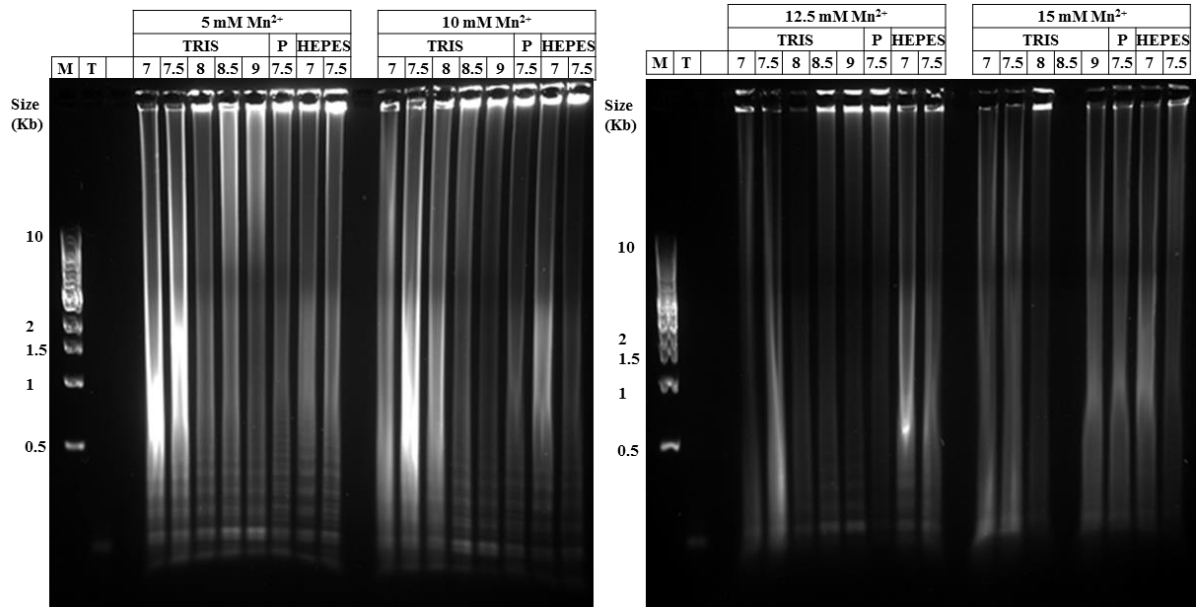


Figure 8.2.1. 0.8% agarose gel analysis of supernatant from Bst 2.0 DNA polymerase catalysed RCA with Mn^{2+} as the cofactor. M: 1 Kb DNA ladder; T: cyclic template T1; P: PIPES; numbers above lanes represent the buffer pH.

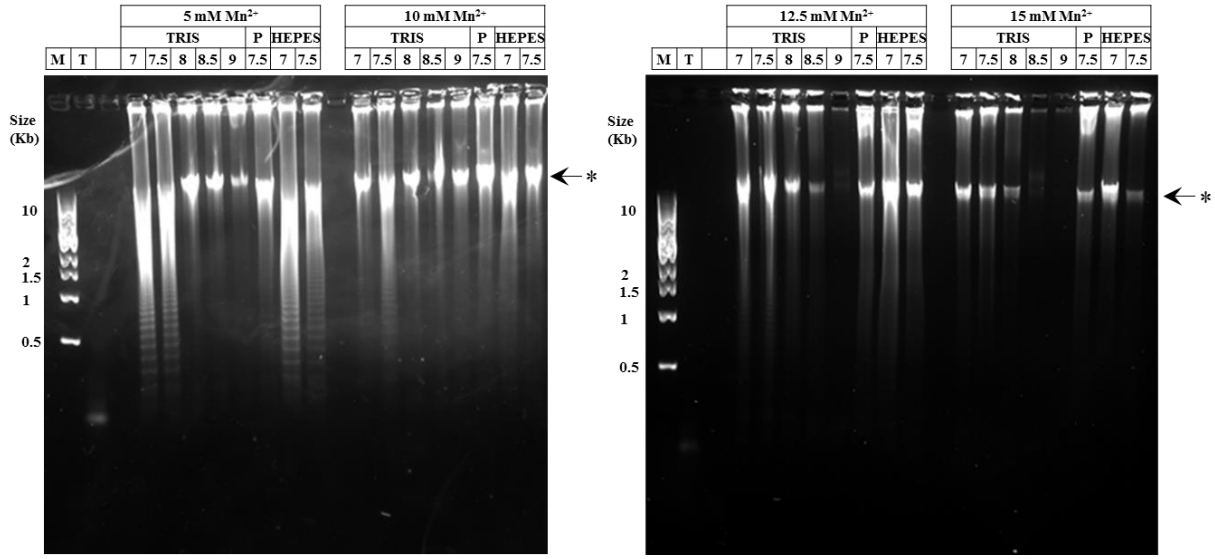


Figure 8.2.2. 0.8% agarose gel analysis of supernatant from Φ-29 DNA polymerase catalysed RCA with Mn^{2+} as the cofactor. M: 1 Kb DNA ladder; T: cyclic template T1; P: PIPES; *: this band is assigned to double-stranded products.[250] Numbers above lanes represent the buffer pH.

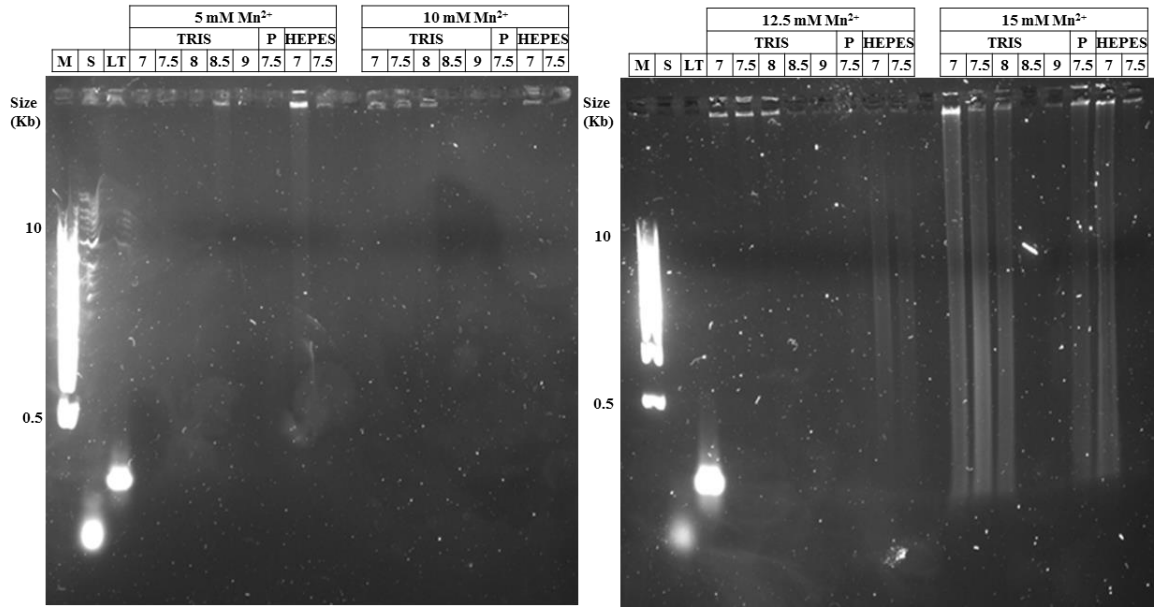


Figure 8.2.3. 0.8% agarose gel analysis of precipitates from Bst 2.0 DNA polymerase catalysed RCA with Mn^{2+} as the cofactor. M: 1 Kb DNA ladder; S: splint S1; T: cyclic template T1; P: PIPES; numbers above lanes represent the buffer pH. DNA is only observed in precipitates at pH 8 and lower. Samples with DNA present were imaged by SEM.

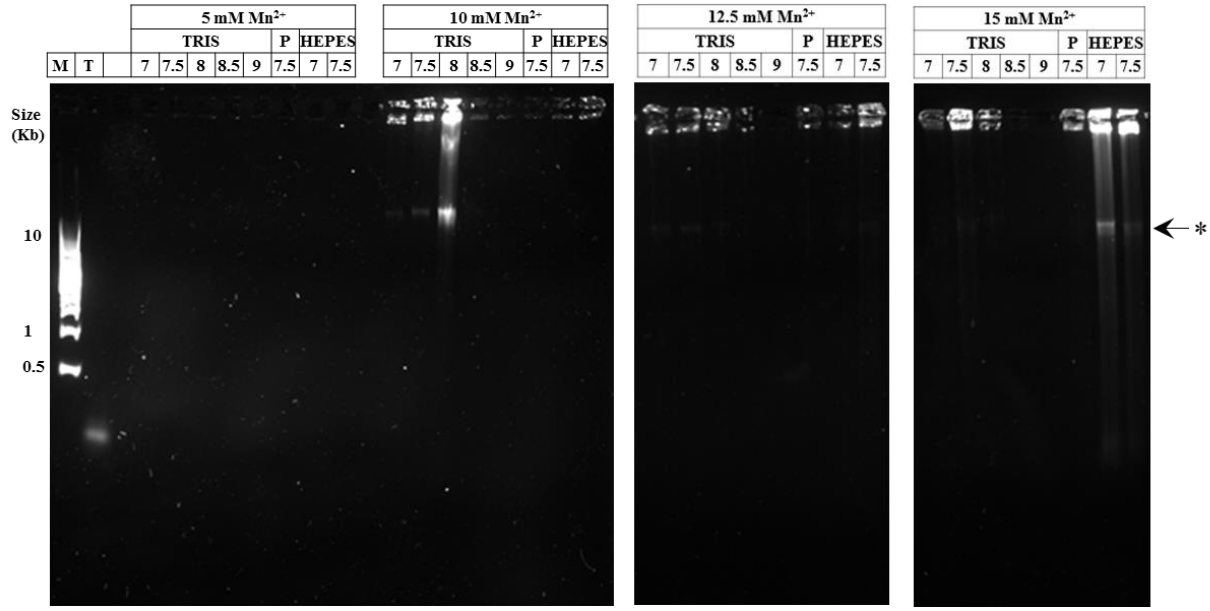


Figure 8.2.4. 0.8% agarose gel analysis of precipitates from Φ-29 DNA polymerase catalysed RCA with Mn^{2+} as the cofactor. M: 1 Kb DNA ladder; T: cyclic template T1; P: PIPES; *: this band is assigned to double-stranded products.[250] Numbers above lanes represent the buffer pH. DNA is only observed in precipitates at pH 8 or lower. Samples with DNA present were imaged by SEM.

8.3 SEM images of particles produced using cyclic T2 and S2

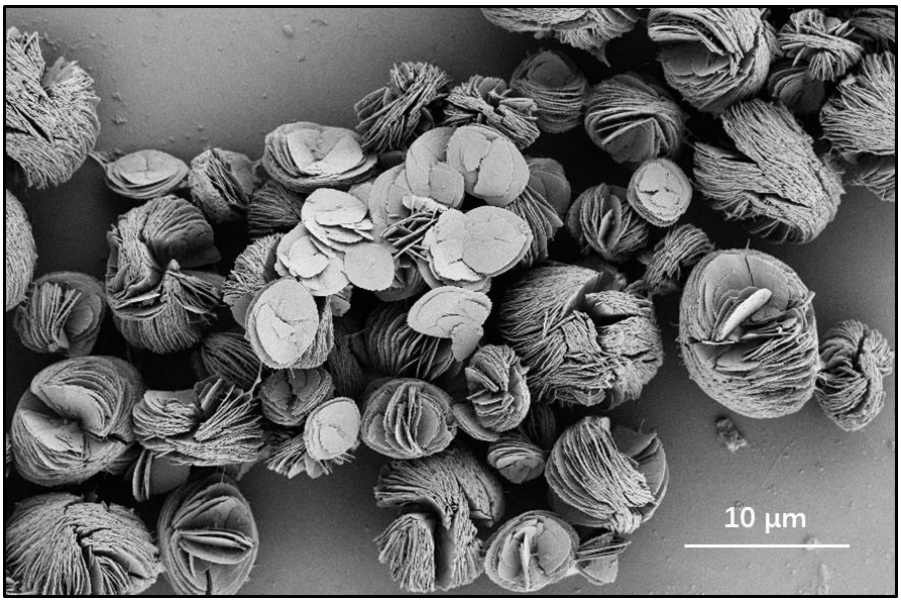


Figure 8.3.1. SEM image of precipitate produced using cyclic T2 and S2. The RCA reaction was performed using Φ-29 DNA polymerase with 5 mM Mn^{2+}.

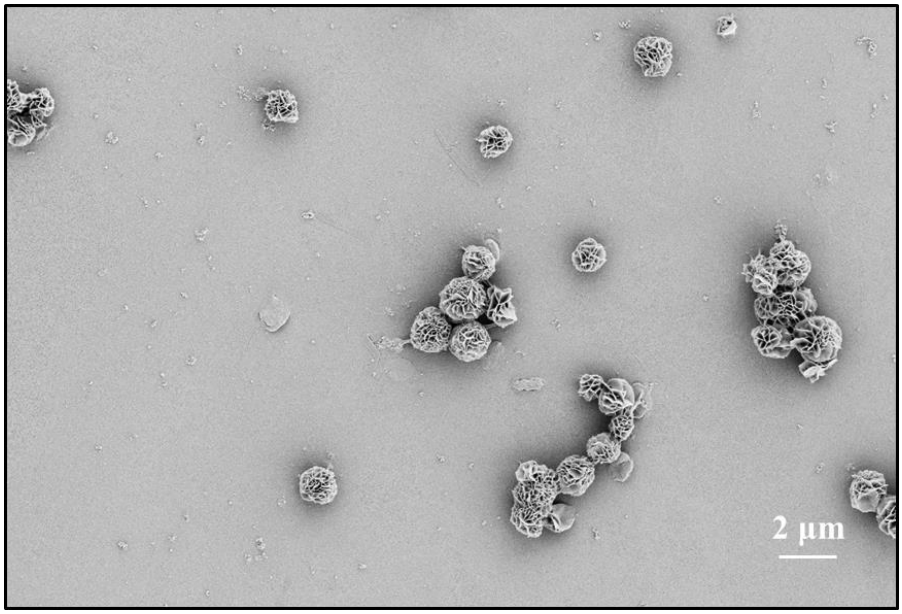


Figure 8.3.2. SEM image of precipitate produced using cyclic T2 and S2. The RCA reaction was performed using Φ-29 DNA polymerase with 10 mM Mn^{2+}.

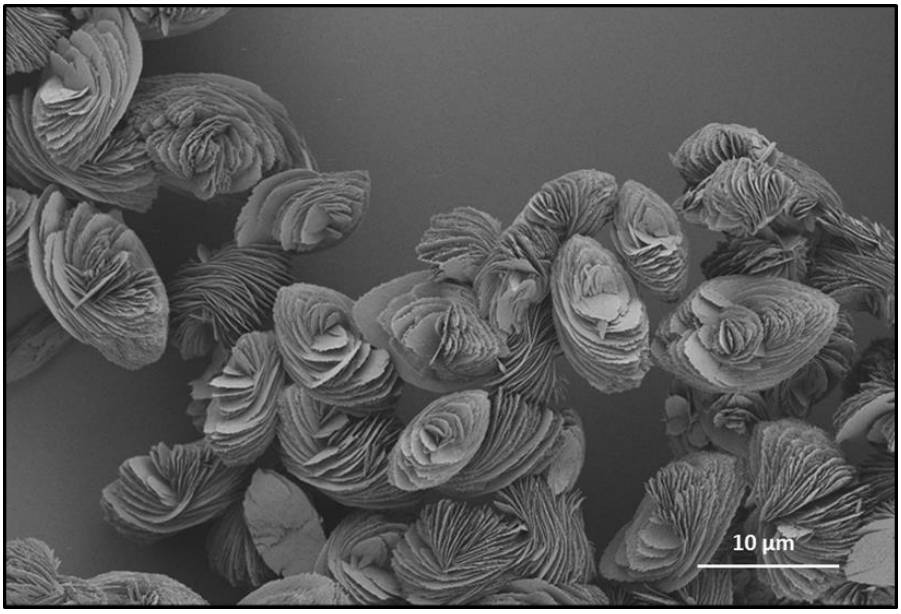


Figure 8.3.3. SEM image of precipitate produced using cyclic T2 and S2. The RCA reaction was performed using Bst 2.0 DNA polymerase with 5 mM Mn^{2+}.

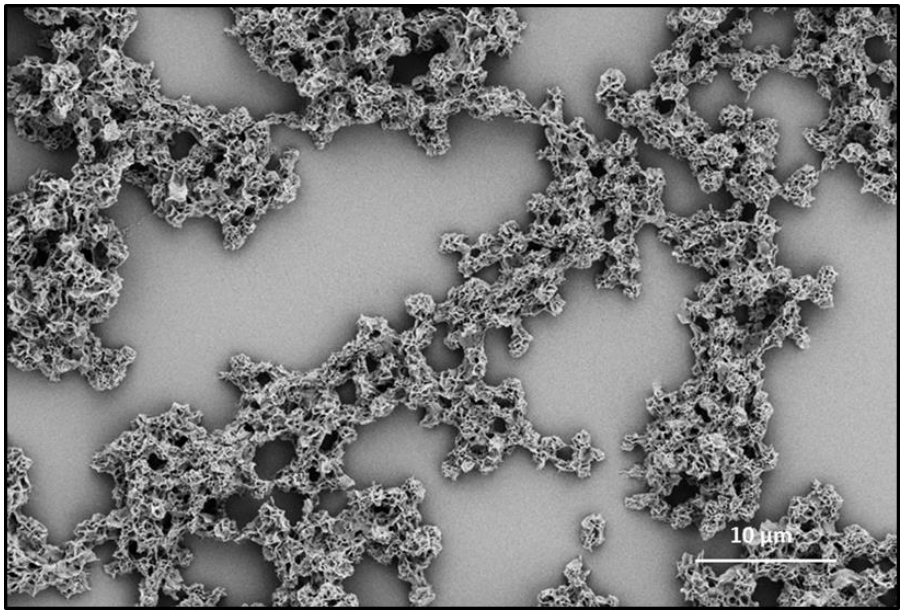


Figure 8.3.4. SEM image of precipitate produced using cyclic T2 and S2. The RCA reaction was performed using Bst 2.0 DNA polymerase with 10 mM Mn^{2+}.

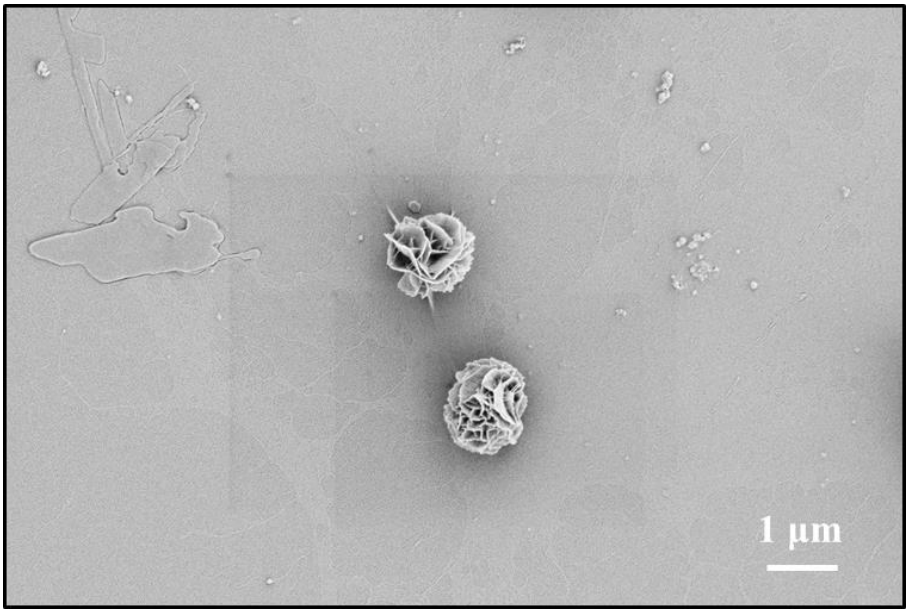


Figure 8.3.5. SEM image of precipitate produced using cyclic T2 and S2. The RCA reaction was performed using Bst 2.0 DNA polymerase with 15 mM Mn^{2+}.

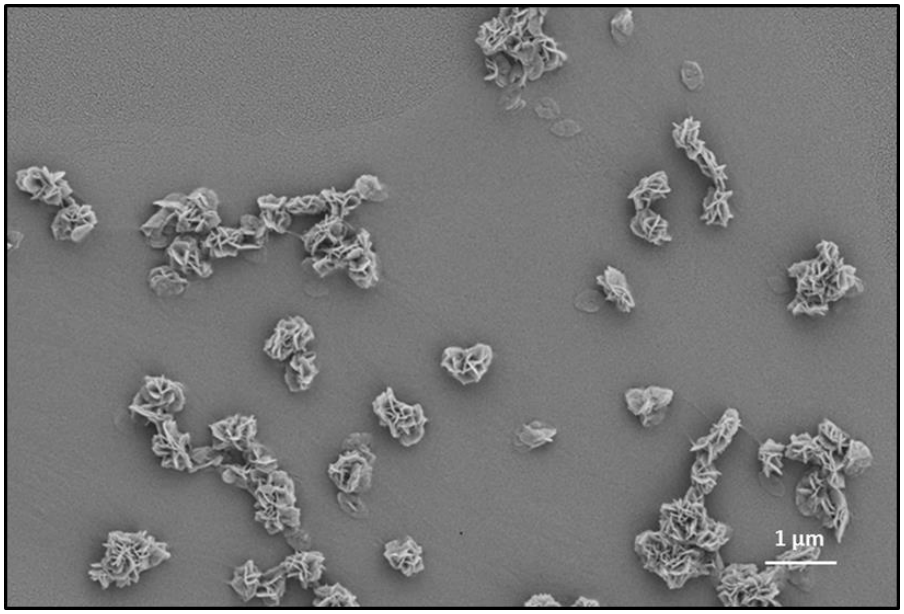


Figure 8.3.6. SEM image of precipitate produced using cyclic T2 and S2. The RCA reaction was performed using Φ-29 DNA polymerase with 10 mM Co^{2+} for 30 h.

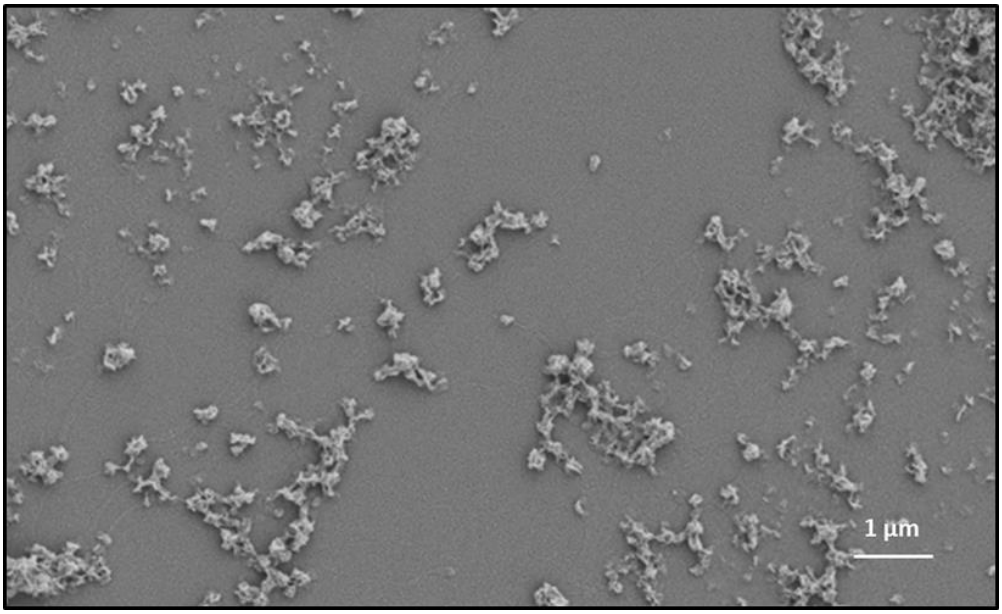


Figure 8.3.7. SEM image of precipitate produced using cyclic T2 and S2. The RCA reaction was performed using Φ-29 DNA polymerase with 15 mM Co^{2+} for 30 h.

8.4 Denaturing PAGE gel analysis

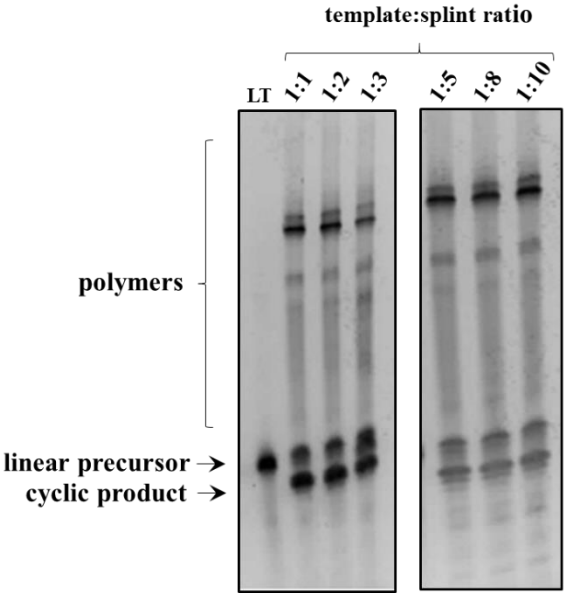


Figure 8.4.1. Splint-mediated enzymatic cyclisation of linear **1**_PO_4 to give the cyclic **1**_PO_4. The crude reaction mixtures were analysed by an 8% denaturing PAGE gel. Samples were imaged after staining with SYBR Gold. LT: linear precursor. The enzymatic cyclisation reaction was carried out with different ratios of template oligonucleotide and splint at RT overnight using T4 DNA ligase and Bio-Rad T100^{TM} thermocycler.

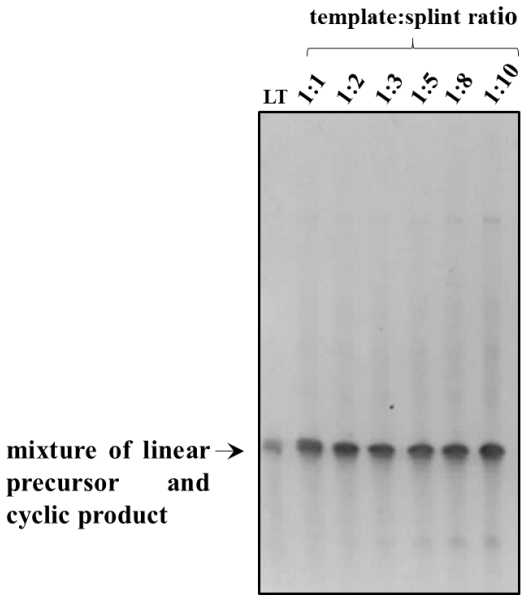


Figure 8.4.2. Splint-mediated enzymatic cyclisation of linear **3**_PO_4 to give the cyclic **3**_PO_4. The crude reaction mixtures were analysed by an 8% denaturing PAGE gel. Samples were imaged after staining with SYBR Gold. LT: linear precursor. The enzymatic cyclisation reaction was carried out with different ratios of template oligonucleotide and splint at RT overnight using T4 DNA ligase and Bio-Rad T100^{TM} thermocycler.

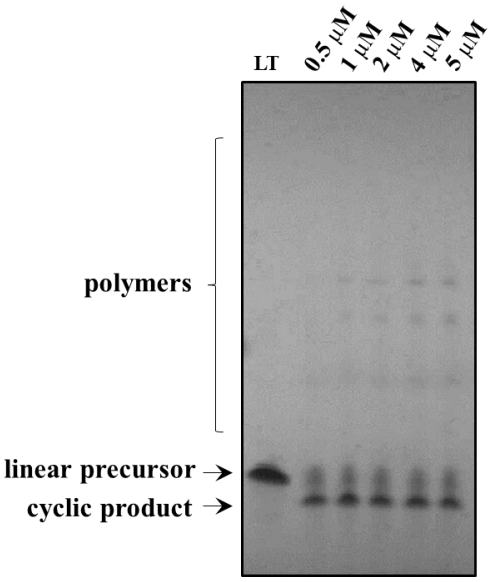


Figure 8.4.3. Non-templated CuAAC reaction to give the cyclic**1**_Tz in the presence of an increasing concentration of linear precursor. The crude reaction mixture was analysed by an 8% denaturing PAGE gel. LT: linear precursor.

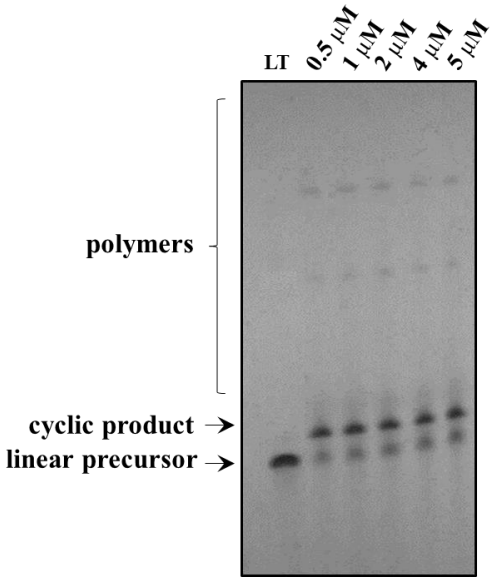


Figure 8.4.4. Non-templated CuAAC reaction to give the cyclic **2**_Tz in the presence of an increasing concentration of linear precursor. The crude reaction mixture was analysed by an 8% denaturing PAGE gel. LT: linear precursor.

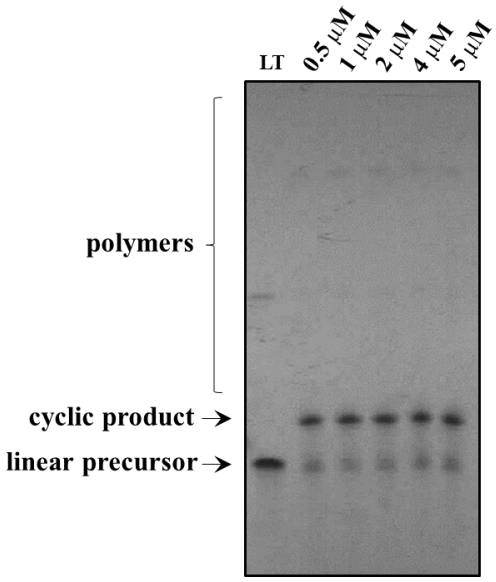


Figure 8.4.5. Non-templated CuAAC reaction to give the cyclic **3**_Tz in the presence of an increasing concentration of linear precursor. The crude reaction mixture was analysed by an 8% denaturing PAGE gel. LT: linear precursor.

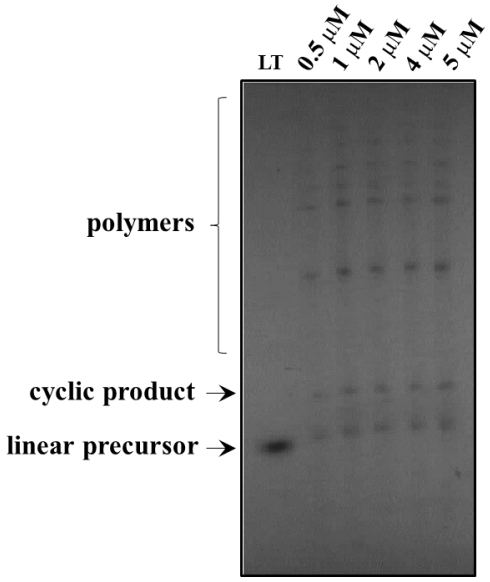


Figure 8.4.6. Non-templated CuAAC reaction to give the cyclic **4**_Tz in the presence of an increasing concentration of linear precursor. The crude reaction mixture was analysed by an 8% denaturing PAGE gel. LT: linear precursor.

8.5 Agarose gel analysis of the effect of Mg^{2+} concentration on RCA

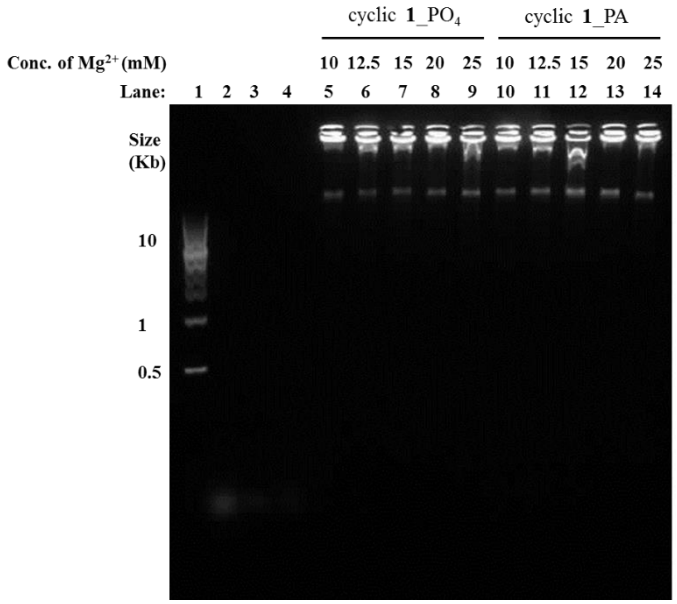


Figure 8.5.1. 0.8% agarose gel analysis of supernatant from cyclic template containing natural phosphodiester backbone linkage (cyclic **1**_PO_4) or phosphoramidate backbone linkage (cyclic **1**_PA). The RCA was carried out for 20 h with different concentrations of Mg^{2+} using Φ-29 DNA polymerase. Lane 1: 1kb DNA ladder; Lane 2: splint (ODN4-1); Lane 3: cyclic **1**_PO_4; Lane 4: cyclic **1**_PA.

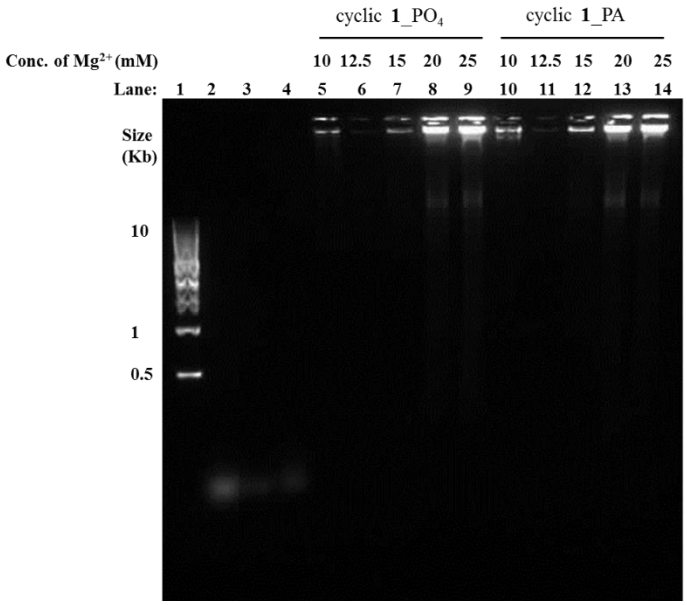


Figure 8.5.2. 0.8% agarose gel analysis of precipitate from cyclic template containing natural phosphodiester backbone linkage (cyclic **1**_PO_4) or phosphoramidate backbone linkage (cyclic **1**_PA). The RCA was carried out for 20 h with different concentrations of Mg^{2+} using Φ-29 DNA polymerase. Lane 1: 1kb DNA ladder; Lane 2: splint (ODN4-1); Lane 3: cyclic **1**_PO_4; Lane 4: cyclic **1**_PA.

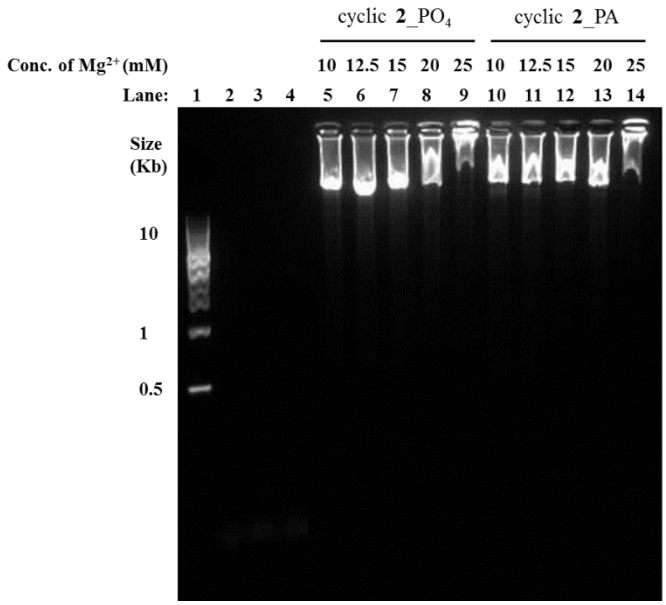


Figure 8.5.3. 0.8% agarose gel analysis of supernatant from cyclic template containing natural phosphodiester backbone linkage (cyclic **2**_PO_4) or phosphoramidate backbone linkage (cyclic **2**_PA). The RCA was carried out for 20 h with different concentrations of Mg^{2+} using Φ-29 DNA polymerase. Lane 1: 1kb DNA ladder; Lane 2: splint (ODN4-2); Lane 3: cyclic **2**_PO_4; Lane 4: cyclic **2**_PA.

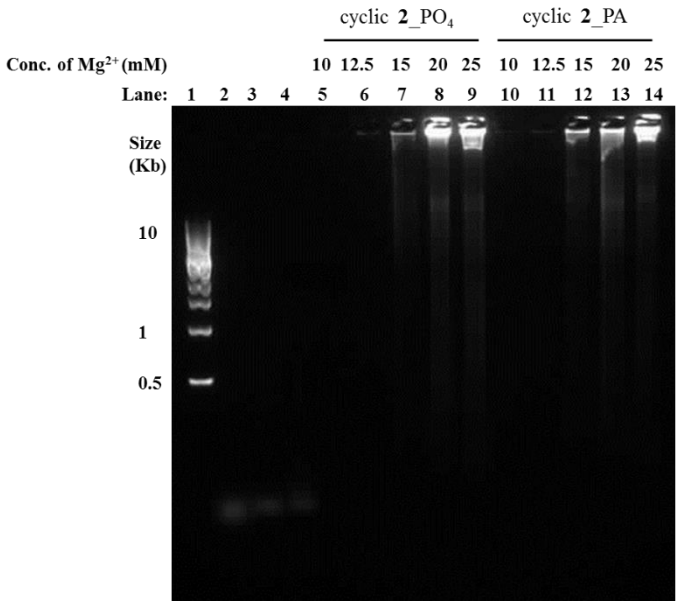


Figure 8.5.4. 0.8% agarose gel analysis of precipitate from cyclic template containing natural phosphodiester backbone linkage (cyclic **2**_PO_4) or phosphoramidate backbone linkage (cyclic **2**_PA). The RCA was carried out for 20 h with different concentrations of Mg^{2+} using Φ-29 DNA polymerase. Lane 1: 1kb DNA ladder; Lane 2: splint (ODN4-2); Lane 3: cyclic **2**_PO_4; Lane 4: cyclic **2**_PA.

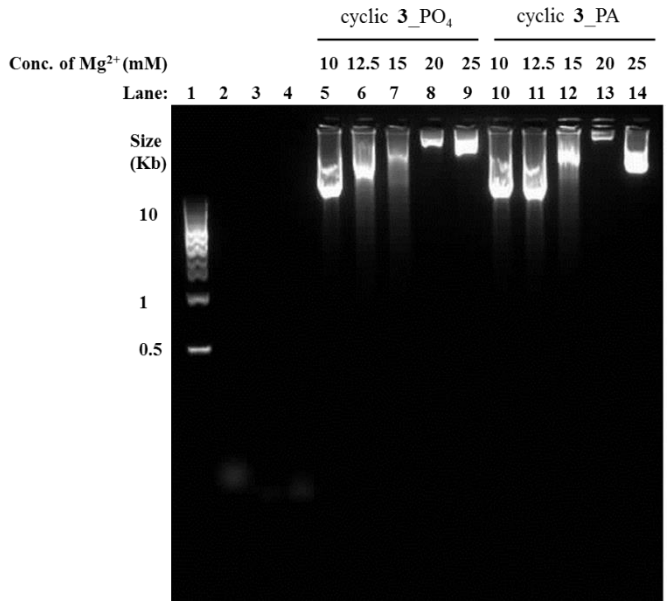


Figure 8.5.5. 0.8% agarose gel analysis of supernatant from cyclic template containing natural phosphodiester backbone linkage (cyclic **3**_PO_4) or phosphoramidate backbone linkage (cyclic **3**_PA). The RCA was carried out for 20 h with different concentrations of Mg^{2+} using Φ-29 DNA polymerase. Lane 1: 1kb DNA ladder; Lane 2: splint (ODN4-3); Lane 3: cyclic **3**_PO_4; Lane 4: cyclic **3**_PA.

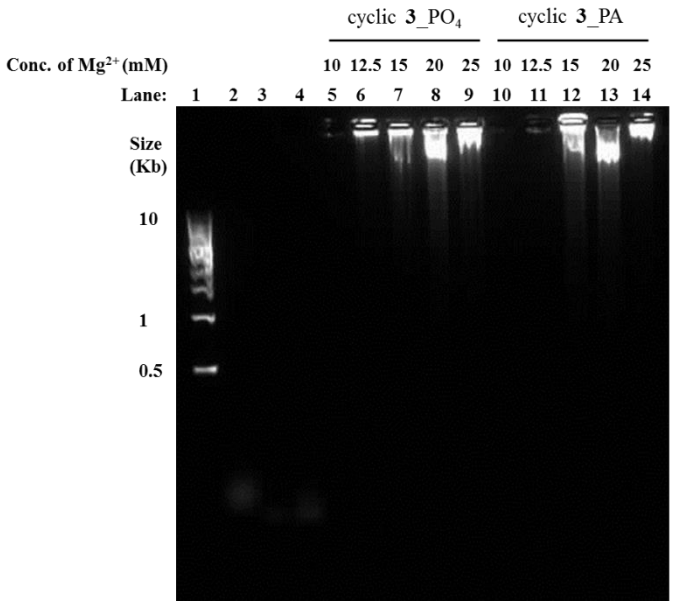


Figure 8.5.6. 0.8% agarose gel analysis of precipitate from cyclic template containing natural phosphodiester backbone linkage (cyclic **3**_PO_4) or phosphoramidate backbone linkage (cyclic **3**_PA). The RCA was carried out for 20 h with different concentrations of Mg^{2+} using Φ-29 DNA polymerase. Lane 1: 1kb DNA ladder; Lane 2: splint (ODN4-3); Lane 3: cyclic **3**_PO_4; Lane 4: cyclic **3**_PA.

8.6 Agarose gel analysis of RCA products produced using Φ-29 with modified backbone linkages

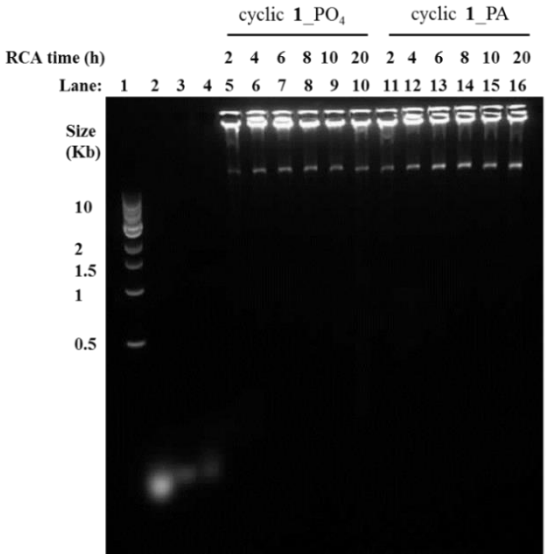


Figure 8.6.1. 0.8% agarose gel analysis of original RCA reaction mixtures from cyclic **1**_PO_4 and cyclic **1**_PA. The RCA was carried out in the presence of 20 mM Mg^{2+} at different time courses using Φ-29 DNA polymerase. Lane 1: 1 kb DNA ladder; Lane 2: RCA primer ODN4-1; Lane 3: cyclic **1**_PO_4; Lane 4: cyclic **1**_PA.

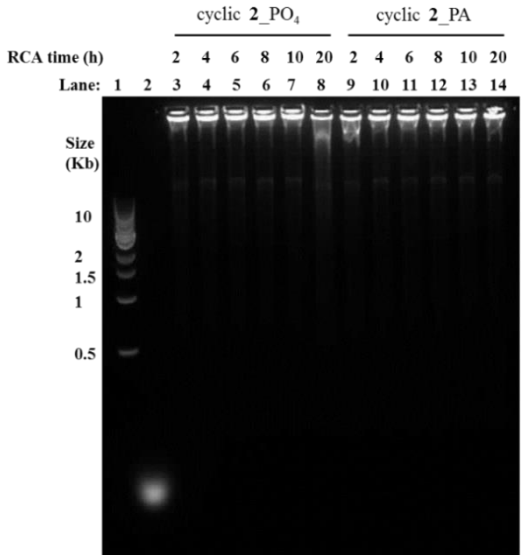


Figure 8.6.2. 0.8% agarose gel analysis of original RCA reaction mixtures from cyclic **2**_PO_4 and cyclic **2**_PA. The RCA was carried out in the presence of 20 mM Mg^{2+} at different time courses using Φ-29 DNA polymerase. After finishing the RCA reactions, EDTA (20 mM final concentration) was added to the reaction mixture in an attempt to break down the precipitate releasing the very long RCA products. Lane 1: 1 kb DNA ladder; Lane 2: RCA primer ODN4-2.

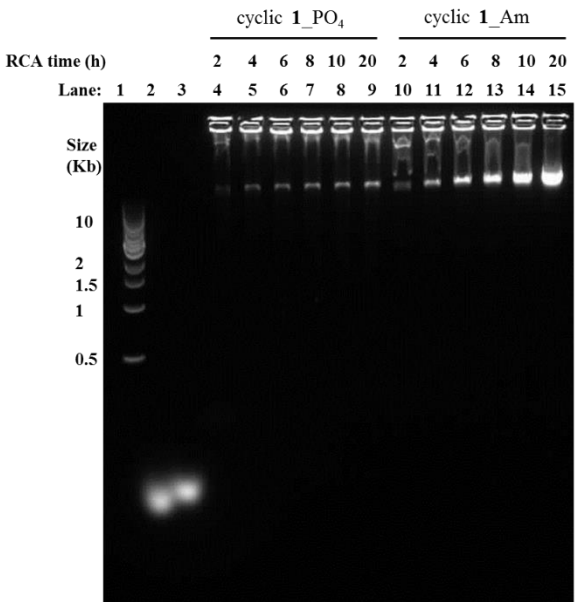


Figure 8.6.3. 0.8% agarose gel analysis of original RCA reaction mixtures from cyclic **1**_PO_4 and cyclic **1**_Am. The RCA was carried out in the presence of 20 mM Mg^{2+} at different time courses using Φ-29 DNA polymerase. Lane 1: 1 kb DNA ladder; Lane 2: RCA primer ODN4-1; Lane 3: RCA primer ODN4-5 for cyclic **1**_Am.

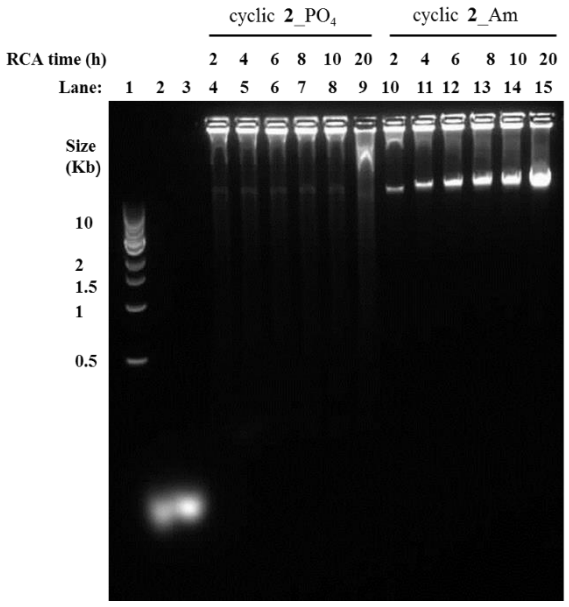


Figure 8.6.4. 0.8% agarose gel analysis of original RCA reaction mixtures from cyclic **2**_PO_4 and cyclic **2**_Am. The RCA was carried out in the presence of 20 mM Mg^{2+} at different time courses using Φ-29 DNA polymerase. After finishing the RCA reactions, EDTA (20 mM final concentration) was added to the reaction mixture in an attempt to break down the precipitate releasing the very long RCA products. Lane 1: 1 kb DNA ladder; Lane 2: RCA primer ODN4-2; Lane 3: RCA primer ODN4-6 for cyclic **2**_Am.

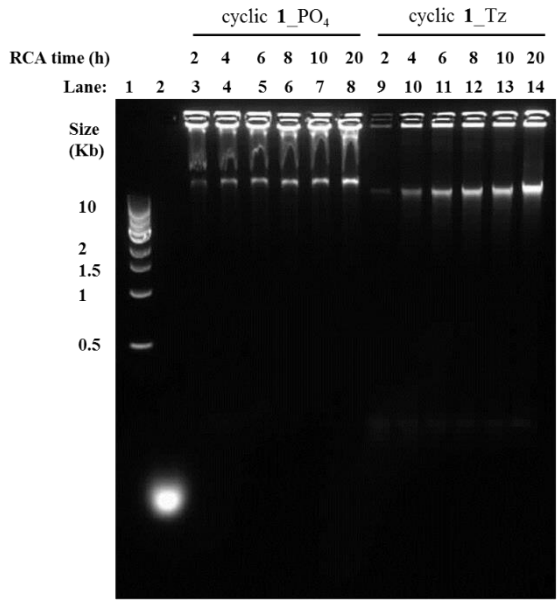


Figure 8.6.5. 0.8% agarose gel analysis of original RCA reaction mixtures from cyclic **1**_PO_4 and cyclic **1**_Tz. The RCA was carried out in the presence of 20 mM Mg^{2+} at different time courses using Φ-29 DNA polymerase. Lane 1: 1 kb DNA ladder; Lane 2: RCA primer ODN4-1.

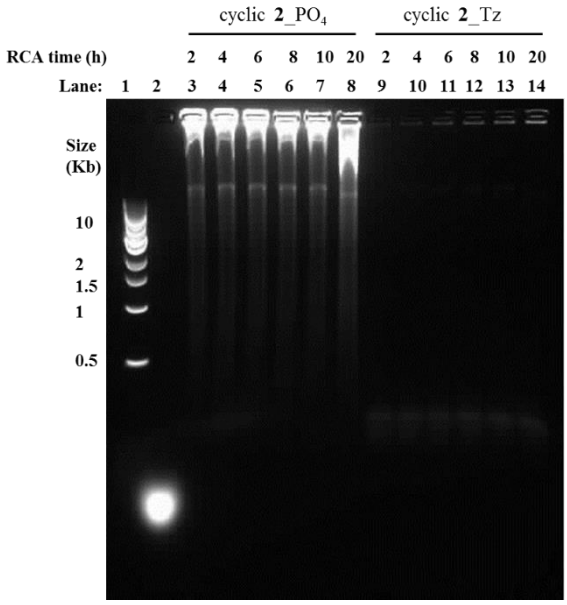


Figure 8.6.6. 0.8% agarose gel analysis of original RCA reaction mixtures from cyclic **2**_PO_4 and cyclic **2**_Tz. The RCA was carried out in the presence of 20 mM Mg^{2+} at different time courses using Φ-29 DNA polymerase. After finishing the RCA reactions, EDTA (20 mM final concentration) was added to the solution mixture in an attempt to break down the precipitate releasing the very long RCA products. Lane 1: 1 kb DNA ladder; Lane 2: RCA primer ODN4-2.

8.7 Agarose gel analysis of RCA products hybridised with fluorescent probe

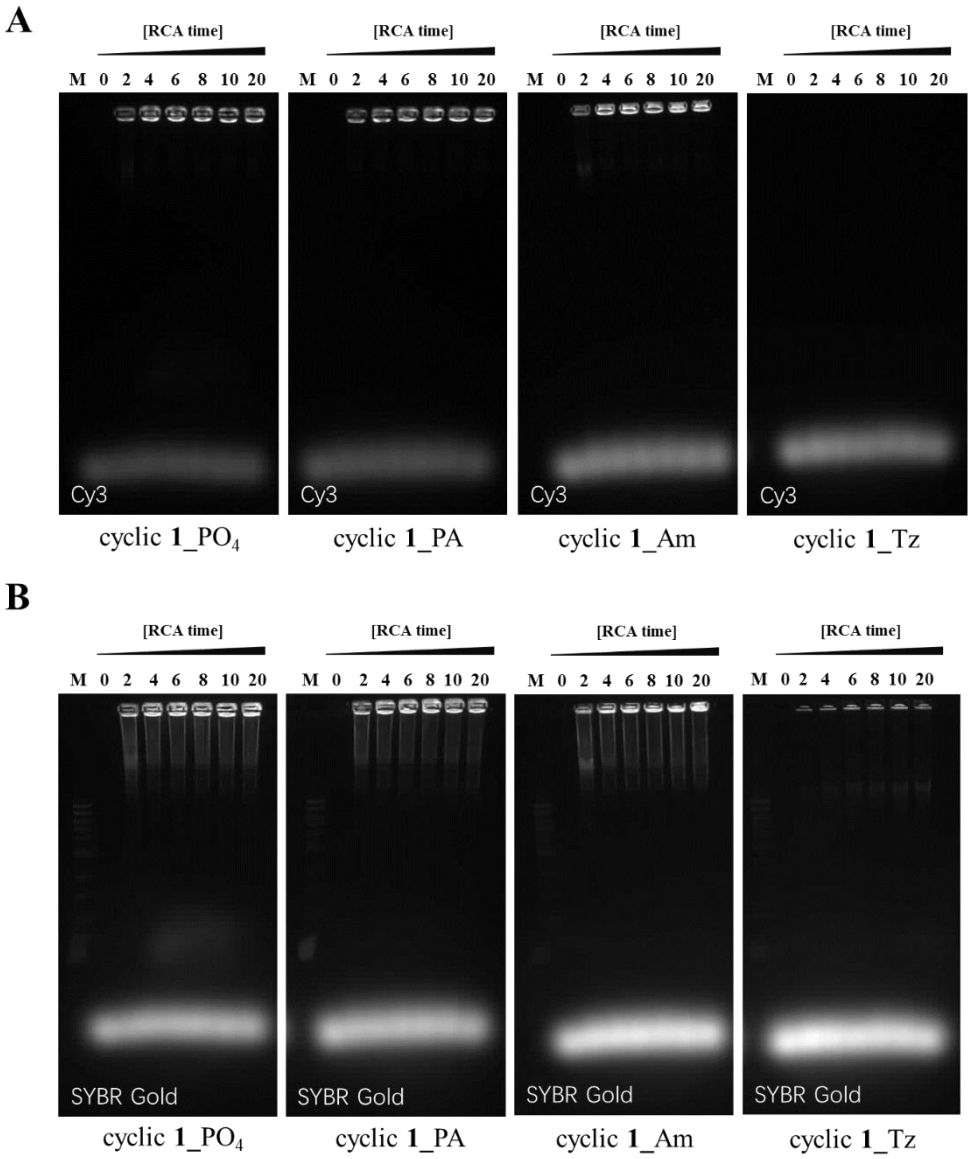


Figure 8.7.1. Probing the nature of the amplified products from Φ-29 DNA polymerase catalysed RCA of the cyclic **1**_PO_4, cyclic **1**_PA, cyclic **1**_Am and cyclic **1**_Tz using fluorescent probe (ODN4-8). After reaction, aliquots of the RCA reactions were heated to inactivate the polymerase at two-hour intervals during a period of 20 h. The RCA reaction mixtures were incubated with a Cy3 labelled fluorescent probe and then were analysed by 0.8% agarose gel electrophoresis. (A) The gels were visualised under the Cy3 fluorescence channel with an excitation at 520 nm. (B) The same gels were reimaged post-staining with SYBR Gold with an excitation at 302 nm.

8.8 Agarose gel analysis of RCA products produced using Bst 2.0 with modified backbone linkages

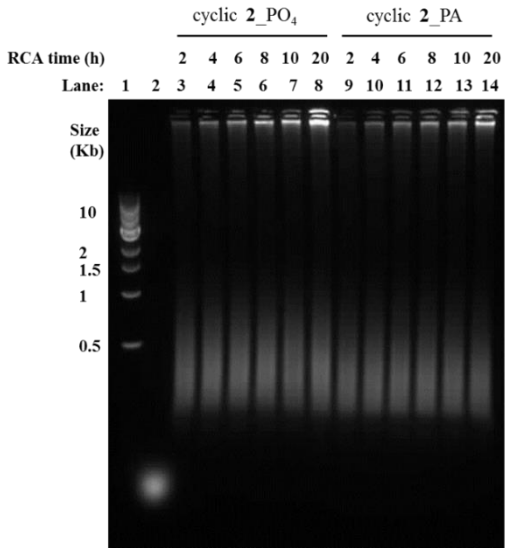


Figure 8.8.1. 0.8% agarose gel analysis of original RCA reaction mixtures from cyclic **2**_PO_4 and cyclic **2**_PA. The RCA was carried out in the presence of 20 mM Mg^{2+} at different time courses using Bst 2.0 DNA polymerase. Lane 1: 1 kb DNA ladder; Lane 2: RCA primer ODN4-2.

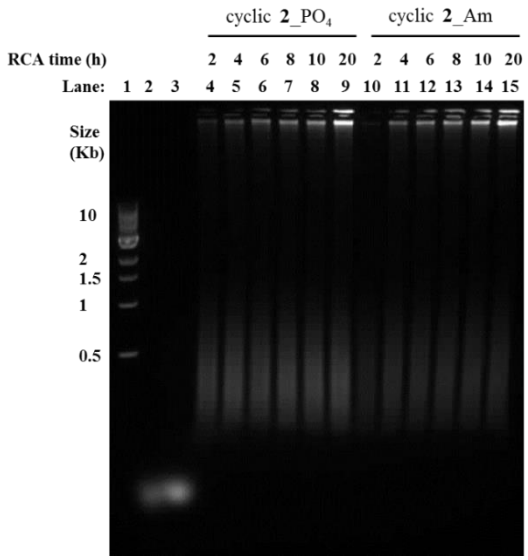


Figure 8.8.2. 0.8% agarose gel analysis of original RCA reaction mixtures from cyclic **2**_PO_4 and cyclic **2**_Am. The RCA was carried out in the presence of 20 mM Mg^{2+} at different time courses using Bst 2.0 DNA polymerase. Lane 1: 1 kb DNA ladder; Lane 2: RCA primer ODN4-2; Lane 3: RCA primer for ODN4-6.

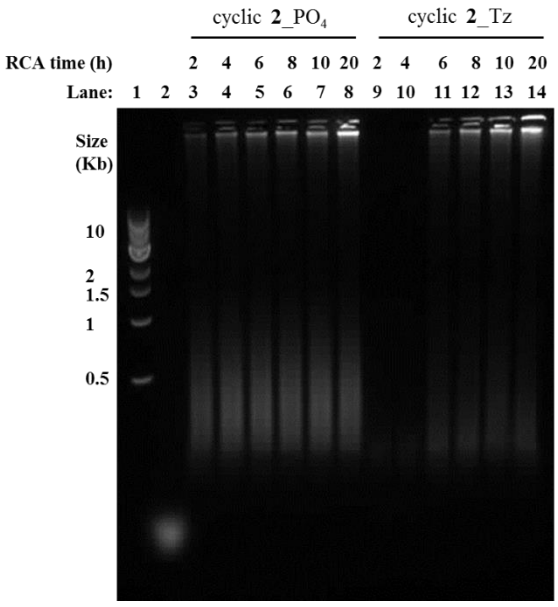


Figure 8.8.3. 0.8% agarose gel analysis of original RCA reaction mixtures from cyclic **2**_PO_4 and cyclic **2**_Tz. The RCA was carried out in the presence of 20 mM Mg^{2+} at different time courses using Bst 2.0 DNA polymerase. Lane 1: 1 kb DNA ladder; Lane 2: RCA primer ODN4-2.

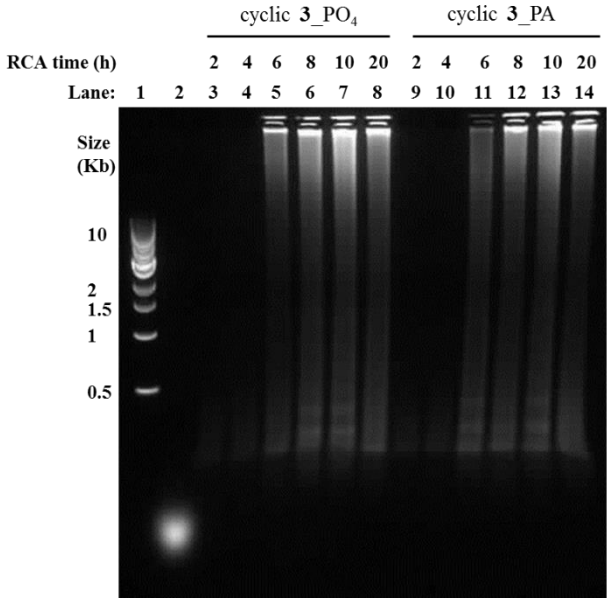


Figure 8.8.4. 0.8% agarose gel analysis of supernatant from cyclic **3**_PO_4 and cyclic **3**_PA. The RCA was carried out in the presence of 20 mM Mg^{2+} at different time courses using Bst 2.0 DNA polymerase. After finishing the RCA reactions, EDTA (20 mM final concentration) was added to the reaction mixture in an attempt to break down the precipitate releasing the very long RCA products. However, the precipitate was still observed. Lane 1: 1kb DNA ladder; Lane 2: RCA primer ODN4-3.

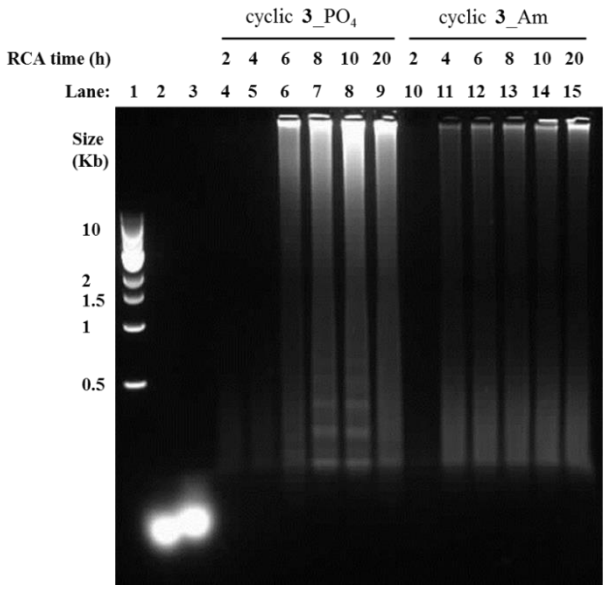


Figure 8.8.5. 0.8% agarose gel analysis of supernatant from cyclic **3**_PO_4 and cyclic **3**_Am. The RCA was carried out in the presence of 20 mM Mg^{2+} at different time courses using Bst 2.0 DNA polymerase. After finishing the RCA reactions, EDTA (20 mM final concentration) was added to the reaction mixture in an attempt to break down the precipitate releasing the very long RCA products. However, the precipitate was still observed. Lane 1: 1kb DNA ladder; Lane 2: RCA primer ODN4-3; Lane 3: RCA primer ODN4-7.

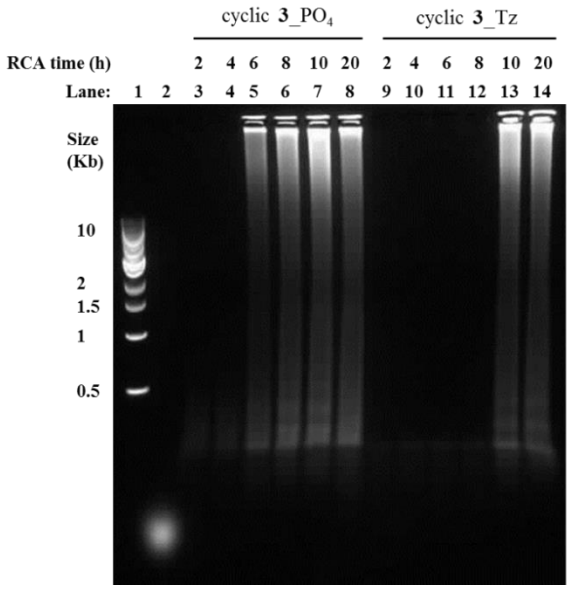


Figure 8.8.6. 0.8% agarose gel analysis of supernatant from cyclic **3**_PO_4 and cyclic **3**_Tz. The RCA was carried out in the presence of 20 mM Mg^{2+} at different time courses using Bst 2.0 DNA polymerase. After finishing the RCA reactions, EDTA (20 mM final concentration) was added to the reaction mixture in an attempt to break down the precipitate releasing the very long RCA products. However, the precipitate was still observed. Lane 1: 1kb DNA ladder; Lane 2: RCA primer ODN4-3.

8.9 SEM images used to measure the particle size

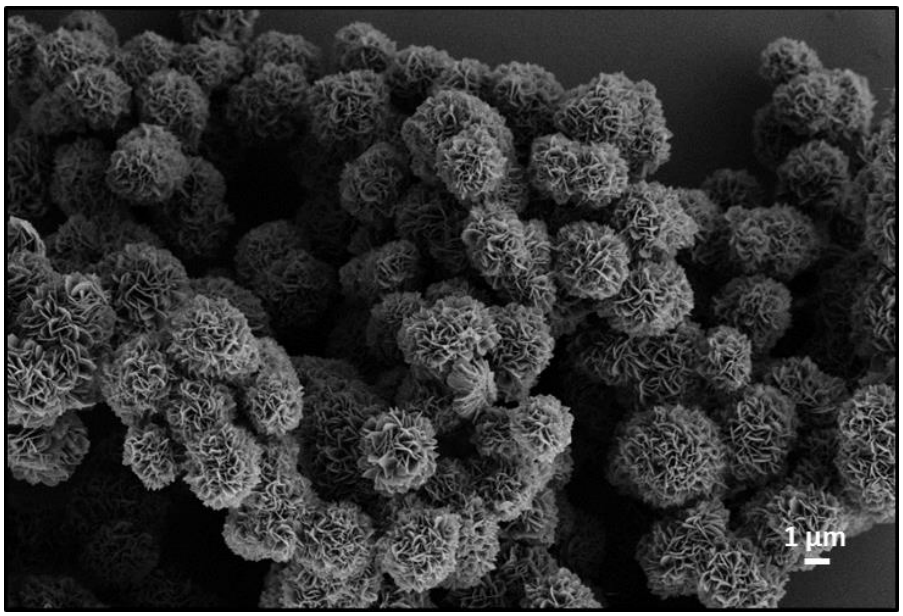


Figure 8.9.1. SEM image used to measure the size distribution of the particles generated from cyclic **1**_PO_4. The RCA reaction was carried out for 20 h in the presence of 10 mM Mg^{2+} using Φ-29 DNA polymerase. ImageJ was used to measure the average diameter of particles: 2.98 ± 0.22 µm, n = 20, n refers to the number of measured particles.

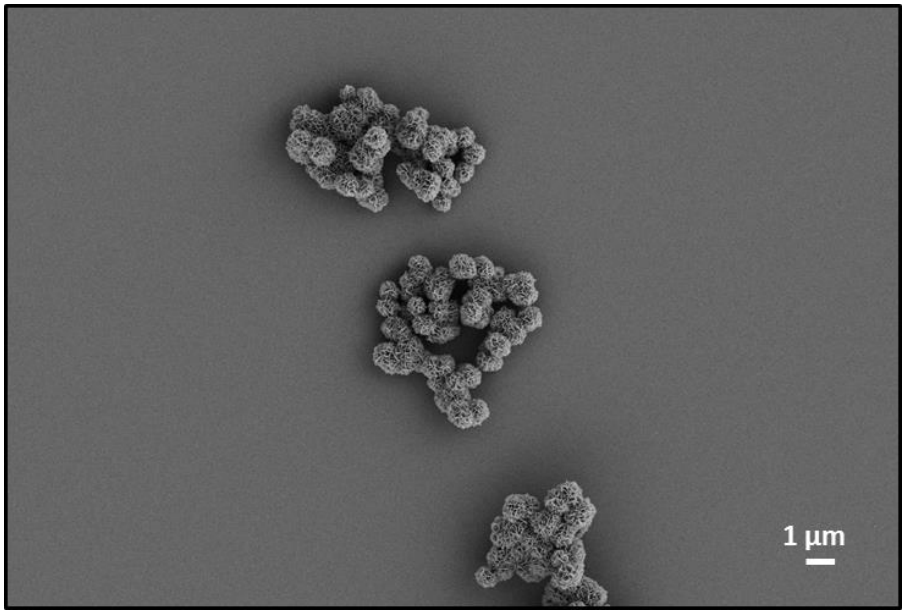


Figure 8.9.2. SEM image used to measure the size distribution of the particles generated from cyclic **1**_PO_4. The RCA reaction was carried out for 20 h in the presence of 25 mM Mg^{2+} using Φ-29 DNA polymerase. ImageJ was used to measure the average diameter of particles: 0.89 ± 0.15µm, n = 20, n refers to the number of measured particles.

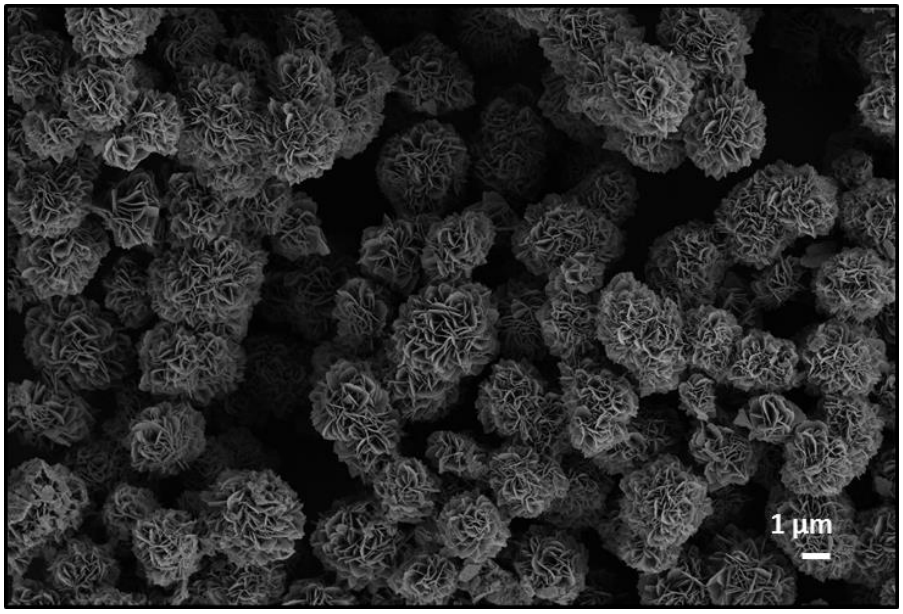


Figure 8.9.3. SEM image used to measure the size distribution of the particles generated from cyclic **1**_PA. The RCA reaction was carried out for 20 h in the presence of 10 mM Mg^{2+} using Φ-29 DNA polymerase. ImageJ was used to measure the average diameter of particles: 3.40 ± 0.35µm, n = 23, n refers to the number of measured particles.

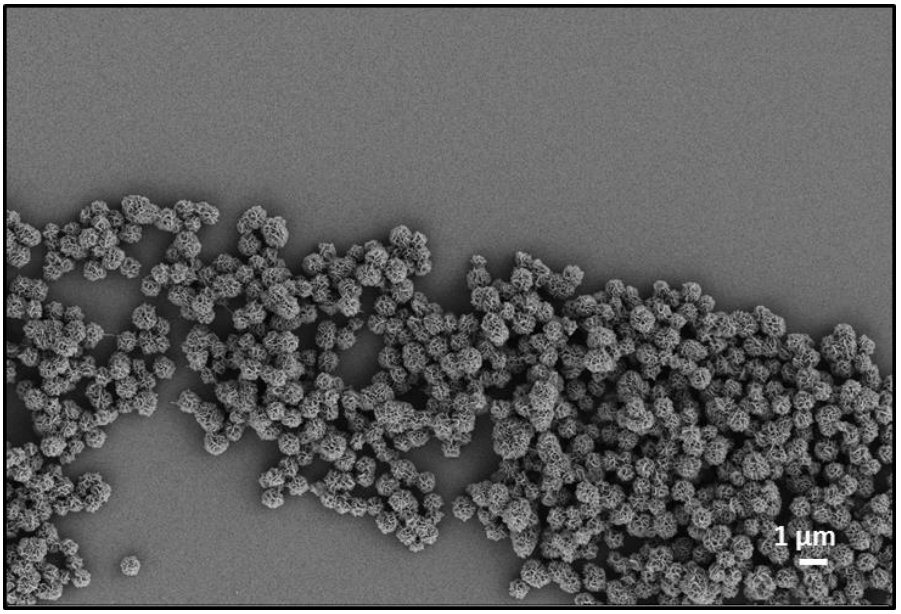


Figure 8.9.4. SEM image used to measure the size distribution of the particles generated from cyclic **1**_PA. The RCA reaction was carried out for 20 h in the presence of 25 mM Mg^{2+} using Φ-29 DNA polymerase. ImageJ was used to measure the average diameter of particles: 0.77 ± 0.07µm, n = 60, n refers to the number of measured particles.

8.10 List of publications

1. Chen, J.; Baker, Y. R.; Brown, A.; El-Sagheer, A. H.; Brown, T. Enzyme-free synthesis of cyclic single-stranded DNA constructs containing a single triazole, amide or phosphoramidate backbone linkage and their use as templates for rolling circle amplification and nanoflower formation. *Chem. Sci.*, **2018**, *9*, 8110-8120.
2. Baker, Y. R.; Chen, J.; Brown, J.; El-Sagheer, A. H.; Wiseman, P.; Johnson, E.; Goddard, P.; Brown, T. Preparation and characterization of manganese, cobalt and zinc DNA nanoflowers with tuneable morphology, DNA content and size. *Nucleic Acids Res.*, **2018**, *46*, 7495-7505.

Chemical Science

EDGE ARTICLE

View Article Online
View Journal | View Issue

Check for updates

Cite this: *Chem. Sci.*, 2018, **9**, 8110

All publication charges for this article have been paid for by the Royal Society of Chemistry

Open Access Article. Published on 24 August 2018. Downloaded on 8/23/2019 1:55:53 PM.
This article is licensed under a Creative Commons Attribution 3.0 Unported Licence.

Received 4th July 2018
Accepted 23rd August 2018

DOI: 10.1039/c8sc02952k

rsc.li/chemical-science

Enzyme-free synthesis of cyclic single-stranded DNA constructs containing a single triazole, amide or phosphoramidate backbone linkage and their use as templates for rolling circle amplification and nanoflower formation†

Jinfeng Chen, [a] Ysobel R. Baker, [a] Asha Brown, [b] Afaf H. El-Sagheer [ac] and Tom Brown *[a]

Cyclic oligonucleotides are valuable targets with a broad range of potential applications spanning molecular biology and nanotechnology. Of particular importance is their role as templates in the rolling circle amplification (RCA) reaction. We describe three different chemical cyclisation methods for the preparation of single-stranded cyclic DNA constructs. These chemical cyclisation reactions are cheaper to carry out than the enzymatic reaction, and more amenable to preparative scale purification and characterisation of the cyclic product. They can also be performed under denaturing conditions and are therefore particularly valuable for cyclic DNA templates that contain secondary structures. The resulting single-stranded cyclic DNA constructs contain a single non-canonical backbone linkage at the ligation point (triazole, amide or phosphoramidate). They were compared to unmodified cyclic DNA in rolling circle amplification reactions using ϕ-29 and Bst 2.0 DNA polymerase enzymes. The cyclic templates containing a phosphoramidate linkage were particularly well tolerated by ϕ-29 polymerase, consistently performing as well in RCA as the unmodified DNA controls. Moreover, these phosphoramidate-modified cyclic constructs can be readily produced in oligonucleotide synthesis facilities from commercially available precursors. Phosphoramidate ligation therefore holds promise as a practical, scalable method for the synthesis of fully biocompatible cyclic RCA templates. The triazole-modified cyclic templates generally gave lower and more variable yields of RCA products, a significant proportion of which were double-stranded, while the performances of the templates containing an amide linkage lie in between those of the phosphoramidate- and triazole-containing templates.

Introduction

Rolling circle amplification (RCA) is an isothermal enzymatic technique that is widely used to make very long single-stranded DNA and RNA.[1,2] The product contains a specific, tandem-repeating sequence which is encoded by the complementary cyclic template.[3,4] This technique has been harnessed as a simple and powerful method of signal amplification in the development of sensitive detection methods for a variety of nucleic acid, protein, cellular and small molecule targets for diagnostic, biosensing and genotyping purposes.[5–14] RCA has also attracted widespread interest as a tool in the synthesis of functional DNA nanomaterials[15] including origami,[16] nanosprings,[17] nanotubes,[18] templating nanoscaffolds,[19,20] hydrogels[21,22] and DNA nanoflowers.[23] Proposed future applications of these materials include biosensors, targeted imaging and drug delivery agents,[24] and components of nanoscale computers and electronic circuits. An RCA reaction requires four components: a circular DNA template, a short DNA primer, a polymerase enzyme and deoxynucleoside triphosphates (dNTPs). The cyclic template is most commonly obtained *via* an enzyme-catalysed cyclisation of a linear DNA strand using DNA ligase enzymes such as T4 ligase or CircLigase. The efficiency of the cyclisation reaction is sensitive to the length of the linear DNA precursor, and is inefficient if the nucleobase sequence leads to secondary structures.[25,26] In addition, the scale on which the cyclisation reaction can be carried out is limited by the cost of the enzyme. In principle these limitations could be circumvented by the use of chemical

[a]*Chemistry Research Laboratory, University of Oxford, Oxford, OX1 3TA, UK. E-mail: tom.brown@chem.ox.ac.uk*

[b]*ATDBio, Magdalen Centre, Oxford Science Park, Oxford, OX4 4GA, UK*

[c]*Chemistry Branch, Department of Science and Mathematics, Suez University, Suez 43721, Egypt*

† Electronic supplementary information (ESI) available: Experimental protocols, mass spectra, and additional gel electrophoresis results and SEM images. See DOI: 10.1039/c8sc02952k

This journal is © The Royal Society of Chemistry 2018

Open Access Article. Published on 24 August 2018. Downloaded on 8/23/2019 1:55:53 PM.
This article is licensed under a Creative Commons Attribution 3.0 Unported Licence.

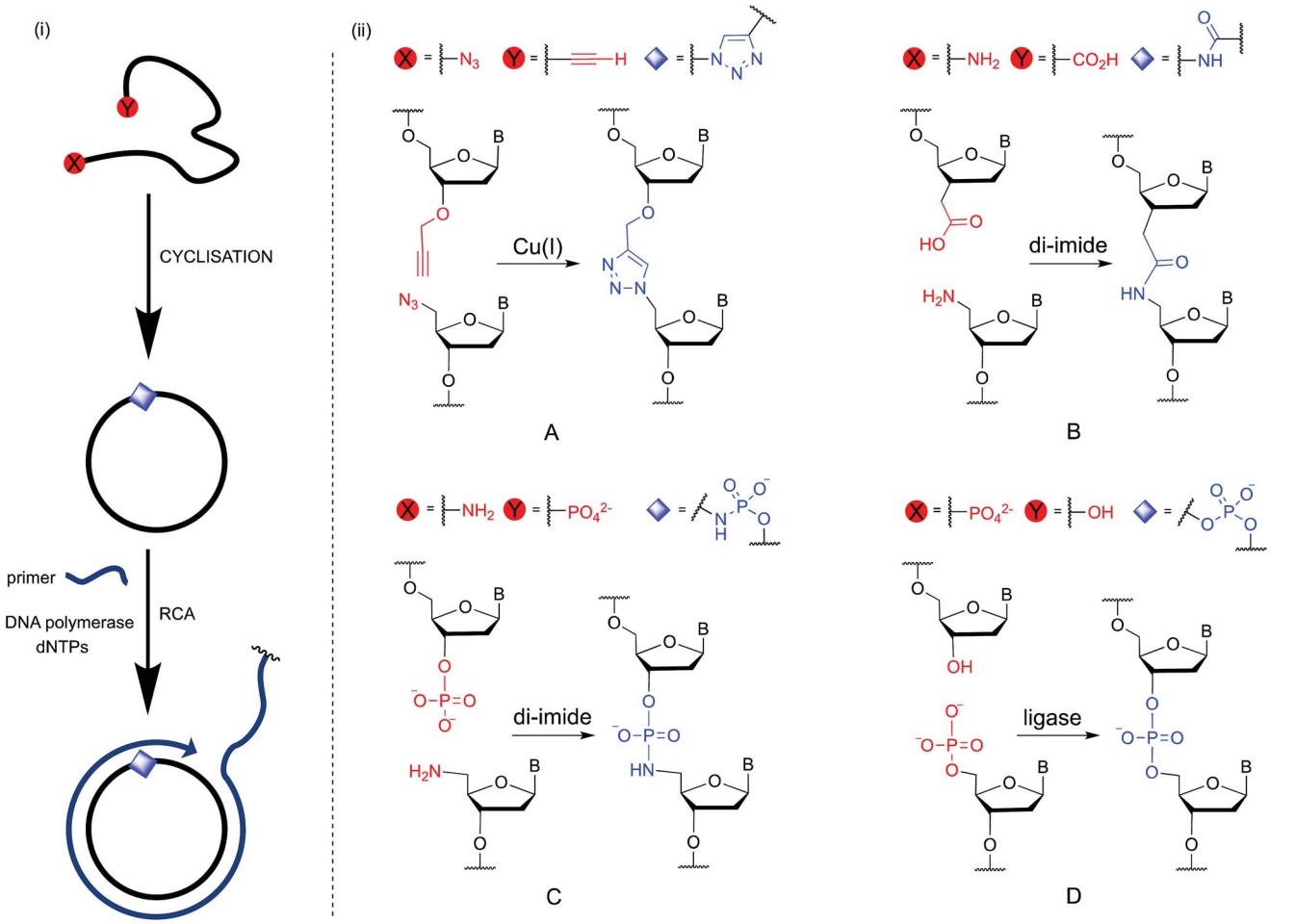


Fig. 1 (i) Cyclisation of single-stranded DNA by chemical ligation methods and rolling circle amplification through the non-canonical linkage. (ii) Details of the chemical and enzymatic ligation strategies investigated in this study: (A) formation of an artificial triazole backbone linkage *via* the Cu(I)-catalysed azide–alkyne cycloaddition (CuAAC) reaction; (B) di-imide-mediated formation of an artificial amide backbone linkage; (C) di-imide-mediated formation of an artificial phosphoramidate backbone linkage; (D) enzyme-catalysed formation of a natural phosphate backbone linkage. B = nucleobase.

ligation (Fig. 1), which is readily scalable, and would allow the use of a wide variety of buffers, including those in which DNA structures are denatured. However, the creation of a canonical phosphodiester linkage by chemical methods in aqueous media is inherently difficult because the nucleophilicity of the attacking hydroxyl group is similar to that of the surrounding water molecules, which are present in great excess. Although chemical methods for carrying out this transformation have been reported, such methods often rely on the use of acutely toxic reagents such as cyanogen bromide.[27] For these reasons artificial DNA backbones which are less challenging to form chemically are an attractive alternative.[28] Prevalent amongst these are the triazole,[29] amide[30,31] and phosphoramidate[32–34] linkages (Fig. 1(ii)). When incorporated into linear oligonucleotides these phosphodiester backbone analogues can be read through by DNA polymerases during linear copying and the polymerase chain reaction (PCR), with accurate transfer of genetic information.[28,32,35] They could potentially be incorporated into cyclic RCA templates provided that they can also be read through by the specific DNA polymerases that are compatible with efficient RCA. However, the use of chemically modified templates in RCA is particularly demanding because it requires the polymerase to accurately read through the modified linkage repeatedly in order to generate very long amplification products. In contrast, during PCR the polymerase needs only to copy the chemically modified template once during the first cycle, after which the reaction can proceed in an exponential manner, with the enzyme almost exclusively copying backbone-unmodified products in all subsequent cycles. Given the widespread importance of the RCA reaction, we undertook to study the cyclisation of DNA using chemical approaches and to examine the suitability of the chemically modified cyclic products as templates during RCA. We then demonstrated that RCA of the cyclic products can be used to prepare DNA nanoflowers.[23,36–41] Finally, we compared the size distribution, morphologies and extent of DNA loading of the DNA nanoflowers assembled from the RCA products of the chemically modified templates.

Open Access Article. Published on 24 August 2018. Downloaded on 8/23/2019 1:55:53 PM.
This article is licensed under a Creative Commons Attribution 3.0 Unported Licence.

Results and discussion

Choice of chemical linkages and template sequences

In the present study we investigate RCA of cyclic oligonucleotides containing a single triazole, amide or phosphoramidate analogue of the DNA phosphodiester backbone. All three modifications have been previously used in PCR amplification of linear DNA.[28,32,35,42–45] Of these, the triazole linkage (Fig. 1(ii)A) is the most thoroughly studied artificial DNA backbone.[29] It can be read through by both DNA and RNA polymerases and has been used in the construction of genes by chemical ligation. Importantly, DNA sequencing experiments did not reveal any increase in the level of mutations observed for cells transformed with the triazole-modified gene compared to those transformed with the canonical analogue.[35] There are two reports of cyclisation of linear DNA that contains 5′-azide and 3′-alkyne followed by RCA of the cyclic template. The first one, from our laboratory,[45] shows that cyclisation and subsequent RCA of a 100-mer DNA sequence designed to be free of secondary structure is possible, despite the presence of the 1,4-triazole linkage. The second study used a triazole-containing DNA template in an RCA-based fluorogenic assay for microRNA, but the authors did not compare the efficiency of the RCA reaction with that of an unmodified template.[46] In this work we also investigate amide and phosphoramidate chemical linkages (Fig. 1(ii)B and C), both of which can be formed by di-imide coupling chemistry. The phosphoramidate linkage is of particular interest as it closely mimics the steric and electronic properties of the canonical phosphodiester backbone.

In order to study the above three non-canonical DNA linkages in RCA we designed three cyclic templates of differing base composition, all of which are predicted to incorporate secondary structures, and two of which include cancer cell surface targeting aptamer sequences (oligonucleotide sequences are given in Table 1, and the predicted structures are shown in Fig. S1, ESI†). Template **1** is based on a randomly generated 50-mer sequence with approximately 50% GC content; template **2** incorporates a dumbbell-shaped double hairpin structure and serves as a template for an aptamer sequence which targets the mucin 1 (MUC1) glycoprotein[47]—an important class of tumour surface marker that is overexpressed on a range of epithelial cancer cells; template **3** is a cytosine-rich sequence encoding a complementary trimeric G quadruplex aptamer which recognises the human epidermal growth factor receptor 2, a major therapeutic target in human cancer treatment.[48] All four versions of each template were made: an unmodified control containing a natural phosphodiester (PO_4) backbone and analogues containing triazole (Tz), amide (Am) and phosphoramidate (PA) linkages at the point of cyclisation.‡ In addition we prepared the unmodified and triazole-modified cyclic templates **4**_PO_4 and **4**_Tz, which incorporate a palindromic sequence. The RCA product of **4**_PO_4 has been reported to assemble into a three-dimensional interwoven 'nanoclew' structure that can be used to deliver anticancer drugs.[39] Following cyclisation of the linear sequences all of the cyclic templates were purified then subjected to RCA using ϕ-29, a highly processive polymerase with strand displacement activity.[49]

Cyclisation of linear oligonucleotides

Linear oligonucleotides incorporating the required 5′-phosphate/3′-hydroxyl, 5′-azide/3′-alkyne, 5′-amine/3′-phosphate and 5′-amine/3′-carboxylate modifications were synthesised using automated solid phase phosphoramidite chemistry, as described in the ESI.† The linear unmodified control sequences were cyclised to give the cyclic templates **1**_PO_4, **2**_PO_4, **3**_PO_4 and **4**_PO_4 using T4 DNA ligase in the presence of a splint oligonucleotide. The splint oligonucleotides incorporate a region which is complementary to each end of the corresponding linear oligonucleotide and hence act as cyclisation templates by bringing the two reacting ends of the linear substrate into close proximity. Cyclisation of the chemically modified linear oligonucleotides was carried out under aqueous

Table 1 Sequences (5′ → 3′) of the cyclic template oligonucleotides used in this study

Cyclic template	Sequence of linear oligonucleotide precursor[a]	Number of bases
1_PO_4	^{P}TCCCAATTGGGTACGCAGTACCCACAGCAGATGTGACTGTGAATCGTGAC	50
1_Tz	^{Z}TCCCAATTGGGTACGCAGTACCCACAGCAGATGTGACTGTGAATCGTGAC^{K}	50
1_Am	^{M}TCCAATTGGGTACGCAGTACCCACAGCAGATGTGACTGTGAATCGTGACT^{X}	50
1_PA	^{M}TCCCAATTGGGTACGCAGTACCCACAGCAGATGTGACTGTGAATCGTGAC^{P}	50
2_PO_4	^{P}TGTCGTTTTACCCATGTGCTATAGCCACTACTGTCGTTTTACCCATGTGCTATAGCCACTAC	62
2_Tz	^{Z}TGTCGTTTTACCCATGTGCTATAGCCACTACTGTCGTTTTACCCATGTGCTATAGCCACTAC^{K}	62
2_Am	^{M}TGTCGTTTTACCCATGTGCTATAGCCACTACTGTCGTTTTACCCATGTGCTATAGCCACTAT^{X}	62
2_PA	^{M}TGTCGTTTTACCCATGTGCTATAGCCACTACTGTCGTTTTACCCATGTGCTATAGCCACTAC^{P}	62
3_PO_4	^{P}TTACCCCACACCGCTGCCCCCACACCGCTGCCCCCACACCGCTGCCTTAC	50
3_Tz	^{Z}TTACCCCACACCGCTGCCCCCACACCGCTGCCCCCACACCGCTGCCTTAC^{K}	50
3_Am	^{M}TACCCCACACCGCTGCCCCCACACCGCTGCCCCCACACCGCTGCCTTACT^{X}	50
3_PA	^{M}TTACCCCACACCGCTGCCCCCACACCGCTGCCCCCACACCGCTGCCTTAC^{P}	50
4_PO_4	^{P}GTTAATATTATTCGACGGGCCTGCTCGAGCTCGAGCTTGCATCGTGCAGCCGAAGCTTGCACGCGTGCTATTAAT	75
4_Tz	^{Z}TTGCACGCGTGCTATTAATGTTAATATTATTCGACGGGCCTGCTCGAGCTCGAGCTTGCATCGTGCAGCCGAAG^{Me}C^{K}	75

[a] P = 5′-PO_4; M = 5′-amine, X = 3′-carboxy, Z = 5′-azide, K = 3′-propargyl, ^{Me}C = methyl cytosine.

This journal is © The Royal Society of Chemistry 2018

Open Access Article. Published on 24 August 2018. Downloaded on 8/23/2019 1:55:53 PM.
This article is licensed under a Creative Commons Attribution 3.0 Unported Licence.

CuAAC or di-imide coupling conditions. In almost every case the linear precursor was successfully converted to the desired cyclic product with moderate to excellent efficiency.§ The linear 5′-azide/3′-alkyne oligonucleotides were cyclised by treatment with $CuSO_4$ in the presence of sodium ascorbate and tris-hydroxypropyltriazole (THPTA) in 0.2 M aqueous NaCl or denaturing organic/aqueous solvent mixtures. In all four cases the cyclisation reaction proceeded smoothly in the absence of a templating splint oligonucleotide. The 5′-amine/3′-phosphate oligonucleotides were cyclised by treatment with 1-ethyl-3-(3-dimethylaminopropyl)carbodiimide hydrochloride (EDC·HCl) and 2-(hydroxyethyl)imidazole in aqueous 0.2 M HEPES buffer (pH 7.2) using an adaptation of our previously reported phosphoramidate ligation method.[32] Similarly the 5′-amine/3′-carboxylate were cyclised using EDC·HCl in combination with *N*-hydroxysuccinimide in aqueous NaCl or HEPES buffer, also using an adaptation of a previously reported method.[28] The phosphoramidate- and amide-modified cyclic constructs **1**_PA and **1**_Am formed readily in the absence of a templating splint oligonucleotide; for the amide and phosphoramidate sequences **2**_PA, **2**_Am, **3**_PA and **3**_Am the cyclisation reactions were found to be less favourable under non-templating conditions and a splint oligonucleotide was therefore added in order to achieve more efficient cyclisation. Crude cyclisation reactions were analysed by polyacrylamide gel-electrophoresis (PAGE). Representative gel images for the template sequences **1**_PO_4, **1**_PA, **1**_Tz and **1**_Am are shown in Fig. 2 (see Fig. S2–S9, ESI† for PAGE analysis of all other cyclisation reactions).

During the EDC-mediated cyclisation reactions to prepare the phosphoramidate-modified templates we observed the formation of adducts of the cyclic products with molecular weights which are 155 mass units higher than those for the expected products by UPLC-mass spectrometry. This is consistent with the chemical addition of EDC to the oligonucleotides. Similar observations have been documented previously: the adducts are proposed to arise from a chemical reaction between the di-imide coupling reagent and the imide group of guanine and thymine DNA bases.[50–54] In support of this we did not observe formation of these adducts upon exposure of poly-adenine and poly-cytosine DNA sequences to 0.1 M EDC in 0.2 M HEPES buffer (pH 7.2) at room temperature, while in contrast a significant degree of EDC adduct formation was observed when the same experiment was performed with sequences containing guanine and thymine bases. Pleasingly it was possible to reverse this unwanted side-reaction by gently heating the crude product mixtures in 0.1 M NaOH after performing the phosphoramidate cyclisation reactions. Interestingly, we did not observe any evidence of the formation of the same EDC adducts during the reactions to prepare the amide-modified cyclic constructs, which were carried out under slightly different conditions and required a lower concentration of the di-imide coupling agent.

All of the modified and unmodified cyclic products were readily purified by PAGE. For the splint-mediated cyclisation reactions it was necessary to use denaturing PAGE conditions during purification, while for the non-templated reactions either denaturing or non-denaturing conditions were selected, depending on which gave better separation between the linear oligonucleotide precursor and cyclic oligonucleotide product. Full details of the cyclisation and purification protocols along with analytical data for all of the cyclic constructs are provided as ESI (Fig. S10–S23, ESI†).

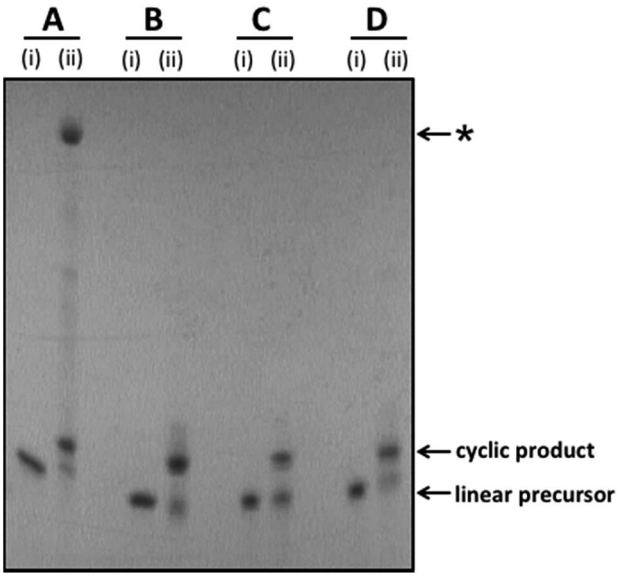


Fig. 2 Representative examples of splint-mediated enzymatic and non-templated chemical cyclisation reactions to give the cyclic oligonucleotide templates **1**_PO_4 (A), **1**_Tz (B), **1**_PA (C) and **1**_Am (D). The crude reaction mixtures were analysed by polyacrylamide gel electrophoresis on a 15% denaturing gel. Samples were imaged by UV shadowing. (A) Enzymatic cyclisation of linear unmodified 5′-phosphate/3′-hydroxyl oligonucleotide using T4 DNA ligase. (B) CuAAC-mediated cyclisation of linear 5′-azide/3′-alkyne oligonucleotide, introducing a triazole linkage. (C) Di-imide-mediated cyclisation of linear 5′-amine/3′-phosphate oligonucleotide, introducing a phosphoramidate linkage. (D) Di-imide-mediated cyclisation of linear 5′-amine/3′-carboxyl oligonucleotide, introducing an amide linkage. (i) = linear oligonucleotide substrate; (ii) = crude cyclisation reaction. *The major, slow-migrating side-product observed in the crude reaction mixture for the enzymatic ligation reaction is assigned as a cyclic dimer (molecular weight determined by UPLC-MS: 30 915 Da; calculated molecular weight for cyclic dimer: 30 912 Da; see Fig. S10, ESI†).

While the efficiency of each cyclisation method described above was observed to vary depending on the individual linear oligonucleotide sequence, it is noteworthy that the chemical ligation methods can offer significant improvements in cyclisation efficiency in cases where the more commonly used enzymatic approach proves problematic. For example, while the T4-DNA ligase-mediated cyclisation of the 'nanoclew' template **4**_PO_4 was low-yielding, producing a number of higher molecular weight oligomeric side-products, the analogous CuAAC-mediated cyclisation reaction—when performed in the presence of denaturing organic solvents to disrupt secondary structure—proceeded more cleanly, generating fewer by-products (Fig. 3). The efficiency of this chemical cyclisation reaction appears comparable to that of the reported CircLigase II-mediated cyclisation of the same template;[39] however, the chemical cyclisation approach is not limited in scale by the high

Open Access Article. Published on 24 August 2018. Downloaded on 8/23/2019 1:55:53 PM.
This article is licensed under a Creative Commons Attribution 3.0 Unported Licence.

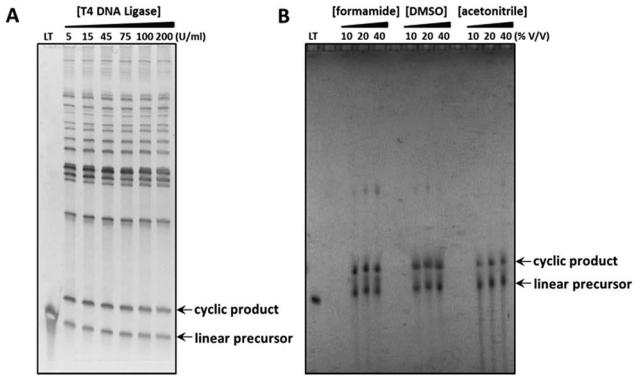


Fig. 3 Comparison of the enzymatic and CuAAC-mediated cyclisations used to prepare the cyclic constructs **4**_PO_4 and **4**_Tz respectively, whose sequences incorporate complex secondary structure. The crude reaction products were analysed using 8% denaturing polyacrylamide gels, which were visualised by post-staining with SYBR Gold (A) or by UV-shadowing (B). (A) Splint-mediated enzymatic cyclisation of the linear oligonucleotide in the presence of an increasing concentration of T4 DNA ligase. LT: linear 5′-phosphate/3′-hydroxyl functionalised oligonucleotide substrate. (B) Non-templated CuAAC-mediated cyclisation of the linear oligonucleotide in the presence of denaturing organic solvents. LT: linear 5′-azide/3′-alkyne functionalised oligonucleotide precursor.

cost associated with the CircLigase enzyme. The chemical ligation methods discussed here therefore provide a greatly expanded toolkit for the cyclisation of linear oligonucleotides, with the potential to carry out the reactions under varied conditions, in the presence of denaturing agents, at varying salt concentration and temperature, and with significantly reduced cost. In addition, chemical ligation reactions are more robust and more scalable than enzymatic reactions, with attendant enhancements in the ease of purification, isolation and characterisation of the cyclic products.

Rolling circle amplification of the cyclic oligonucleotides

RCA using the ϕ-29 polymerase. For all fourteen cyclic templates, RCA was carried out using ϕ-29 polymerase, a 16 or 18 nucleobase primer, 2 mM dNTPs and 20 mM Mg^{2+} at 30 °C.¶ Analysis of the product mixtures using agarose gel-electrophoresis indicated that in all cases the RCA reactions were successful (Fig. 4 and S24–S32, ESI†). However, there were significant differences in the quantities and size distributions of the products, which depended on the nature of the modified linkage in the cyclic template. Each reaction produced a detectable quantity of very slow-migrating products which were retarded in the wells of the gel and, in some cases, a second discrete band with higher gel mobility was also observed to form a substantial proportion of the product distribution (Fig. 4). By analogy with a recent literature report,[55] this faster-running band was assigned to double-stranded products, while the material which is retarded in the wells is assigned to the expected very long single-stranded products. A possible mechanism for the formation of double-stranded side-products during RCA is illustrated in Fig. 5. It is noteworthy that the faster-running band assigned to double-stranded DNA side-

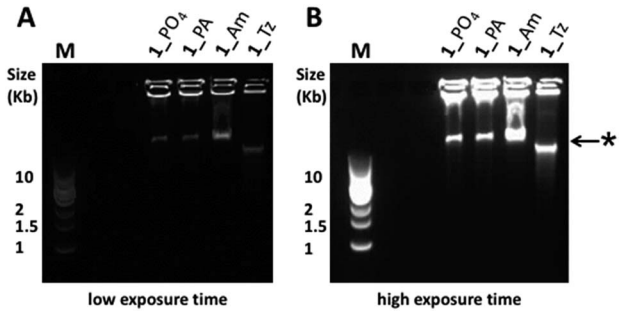


Fig. 4 Agarose gel (0.8% agarose) analysis of the products formed during ϕ-29 polymerase catalysed RCA using cyclic templates **1**_PO_4, **1**_Tz, **1**_Am and **1**_PA (8 hour amplification time). The RCA products were visualised by pre-casting the gel to contain a 0.5× concentration of SYBR® Gold nucleic acid gel stain. (A) Gel image using a short exposure time. (B) The same gel imaged using a longer exposure time, enabling visualisation of all products. M: 1 kb DNA ladder; *: this band is assigned to double-stranded DNA side-products.[55]

products was not observed after RCA of the cyclic templates **3**_PO_4, **3**_Am, **3**_PA and **3**_Tz, which encode a complementary trimeric G quadruplex aptamer sequence (Fig. S30–S32, ESI†). One possible explanation is that the mechanism of double-stranded DNA formation is suppressed by the tendency for the emerging RCA product to fold up into a G quadruplex secondary structure. The phosphoramidate modification gave very efficient RCA, consistently yielding product distributions which were indistinguishable from those of the unmodified templates (Fig. 4, S24, S27 and S30, ESI†). The amide-modified cyclic templates also appeared to be well-tolerated by the ϕ-29 polymerase, producing similar product distributions to the unmodified control sequences in all cases (Fig. 4, S25, S28 and S31, ESI†). In contrast, the triazole-containing templates gave

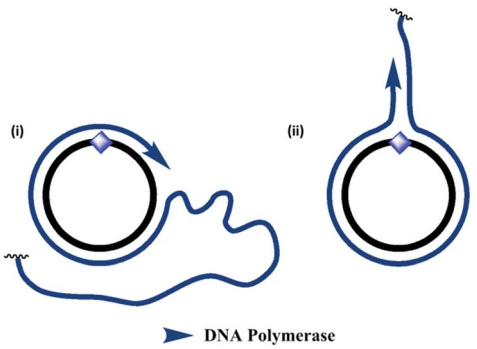


Fig. 5 Proposed mechanism for the formation of double-stranded products during RCA of the triazole- and amide-modified cyclic templates. (i) In the normal RCA mechanism, the amplified single-stranded product is continuously displaced from the cyclic template, resulting in the formation of very long single-stranded products. (ii) An alternative mechanism allows the enzyme to dissociate from the cyclic template oligonucleotide and copy the emerging single-stranded product, resulting in the formation of double-stranded side-products. This process sequesters the cyclic template and inhibits RCA. This mechanism may be favoured in the presence of the unnatural triazole- and amide-backbone linkages, which the enzyme has greater difficulty in reading through.

This journal is © The Royal Society of Chemistry 2018

Open Access Article. Published on 24 August 2018. Downloaded on 8/23/2019 1:55:53 PM.
This article is licensed under a Creative Commons Attribution 3.0 Unported Licence.

weaker and more variable results. While the triazole-modified cyclic template **1**_Tz performed moderately in comparison to the unmodified and amide- and phosphoramidate-modified analogues, the cyclic templates **2**_Tz, **3**_Tz and **4**_Tz consistently produced much lower yields of very long, slow-migrating RCA products (Fig. 4; S26, S29 and S32, ESI†). The overall performance of the triazole-containing templates therefore appears to be compromised in comparison to those of the unmodified and phosphoramidate-containing analogues. This is a salient observation given that a recent publication uses a triazole-containing cyclic template with ϕ-29 in an RCA-based fluorescent switch-based diagnostic assay for microRNA detection.[46] It is also interesting that during RCA of the amide- and triazole-modified templates **1**_Am, **1**_Tz and **2**_Am the proportion of double-stranded side-products appears to increase with extended amplification time. In contrast the relative proportions of the bands assigned to single- and double-stranded products respectively appear to stay approximately constant throughout the course of the RCA reactions for all of the unmodified and phosphoramidate-modified templates (Fig. S24–S28 and S30, ESI†).‖

Probing the single-stranded RCA products with complementary fluorescent oligonucleotides. To obtain further information about the nature of the products from the RCA reactions on the modified phosphoramidate-, amide- and triazole-containing cyclic templates we developed a fluorescent probe assay to allow differentiation between single- and double-stranded RCA products by gel-electrophoresis. A single-stranded Cy3-labelled fluorescent hybridisation probe with a sequence which is complementary to those of the single stranded products obtained from RCA of the cyclic templates **1**_PO_4, **1**_Tz, **1**_PA and **1**_Am was synthesised. In order to validate the assay, a scrambled version of the probe was also prepared, and we performed a preliminary control experiment using the complementary and scrambled versions of the hybridisation probe in order to confirm that the complementary probe binds specifically with the RCA product of the cyclic template **1**_PO_4 through base paring (Fig. S33, ESI†). RCA of the four cyclic templates **1**_PO_4, **1**_Tz, **1**_PA and **1**_Am was then performed using the ϕ-29-polymerase enzyme and individual RCA reactions were stopped by heat inactivation of the polymerase at two hour intervals over a twenty hour time period. The product mixtures were then incubated with the fluorescent hybridisation probe for two hours at room temperature before analysis using agarose gel electrophoresis. The gels were imaged with excitation at 520 nm under the Cy3 fluorescence channel of a Syngene G:BOX imager (Fig. 6). Finally, the same gels were post-stained with a solution of SYBR Gold, which can sensitively detect both double- and single-stranded DNA, and re-imaged with excitation at 302 nm (Fig. S34, ESI†). The results show that a strong fluorescence signal from the bound Cy3 labelled probe is detected after amplification of the unmodified, amide-modified and phosphoramidate-modified templates **1**_PO_4, **1**_PA and **1**_Am. This demonstrates that the fluorescent probe has successfully hybridised to the RCA products, confirming their single-stranded nature. Conversely, after amplification of the triazole-modified template, no appreciable signal

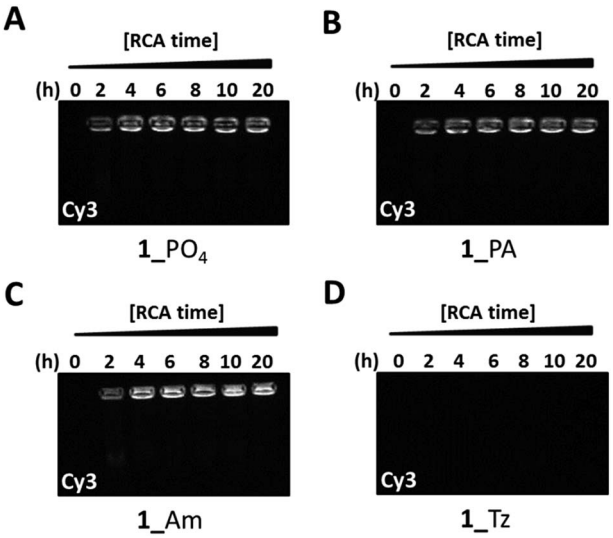


Fig. 6 Probing the nature of the amplified products from ϕ-29-mediated RCA of the cyclic templates **1**_PO_4 (A), **1**_PA (B), **1**_Am (C) and **1**_Tz (D) using a fluorescent probe hybridisation assay. Aliquots of the RCA reactions were stopped by heat inactivation at regular two hour intervals for a total period of 20 hours. A Cy3-labelled fluorescent probe with a sequence which is complementary to the RCA products was added to each aliquot and the mixtures were analysed by agarose gel electrophoresis (0.8% agarose). The gels were imaged under the Cy3 fluorescence channel. The gels were subsequently stained with SYBR Gold (Fig. S34, ESI†).

from the Cy3 fluorophore is detected, although some slow-migrating RCA products are weakly detected in the wells of the gel after post-staining with SYBR Gold. This suggests that the products of the RCA reaction using the triazole-modified template contain a significantly lower quantity of both single- and double-stranded DNA.

Probing the nature and quantity of the RCA products *via* a fluorometric plate-reading assay. In order to corroborate the results from the gel-imaging we used a fluorometric plate-reading assay to allow a semi-quantitative comparison of the rates and total DNA yields of RCA reactions performed using ϕ-29 polymerase and the cyclic templates **1**_PO_4, **1**_Tz, **1**_PA and **1**_Am over a 10 hour time course. After the desired time period the reactions were stopped by heat inactivation of the polymerase and then analysed, using three different DNA-binding dyes to provide a fluorescence signal: SYBR Gold, SYBR Green I and SYBR Green II. The intensities of the measured fluorescence signals are approximately proportional to the total concentrations of DNA in each reaction mixture, with some expected deviations as a result of the differing proportions of single- and double-stranded DNA amplification products. In agreement with the gel-imaging results, the reaction rates and product yields for the RCA reactions with the cyclic phosphoramidate-containing template **1**_PA are essentially the same as those for the unmodified cyclic template **1**_PO_4, and the cyclic amide template **1**_Am performs almost as well. The cyclic triazole template **1**_Tz is shown to be inferior: at each time-point the measured fluorescence intensities are weaker for the RCA reaction involving the triazole-containing template

Open Access Article. Published on 24 August 2018. Downloaded on 8/23/2019 1:55:53 PM.
This article is licensed under a Creative Commons Attribution 3.0 Unported Licence.

1_Tz than for those involving the other three templates, indicating that a lower quantity of DNA is produced when **1**_Tz is used as a substrate. By taking into account the differing selectivities of the three DNA binding dyes for double-stranded DNA over single-stranded DNA it also possible to draw inferences about the nature of the products. While all three dyes are known to bind both double- and single-stranded DNA to some extent, SYBR Green I has the most pronounced selectivity for double-stranded DNA over single-stranded DNA.[56–58] The measured fluorescence intensities for the samples containing the triazole-modified template relative to those containing the phosphate and phosphoramidate templates are noticeably higher in the presence of SYBR Green I than in the presence of the SYBR Gold and SYBR Green II dyes (Fig. 7). Hence there is a strong indication that a significant amount of double-stranded DNA is produced in the RCA reaction on the triazole-containing template, which is consistent with the prior gel-imaging results. The same phenomenon is observed for the amide-modified template **1**_Am, but to a much smaller extent. This is probably because each time the polymerase encounters the modified linkage in the cyclic template, it can choose between processively reading through the modified linkage or dissociating from the cyclic template and instead copying the RCA product as it emerges, thereby producing double-stranded products (Fig. 5).[55] Since the triazole linkages are seemingly more difficult/slower to read through, it is likely that the alternative mechanism is more strongly favoured in their presence, resulting in the formation of a higher proportion of double-stranded products which would be of shorter length. This process may also sequester the cyclic template, contributing to the lower overall yield of DNA product.

RCA using the Bst 2.0 DNA polymerase. In light of the disappointing performances of the triazole-containing templates in the ϕ-29-mediated RCA reactions, we also investigated RCA using the Bst 2.0 DNA polymerase for two of the cyclic triazole templates **1**_Tz and **4**_Tz and their unmodified analogues **1**_PO_4 and **4**_PO_4, in order to ascertain whether the triazole linkage can be read through more efficiently by this alternative polymerase. The Bst 2.0 enzyme was previously used for RCA of the cyclic template **4**_PO_4 [39] and is known to efficiently incorporate modified dNTPs during RCA but its ability to read through modified backbone linkages has not yet been thoroughly tested.[59,60] Agarose electrophoretic analysis of the RCA products indicated that, while the ϕ-29 enzyme again exhibited higher RCA efficiencies with the unmodified templates **1**_PO_4 and **4**_PO_4 compared to the triazole-containing analogues **1**_Tz and **4**_Tz, Bst 2.0 was able to process the triazole-modified templates more efficiently (Fig. 8). For example, reactions performed using the Bst 2.0 enzyme produced similar yields and product distributions for the triazole-modified and unmodified cyclic templates **1**_Tz and **1**_PO_4, which are based on a randomly generated sequence (Fig. 8B). Moreover, for the nanoclew template sequences **4**_Tz and **4**_PO_4 the Bst 2.0 DNA enzyme appeared to generate a significantly greater quantity of very long, slow-migrating RCA products from the triazole-containing template **4**_Tz than from the unmodified control **4**_PO_4. Although unexpected, this result exemplifies the utility of having an available choice of chemical cyclisation methods in cases where the cyclisation and/or

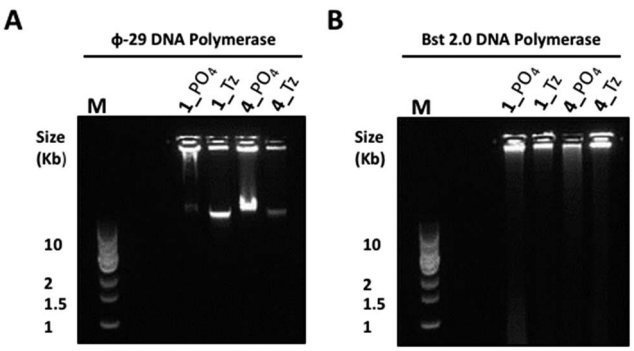


Fig. 8 Agarose gel (0.8%) analysis of the product distributions from RCA of the triazole-modified cyclic templates **1**_Tz and **4**_Tz and the unmodified analogues **1**_PO_4 and **4**_PO_4 using ϕ-29 (A) and Bst 2.0 (B) polymerase enzymes after 20 hours. M: 1 kb DNA ladder; gels were pre-cast to contain a 0.5× concentrated solution of SYBR® Gold nucleic acid gel stain.

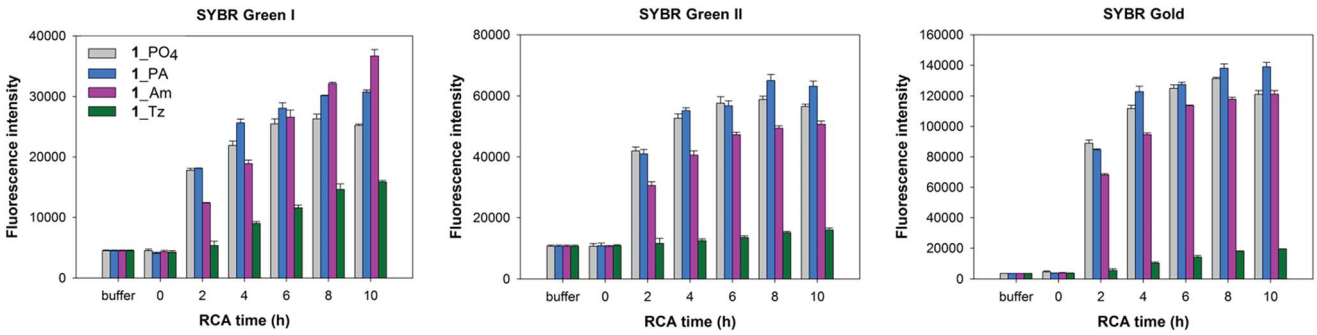


Fig. 7 Fluorescence quantification of amplified DNA products from RCA reactions using the cyclic templates **1**_PO_4, **1**_Am, **1**_PA and **1**_Tz and the ϕ-29 DNA polymerase over a 10 hour time course. EDTA was added to break down the precipitate releasing extended DNA prior to incubation with DNA binding dyes. Measurements are recorded in the presence of SYBR Gold, SYBR Green I and SYBR Green II fluorescent DNA binding dyes. Error bars represent the standard deviation of three measurements taken from a single RCA reaction. The reactions were also repeated in duplicate and the same trends were observed in both cases.

This journal is © The Royal Society of Chemistry 2018

Open Access Article. Published on 24 August 2018. Downloaded on 8/23/2019 1:55:53 PM.
This article is licensed under a Creative Commons Attribution 3.0 Unported Licence.

amplification of a specific canonical sequence proves to be inefficient. The RCA products from the reactions using the Bst 2.0 polymerase were also quantified *via* a fluorometric plate-reading assay, which corroborated the gel-imaging results. However it is notable that in all four reactions the Bst 2.0 enzyme generated a higher proportion of double-stranded products than the ϕ-29 enzyme (Fig. 9A and B)—reflecting the Bst enzyme's inferior processivity and strand displacement activity under the conditions used in our RCA experiments.

Nanoflower formation

Long RCA products are known to spontaneously self-assemble into densely-packed DNA–inorganic hybrid nanoflower (DNA-NF) structures in the presence of a magnesium pyrophosphate co-precipitant, which is also generated as a by-product of the RCA reaction. The DNA-NF structures are thought to comprise an inorganic magnesium pyrophosphate core onto which the long single-stranded DNA RCA products are adsorbed. These nanoflower structures have several attractive features which are driving their investigation as potential diagnostic and therapeutic agents: they are easy to prepare; they are size-tuneable and biodegradable, yet resistant to digestion by exonuclease enzymes; they can be designed to incorporate a functional aptamer, DNAzyme, restriction enzyme, antisense or drug-loading sequence for targeted recognition and delivery; and they have been shown to be capable of cellular transfection.[23,36–41] Scanning electron microscopy (SEM) experiments were used to map the size and morphology of the nanoflowers formed at different time points during the RCA reactions performed using the unmodified and modified cyclic templates. After time periods of eight and twenty hours aliquots of the reactions were removed and heated to inactivate the enzyme. The precipitated nanoflowers were then collected by centrifugation, thoroughly washed with deionised water and subjected to SEM imaging experiments. The extent of DNA loading was also examined by agarose gel electrophoresis (Fig. S35–S36, ESI†). The SEM images (Fig. 10 and 11) indicated that there was no significant difference in the size and morphology of the DNA nanoflowers generated from the four types of cyclic template, even though the triazole containing sequences are less efficient as RCA templates. In all cases DNA-NF structures with diameters of >1 μm and petal-like surface morphologies were formed in the RCA reaction mixture within eight hours, and their sizes were observed to have marginally increase after 20 hours. Variation of the Mg^{2+} concentration was found to have a significant effect on the particle size and DNA loading. At Mg^{2+} concentrations of ≤10 mM the particles were found to contain negligible quantities of DNA; as the Mg^{2+} concentration was increased from 10–25 mM the extent of DNA loading steadily increased, with a concomitant reduction in the size of the particles from ~3 μm to ~0.8 μm (Fig. 11 and S37–S46, ESI†). Although the reason for the contraction of the nanoparticles with increasing Mg^{2+} concentration is not immediately obvious, it is possible that this reflects an increased rate of nucleation at higher metal ion concentration, which might be expected to produce a higher number of particles with a smaller average diameter.

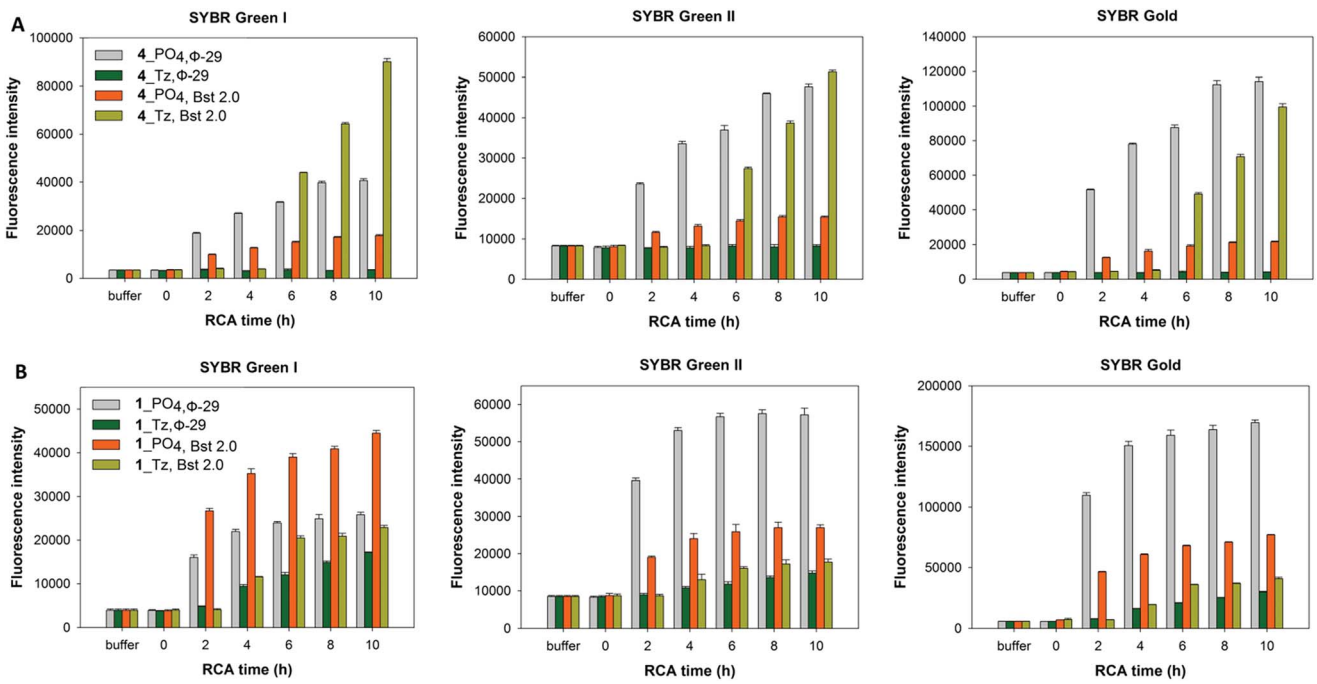


Fig. 9 Fluorescence quantification of amplified DNA products from RCA reactions using the cyclic templates ((A) **4**_PO_4, and **4**_Tz; (B) **1**_PO_4, and **1**_Tz) and enzyme over a 10 hour time course. The performances of the ϕ-29 and Bst 2.0 DNA polymerases are compared. EDTA was added to break down the precipitate releasing extended DNA prior to incubation with DNA binding dyes. Measurements are recorded in the presence of SYBR Gold, SYBR Green I and SYBR Green II fluorescent DNA binding dyes. Error bars represent the standard deviation of three measurements taken from a single RCA reaction. The reactions were also repeated in duplicate and the same trends were observed in both cases.

Open Access Article. Published on 24 August 2018. Downloaded on 8/23/2019 1:55:53 PM.
This article is licensed under a Creative Commons Attribution 3.0 Unported Licence.

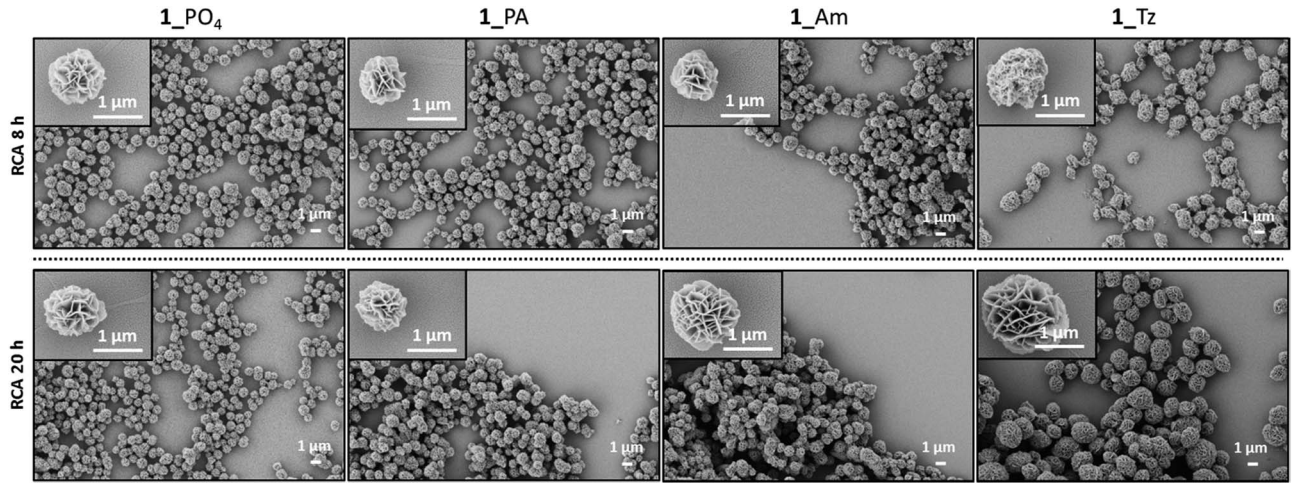


Fig. 10 SEM images of the DNA-NFs generated from RCA of the cyclic templates **1**_PO_4, **1**_PA, **1**_Am and **1**_Tz using the ϕ-29 polymerase in the presence of 20 mM Mg^{2+} after 8 hours and 20 hours.

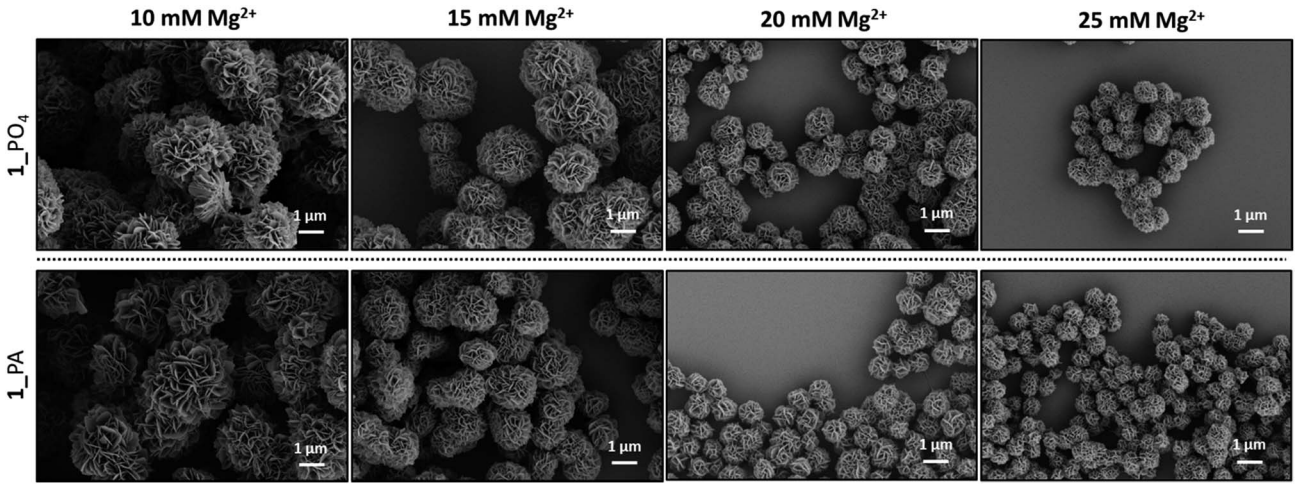


Fig. 11 SEM images of the DNA-NFs formed from RCA of the cyclic templates **1**_PO_4 (top) and **1**_PA (bottom) using the ϕ-29 polymerase in the presence of different concentrations of Mg^{2+}. The RCA reactions were left for 20 hours and the Mg^{2+} concentrations ranged from 10–25 mM.

Conclusions

We have shown that single-stranded DNA templates can be efficiently cyclised using three different chemical ligation methods. The resulting cyclic constructs contain a single unnatural triazole, amide or phosphoramidate linkage at the point of ligation. These chemical cyclisation methods offer several advantages over the more limited enzymatic approach: they are cheaper and easier to carry out, allowing for the large-scale synthesis and purification of the cyclic oligonucleotide products; they can also be performed under a wider variety of conditions, including denaturing ones, and are therefore particularly useful for cyclising linear oligonucleotides which contain problematic secondary structure. The chemical cyclisation methods described here therefore provide a versatile expanded toolkit for the preparation of cyclic oligonucleotides, which have an expansive range of potential applications across molecular biology[61–65] and nanotechnology.[66–69] Here we investigated the use of the chemically modified cyclic products as templates for the production of long single-stranded DNA concatemers *via* the highly demanding rolling circle amplification reaction, an important technique which is currently attracting widespread interest. The cyclic templates containing a non-canonical phosphoramidate backbone linkage performed particularly well during RCA—with overall yields, product distributions and reaction rates which were indistinguishable from those of the analogous unmodified templates. In contrast, the triazole-modified templates were less well tolerated by the ϕ-29 polymerase, showing a tendency to produce double-stranded DNA side-products and varying overall yields. The performance of the templates containing an amide modification falls in between those of the phosphoramidate and triazole linkages. Interestingly, for one of the cyclic template sequences, the Bst 2.0 polymerase enzyme was found to amplify the

 This journal is © The Royal Society of Chemistry 2018

Open Access Article. Published on 24 August 2018. Downloaded on 8/23/2019 1:55:53 PM.
This article is licensed under a Creative Commons Attribution 3.0 Unported Licence.

triazole-modified template with greater efficiency than the unmodified analogue, suggesting that different combinations of chemical ligation method and polymerase enzyme may find application where RCA proves challenging. Of all the cyclic templates investigated, the phosphoramidate-containing versions are the most straightforward to synthesise and could be produced in commercial DNA synthesis facilities from readily available precursors. We propose that phosphoramidate cyclisation is a practical, scalable and convenient method for the production of biocompatible cyclic DNA constructs for use in many applications, including RCA.

Conflicts of interest

There are no conflicts to declare.

Acknowledgements

This work was supported by the Leverhulme Trust [grant number RPG-2015-005], the Biotechnology and Biological Sciences Research Council [grant number BB/J001694/2] and ATDBio Ltd. Electron microscopy was performed at the Dunn School of Pathology EM facility. We also thank Maria Font Farre (Department of Plant Sciences, Oxford) for assistance with gel imaging.

Notes and references

‡ Where necessary slight modifications were made to the ordering of the terminal nucleobases in order to make the sequences compatible with the chemistry used to introduce the required amino, azido or alkyne functionality at the 5′ and 3′ ends. Each phosphoramidate sequence contains 5′-amino dT; each amide sequence contains both 5′-amino dT and 3′-carboxy dT; and each triazole sequence contains 5′-azido dT and 3′-propargyl dC. See the ESI† for further details of the oligonucleotide synthesis chemistry.

§ The only exception is that the amide cyclisation reaction to give the cyclic template **3**_Am was inefficient, yielding a significant quantity of higher molecular weight side-products. Although we were able to isolate a sample of the cyclic template **3**_Am, it was found to contain impurities by HPLC mass spectrometry analysis (see Fig. S20, ESI†). Nonetheless, this sample was successfully used as a template in RCA, with promising results.

¶ A lower Mg^{2+} concentration of 10 mM is recommended by the enzyme supplier. Our experiments indicated that, although RCA proceeds efficiently over a wide Mg^{2+} concentration range of 10–25 mM, the preparation on DNA-NFs is more sensitive to Mg^{2+} concentration: at 10 mM Mg^{2+} concentrations the extent of DNA loading is often negligible, whereas a higher 20 mM Mg^{2+} gives higher and more consistent levels of DNA loading. Taking this into account, we chose to use a 20 mM concentration of Mg^{2+} throughout our RCA experiments.

‖ We also investigated whether the formation of double-stranded amplification products could be suppressed by addition of single-stranded DNA binding protein to ϕ-29 mediated RCA reactions of the cyclic templates **1**_PO_4 and **1**_PA, as previously described by Högberg and co-workers.[55] However, when using our smaller, chemically modified templates we did not observe any significant differences in the product distributions of the RCA reactions carried out in the absence and presence of the single-stranded binding protein (see Fig. S47, ESI for further details†).

1 M. M. Ali, F. Li, Z. Zhang, K. Zhang, D.-K. Kang, J. A. Ankrum, X. C. Le and W. Zhao, *Chem. Soc. Rev.*, 2014, **43**, 3324–3341.
2 M. G. Mohsen and E. T. Kool, *Acc. Chem. Res.*, 2016, **49**, 2540–2550.
3 P. M. Lizardi, X. Huang, Z. Zhu, P. Bray-Ward, D. C. Thomas and D. C. Ward, *Nat. Genet.*, 1998, **19**, 225–232.
4 J. Banér, M. Nilsson, M. Mendel-Hartvig and U. Landegren, *Nucleic Acids Res.*, 1998, **26**, 5073–5078.
5 A. T. Christian, M. S. Pattee, C. M. Attix, B. E. Reed, K. J. Sorensen and J. D. Tucker, *Proc. Natl. Acad. Sci. U. S. A.*, 2001, **98**, 14238–14243.
6 B. Schweitzer, S. Roberts, B. Grimwade, W. Shao, M. Wang, Q. Fu, Q. Shu, I. Laroche, Z. Zhou, V. T. Tchernev, J. Christiansen, M. Velleca and S. F. Kingsmore, *Nat. Biotechnol.*, 2002, **20**, 359–365.
7 E. J. Cho, L. Yang, M. Levy and A. D. Ellington, *J. Am. Chem. Soc.*, 2005, **127**, 2022–2023.
8 F. Maruyama, T. Kenzaka, N. Yamaguchi, K. Tani and M. Nasu, *Appl. Environ. Microbiol.*, 2005, **71**, 7933–7940.
9 M. Nilsson, *Histochem. Cell Biol.*, 2006, **126**, 159–164.
10 S. Margeridon, S. Carrouée-Durantel, I. Chemin, L. Barraud, F. Zoulim, C. Trépo and A. Kay, *Antimicrob. Agents Chemother.*, 2008, **52**, 3068–3073.
11 M. M. Ali and Y. Li, *Angew. Chem., Int. Ed.*, 2009, **48**, 3512–3515.
12 C. Ma, W. Wang, Q. Yang, C. Shi and L. Cao, *Biosens. Bioelectron.*, 2011, **26**, 3309–3312.
13 J. Ge, L.-L. Zhang, S.-J. Liu, R.-Q. Yu and X. Chu, *Anal. Chem.*, 2014, **86**, 1808–1815.
14 Q. Sheng, N. Cheng, W. Bai and J. Zheng, *Chem. Commun.*, 2015, **51**, 2114–2117.
15 W. Zhao, M. M. Ali, M. A. Brook and Y. Li, *Angew. Chem., Int. Ed.*, 2008, **47**, 6330–6337.
16 Y. Ma, H. Zheng, C. Wang, Q. Yan, J. Chao, C. Fan and S.-J. Xiao, *J. Am. Chem. Soc.*, 2013, **135**, 2959–2962.
17 K. Zhang, R. Deng, Y. Sun, L. Zhang and J. Li, *Chem. Sci.*, 2017, **8**, 7098–7105.
18 G. D. Hamblin, K. M. M. Carneiro, J. F. Fakhoury, K. E. Bujold and H. F. Sleiman, *J. Am. Chem. Soc.*, 2012, **134**, 2888–2891.
19 W. Zhao, Y. Gao, S. A. Kandadai, M. A. Brook and Y. Li, *Angew. Chem., Int. Ed.*, 2006, **45**, 2409–2413.
20 O. I. Wilner, S. Shimron, Y. Weizmann, Z.-G. Wang and I. Willner, *Nano Lett.*, 2009, **9**, 2040–2043.
21 J. B. Lee, S. Peng, D. Yang, Y. H. Roh, H. Funabashi, N. Park, E. J. Rice, L. Chen, R. Long, M. Wu and D. Luo, *Nat. Nanotechnol.*, 2012, **7**, 816–820.
22 H. Qi, M. Ghodousi, Y. Du, C. Grun, H. Bae, P. Yin and A. Khademhosseini, *Nat. Commun.*, 2013, **4**, 2275.
23 R. Hu, X. Zhang, Z. Zhao, G. Zhu, T. Chen, T. Fu and W. Tan, *Angew. Chem., Int. Ed.*, 2014, **53**, 5821–5826.
24 J. B. Lee, J. Hong, D. K. Bonner, Z. Poon and P. T. Hammond, *Nat. Mater.*, 2012, **11**, 316–322.
25 R. An, Q. Li, Y. Fan, J. Li, X. Pan, M. Komiyama and X. Liang, *Nucleic Acids Res.*, 2017, **45**, e139.
26 Y. Cui, X. Han, R. An, G. Zhou, M. Komiyama and X. Liang, *RSC Adv.*, 2018, **8**, 18972–18979.
27 G. Prakash and E. T. Kool, *J. Am. Chem. Soc.*, 1992, **114**, 3523–3527.
28 A. Shivalingam, A. E. S. Tyburn, A. H. El-Sagheer and T. Brown, *J. Am. Chem. Soc.*, 2017, **139**, 1575–1583.

Open Access Article. Published on 24 August 2018. Downloaded on 8/23/2019 1:55:53 PM. This article is licensed under a Creative Commons Attribution 3.0 Unported Licence.

29 A. H. El-Sagheer and T. Brown, *Acc. Chem. Res.*, 2012, **45**, 1258–1267.
30 A. D. Mesmaeker, A. Waldner, J. Lebreton, P. Hoffmann, V. Fritsch, R. M. Wolf and S. M. Freier, *Angew. Chem., Int. Ed. Engl.*, 1994, **33**, 226–229.
31 M. Kuwahara, H. Takeshima, J. Nagashima, S. Minezaki, H. Ozaki and H. Sawai, *Bioorg. Med. Chem.*, 2009, **17**, 3782–3788.
32 A. H. El-Sagheer and T. Brown, *Chem. Commun.*, 2017, **53**, 10700–10702.
33 M. Kalinowski, R. Haug, H. Said, S. Piasecka, M. Kramer and C. Richert, *ChemBioChem*, 2016, **17**, 1150–1155.
34 S. M. Gryaznov and R. L. Letsinger, *Nucleic Acids Res.*, 1992, **20**, 3403–3409.
35 M. Kukwikila, N. Gale, A. H. El-Sagheer, T. Brown and A. Tavassoli, *Nat. Chem.*, 2017, **9**, 1089–1098.
36 L. Zhang, G. Zhu, L. Mei, C. Wu, L. Qiu, C. Cui, Y. Liu, I.-T. Teng and W. Tan, *ACS Appl. Mater. Interfaces*, 2015, **7**, 24069–24074.
37 Y. Lv, R. Hu, G. Zhu, X. Zhang, L. Mei, Q. Liu, L. Qiu, C. Wu and W. Tan, *Nat. Protoc.*, 2015, **10**, 1508–1524.
38 G. Zhu, R. Hu, Z. Zhao, Z. Chen, X. Zhang and W. Tan, *J. Am. Chem. Soc.*, 2013, **135**, 16438–16445.
39 W. Sun, T. Jiang, Y. Lu, M. Reiff, R. Mo and Z. Gu, *J. Am. Chem. Soc.*, 2014, **136**, 14722–14725.
40 Y. Jin, Z. Li, H. Liu, S. Chen, F. Wang, L. Wang, N. Li, K. Ge, X. Yang, X.-J. Liang and J. Zhang, *NPG Asia Mater.*, 2017, **9**, e365.
41 E. Kim, L. Zwi-Dantsis, N. Reznikov, C. S. Hansel, S. Agarwal and M. M. Stevens, *Adv. Mater.*, 2017, **29**, 1701086.
42 A. Shivalingam and T. Brown, *Biochem. Soc. Trans.*, 2016, **44**, 709–715.
43 C. N. Birts, A. P. Sanzone, A. H. El-Sagheer, J. P. Blaydes, T. Brown and A. Tavassoli, *Angew. Chem., Int. Ed.*, 2014, **53**, 2362–2365.
44 A. P. Sanzone, A. H. El-Sagheer, T. Brown and A. Tavassoli, *Nucleic Acids Res.*, 2012, **40**, 10567–10575.
45 A. H. El-Sagheer, A. P. Sanzone, R. Gao, A. Tavassoli and T. Brown, *Proc. Natl. Acad. Sci. U. S. A.*, 2011, **108**, 11338–11343.
46 Y. Li, Q. Pu, J. Li, L. Zhou, Y. Tao, Y. Li, W. Yu and G. Xie, *Microchim. Acta*, 2017, **184**, 4323–4330.
47 C. S. M. Ferreira, M. C. Cheung, S. Missailidis, S. Bisland and J. Gariépy, *Nucleic Acids Res.*, 2009, **37**, 866–876.
48 G. Mahlknecht, R. Maron, M. Mancini, B. Schechter, M. Sela and Y. Yarden, *Proc. Natl. Acad. Sci. U. S. A.*, 2013, **110**, 8170–8175.
49 F. B. Dean, J. R. Nelson, T. L. Giesler and R. S. Lasken, *Genome Res.*, 2001, **11**, 1095–1099.
50 P. T. Gilham, *J. Am. Chem. Soc.*, 1962, **84**, 687–688.
51 N. W. Y. Ho and P. T. Gilham, *Biochemistry*, 1967, **6**, 3632–3639.
52 Z. A. Shabarova, N. G. Dolinnaya, V. L. Drutsa, N. P. Mehiikova and A. A. Purmal, *Nucleic Acids Res.*, 1981, **9**, 5747–5761.
53 N. G. Dolinnaya, N. I. Sokolova, O. I. Gryaznova and Z. A. Shabarova, *Nucleic Acids Res.*, 1988, **16**, 3721–3738.
54 R. M. Franzini, F. Samain, M. Abd Elrahman, G. Mikutis, A. Nauer, M. Zimmermann, J. Scheuermann, J. Hall and D. Neri, *Bioconjugate Chem.*, 2014, **25**, 1453–1461.
55 C. Ducani, G. Bernardinelli and B. Högberg, *Nucleic Acids Res.*, 2014, **42**, 10596–10604.
56 K. M. Ririe, R. P. Rasmussen and C. T. Wittwer, *Anal. Biochem.*, 1997, **245**, 154–160.
57 R. S. Tuma, M. P. Beaudet, X. Jin, L. J. Jones, C.-Y. Cheung, S. Yue and V. L. Singer, *Anal. Biochem.*, 1999, **268**, 278–288.
58 C. Battaglia, G. Salani, C. Consolandi, L. R. Bernardi and G. B. De, *BioTechniques*, 2000, **29**, 78–81.
59 P. Kielkowski, J. Fanfrlík and M. Hocek, *Angew. Chem., Int. Ed.*, 2014, **53**, 7552–7555.
60 H. Cahová, A. Panattoni, P. Kielkowski, J. Fanfrlík and M. Hocek, *ACS Chem. Biol.*, 2016, **11**, 3165–3171.
61 E. T. Kool, *Annu. Rev. Biophys. Biomol. Struct.*, 1996, **25**, 1–28.
62 E. T. Kool, *Acc. Chem. Res.*, 1998, **31**, 502–510.
63 H. Kuai, Z. Zhao, L. Mo, H. Liu, X. Hu, T. Fu, X. Zhang and W. Tan, *J. Am. Chem. Soc.*, 2017, **139**, 9128–9131.
64 L. Yang, H. B. Kim, J.-Y. Sul, S. B. Yeldell, J. H. Eberwine and I. J. Dmochowski, *ChemBioChem*, 2018, **19**, 1250–1254.
65 Y. Jiang, X. Pan, J. Chang, W. Niu, W. Hou, H. Kuai, Z. Zhao, J. Liu, M. Wang and W. Tan, *J. Am. Chem. Soc.*, 2018, **140**, 6780–6784.
66 C.-H. Lu, A. Cecconello, J. Elbaz, A. Credi and I. Willner, *Nano Lett.*, 2013, **13**, 2303–2308.
67 T. Li, F. Lohmann and M. Famulok, *Nat. Commun.*, 2014, **5**, 4940.
68 C.-H. Lu, A. Cecconello, X.-J. Qi, N. Wu, S.-S. Jester, M. Famulok, M. Matthies, T.-L. Schmidt and I. Willner, *Nano Lett.*, 2015, **15**, 7133–7137.
69 J. Valero, N. Pal, S. Dhakal, N. G. Walter and M. Famulok, *Nat. Nanotechnol.*, 2018, **13**, 496–503.

This journal is © The Royal Society of Chemistry 2018

Published online 12 July 2018

Nucleic Acids Research, 2018, Vol. 46, No. 15 ***7495–7505***
doi: 10.1093/nar/gky630

Preparation and characterization of manganese, cobalt and zinc DNA nanoflowers with tuneable morphology, DNA content and size

Ysobel R. Baker[1], Jinfeng Chen[1], Jason Brown[2], Afaf H. El-Sagheer[1,3], Philip Wiseman[1], Errin Johnson[4], Paul Goddard[5] and Tom Brown[1,*]

[1]Department of Chemistry, University of Oxford, Oxford, Oxfordshire OX1 3TA, UK, [2]Department of Physics, University of Oxford, Oxford, Oxfordshire OX1 3PU, UK, [3]Chemistry Branch, Faculty of Petroleum and Mining Engineering, Suez University, Suez 43721, Egypt, [4]Sir William Dunn School of Pathology, University of Oxford, Oxford, Oxfordshire OX1 3RE, UK and [5]Department of Physics, University of Warwick, Coventry, Warwickshire CV4 7AL, UK

Received June 06, 2018; Editorial Decision June 20, 2018; Accepted June 29, 2018

ABSTRACT

Recently reported DNA nanoflowers are an interesting class of organic-inorganic hybrid materials which are prepared using DNA polymerases. DNA nanoflowers combine the high surface area and scaffolding of inorganic $Mg_2P_2O_7$ nanocrystals with the targeting properties of DNA, whilst adding enzymatic stability and enhanced cellular uptake. We have investigated conditions for chemically modifying the inorganic core of these nanoflowers through substitution of Mg^{2+} with Mn^{2+}, Co^{2+} or Zn^{2+} and have characterized the resulting particles. These have a range of novel nanoarchitectures, retain the enzymatic stability of their magnesium counterparts and the Co^{2+} and Mn^{2+} DNA nanoflowers have added magnetic properties. We investigate conditions to control different morphologies, DNA content, hybridization properties, and size. Additionally, we show that DNA nanoflower production is not limited to Φ29 DNA polymerase and that the choice of polymerase can influence the DNA length within the constructs. We anticipate that the added control of structure, size and chemistry will enhance future applications.

INTRODUCTION

State-of-the art materials with increasingly sophisticated properties are at the forefront of scientific research and modern technology. Hybrid materials aim to merge the best properties of the biological, organic and inorganic components, whilst instilling new functionality not otherwise possible (1). By coupling biological and inorganic materials it is possible to overcome their associated limitations such as instability and lack of biocompatibility (2). For example, hybrid materials that combine magnetic materials with biological components have found a wide range of biomedical applications (3,4). They can be directed to a particular location using an external magnetic field to deliver therapeutics (5,6), used to generate heat locally (7) or combined with biological molecules such as antibodies, enabling magnetic capture and isolation of materials (8). Alternatively, magnetic materials can be combined with enzymes to produce enzyme nanogels which are stable, catalytically active, and can be readily recovered and reused (9).

DNA nanoflowers (DNFs) are an interesting example of inorganic hybrid materials that combine DNA and $Mg_2P_2O_7$ in hierarchically structured materials with flower shaped morphology. DNFs are prepared enzymatically by rolling circle amplification (RCA) in which a DNA polymerase repeatedly traverses a circular DNA template synthesizing a long strand of DNA which then self-assembles (10,11). Incorporation of nucleotides during RCA releases pyrophosphate, which co-crystallizes with both the growing DNA and Mg^{2+} ions present in the amplification buffer (Figure 1) (12). A similar phenomenon also occurs during rolling circle transcription which is analogous to RCA, giving similar materials termed RNA microsponges (MSs) (13). In principle, DNFs and RNA MSs combine the structure and stability of $Mg_2P_2O_7$ with the biological and programmable advantages of DNA or RNA. These have already shown potential in a number of applications, including the targeted delivery of chemotherapeutics by encoding aptamers into the DNA product (10,11), the delivery of miRNA for gene inhibition (13,14), cellular delivery of proteins (15), the delivery of DNAzymes (16), as immunostimulators (17), and in the immobilization and catalytic enhancement of enzymes (18).

*To whom correspondence should be addressed. Tel: +44 1865 275413; Email: tom.brown@chem.ox.ac.uk

© The Author(s) 2018. Published by Oxford University Press on behalf of Nucleic Acids Research.
This is an Open Access article distributed under the terms of the Creative Commons Attribution License (http://creativecommons.org/licenses/by/4.0/), which permits unrestricted reuse, distribution, and reproduction in any medium, provided the original work is properly cited.

Downloaded from https://academic.oup.com/nar/article-abstract/46/15/7495/5052372 by Oxford University user on 23 August 2019

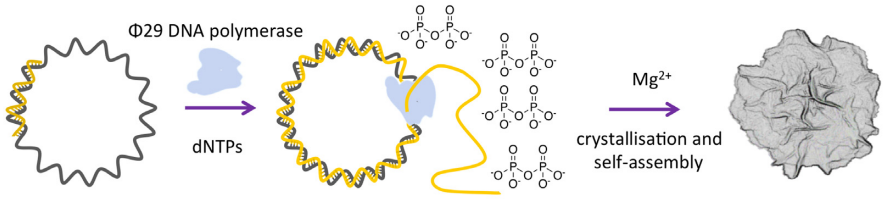


Figure 1. The self-assembly of DNFs using DNA polymerase enzymes. The grey circle represents a cyclic DNA template and the splint that is elongated is shown in yellow.

Research aimed at tailoring the functions of these hybrids has focused on the organic components and includes: encoding functionality through the template (19), incorporating dye modified triphosphates (11,20), adding biologically relevant proteins (15,18), hybridization with dye-functionalized nucleic acids (14), condensing the structures with polycations (20) and intercalating drugs such as doxorubicin (10). We envisaged that by altering the inorganic component it would be possible to harness additional functionalities. Metal phosphates and pyrophosphates have been used in catalysis (21–24), electrochemical detection (25), as electrodes (26), and in supercapacitors (27). They also have multiple potential biomedical applications in therapeutics (28), as artificial bone and tooth scaffolds (29), as MRI contrast agents (30), and as photoluminescent probes (31). Altering the metal ion component of the pyrophosphate salts could therefore potentially expand the versatility and applicability of DNFs. Indeed, a similar strategy was very recently reported for preparing manganese and cobalt DNFs (32). Herein, we expand on the published study by identifying and evaluating variables to manipulate size, alter the morphology, and tailor the DNA content of the particles. We show for the first time that it is possible to prepare zinc DNFs and that DNF preparation is not limited to Φ29 DNA polymerase. We have also investigated the surface potential and hybridization properties of Mn, Co, Zn, and Mg particles, and demonstrate their stability towards enzymatic degradation. In addition, we describe, for the first time, the magnetic properties and structure of one such bio-inorganic hybrid, and show that it is possible to manipulate such materials with an external magnetic field.

MATERIALS AND METHODS

General methods, protocols for the synthesis of oligonucleotides and cyclization of templates, details for the preparation of each type of DNF described in the manuscript, and protocols for analytical techniques are given in the Supplementary Information. Sequences of oligonucleotides used in this study are given in Table 1.

Investigating conditions for DNF formation

Before starting the experiment, 200 mM buffer stock solutions were prepared for the following: Tris pH 7.0, Tris pH 7.5, Tris pH 8.0, Tris pH 8.5, Tris pH 9.0, PIPES pH 7.5, HEPES pH 7.0, HEPES pH 7.5. 66.6 mM, 50 mM, 40 mM, 33.3 mM and 16.7 mM stock solutions of $MnCl_2$, $CoCl_2$ and $ZnCl_2$ in MilliQ water.

Bst 2.0 DNA polymerase. The buffer stock solution (2 μl) and the divalent cation stock solution (6 μl) were added to a 200 μl PCR tube. An enzyme stock solution composed of T4 ligase cyclized T1 (0.5 μM), S1 (1 μM), dNTPs (3.33 mM), ammonium sulphate (16.7 mM), KCl (83.3 mM), 0.17% Tween 20 and Bst 2.0 (0.27 U/μl) in water was then prepared, adding the enzyme last. The solution was quickly vortexed and 12 μl was rapidly added to each PCR tube. The tubes were mixed by vortexing and incubated at 61.5°C for 14 h followed by 85°C for 20 min before rapidly cooling to 4°C. The tubes were centrifuged and the supernatant analysed by 0.8% agarose gel electrophoresis. Any precipitates that formed were washed 3 times with H_2O, suspended in 20 μl of H_2O and 7.5 μl of the samples were analysed by 0.8% agarose gel electrophoresis. The samples were then imaged by SEM if DNA was detected.

Φ29 DNA polymerase. The buffer stock solution (5 μl) and the divalent cation stock solution (6 μl) were added to a 200 μl PCR tube. An enzyme stock solution composed of T4 ligase cyclized T1 (0.67 μM), S1 (1.33 μM), dNTPs (4.44 mM), ammonium sulphate (22.2 mM), DTT (8.89 mM), and Φ29 (0.57 U/μl) in water was then prepared, adding the enzyme last. It was necessary to omit the DTT for the $CoCl_2$ and $ZnCl_2$ experiments. The solution was quickly vortexed and 9 μl was rapidly added to each PCR tube. The tubes were mixed by vortexing and incubated at 30°C for 20 h followed by 65°C for 10 min before rapidly cooling to 4°C. The tubes were centrifuged and the supernatant analysed by agarose gel electrophoresis. Any precipitates that formed were washed 3 times with H_2O, and suspended in 20 μl of H_2O. 7.5 μl of the samples were analysed by 0.8% agarose gel electrophoresis. The samples were then imaged by SEM if DNA was detected.

RESULTS AND DISCUSSION

Manganese DNA nanoflowers

Divalent manganese has similar chemical and biochemical behaviour to magnesium, and many DNA polymerases, including Bst 2.0 DNA polymerase (Bst) at 65°C or Φ29 DNA polymerase (Φ29), remain functional when Mg^{2+} cations in their active sites are replaced with Mn^{2+} (33,34). Unlike Mg^{2+}, Mn^{2+} has five unpaired d electrons giving rise to magnetic properties. Consequently, we anticipated preparing manganese DNFs (MnDNFs) that could be manipulated by a magnetic field whilst still maintaining the desirable features of their magnesium counterparts (MgDNFs), such as large surface area, nanoscale dimensions, and enzymatic stability.

Downloaded from https://academic.oup.com/nar/article-abstract/46/15/7495/5052372 by Oxford University user on 23 August 2019

Table 1. Sequences of oligonucleotides used in this study. HPLC traces and mass spectra for oligonucleotides used in RCA are shown in the Supplementary Information. P represents a 5′ phosphate

Name	Sequence
Template 1 (T1)	5′-PTATAGCCCATGTGCTGCTGCTGCAGCGATACGCGTATCGCTATGGCATATCGTACGA TATGCCGCAGCAGCATTACCGTCGTT-3′
Template 2 (T2)	5′-PATAGTGAGTCGTATTAGCTCGAGCTCGAGCAGCCGCGCCCTACCCTATCCCTCCCCT CGCGGCTGCTCGAGCTCGAGCATCCCT-3′
Splint 1 (S1)	5′-GCACATGGGCTATAAACGACGGTAA-3′
Splint 2 (S2)	5′-TAATACGACTCACTATAGGGAT-3′
Match probe	5′-TTACCGTCGTTTATAGC-Cy3-3′
Mismatch probe	5′-GTTGTCACTTAGTCCTA-Cy3-3′

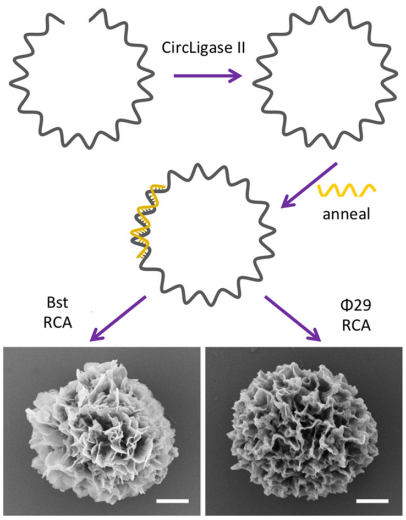


Figure 2. Initial method for the synthesis of MnDNFs. Scale bar represents 1 μm.

To test this, we replaced all Mg^{2+} sources present during MgDNF preparation with Mn^{2+} via $MnCl_2$ and investigated using both Bst and Φ29. Despite being reported to catalyse RCA with reasonable DNA yield (35), Bst has not previously been used in the preparation of any DNFs, and we first determined whether Bst could be used to produce MgDNFs. We found that it could, providing the buffer has a final Mg^{2+} concentration of 15 mM or greater (SEM images are given in the SI, Figure S1).The published approach for preparing MgDNFs uses a cyclic DNA template made by T4 ligase-mediated circularization of a linear DNA strand in the RCA step without its isolation from the ligation mixture. As such, all components present in the buffer including Mg^{2+} are carried forward (10,19). T4 ligase, which requires Mg^{2+}, was substituted with CircLigase II which uses Mn^{2+} as its cofactor. After addition of a primer to the CircLigase II ligation mixture, the sample was used in RCA reactions catalysed by Bst at 65°C or Φ29 at 30°C (Figure 2). In the amplification step we adopted the recommended buffer compositions, but replaced the Mg^{2+} sources with $MnCl_2$. The final amplification buffer for the Bst catalyzed RCA contained 3.25 mM $MnCl_2$ and had a mixture of Tris buffer (pH 8.8) and Tris-acetate buffer (pH 7.5) as a carryover from the ligation step. Similarly, the Φ29 buffer contained 11.25 mM $MnCl_2$ and was a mixture of the CircLigase II Tris-acetate buffer (pH 7.5) from the ligation step and Tris buffer (pH 7.5).

Fortunately both polymerases produced a precipitate, and scanning electron microscopy (SEM) analysis revealed that these materials had hierarchical morphology (Figure 2). There was a clear difference between the two samples; Bst produced discrete particles with a size range of 3.6 ± 1.2 μm (number of particles counted (n) = 90; Supplementary Figure S2) whereas the Φ29 RCA product appeared softer with thick sheets and a broad size range (Supplementary Figure S3). In addition, agarose gel analysis indicated that the precipitate prepared using Φ29 incorporated DNA whereas those prepared using Bst did not (Supplementary Figure S4). Therefore, we suspected that the different morphologies are linked to the presence or absence of DNA.

Variables for controlling morphology and DNA levels within the DNFs. Three main differences were identified between the Bst and Φ29 RCA reactions: Mn^{2+} concentration, pH and temperature. We hypothesized that one or a combination of these factors controlled DNA levels within MnDNFs, and screened different RCA conditions, aiming to identify variables that control both DNA levels and particle size distribution. Due to the cost associated with CircLigase II, T4 ligase was used to cyclize the DNA template for subsequent experiments. In addition, purified cyclic templates were used in these experiments, removing any potential batch-to-batch variability associated with the efficiency of enzymatic ligation, and the cyclic product was desalted thoroughly before use, removing any Mg^{2+} remaining from the ligation buffer. Both Bst and Φ29 were investigated in the pH range of 7.0–9.0 with Mn^{2+} concentrations between 5 and 15 mM (Full details are given in the SI). After RCA, the reaction tubes were centrifuged and the supernatants were analysed to evaluate RCA efficiency (Supplementary Figures S6 and S8). Precipitates were washed with water, agarose gel electrophoresis was used to identify the presence of DNA (Supplementary Figures S5 and S7) and selected products were imaged by SEM. For direct comparison between MnDNFs and MgDNFs, the experiments were repeated using $MgSO_4$ (Supplementary Figures S9–S12).

Gel-electrophoresis analysis of the supernatants revealed that long extended DNA strands were produced by both polymerases during Mn^{2+} RCA, with Bst becoming more processive with increasing pH whereas the efficiency of Φ29 was reduced at the higher pH. Interestingly, although the main DNA component present in the particles was too long to migrate out of the well of the gel, the Φ29 precipitates also contained a second band between the 10 kb marker and

Downloaded from https://academic.oup.com/nar/article-abstract/46/15/7495/5052372 by Oxford University user on 23 August 2019

Table 2. Average size of particles formed as a function of Mn^{2+} concentration. The Bst RCA reaction was incubated for 14 h at pH 7.0 whereas the Φ29 pH incubation time was 20 h and the pH was 8.0. Sizes refer to the longest dimension and *n* refers to the number of particles measured. Analysis was performed using ImageJ. See Supplementary Figures S18–S23 for SEM images used in the analysis

Enzyme	Concentration (mM)	Size range (μm)	*n*
Bst	5	15.8 ± 2.7	60
	10	1.4 ± 0.5	26
	15	2.6 ± 0.3	93
Φ29	5	8.8 ± 1.2	20
	10	1.3 ± 0.2	72
	15	0.312 ± 0.006	111

the well of the gel. This band was also present in the supernatant. This agrees with previous reports and is likely to be a double stranded amplification product (36). This band was not observed during Bst catalysed RCA.

SEM imaging revealed that Mn^{2+} concentration has a striking effect on particle morphology (Figure 3A). At 5 mM, Bst-mediated RCA produced large shell-like particles with a layered structure and average length of 16 μm. At 10 mM, smaller particles of ∼1.5 μm in size begin to form in a mesh, and sonication yielded individual small NF particles. At 15 mM, MnDNFs with morphology similar to the reported MgDNFs were formed (10,11,15). These had similar size (∼2.5 μm) and morphology to the precipitate formed in the earlier experiments using Bst with the CircLigase II cyclized template, albeit with a narrower distribution (Table 2). Increasing the Mn^{2+} concentration further resulted in a large mesh formed of sheets (Supplementary Figure S13). A similar trend in morphology was observed for the material produced by Φ29. At 5 mM large particles formed with a layered structure but more square than those produced by Bst, the average longest length of these particles was 9 μm. At 10 mM Mn^{2+}, Φ29 produced particles with an average diameter ∼1.3 μm which resemble the particles produced by Bst at 15 mM Mn^{2+} and the previously reported MgDNFs (10,11,15). Increasing the concentration of Mn^{2+} further resulted in much smaller particles ∼300 nm in diameter. This pattern in morphology was not observed when using Mg^{2+}; at concentrations below 10 mM, no DNA was detected in any precipitates that formed and at the higher Mg^{2+} concentration (15 mM) nanoflower structures still formed. This was the case for both polymerases. We also observed that Tris buffer gave particles with narrower size distribution than HEPES buffer (Supplementary Figures S14–S16) and that the concentration of ammonium sulphate did not alter the morphology (Supplementary Figure S17).

To further investigate the effect of pH and Mn^{2+} concentration of the DNA levels within the particles we used SYBR gold (a fluorescent dye that exhibits high fluorescence enhancement on binding to both single and double stranded DNA) to compare the relative quantities of DNA present in both the supernatants and the precipitates from a fixed RCA volume (Figure 3B). Samples were incubated in Tris-borate-EDTA (TBE) buffer overnight to sequester any Mn^{2+} cations and breakdown any precipitates prior to incubation with the dye and measurement. Using the earlier electrophoresis experiments as a guide, we used a 15 mM concentration of $MnCl_2$ to evaluate the effect of pH. We identified that the pH at which the RCA reaction was conducted strongly affects the DNA levels within the particles and, whilst precipitation was observed for all pH's when 15 mM Mn^{2+} was used in the reaction, pH 7.0 resulted in the highest levels of precipitated DNA for both polymerases. Next, we compared the effect of Mn^{2+} concentration; pH 8.0 was chosen for the Φ29 experiments and pH 7.0 for the Bst experiments. These conditions were chosen based on the earlier gel-electrophoresis results. Here, we observed that both polymerases produced the greatest amount of DNA at the lower Mn^{2+} concentrations (2–5 mM), and that this was greatly reduced with increasing levels of Mn^{2+}. This is presumably due to the DNA product being trapped within the precipitates, preventing further extension. The same pattern was seen with SYBR green I and SYBR green II (Supplementary Figures S24 and S25), these dyes were used in addition to the universal nucleic acid stain SYBR gold (37) as they display different sensitivities towards nucleic acids; SYBR green I is known to bind double stranded DNA selectively (38,39), and SYBR green II is more sensitive towards single stranded DNA and RNA (40). Interestingly, when compared with Mg^{2+} (Supplementary Figure S26) higher DNA levels were found for Bst with Mn^{2+}, but Mg^{2+} gave higher DNA levels with Φ29.

As mentioned above, this study demonstrates that Φ29 can be replaced with Bst in the preparation of MgDNFs providing that the buffer is supplemented with additional Mg^{2+} and, whilst the morphology remains similar, that the DNA component of the Bst MgDNFs is of shorter length. As with the MnDNFs a second band between the 10 kb marker and the well of the gel was observed for the DNFs produced using Φ29 but not when using Bst, suggesting that Bst does not produce a significant amount of double stranded DNA during RCA (36).

Cobalt DNA nanoflowers

Next we confirmed that Co^{2+}-catalysed RCA also produced DNFs, proving that divalent cations other than Mg^{2+} and Mn^{2+} can be used. Co^{2+} was chosen as it also has unpaired d electrons, so the nanoconstructs should possess magnetic properties, and most DNA polymerases can utilize Co^{2+} as a cofactor (33). Dithiothreitol (DTT) present in the buffer was found to be incompatible with $CoCl_2$, resulting in a dark precipitate forming instantly on addition of the DTT. In contrast with previous literature, (32) we found it necessary to remove DTT when preparing CoDNFs. We screened different RCA conditions using the approach described above and identified those where nanomaterials were produced (Supplementary Figures S27-S30). Precipitates that were identified as containing DNA by gel electrophoresis were imaged by SEM (Figure 4A and Table 3). We also evaluated DNA levels using the SYBR dyes (Figure 4B, Supplementary Figures S37-S38). DNA was most efficiently incorporated into the nanostructures at pH 7–7.5 for Φ29 and pH 7–8 for Bst. As with Mn^{2+}catalysed RCA, more free DNA is produced at lower metal cation concentrations and more DNA is captured in the precipitates at the

Downloaded from https://academic.oup.com/nar/article-abstract/46/15/7495/5052372 by Oxford University user on 23 August 2019

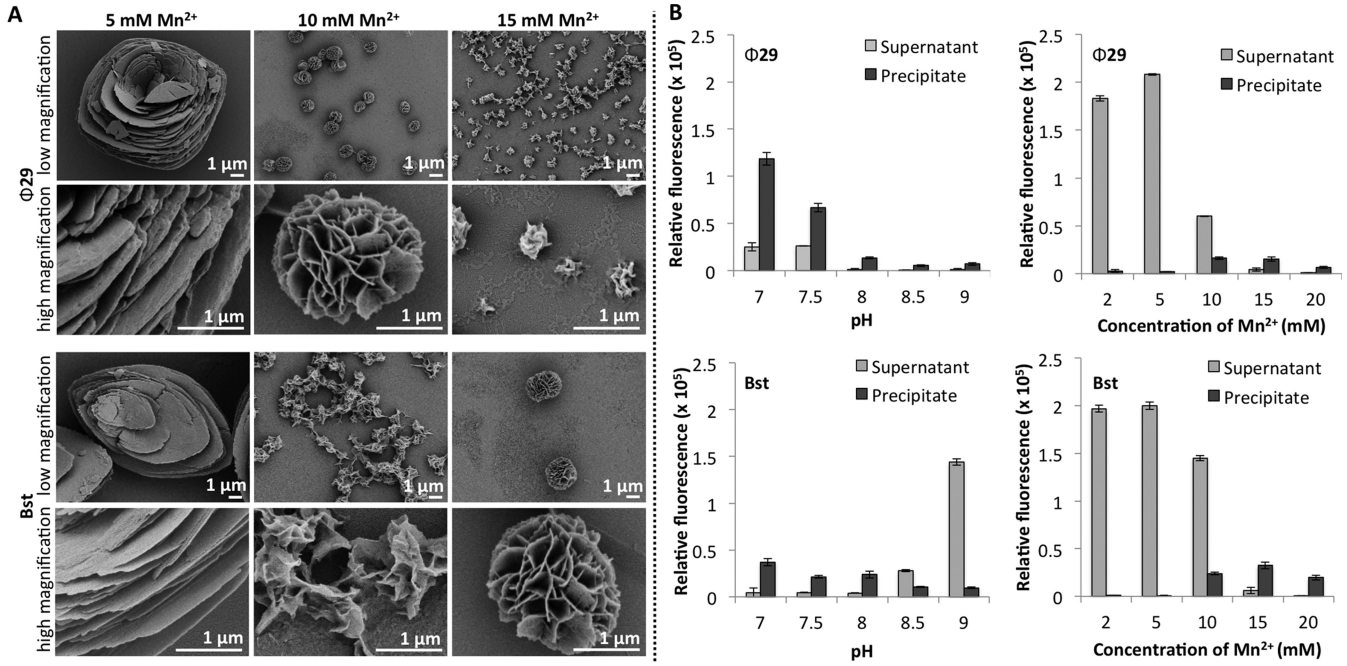


Figure 3. (**A**) SEM images illustrating the effect of $MnCl_2$ concentration and choice of polymerase on the morphology and size of particles formed during RCA. The Bst RCA incubation time was 14 h at pH 7.5 and the Φ29 incubation time was 20 h at pH 8.0. (**B**) Fluorescence-based analysis comparing the levels of free DNA and DNA incorporated into the nanoconstructs as a function of enzyme, pH, and cation concentration. Samples were broken down using TBE to release DNA prior to incubation with SYBR gold. A plate reader was then used to compare the DNA levels. The effect of pH on Φ29 RCA was compared at 15 mM $MnCl_2$ and the effect of concentration was evaluated at pH 8.0. The effect of pH on Bst was determined at 15 mM $MnCl_2$ and the effect of concentration was evaluated at pH 7.0.

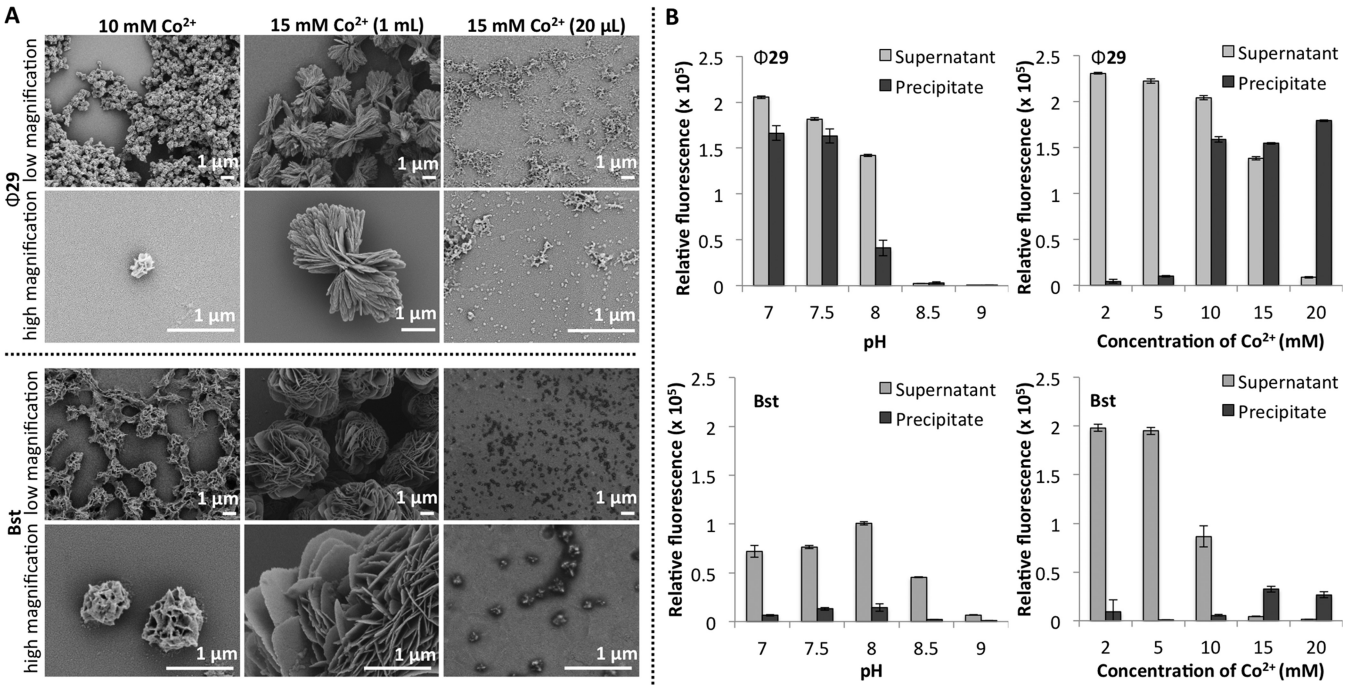


Figure 4. A) SEM images illustrating the effect of $CoCl_2$ concentration and reaction scale on the morphology and size of particles formed during RCA at pH 7.0. The Bst RCA incubation time was 14 h whereas the Φ29 incubation time was 20 h. B) Fluorescence-based analysis comparing the levels of free DNA and DNA incorporated into the nanoconstructs as a function of enzyme, pH, and cation concentration. Samples were broken down using TBE to release DNA prior to incubation with SYBR gold. A plate reader was then used to compare the DNA levels. The effect of pH on Φ29 and Bst RCA was determined at 10 mM $CoCl_2$ and the effect of concentration was evaluated at pH 7.0.

Downloaded from https://academic.oup.com/nar/article-abstract/46/15/7495/5052372 by Oxford University user on 23 August 2019

higher concentrations (Figure 4B). Interestingly, if the total DNA in the precipitate is combined with the total free DNA our study shows that Φ29 with Co^{2+} produces more DNA than with Mn^{2+} or Mg^{2+}. It also indicates that Φ29 has a greater tolerance to higher concentrations of Co^{2+} than Bst, and this will be the subject of further investigation. Of note, unlike the Mn^{2+} RCA reactions, the RCA reaction volume greatly altered the morphology of the materials that formed (Figure 4A). The reason for this is not known, and could be linked to the high levels of DNA and precipitate settling.

Zinc DNA nanoflowers

We also evaluated Zn^{2+} as the cofactor in the preparation of DNFs as Bst has been reported to tolerate Zn^{2+} (A.K. Vashishtha, J. Wang, and W.H. Konigsberg, unpublished results) (33). Surprisingly, both polymerases produced DNA at the lower Zn^{2+} concentrations, with Bst showing greater DNA yields (Figure 5B). As with Mn^{2+}, Mg^{2+} and Co^{2+} greater DNA levels in the precipitates were observed at higher cation concentrations. SEM analysis revealed that whilst DNA was observed in the precipitates produced at all pHs tested, only the RCA reactions at pH 7.0 produced discrete particles (Figure 5A). Unlike MnDNFs, MgDNFs and CoDNFs these ZnDNFs are much smaller with spherical morphology and it is possible these are amorphous particles formed of $Zn_2P_2O_7$ and DNA explaining their smaller size and shape.

Finally, to determine if the trends in morphology are dependent on the DNA sequence, a second template and splint pair was prepared with a different nucleobase sequence and base composition (Table 1). These were then used in RCA reactions with several of the conditions described earlier in the text. The particles that formed showed a similar trend in morphology and size to those observed with the first template, representative images are shown in the SI (Supplementary Figures S39–S43). In brief, the MnDNFs that formed at 5 mM Mn^{2+} were large and layered, and increasing the concentration of Mn^{2+} resulted in the formation of the spherical flower morphology. The CoDNFs also formed petal like structures at 10 mM Co^{2+} and these were smaller at 15 mM. These results suggest that the morphology depends on the cation concentration to a greater extent than the nucleobase sequence.

Characterization and properties of the nanoflowers

Elemental composition. Energy-dispersive X-ray spectroscopy (EDX) was used to analyse the elemental composition of the MnDNFs, CoDNFs, and ZnDNFs (Figure 6 and Supplementary Figure S44). This confirmed that the MnDNFs were composed of Mn, P, O, N and C. The CoDNFs were formed of Co, P, O, N and C and the ZnDNFs were composed of Zn, P, O, N and C. We also carried out elemental analysis at different Mn^{2+} concentrations and the data are given in the SI (Supplementary Figures S45–S48). In agreement with the SYBR gold assay, increasing the concentration of Mn^{2+} during RCA resulted in precipitates with higher nitrogen content, presumably from the DNA (Supplementary Figure S48). Sulfur was not identified in the MnDNFs formed using HEPES buffer (Supplementary Figures S45–S47), providing evidence that buffer is not incorporated into the nanostructures.

Fourier-transform infrared spectroscopy (FTIR). We used FTIR to support our theory that $M_2P_2O_7$ (where M is a divalent metal cation) form the core of the particles, rather than alternative phosphate derivatives such as $M_3(PO_4)_2$. The MnDNFs, CoDNFs and ZnDNFs all showed an asymmetric POP bridge stretch (ν^{as} POP) at around 900 cm^{-1} and a symmetric POP bridge (ν^{s} POP) stretch at 730 cm^{-1}. The asymmetric vibration modes of the PO_3 (ν^{as} PO_3) gave a strong peak in the region of 1090–1070 cm^{-1} and the DNFs also show several overlapping broad bands in the region that corresponds to the stretching vibration of water (2800–3800 cm^{-1}) with multiple bending vibrations of H_2O (δ H_2O) around 1640 cm^{-1}. This suggests that the water molecules associated with the samples are in different environments. Additionally, the infrared (IR) spectrum of the MnDNFs (Supplementary Figure S50) was similar to that of previously published $Mn_2P_2O_7.2H_2O$ (41). We then compared the IR spectra with Mn^{2+} and Co^{2+} phosphate and pyrophosphate salts, which were prepared by mixing corresponding metal dichloride with buffered pyrophosphate or phosphate based on a literature procedure for the synthesis of hydrated manganese(II) phosphate ($Mn_3(PO_4)_2{\cdot}3H_2O$) (22). In all cases, the IR spectra matched with the pyrophosphate salts suggesting that the DNFs are composed of a derivative of M^{2+} with $P_2O_7{}^{4-}$, most likely $M_2P_2O_7$ rather than phosphate salts (Supplementary Figures S50–S58).

Surface potential. The surface potentials of the particles prepared under different conditions were compared using a Malvern Zetasizer Ultra instrument (Supplementary Tables S2 and S3). Particles were suspended in 10 mM aqueous NaCl. Due to the limitation of the technique, high quality data could not be obtained for some of the larger particles which have a tendency to settle. As expected, there was a significant degree of correlation between DNA incorporated into the MnDNFs and the magnitude of zeta potential which ranged from: –41.6 mV to –2.5 mV (most to least DNA) (Figure 3, Supplementary Tables S2 and S3). This suggests that the presence of DNA increases the surface charge and stability of the materials. The correlation for the CoDNFs and ZnDNFs, however, was less pronounced. As the surface potential of the particles can be controlled using the methods described in this paper these results will be of importance to other researches developing similar nanostructures for therapeutic applications such as MRI contrast agents or as targeted delivery agents.

Serum stability of DNFs. We next confirmed that the DNA within DNFs retained the high serum stability previously observed for MgDNFs (15). ZnDNFs, CoDNFs and MnDNFs were incubated in cell culture medium supplemented with 10% fetal bovine serum (FBS) and the DNA content was analysed at various time points. FBS was chosen to simulate the extracellular conditions to which a therapeutic oligonucleotide would be exposed and contains predominantly endonucleases. The stability of the DNA in the particles was determined using agarose gel electrophoresis and compared with the stability of free λ-DNA incubated

Downloaded from https://academic.oup.com/nar/article-abstract/46/15/7495/5052372 by Oxford University user on 23 August 2019

Table 3. Average size and standard deviation of particles formed during Co^{2+} RCA at pH 7.0. The Bst RCA incubation time was 14 h whereas the Φ29 incubation time was 20 h. Sizes refer to the longest dimension and *n* refers to the number of particles measured. Analysis was performed using ImageJ. See Supplementary Figures S31-S36 for SEM images used in the analysis

Enzyme	Scale (μl)	Concentration (mM)	Size range (μm)	*n*
Bst	100	10	0.79 ± 0.13	52
	20	15	0.210 ± 0.043	26
	1000	15	6.1 ± 0.7	26
Φ29	100	10	0.446 ± 65	108
	20	15	0.038 ± 0.008	176
	1000	15	3.8 ± 0.4	31

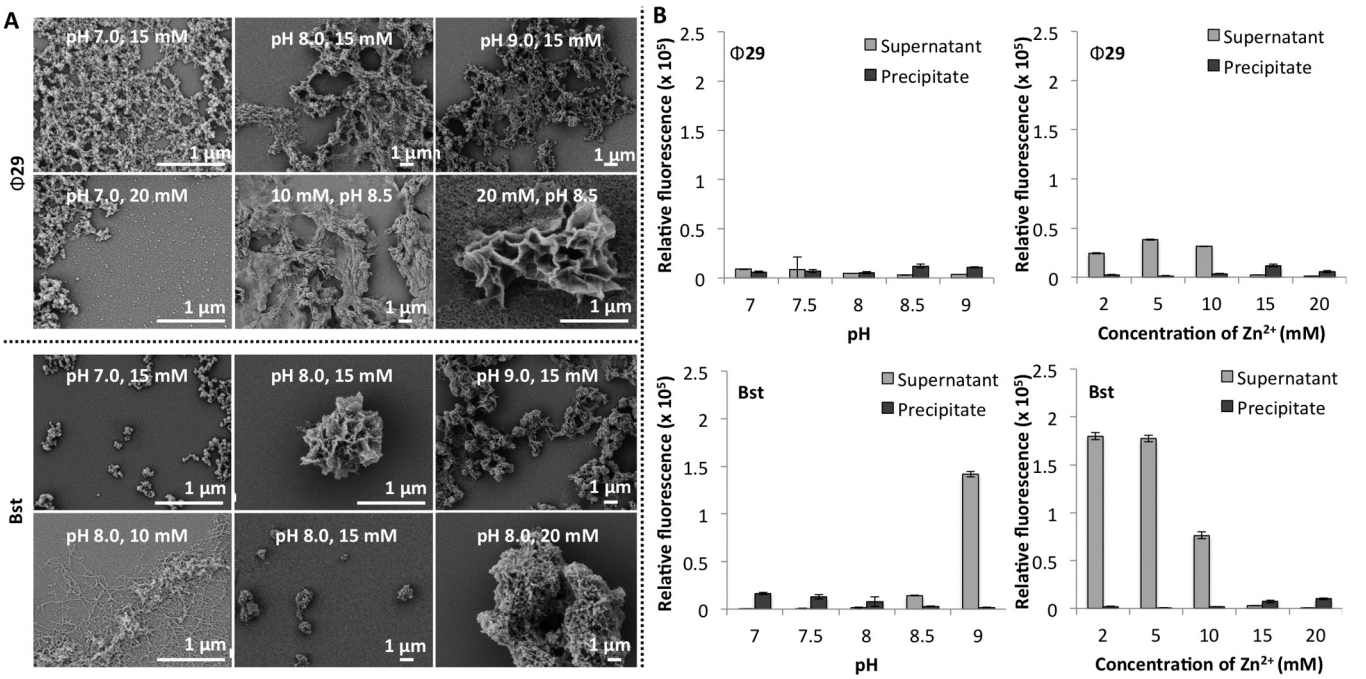


Figure 5. (**A**) SEM images illustrating the effect of $ZnCl_2$ concentration and pH on the morphology and size of particles formed during RCA. The Bst RCA incubation time was 14 h whereas the Φ29 incubation time was 20 h. (**B**) Fluorescence-based analysis comparing the levels of free DNA and DNA incorporated into the nanoconstructs as a function of enzyme, pH, and cation concentration. Samples were broken down using TBE to release DNA prior to incubation with SYBR gold. A plate reader was then used to compare the DNA levels. The effect of pH on Φ29 RCA was determined at 15 mM $ZnCl_2$ and the effect of concentration was evaluated at pH 8.5. The effect of pH on Bst was determined at 15 mM $ZnCl_2$ and the effect of concentration was evaluated at pH 8.0.

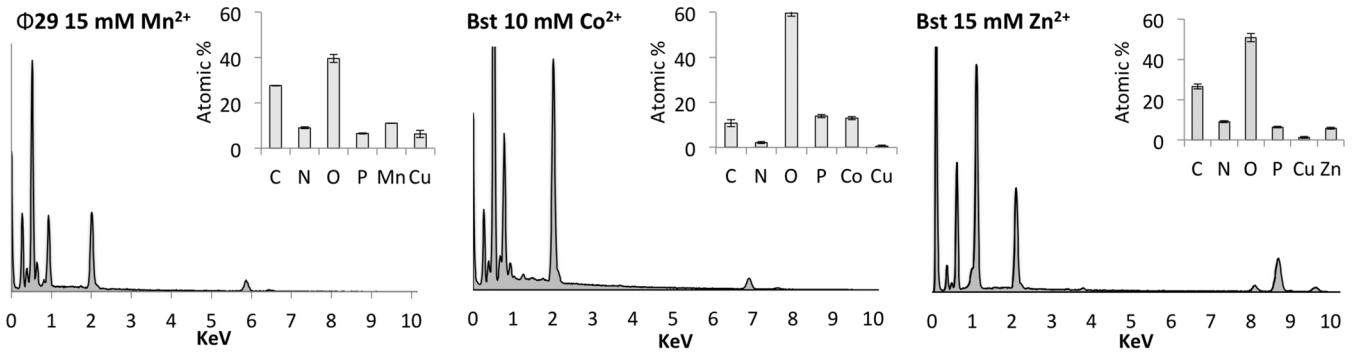


Figure 6. Exemplar SEM-based EDX characterization of the elemental compositions of the DNFs. EDX data is shown for MnDNFs prepared using Φ29 in Tris buffer pH 8.0, CoDNFs prepared in Tris buffer pH 7.0 and ZnDNFs prepared in Tris buffer pH 7.0. The CoDNFs prepared using a 1 ml RCA volume. Samples were analysed on a carbon support film with a copper mesh to minimize signals from mounting, which is why high carbon levels and copper are detected. See SI Figure S39 for other samples.

Downloaded from https://academic.oup.com/nar/article-abstract/46/15/7495/5052372 by Oxford University user on 23 August 2019

under the same conditions. In all cases, the original morphology of the particles remained intact, even after 48 h (Supplementary Figures S60–S67). Whilst the DNA component of all DNFs proved more stable than the λ-DNA control (Supplementary Figure S59), our data indicates that the smaller particles are more stable to digestion than the larger micron-sized particles. The results also suggest that the CoDNFs are more stable than the MnDNFs. We noticed that after treatment with 10% FBS the particles were less aggregated, one possible explanation for this is that the individual particles may be joined to each other by long DNA strands, and that the naked DNA between the particles is digested.

Magnetic properties of MnDNFs and CoDNFs. We have also investigated the magnetic properties of the MnDNFs and CoDNFs. Previous studies have used isothermal methods to prepare nucleic acid materials that can be manipulated using a magnet but these used folate-labelled primer strands to allow immobilization on streptavidin coated magnetic beads (42,43). Interestingly, the study using RCT shows a TEM image with MgDNF-like structures (43). It is possible that these materials are RNA NFs or MSs formed from magnesium pyrophosphate and RNA with the magnetic particles embedded in the structure, rather than RNA coated magnetic nanoparticles. Unlike the reported studies, the magnetic materials here are prepared during RCA, the constructs are considerably larger, and the approach does not require the use of streptavidin nanoparticles or modified nucleic acids during the preparation. After confirming that the MnDNFs and CoDNFs could be manipulated using a magnet and could be captured on a commercial magnetic rack (Supplementary Figure S68), the low-temperature magnetic properties of the materials were then studied in more detail. The magnetometry data collected on the MnDNFs are shown in Figure 7. While it is difficult to draw definitive conclusions from powder susceptibility in anisotropic systems, some information can be inferred from the data. The mass susceptibility of all MnDNF samples (Figure 7A, main panel) initially increases on cooling in a Curie-Weiss manner. The zero-field cooled (ZFC) and field cooled (FC) curves displayed no noticeable differences, and no clear evidence of magnetic ordering is present down to the lowest temperature measured. The product χT of each material (Figure 7B, main panel) shows a steady value at high temperatures indicating that the compounds are in the paramagnetic phase where temperature fluctuations overcome internal interactions. Variations in χT on cooling are indicative of departures from paramagnetic behaviour, and can be caused by interactions between the spins, or the thermal depopulation of crystal-field split magnetic energy levels. The MnDNFs all exhibit a drop in χT as the temperature is cooled below 100–150 K. This is most likely caused by antiferromagnetic interactions between Mn^{2+} ions, as observed in several manganese pyrophosphates, including $Mn_2P_2O_7$ (44–47). The magnetic susceptibility data above $T = 50$ K was fitted to a Curie-Weiss law and the fitted lines are plotted, along with the data displayed as $1/\chi(T)$ in the inset to Figure 7a. The Curie-Weiss temperatures (Θ_{CW}) determined from the fits are in the range –15 to –21 K and are tabulated in Table 4. This is similar to $\Theta_{CW} = -13$ K found for $Mn_2P_2O_7$ (44). However, while $Mn_2P_2O_7$ orders antiferromagnetically at 14 K, none of our MnDNFs exhibit clear signs of long-range magnetic order. Moreover, as temperature is reduced below 7 K the χT for all samples begins to increase. The temperatures of the minima in susceptibility T_{min} are recorded in Table 4. This increase in χT points towards the presence of additional ferromagnetic interactions, or the onset of canted antiferromagnetism (also known as weak ferromagnetism), in which the non-colinear arrangement of antiferromagnetically aligned spins gives rise to a net ferromagnetic moment in a particular direction.

Also shown in Table 4 is an estimate of the number of Mn^{2+} spins per gram of sample deduced from the Curie-Weiss fit, assuming a high-spin $S = 5/2$ configuration and a g-factor of 2. The data show that a higher number of spins in the final product is obtained for the samples prepared using 10 mM $MnCl_2$ in the reaction compared to the 15 mM reactions, and that the Bst polymerase yields more spins per mass than the Φ29. These numbers are in good agreement with the results of the EDX analysis shown in Figure 6 and Supplementary Figure S44.

The magnetization of the MnDNFs measured at 1.8 K (inset to Figure 7B) shows a gradual rise and no saturation up to 0.5 T. There is no hysteresis between up and down sweeps of the magnetic field.

The data for the CoDNFs (Figure 7C) show similarities with that of MnDNFs: it exhibits paramagnetic behaviour at high temperatures with a $\Theta_{CW} = -22.2(5)$ K; a decrease in χT once the temperature is cooled below 150 K, followed by an increase below $T_{min} = 10.5(1)$ K; and a slow non-hysteretic rise in magnetization up to 0.5 K (not shown). However, the CoDNF sample also exhibits a bifurcation of the ZFC and FC susceptibility curves below a temperature of 4 K (Figure 7C, main panel). In addition, χT begins to decrease again below $T_{max} = 2.7(1)$ K (Figure 7C, inset). This could indicate the presence of further antiferromagnetic interactions, a reconfiguration of canted spins, or the splitting of the Co^{2+} spin multiplet. We note that bulk $Co_2P_2O_7$ displays antiferromagnetic order below 10.1 K (48), which is close to the value of T_{min} observed for our CoDNFs. The number of spins per gram shown in Table 4 was estimated assuming $S = 3/2$ and $g = 2$ for each Co^{2+} ion.

In summary, at high temperatures the magnetic data for the MnDNFs and CoDNFs are similar to that for bulk $Mn_2P_2O_7$ (44) and $Co_2P_2O_7$ (48), respectively. However, at lower temperatures additional energy scales are present in the DNFs that give rise to changes in χT not observed in the bulk materials. Possible explanations for this observation include: (i) the spins in the DNFs are interacting strongly with or via their surroundings; (ii) although the individual DNFs investigated fall in the size range of 300 nm to 10 μm, the complex nanoscale structure of the flowers leads to non-bulk behaviour; (iii) disorder inherent in the bulk material that makes up the DNF is affecting the spin response; or (iv) the crystal structure of the transition-metal DNFs is not the same as the equivalent diphosphate materials. This is a subject of ongoing investigations.

Hybridization properties. For the DNFs described here to find use in targeted delivery through aptamer incorpora-

Downloaded from https://academic.oup.com/nar/article-abstract/46/15/7495/5052372 by Oxford University user on 23 August 2019

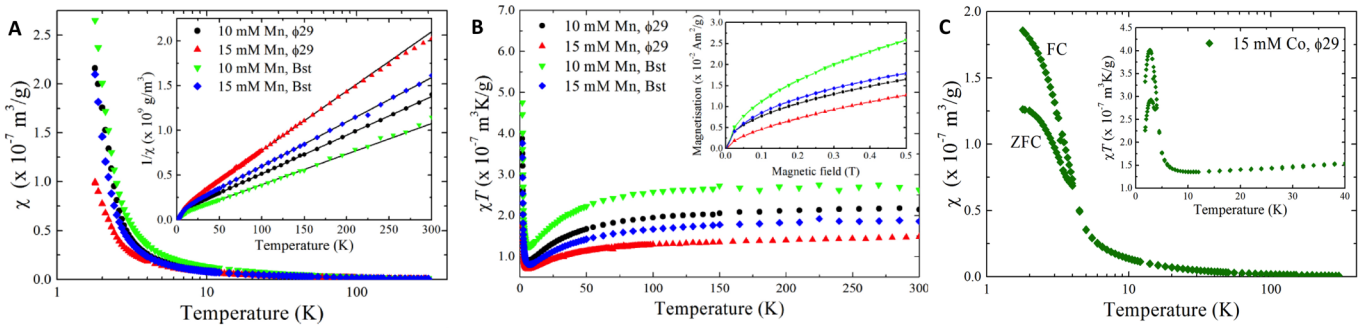


Figure 7. (**A**) Field-cooled powder magnetic susceptibility χ as a function of temperature of four MnDNF samples taken in an applied dc magnetic field of $\mu_0 H = 0.025$ T. The inset shows the inverse susceptibility data (symbols) and the associated fits of $\chi(T)$ to the Curie-Weiss law (lines). (**B**) The same data plotted as χT. The inset shows the magnetization measured at $T = 1.8$ K in the same samples. (**C**) Zero-field-cooled (ZFC) and field-cooled (FC) powder magnetic susceptibility χ as a function of temperature of a CoDNF sample taken in an applied dc magnetic field of $\mu_0 H = 0.025$ T. The inset shows the same data plotted as χT in the low-temperature region. CoDNFs prepared using a 1 ml RCA volume with 15 mM $CoCl_2$ were used.

Table 4. Parameters derived from the magnetic susceptibility data. Θ_{CW} is the Curie–Weiss temperature resulting from fits of $\chi(T)$ to the Curie-Weiss law. N is an estimate of the number of spins per gram assuming a high-spin state ($S = 5/2$ for Mn and 3/2 for Co) and a g-factor of 2. T_{min} (T_{max}) is the temperature of the minimum (maximum) observed in the χT data

Sample	Θ_{cw} (K)	N ($\times 10^{21}$)	T_{min} (K)	T_{max} (K)
Φ29 10 mM Mn^{2+}	−19.3(2)	2.5	6.5(3)	-
Φ29 15 mM Mn^{2+}	−16.4(1)	1.6	6.0(3)	-
Bst 10 mM Mn^{2+}	−15.0(7)	3.2	6.8(1)	-
Bst 15 mM Mn^{2+}	−21.0(3)	2.2	7.1(1)	-
Φ29 15 mM Co^{2+} (1 ml)	−22.2(5)	5.9	10.5(3)	2.7(1)

tion or in bio-separation based applications it is imperative that the DNA component of the DNFs is available to interact with and bind to the intended target. To test this, we evaluated the ability of the different DNFs to selectively hybridize with a complementary oligonucleotide, and compared this to a scrambled base sequence control (Figure 8). The conditions of incubation greatly affected the ability of the DNFs to selectively hybridize and capture the matched sequence over the scrambled control. Incubation of the DNFs with the probes in 200 mM NaCl resulted in the greatest discrimination suggesting that DNFs could find application in magnetic assisted bio-separation or targeted delivery. Our current hypothesis for improved selectivity in saline over water is that NaCl screens the charges of the phosphate backbone in the probe preventing ionic interactions between the inorganic component and the probes, allowing specific base-pairing to dominate relative to non-specific charge-charge interactions. Whilst we expected pH buffering would improve the selectivity, in the majority of cases incubation in PBS resulted in reduced hybridization and it is feasible that PBS reduced hybridization through competitive interactions. Of particular note, the presence of divalent cations resulted in the capture of both the matched and mismatched probes (data not shown). We suspect that the divalent cations lead to non-selective probe capture either by forming salt bridges between the inorganic scaffold and the probes or by interactions through the nitrogen atoms in the DNA bases.

CONCLUSIONS

We have developed methodology to produce nano- and microscale hybrid DNA-inorganic materials that can be prepared in a range of shapes, show enhanced stability against DNA degradation and can be manipulated using an external magnetic field. These particles can be prepared enzymatically using different divalent cations (Mn^{2+}, Co^{2+} and Zn^{2+}) which co-crystallize with DNA and pyrophosphate anions, constituting a novel class of materials. By simply altering the composition of the enzyme buffers we show that it is possible to alter the inorganic core of DNFs, control the morphology and size between 40 nm to 16 μm, manipulate the DNA levels within the particles, and alter their surface potential. By changing the polymerase enzyme it is also possible to control the morphology further and vary the length of DNA within the constructs. We have also investigated the magnetic properties of the materials providing insight into the structures of these materials. Finally, we have shown that under certain conditions these structures are capable of selectively binding to their complementary DNA target, and consequently the DNA is free to interact, rather than being tied up in the structures. The tuneable and selective properties of these materials suggests applications in drug delivery, sensing, biocatalysis, energy (as supercapacitors), and separation technologies.

DATA AVAILABILITY

Compositions of enzyme buffers are available on supplier's websites (http://www.lucigen.com/phi29-DNA-Polymerase/ and https://www.neb.com/products/m0537-bst-20-dna-polymerase#Product%20Information_Properties%20and%20Usage). The magnetometry data presented in this paper will be made available at http://wrap.warwick.ac.uk/103500.

Downloaded from https://academic.oup.com/nar/article-abstract/46/15/7495/5052372 by Oxford University user on 23 August 2019

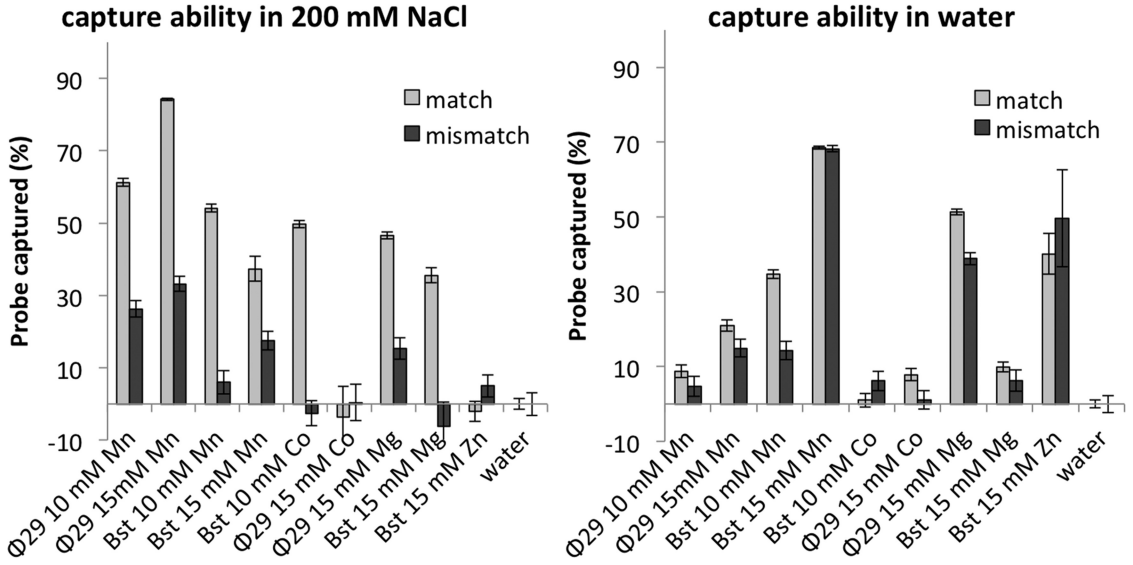


Figure 8. The ability of different DNFs to hybridize with and capture a complementary DNA strand. DNFs prepared from the equivalent of 20 μl RCA volume were incubated with 100 μl of either 50 nM Cy3 labelled complementary DNA probe (match) or 50 nM of a scrambled version (mismatch) at room temperature for 1 h in the presence of 200 mM NaCl (left) or water (right). The particles were collected by centrifugation and the percentage of probe left in solution was determined using a fluorescence plate reader. Greater selectivity was observed in saline than water, and overall particles prepared using Bst appear to show greater specificity than their Φ29 counterparts.

SUPPLEMENTARY DATA

Supplementary Data are available at NAR Online.

ACKNOWLEDGEMENTS

SEM work was performed at the Dunn School EM Facility and EDX analysis was performed at the Nanofabrication and Electron Microscopy Facility, Department of Physics, University of Oxford. The magnetometry data presented in this paper was performed at the University of Warwick. The authors would also like to thank the reviewers for their helpful comments in improving the manuscript and Dr Makwana at Malvern Panalytical for assistance with data analysis.

FUNDING

Leverhulme Trust [RPG-2015-005 to Y.B. and T.B.]; UK BBSRC [BB/J001694/2 to A.E.H. and T.B.]; P.G. thanks the University of Oxford for the provision of a visiting lectureship. Funding for open access charge: UK BBSRC [BB/J001694/2].
Conflict of interest statement. None declared.

REFERENCES

1. Sanchez,C., Belleville,P., Popall,M. and Nicole,L. (2011) Applications of advanced hybrid organic-inorganic nanomaterials: from laboratory to market. *Chem. Soc. Rev.*, **40**, 696–753.
2. Darder,M., Aranda,P. and Ruiz-Hitzky,E. (2007) Bionanocomposites: a new concept of ecological, bioinspired, and functional hybrid materials. *Adv. Mater.*, **19**, 1309–1319.
3. Mohammed,L., Gomaa,H.G., Ragab,D. and Zhu,J. (2017) Magnetic nanoparticles for environmental and biomedical applications: A review. *Particuology*, **30**, 1–14.
4. Yoo,D., Lee,J.-H., Shin,T.-H. and Cheon,J. (2011) Theranostic magnetic nanoparticles. *Acc. Chem. Res.*, **44**, 863–874.
5. Hauser,A.K., Wydra,R.J., Stocke,N.A., Anderson,K.W. and Hilt,J.Z. (2015) Magnetic nanoparticles and nanocomposites for remote controlled therapies. *J. Control. Release*, **219**, 76–94.
6. Felfoul,O., Becker,A.T., Fagogenis,G. and Dupont,P.E. (2016) Simultaneous steering and imaging of magnetic particles using MRI toward delivery of therapeutics. *Sci. Rep.*, **6**, 33567.
7. Périgo,E.A., Hemery,G., Sandre,O., Ortega,D., Garaio,E., Plazaola,F. and Teran,F.J. (2015) Fundamentals and advances in magnetic hyperthermia. *Appl. Phys. Rev*, **2**, 041302.
8. Iranmanesh,M. and Hulliger,J. (2017) Magnetic separation: its application in mining, waste purification, medicine, biochemistry and chemistry. *Chem. Soc. Rev.*, **46**, 5925–5934.
9. Lin,M., Lu,D., Zhu,J., Yang,C., Zhang,Y. and Liu,Z. (2012) Magnetic enzyme nanogel (MENG): a universal synthetic route for biocatalysts. *Chem. Commun.*, **48**, 3315–3317.
10. Zhu,G., Hu,R., Zhao,Z., Chen,Z., Zhang,X. and Tan,W. (2013) Noncanonical self-assembly of multifunctional DNA nanoflowers for biomedical applications. *J. Am. Chem. Soc.*, **135**, 16438–16445.
11. Hu,R., Zhang,X., Zhao,Z., Zhu,G., Chen,T., Fu,T. and Tan,W. (2014) DNA nanoflowers for multiplexed cellular imaging and traceable targeted drug delivery. *Angew. Chem. Int. Ed.*, **53**, 5821–5826.
12. Shopsowitz,K.E., Roh,Y.H., Deng,Z.J., Morton,S.W. and Hammond,P.T. (2014) RNAi-microsponges form through Self-Assembly of the organic and inorganic products of transcription. *Small*, **10**, 1623–1633.
13. Lee,J.B., Hong,J., Bonner,D.K., Poon,Z. and Hammond,P.T. (2012) Self-assembled RNA interference microsponges for efficient siRNA delivery. *Nat. Mater.*, **11**, 316–322.
14. Roh,Y.H., Deng,J.Z., Dreaden,E.C., Park,J.H., Yun,D.S., Shopsowitz,K.E. and Hammond,P.T. (2016) A Multi-RNAi microsponge platform for simultaneous controlled delivery of multiple small interfering RNAs. *Angew. Chem. Int. Ed.*, **55**, 3347–3351.
15. Kim,E., Zwi-Dantsis,L., Reznikov,N., Hansel,C.S., Agarwal,S. and Stevens,M.M. (2017) One-pot synthesis of multiple protein-encapsulated DNA flowers and their application in intracellular protein delivery. *Adv. Mater.*, **29**, 1701086.
16. Jin,Y., Li,Z., Liu,H., Chen,S., Wang,F., Wang,L., Li,N., Ge,K., Yang,X., Liang,X.-J. *et al.* (2017) Biodegradable, multifunctional DNAzyme nanoflowers for enhanced cancer therapy. *NPG Asia Mater*, **9**, e365.

Downloaded from https://academic.oup.com/nar/article-abstract/46/15/7495/5052372 by Oxford University user on 23 August 2019

17. Zhang,L., Zhu,G., Mei,L., Wu,C., Qiu,L., Cui,C., Liu,Y., Teng,I.T. and Tan,W. (2015) Self-assembled DNA immunonanoflowers as multivalent CpG nanoagents. *ACS Appl. Mater. Interfaces*, **7**, 24069–24074.
18. Kim,J., Kim,D. and Lee,J.B. (2017) DNA aptamer-based carrier for loading proteins and enhancing the enzymatic activity. *RSC Adv.*, **7**, 1643–1645.
19. Lv,Y., Hu,R., Zhu,G., Zhang,X., Mei,L., Liu,Q., Qiu,L., Wu,C. and Tan,W. (2015) Preparation and biomedical applications of programmable and multifunctional DNA nanoflowers. *Nat. Protoc.*, **10**, 1508–1524.
20. Roh,Y.H., Lee,J.B., Shopsowitz,K.E., Dreaden,E.C., Morton,S.W., Poon,Z., Hong,J., Yamin,I., Bonner,D.K. and Hammond,P.T. (2014) Layer-by-Layer assembled antisense DNA microsponge particles for efficient delivery of cancer therapeutics. *ACS Nano*, **8**, 9767–9780.
21. Centi,G. (1993) Vanadyl pyrophosphate - a critical overview. *Catal. Today*, **16**, 5–26.
22. Jin,K., Park,J., Lee,J., Yang,K.D., Pradhan,G.K., Sim,U., Jeong,D., Jang,H.L., Park,S., Kim,D. *et al.* (2014) Hydrated manganese(II) phosphate ($Mn_3(PO_4)_2{\cdot}3H_2O$) as a water oxidation catalyst. *J. Am. Chem. Soc.*, **136**, 7435–7443.
23. Takashima,T., Hotori,Y. and Irie,H. (2015) Development of optically transparent water oxidation catalysts using manganese pyrophosphate compounds. *J. Photochem. Photobiol. B*, **152**, 139–145.
24. Kim,H., Park,J., Park,I., Jin,K., Jerng,S.E., Kim,S.H., Nam,K.T. and Kang,K. (2015) Coordination tuning of cobalt phosphates towards efficient water oxidation catalyst. *Nat. Commun.*, **6**, 8253.
25. Zhang,Z., Zhang,Y., Song,R., Wang,M., Yan,F., He,L., Feng,X., Fang,S., Zhao,J. and Zhang,H. (2015) Manganese(II) phosphate nanoflowers as electrochemical biosensors for the high-sensitivity detection of ractopamine. *Sens. Actuators B Chem.*, **211**, 310–317.
26. Naoaki,Y. and Shinichi,K. (2014) Recent research progress on iron- and manganese-based positive electrode materials for rechargeable sodium batteries. *Sci. Technol. Adv. Mater.*, **15**, 043501.
27. Pang,H., Yan,Z., Ma,Y., Li,G., Chen,J., Zhang,J., Du,W. and Li,S. (2013) Cobalt pyrophosphate nano/microstructures as promising electrode materials of supercapacitor. *J. Solid State Electrochem.*, **17**, 1383–1391.
28. Fishbane,S.N., Singh,A.K., Cournoyer,S.H., Jindal,K.K., Fanti,P., Guss,C.D., Lin,V.H., Pratt,R.D. and Gupta,A. (2015) Ferric pyrophosphate citrate (Triferic™) administration via the dialysate maintains hemoglobin and iron balance in chronic hemodialysis patients. *NDT*, **30**, 2019–2026.
29. Wang,P., Zhao,L., Liu,J., Weir,M.D., Zhou,X. and Xu,H.H.K. (2014) Bone tissue engineering via nanostructured calcium phosphate biomaterials and stem cells. *Bone Res.*, **2**, 14017.
30. Dumont,M.F., Baligand,C., Li,Y., Knowles,E.S., Meisel,M.W., Walter,G.A. and Talham,D.R. (2012) DNA surface modified gadolinium phosphate nanoparticles as MRI contrast agents. *Bioconjugate Chem.*, **23**, 951–957.
31. Doat,A., Pellé,F. and Lebugle,A. (2005) Europium-doped calcium pyrophosphates: allotropic forms and photoluminescent properties. *J. Solid State Chem.*, **178**, 2354–2362.
32. Lee,J.S., Kim,H., Jo,C., Jeong,J., Ko,J., Han,S., Lee,M.S., Lee,H.-Y., Han,J.W., Lee,J. *et al.* Enzyme-driven Hasselback-like DNA-based inorganic superstructures. *Adv. Funct. Mater.*, **27**, 1704213.
33. Vashishtha,A.K., Wang,J. and Konigsberg,W.H. (2016) Different divalent cations alter the kinetics and fidelity of DNA polymerases. *J. Biol. Chem.*, **291**, 20869–20875.
34. Saturno,J., Lázaro,J.M., Blanco,L. and Salas,M. (1998) Role of the first aspartate residue of the 'YxDTDS' motif of Φ29 DNA polymerase as a metal ligand during both TP-primed and DNA-primed DNA synthesis. *J. Mol. Biol.*, **283**, 633–642.
35. Joffroy,B., Uca,Y.O., Prešern,D., Doye,Jonathan P.K. and Schmidt,T.L. (2018) Rolling circle amplification shows a sinusoidal template length-dependent amplification bias. *Nucleic Acids Res.*, **46**, 538–545.
36. Ducani,C., Bernardinelli,G. and Högberg,B. (2014) Rolling circle replication requires single-stranded DNA binding protein to avoid termination and production of double-stranded DNA. *Nucleic Acids Res.*, **42**, 10596–10604.
37. Tuma,R.S., Beaudet,M.P., Jin,X., Jones,L.J., Cheung,C.-Y., Yue,S. and Singer,V.L. (1999) Characterization of SYBR gold nucleic acid gel Stain: a dye optimized for use with 300-nm ultraviolet transilluminators. *Anal. Biochem.*, **268**, 278–288.
38. Xie,L., Cheng,H., Qi,H., Wang,T., Zhao,H., Huang,G. and Du,Y. (2015) Nanostructural morphology master-regulated the cell capture efficiency of multivalent aptamers. *RSC Adv.*, **5**, 39791–39798.
39. Ririe,K.M., Rasmussen,R.P. and Wittwer,C.T. (1997) Product differentiation by analysis of DNA melting curves during the polymerase chain reaction. *Anal. Biochem.*, **245**, 154–160.
40. Guan,Z., Liu,J., Bai,W., Lv,Z., Jiang,X., Yang,S., Chen,A. and Lv,G. (2014) Label-free and sensitive fluorescent detection of sequence-specific single-strand DNA based on S1 nuclease cleavage effects. *PLoS ONE*, **9**, e108401.
41. Brouzi,K., Ennaciri,A. and Harcharras,M. (2004) Thermal transformations and infrared studies of $Mn_2P_2O_7{\cdot}2H_2O$. *Phosphorus Sulfur Silicon Relat. Elem.*, **179**, 1329–1339.
42. Guo,Y., Wang,Y., Li,S., Niu,L., Wei,D. and Zhang,S. (2017) DNA-spheres decorated with magnetic nanocomposites based on terminal transfer reactions for versatile target detection and cellular targeted drug delivery. *Chem. Commun.*, **53**, 4826–4829.
43. Guo,Y., Li,S., Wang,Y. and Zhang,S. (2017) Diagnosis–Therapy integrative systems based on magnetic RNA nanoflowers for Co-drug delivery and targeted therapy. *Anal. Chem.*, **89**, 2267–2274.
44. Fowlis,D.C. and Stager,C.V. (1969) Magnetic susceptibility of $Mn_2P_2O_7$. *Can. J. Phys.*, **47**, 371–373.
45. Adams,R.D., Layland,R. and Payen,C. (1995) New manganese pyrophosphates: The syntheses, crystallographic characterizations and magnetic properties of $BaMnP_2O_7$ and $CaMnP_2O_7$. *Polyhedron*, **14**, 3473–3480.
46. Krishnamohan Sharma,C.V., Chusuei,C.C., Clérac,R., Möller,T., Dunbar,K.R. and Clearfield,A. (2003) Magnetic property studies of manganese−phosphate complexes. *Inorg. Chem.*, **42**, 8300–8308.
47. Volkova,O.S., Shvanskaya,L.V., Ovchenkov,E.A., Zvereva,E.A., Volkov,A.S., Chareev,D.A., Molla,K., Rahaman,B., Saha-Dasgupta,T. and Vasiliev,A.N. (2016) Structure-property relationships in α-, β′-, γ-modifications of $Mn_3(PO_4)_2$. *Inorg. Chem.*, **55**, 10692–10700.
48. Forsyth,J.B., Wilkinson,C., Paster,S. and Wanklyn,B.M. (1989) The magnetic structure of cobalt diphosphate $Co_2P_2O_7$. *J. Phys.: Condens. Matter*, **1**, 169–178.

Downloaded from https://academic.oup.com/nar/article-abstract/46/15/7495/5052372 by Oxford University user on 23 August 2019